

**DENSITY FUNCTIONAL TIGHTBINDING STUDIES OF TiO<sub>2</sub> POLYMORPHS**

by

**Gandamipfa Mulatedzi**

Thesis submitted in fulfilment of the requirements for the degree of

**Doctor of Philosophy (PhD)**

in

Physics

In the

**FACULTY OF SCIENCE AND AGRICULTURE**

**(School of Physical and Minerals Science)**

At the

**UNIVERSITY OF LIMPOPO,**

**SOUTH AFRICA**

**SUPERVISOR: Prof. P.E. Ngoepe**

**2020**

# ABSTRACT

Titanium dioxide is among the most abundant materials and it has many of interesting physical and chemical properties (i.e., low density, high thermal and mechanical strength, insensitivity to corrosion) that make it a compound of choice for electrodes materials in energy storage. There are, however, limitations on the theoretical side to using the main electronic structure theories such as Hartree-Fock (HF) or density-functional (DFT) especially for large periodic and molecular systems.

The aim of the theses is to develop a new, widely transferable, self-consistent density functional tight binding SCC-DFTB data base of  $\text{TiO}_2$ , which could be applied in energy storage anodes with a large number of atoms. The  $\text{TiO}_2$ ,  $\text{LiTiO}_2$  and  $\text{NaTiO}_2$  potentials were derived following the SCC-DFTB parameterization procedure; where the generalized gradient approximation (GGA) and local density approximation (LDA) exchange-correlation functional were employed yielding Slater-Koster DFTB parameters. The results of derived parameters were validated by being compared with those of the bulk rutile and brookite polymorphs. The structural lattice parameters and electronic properties, such as the bandgaps were well reproduced. Most mechanical properties were close to those in literature, except mainly for  $C_{33}$  which tended to be underestimated due to the choice of exchange-correlation functional. The variation of the bulk lattice parameter and volume with lithiation and sodiation were predicted and compared reasonably with those in literature.

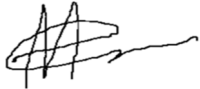
The newly derived DFTB parameters were further used to calculate bulk properties of the anatase, which is chemically more stable than other polymorphs. Generally, the accuracy of the lattice structural, electronic and mechanical properties of the bulk anatase were consistent with those of the rutile and brookite polymorphs. Furthermore, nanostructures consisting of a large number of atoms, which extend beyond the normal scope of the conventional DFT calculations, were modelled both structurally and electronically. Structural variations with lithiation was consistent with experimental and sodiation tends to enhance volume expansion than lithiation. Anatase  $\text{TiO}_2$  and  $\text{LiTiO}_2$  nanotubes of various diameters were generated using NanoWrap builder within MedeA<sup>®</sup> software. Its outstanding resistance to expansion during lithium insertion and larger surface area make the  $\text{TiO}_2$  nanotube a promising

candidate for rechargeable lithium ion batteries. The outcomes of this study will be beneficial to future development of TiO<sub>2</sub> nanotube and other nanostructures.

Lastly, our DFTB Slater-Koster potentials were applied to recently discovered trigonal bipyramid (TB), *i.e.* TiO<sub>2</sub> (TB)-I and TiO<sub>2</sub> (TB)-II polymorphs, which have enormous 1-D channels that provide suitable pathways for mobile ion transport. All structural, electronic properties were consistent with those in literature and all elastic properties agreed excellently with those that were calculated using DFT methods. Finally, the bulk structures of the two polymorphs, were lithiated and sodiated versions and electronic and structural properties were studied, together with the lithiated versions of associated nanostructures consisting of a large number of atoms. Generally, the TiO<sub>2</sub> (TB)-I structure was found to be mechanically, energetically more stable and ductile than TiO<sub>2</sub> (TB)-II. Hence, it will be beneficial to use TiO<sub>2</sub> (TB)-I as an anode material for sodium ion batteries (SIB), due to its unique ductility and larger 1D channels.

# DECLARATION

I declare that the thesis hereby submitted to the University of Limpopo, for the degree of Doctor of Philosophy in Physics has not previously been submitted by me for a degree at this or any other University; that it is my work in design and in execution, and that all material contained herein has been duly acknowledged.

A handwritten signature in black ink, consisting of several overlapping loops and a long horizontal stroke extending to the right.

17 September 2020

Signature

Date

# DEDICATIONS

TO MY LATE PARENTS  
NDITSHENI AND TSHINAKAHO

MY WIFE

MAPULA

MY SON

TSHIFHIWA

AND MY DAUGHTER

MUVHUSO

# ACKNOWLEDGEMENTS

The research work presented in this thesis was carried under the supervision of Professor P. E. Ngoepe from Materials Modeling Centre, University of Limpopo, who provided excellent guidance towards execution of this thesis for the Doctor of Philosophy degree (PhD) in physics. I would also like to thank all my colleagues in the Materials Modeling Centre and Department of Physics for being cooperative during the execution of this work.

Special gratitude to the National Research Fund (NRF), the Department of Science and Innovation (DSI) Energy Storage Research Development and Innovation initiative and Materials Modeling Centre for the financial support provided during the execution of this work.

I would like to thank my late parents who encouraged me to go to school, even though they never got to celebrate my achievements with me.

Finally, special thanks to my wife Mapula, my kids Tshifhiwa and Muvhuso for their support and understanding. Most of all, I would like to thank the Almighty for over-viewing and keeping me safe throughout.

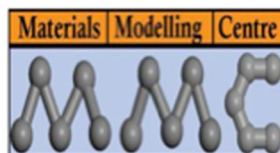


# TABLE OF CONTENTS

ABSTRACT .....	I
DECLARATION .....	III
DEDICATIONS .....	IV
ACKNOWLEDGEMENTS .....	V
TABLE OF CONTENTS .....	VI
LIST OF FIGURES .....	X
LIST OF TABLES .....	XVII
<b>CHAPTER 1: BACKGROUND .....</b>	<b>1</b>
1.1 ENVIRONMENTAL IMPACT OF AGILITY ON SOCIETY AND SUSTAINABLE ENERGY .....	1
1.2 ENERGY STORAGE DEVICES .....	2
1.3 LITERATURE REVIEW .....	3
1.3.1 TiO <sub>2</sub> Nanotubes .....	3
<b>Synthesis of TiO<sub>2</sub> nanotubes and nanoporous .....</b>	<b>4</b>
1.3.2 TiO <sub>2</sub> flakes .....	6
1.3.3 TiO <sub>2</sub> (B) .....	7
<b>Synthesis of TiO<sub>2</sub> (B) .....</b>	<b>8</b>
1.3.4 Bulk anatase TiO <sub>2</sub> .....	8
<b>Synthesis of bulk anatase TiO<sub>2</sub> .....</b>	<b>10</b>
1.3.5 Brookite .....	10
1.3.6 Rutile .....	11
1.3.7 TiO <sub>2</sub> trigonal bipyramid (TB) .....	12
1.3.8 TiO <sub>2</sub> nanospheres .....	12
<b>Synthesis of TiO<sub>2</sub> nanospheres .....</b>	<b>13</b>
1.4 MOTIVATION .....	14
1.5 SPECIFIC OBJECTIVES .....	14
1.6 OUTLINE OF THE STUDY .....	14
<b>CHAPTER 2: METHODOLOGY .....</b>	<b>16</b>
2.1 DENSITY-FUNCTIONAL BASED TIGHT-BINDING (DFTB) .....	16
2.1.1 Introduction .....	16
2.1.2 The Kohn–Sham Method .....	18

2.1.3 DFT as Basis for a Tight–Binding Method.....	21
2.2 THE ROLE OF DFTB IN MATERIALS MODELLING .....	24
2.2.1 The Standard DFTB Model without Self-Consistency .....	26
2.2.2 The Self–Consistent Charge Correction: SCC-DFTB.....	30
2.2.3 Weak Forces: Dispersion-Corrected SCC-DFTB .....	35
2.3 CASTEP CODE.....	37
2.3.1 Plane-Wave Basis Sets.....	37
2.3.2 Pseudopotentials.....	39
2.3.3 Ultrasoft pseudopotentials.....	40
2.4 MOLECULAR DYNAMICS .....	41
2.5 THEORETICAL BACKGROUND OF THE CALCULATED PROPERTIES .....	42
2.5.1 Density of States.....	42
2.5.2 Optical Properties.....	42
2.5.3 Elasticity .....	43
2.6 GENERATION OF TiO <sub>2</sub> NANOTUBES.....	49
2.7 GENERATION OF NANOSPHERES .....	50
<b>CHAPTER 3: DERIVATION OF DFTB POTENTIALS WITH VALIDATION USING</b>	
<b>THE RUTILE AND BROOKITE STRUCTURES .....</b>	<b>52</b>
<b>OVERVIEW.....</b>	<b>52</b>
3.1 SEVERAL CONSIDERATIONS WHEN PARAMETERIZING.....	52
3.1.1 DFT and DFTB calculations .....	52
3.1.2 The fitting process.....	52
3.1.3 Slater-Koster library file generation .....	53
3.1.4 Data coverage.....	53
3.1.5 Degrees of freedom and number of trials.....	53
3.1.6 Element-pair coverage .....	53
3.2 PARAMETERIZATION.....	54
3.2.1 Automatic parametrization scheme .....	55
3.3 VALIDATION OF DFTB SLATER-KOSTER POTENTIALS.....	56
3.3.1 Methodology.....	57
3.4 STRUCTURAL PROPERTIES .....	57
3.4.1 Rutile.....	57
3.4.2 Brookite .....	59



3.5 MECHANICAL PROPERTIES.....	60
3.5.1 Rutile.....	60
3.5.2 Brookite.....	61
3.6 ELECTRONIC PROPERTIES (RUTILE AND BROOKITE).....	62
3.7 LITHIATION.....	67
3.7.1 Rutile preferable sites.....	67
3.7.2 Rutile – Lithiated induced structural change.....	70
3.7.3 Brookite - Lithiated induced structural change.....	72
3.8 SUMMARY.....	74

## **CHAPTER 4: STRUCTURAL AND ELECTRONIC PROPERTIES OF ANATASE**

<b>TiO<sub>2</sub> POLYMORPH.....</b>	<b>76</b>
4.1 INTRODUCTION.....	76
4.2 METHODOLOGY.....	76
4.3 STRUCTURAL PROPERTIES (BULK).....	76
4.4 MECHANICAL AND ELECTRONIC PROPERTIES (BULK).....	78
4.5 LITHIATION (BULK).....	80
4.5.1 Preferable sites.....	80
4.5.2 Change in volume and lattice parameters for various (Li/Ti and Na/Ti)....	84
4.6 ANATASE TiO <sub>2</sub> NANOTUBES.....	88
4.6.1 Generating nanotubes with various diameters.....	88
4.6.2 Band gap energies of pure TiO <sub>2</sub> nanotube with various diameters.....	89
4.6.3 Band gap energies of Li <sub>x</sub> TiO <sub>2</sub> nanotubes with various diameters.....	90
4.7 ANATASE TiO <sub>2</sub> NANOSPHERES.....	92
4.7.1 Structural change for various (Li/Ti and Na/Ti).....	92
4.8 MOLECULAR DYNAMICS OF TiO <sub>2</sub> NANOTUBES).....	100
4.8.1 Methodology.....	100
4.9 MOLECULAR DYNAMICS FOR ANATASE TiO <sub>2</sub> NANOTUBE.....	100
4.10 SUMMARY.....	101

## **CHAPTER 5: STRUCTURAL AND ELECTRONIC PROPERTIES OF TiO<sub>2</sub> (TB-I)**

<b>AND (TB-II) POLYMORPHS.....</b>	<b>103</b>
5.1 INTRODUCTION.....	103
5.2 METHODOLOGY.....	104
5.3 BULK TiO <sub>2</sub> TB-I.....	104

5.3.1 Structural and mechanical properties of TiO <sub>2</sub> (TB)-I.....	104
5.3.2 Structural and energy change of TiO <sub>2</sub> (TB)-I during lithium/sodium intercalation.....	106
5.4 ELECTRONIC PROPERTIES OF BULK Na <sub>x</sub> TiO <sub>2</sub> TB-I.....	111
5.5 LITHIATION OF TiO <sub>2</sub> TB-I NANOSPHERE.....	112
5.5.1 Lithiation and structural properties of TiO <sub>2</sub> (TB)-I nanospheres.....	112
5.5.2 Electronic properties of TiO <sub>2</sub> (TB)-I nanospheres.....	115
5.5.3 Summary on impact of lithiation for TiO <sub>2</sub> (TB)-I nanospheres.....	115
5.6 STRUCTURAL PROPERTIES OF BULK TiO <sub>2</sub> (TB)-II DURING LITHIATION/SODIATION ...	119
5.7 ELECTRONIC PROPERTIES OF BULK Na <sub>x</sub> TiO <sub>2</sub> AND Li <sub>x</sub> TiO <sub>2</sub> TB-II.....	122
5.8 STRUCTURAL PROPERTIES OF TiO <sub>2</sub> (TB)-II NANOSPHERE DURING LITHIATION.....	124
5.9 SUMMARY.....	125
<b>CHAPTER 6: CONCLUSIONS AND RECOMMENDATIONS.....</b>	<b>128</b>
6.1 CONCLUSION.....	128
6.2 RECOMMENDATIONS.....	130
6.3 CONTRIBUTIONS OF THE STUDY.....	130
6.4 LIMITATIONS OF THE STUDY.....	131
<b>BIBLIOGRAPHY.....</b>	<b>132</b>
<b>APPENDIX A.....</b>	<b>158</b>
<b>STEEPEST DESCENT MINIMIZATION METHOD.....</b>	<b>158</b>
<b>APPENDIX B.....</b>	<b>159</b>
<b>ADOPTED BASIS NEWTON-RAPHSON (ABNR).....</b>	<b>159</b>
<b>APPENDIX C.....</b>	<b>160</b>
<b>SMART ALGORITHM.....</b>	<b>160</b>
<b>APPENDIX D.....</b>	<b>161</b>
<b>PAPER PRESENTED AT CONFERENCES.....</b>	<b>161</b>
<b>APPENDIX E.....</b>	<b>163</b>
<b>ACRONYMS.....</b>	<b>163</b>

## LIST OF FIGURES

Figure 1.1. Contribution of carbon emission sectors globally [1].	1
Figure 1.2. (a) A side and (b) cross sectional view of optimized 6-layer (6, 0) TiO <sub>2</sub> with a [101] orientation of the axis.	4
Figure 1.3. Schematic of fabrication process of obtaining TiO <sub>2</sub> nanotubes with nanoporous layers on top and complete titania nanoporous (TNP) structure via two-steps anodization: (a) Ti-foil, (b) First anodization and formation of TNTs with oxide layer on top, (c) TNTs with clear top end, (d) Ti-substrate after separation of TNTs, (e) TNTs covered with thin nanoporous layer, (f) complete TNP structure with uniform and parallel nanochannels [14].	5
Figure 1.4. Scanning electron microscope (SEM) images of TiO <sub>2</sub> samples. (a) TiO <sub>2</sub> Flakes, (b) calcined TiO <sub>2</sub> Flakes, (c) edge of TiO <sub>2</sub> Flakes and (d) edge of calcined TiO <sub>2</sub> Flakes [20].	7
Figure 1.5. A unit cell of anatase TiO <sub>2</sub> with tetragonal and space group of I41/amd, grey and red balls represent Ti and O atoms respectively.	9
Figure 1.6. Schematic image of Li ions (purple spheres) inserted into anatase bulk TiO <sub>2</sub> structure.	10
Figure 1.7. Unit cell of brookite TiO <sub>2</sub> (oxygen and titanium atoms are represented by red sphere and grey octahedral site, respectively).	11
Figure 1.8. Unit cell of rutile TiO <sub>2</sub> (oxygen and titanium atoms are represented by red sphere and grey octahedral site, respectively).	12
Figure 1.9. TiO <sub>2</sub> (TB) phases consist of a [TiO <sub>5</sub> ] trigonal bipyramid structure unit....	12
Figure 1.10. (A) Schematic illustration (cross-sectional view) of the ripening process and two types (i and ii) of hollow structures. Evolution (TEM images) of TiO <sub>2</sub> nanospheres synthesized with 30 mL of TiF <sub>4</sub> (1.3 mM) at 180°C with different reaction times: (B) 2h (scale bar=200mm), (C) 20h (scale bar=200mm), (D) 50h (scale bar=500mm) [51].	13
Figure 2.1. Flow-chart of a typical DFT calculation within the Kohn-Sham method [63].	20

Figure 2.2. Hierarchy for some of the method for the atomistic modeling of materials. .....	25
Figure 2.3. Flow chart describing the computational procedure for the calculation of the total energy of a solid with molecular dynamics [63]. .....	41
Figure 2.4. Generation of TiO <sub>2</sub> nanotubes with various wrapping direction.....	50
Figure 2.5 Image of nanosphere structures generated from bulk TiO <sub>2</sub> (pure and lithiated respectively). Ti, O and Li atoms are in grey, red and purple spheres respectively. ....	51
Figure 3.1. The atomic structure of rutile TiO <sub>2</sub> with channels. Red spheres denote oxygen.....	58
Figure 3.2. The atomic structure of brookite TiO <sub>2</sub> with channels. Red sphere denote oxygen.....	59
Figure 3.3. The total and partial density of states (DOS) of rutile TiO <sub>2</sub> computed from DFTB.....	63
Figure 3.4. The total and partial density of states (DOS) of brookite TiO <sub>2</sub> computed from DFTB.....	64
Figure 3.5. Band structure and the corresponding DOS of brookite obtained with (a) DFTB+ (This work), (b) DFT-GGA [141] and (c) DFT-GGA [139].....	65
Figure 3.6. Band structure and the corresponding DOS of rutile obtained with (a) DFTB+, (b) DFT-GGA [141] and (c) DFT-GGA [139]. ....	66
Figure 3.7. The lithium rutile phase in the LiTiO <sub>2</sub> sample indicating two possible Li positions. Ti, O and Li atoms are in grey, red and purple spheres respectively. ....	67
Figure 3.8. (a) The total DOS, (b) the lithium rutile phase in the Li <sub>x</sub> TiO <sub>2</sub> sample indicating possible Li ion position (I) and insert of the energy at the Fermi level.....	68
Figure 3.9. (a) The total DOS, (b) the lithium rutile phase in the Li <sub>x</sub> TiO <sub>2</sub> sample indicating possible Li ion position (II) and insert of the energy at the Fermi level.....	69

Figure 3.10. DOS of the rutile TiO <sub>2</sub> with two different sites calculated using the DFTB+. .....	70
Figure 3.11. (a) The rutile system used consists of a primitive cell built up of 2 × 2 × 2 unit cells (16 Ti and 32 O atoms) and (b) experimental lattice parameters changes of a single Li ion in a primitive cell.....	71
Figure 3.12. (a) The system used consists of a primitive cell built up of 2 × 2 × 4 unit cells (32 Ti and 64 O atoms) and (b) experimental volume changes of a single Li ion in a primitive cell.....	72
Figure 3.13. (a) and (b) Ti-Ti bond length before and after lithiation, (c) and (d) O-O bond length before and after lithiation respectively. Ti, O and Li atoms are in grey, red and purple spheres respectively.....	73
Figure 3.14. (a) Lattice parameters change of a unit cell of brookite Li <sub>n</sub> Ti <sub>16</sub> O <sub>32</sub> as a function of Li/Ti ratio and (b) from literature the cell parameters (a, b, c) of brookite during the Li intercalation [151]. .....	74
Figure 4.1 (a) The tetragonal crystal cell of anatase, (b) The atomic structure of TiO <sub>6</sub> octahedron in anatase TiO <sub>2</sub> . Grey and red spheres denote titanium and oxygen, respectively. ....	77
Figure 4.2. Comparison of the total and partial electronic density of states of anatase TiO <sub>2</sub> calculated using the (a) DFTB (b) and (c) VASP (HSE06 hybrid density functional) [156] [157]. .....	79
Figure 4.3. The anatase LiTiO <sub>2</sub> structure indicating three possible Li positions, I, II, and III; Ti, O and Li atoms are indicated in grey, red and purple spheres respectively. ...	80
Figure 4.4. The lithium anatase phase in the Li <sub>x</sub> TiO <sub>2</sub> sample indicating possible Li position(I). .....	81
Figure 4.5. The lithium anatase phase in the Li <sub>x</sub> TiO <sub>2</sub> sample indicating possible Li position(II). .....	82
Figure 4.6. The lithium anatase phase in the Li <sub>x</sub> TiO <sub>2</sub> sample indicating possible Li position (III). .....	83

Figure 4.7. DOS of the anatase TiO <sub>2</sub> with three different sites calculated using the DFTB+.....	83
Figure 4.8. (a) and (b) DFTB calculated lattice parameters change of a unit cell of Li <sub>n</sub> TiO <sub>2</sub> as a function of Li/Ti ratio (c) and (d) Lattice parameters of a unit cell of Li <sub>n</sub> TiO <sub>2</sub> as a function of Li concentration during intercalation [163], (e) and (f) cell dimensions of Li <sub>x</sub> TiO <sub>2</sub> as a function of x lithium [164].....	84
Figure 4.9. (a) and (b) O-O bond length before and after lithiation, (c) and (d) Ti-Ti bond length before and after lithiation. Ti, O and Li atoms are in grey, red and purple spheres respectively.....	86
Figure 4.10. (a) Volume change of a unit cell of Li <sub>x</sub> TiO <sub>2</sub> as a function of Li/Ti ratio, (b)Volume change of a unit cell of Li <sub>x</sub> TiO <sub>2</sub> as a function of Li concentration during intercalation, (c) Cell volume of Li <sub>x</sub> TiO <sub>2</sub> plotted [164] against lithium x (experimental work). ....	86
Figure 4.11. Predicted cell volume of Na <sub>x</sub> TiO <sub>2</sub> plotted against sodium concentrations. ....	88
Figure 4.12. Anatase LiTiO <sub>2</sub> nanotubes with diameter range (19-29Å) generated from bulk anatase.....	88
Figure 4.13. Unrelaxed and relaxed anatase TiO <sub>2</sub> nanotube structure. Ti and O atoms are in grey and red spheres respectively.....	90
Figure 4.14. DFTB+ band structure and total density of states of a fully optimized LiTiO <sub>2</sub> (19-29 Å). ....	92
Figure 4.15. DFTB+ optimized structures for stoichiometric Li <sub>x</sub> TiO <sub>2</sub> (x=0.1, 0.6, 0.9 and 1.0). Ti, O and Li atoms are in grey, red and purple spheres respectively. ....	94
Figure 4.16. Radial distribution functions (RDFs) for anatase Li <sub>x</sub> TiO <sub>2</sub> (x=0.1 - 1) nanospheres. ....	94
Figure 4.17. The energies and volumes of Li <sub>x</sub> TiO <sub>2</sub> nanospheres where x= 0.0, 0.1, 0.6, 0.9 and 1.0. ....	95
Figure 4.18. Partial density of states (PDOS) for anatase Li <sub>x</sub> TiO <sub>2</sub> nanosphere.....	96

Figure 4.19. DFTB+ optimized structures for stoichiometric $\text{Na}_x\text{TiO}_2$ ( $x=0.25, 0.5, 0.75$ and $1.0$ ). Ti, O and Na atoms are in grey, red and purple spheres respectively.....	97
Figure 4.20. Radial distribution function (RDF) for anatase $\text{Na}_x\text{TiO}_2$ nanosphere. ....	97
Figure 4.21. The graph for volumes of $\text{Na}_x\text{TiO}_2$ nanospheres vs Na/Ti (from 0.0 to 1.0). .....	98
Figure 4.22. DFT optimized structures for stoichiometric $\text{NaTiO}_2$ . Left panel: rhombohedral layered structure [175]. Right panel: tetragonal $\text{LiTiO}_2$ structure [176]. .....	98
Figure 4.23. Partial density of states (PDOS) for anatase $\text{Na}_x\text{TiO}_2$ ( $x=0.2 - 1$ ) nanospheres. ....	99
Figure 4.24. Structure of anatase $\text{TiO}_2$ nanotube at different temperatures using MD NVT ensemble. Ti and O atoms are in blue and red spheres respectively.....	101
Figure 4.25. Bandgap vs. temperature for anatase $\text{TiO}_2$ nanotube (a) using NVT ensemble molecular dynamics and (b) one obtained from diffuse reflectance experiments [177]......	101
Figure 5.1. The crystal structures for $\text{TiO}_2$ (TB)-I phase: Ti, grey balls; O, red balls. .....	105
Figure 5.2. The total energy of fully lithiated $\text{TiO}_2$ (TB)-I at various sites, 4a, 4b and 4c (Li-purple, O-red and Ti-grey).....	107
Figure 5.3. The total energy of fully sodiated $\text{TiO}_2$ (TB)-I at various sites 4a, 4b and 4c (Na-pink, O-red and Ti-grey). ....	108
Figure 5.4. Cell dimensions of $\text{Li}_x\text{Ti}_4\text{O}_2$ (TB)-I as a function of x lithium at (I) 4a, (II) 4b and (III) 4c site. (IV) Volume change for 4a, 4b and 4c sites.....	109
Figure 5.5. Cell dimensions of $\text{Na}_x\text{Ti}_2\text{O}_4$ as a function of x sodium at (I) 4a, (II) 4b and (III) 4c site. (IV) Volume change for 4a, 4b and 4c sites.....	110
Figure 5.6. The total energy of various (I) lithium and (II) sodium concentrations into $\text{TiO}_2$ (TB)-I at various sites. ....	110

Figure 5.7. Partial density of states of $\text{Na}_x\text{TiO}_2$ compounds in the TB-I phase at different values of Na content $x$ , calculated with the DFTB method. ....	111
Figure 5.8. Projected density of states of $\text{Na}_x\text{TiO}_2$ compounds in TB-I phase at different-Na $x$ content, calculated with the PBsol XC functional [189]. ....	111
Figure 5.9. Partial density of states of $\text{Li}_x\text{TiO}_2$ compounds in the TB-I phase at different values of Li content $x$ , calculated with the DFTB method. ....	112
Figure 5.10. Volume profile of $\text{TiO}_2$ (TB)-I nanosphere during lithiation. ....	113
Figure 5.11. $\text{TiO}_2$ (TB)-I nanospheres with various lithium ions concentration into 4a site. Ti, O and Li atoms are in grey, red and purple spheres respectively. ....	114
Figure 5.12. $\text{TiO}_2$ (TB)-I nanospheres with various lithium ions concentration into 4b site. Ti, O and Li atoms are in grey, red and purple spheres respectively. ....	114
Figure 5.13 $\text{TiO}_2$ (TB)-I nanospheres with various lithium ions concentration into 4c site. Ti, O and Li atoms are in grey, red and purple spheres respectively. ....	115
Figure 5.14. Partial density of states (PDOS) for $\text{TiO}_2$ (TB)-I nanospheres with various lithium ions concentration into 4a site. ....	116
Figure 5.15. Partial density of states (PDOS) for $\text{TiO}_2$ (TB)-I nanospheres with various lithium ions concentration into 4b site. ....	117
Figure 5.16. Partial density of states (PDOS) for $\text{TiO}_2$ (TB)-I nanospheres with various lithium ions concentration into 4c site. ....	118
Figure 5.17. The crystal structure of $\text{TiO}_2$ (TB)-II polymorph. Ti and O atoms are in grey and red spheres respectively. ....	119
Figure 5.18. Cell dimensions of (i) $\text{Li}_x\text{Ti}_4\text{O}_2$ and (ii) $\text{Na}_x\text{Ti}_4\text{O}_2$ as a function of $x$ lithium/sodium at 8d sites. ....	121
Figure 5.19. Volume profile of bulk $\text{TiO}_2$ (TB)-II during lithiation (i) and sodiation (ii). ....	122
Figure 5.20. Partial density of states of $\text{Na}_x\text{TiO}_2$ compounds in the TB-II phase at different values of Na content $x$ , calculated with the DFTB method. ....	123



Figure 5.21. Partial density of states of $\text{Li}_x\text{TiO}_2$ compounds in the TB-II phase at different values of Li content $x$ , calculated with the DFTB method. ....	123
Figure 5.22. $\text{TiO}_2$ (TB)-II nanospheres with various lithium ions concentration into 8d site. Ti, O and Li atoms are in grey, red and purple spheres respectively. ....	124
Figure 5.23. Volume profile for lithiated $\text{TiO}_2$ (TB)-II nanosphere.....	125
Figure 5.24. Partial density of states (PDOS) for $\text{TiO}_2$ (TB)-II nanospheres with various lithium ions concentration into 8d site.....	127

# LIST OF TABLES

Table 2.1. Critical K-points in the first Brillouin zone. ....	43
Table 3.1. Lattice parameters (a, b and c) and volume (V) of rutile TiO <sub>2</sub> calculated with DFTB compared with other theoretical and experimental data.....	58
Table 3.2. Lattice parameters (a, b and c) and volume (V) of brookite TiO <sub>2</sub> calculated with DFTB compared with the LDA, GGA and experimental. ....	60
Table 3.3. Elastic constants C <sub>ij</sub> (GPa), bulk modulus B(GPa), shear modulus G(GPa), Young's modulus E(GPa), Pugh modulus ratio G/B and Possion's ratio (M) for the bulk rutile TiO <sub>2</sub> . ....	61
Table 3.4. Elastic constants C <sub>ij</sub> (GPa), bulk modulus B(GPa), shear modulus G(GPa), Young's modulus E(GPa), Pugh modulus ratio G/B and Possion's ratio for bulk TiO <sub>2</sub> brookite. ....	62
Table 3.5. Results band gap energies for TiO <sub>2</sub> polymorphs (rutile and brookite). The results are compared with available experimental data and other computational results.....	63
Table 3.6 Relative energies and lattice parameters for the most stable Li intercalation sites in rutile TiO <sub>2</sub> . ....	70
Table 4.1. Titanium—Oxygen compound handmade parametrization (tiorg), automatically created one (auto) and the one that we created. Atom pairs denote distance in Å.....	77
Table 4.2. Lattice parameters (a, b and c) and volume (V) of anatase TiO <sub>2</sub> calculated with DFTB method compared with the theoretical and experimental values. ....	78
Table 4.3. Elastic constants C <sub>ij</sub> (GPa), bulk modulus B (GPa), shear modulus G (GPa), Young's modulus E(GPa), Pugh modulus ratio G/B and Possion's ratio for anatase bulk TiO <sub>2</sub> . ....	79
Table 4.4. Relative energies and lattice parameters for the most stable Li intercalation sites in anatase TiO <sub>2</sub> . ....	81
Table 4.5. Lattice parameters and energies of Na <sub>x</sub> TiO <sub>2</sub> . ....	87

Table 4.6. Energy gaps of anatase TiO <sub>2</sub> nanotube with different diameters.....	89
Table 5.1. Geometry lattice parameters for crystalline TiO <sub>2</sub> TB-I. ....	104
Table 5.2. Elastic constants C <sub>ij</sub> (GPa), (Russ's, Voigt's and Hill's) bulk modulus B <sub>RVH</sub> (GPa) and shear modulus G <sub>RVH</sub> (GPa) for TiO <sub>2</sub> (TB)-I together with the theoretical and experimental results at zero pressure. ....	106
Table 5.3. Lattice parameters of TiO <sub>2</sub> (TB)-II. ....	119
Table 5.4. Elastic constants C <sub>ij</sub> (GPa), (Russ's,Voigt's and Hill's), bulk modulus B <sub>RVH</sub> and shear modulus G <sub>RVH</sub> for TiO <sub>2</sub> (TB)-II together with the theoretical and experimental.....	120

# Chapter 1: Background

## 1.1 Environmental impact of agility on society and sustainable energy

Human race reliance on fossil fuels has been cherished into the worldwide financial arrangement, but this made biology unsustainable. To meet the rising vitality and crude fabric requests of a developing and creating populace, the over-exploitation of fossil fuels has compromised the biological system antagonistically and irreversibly.

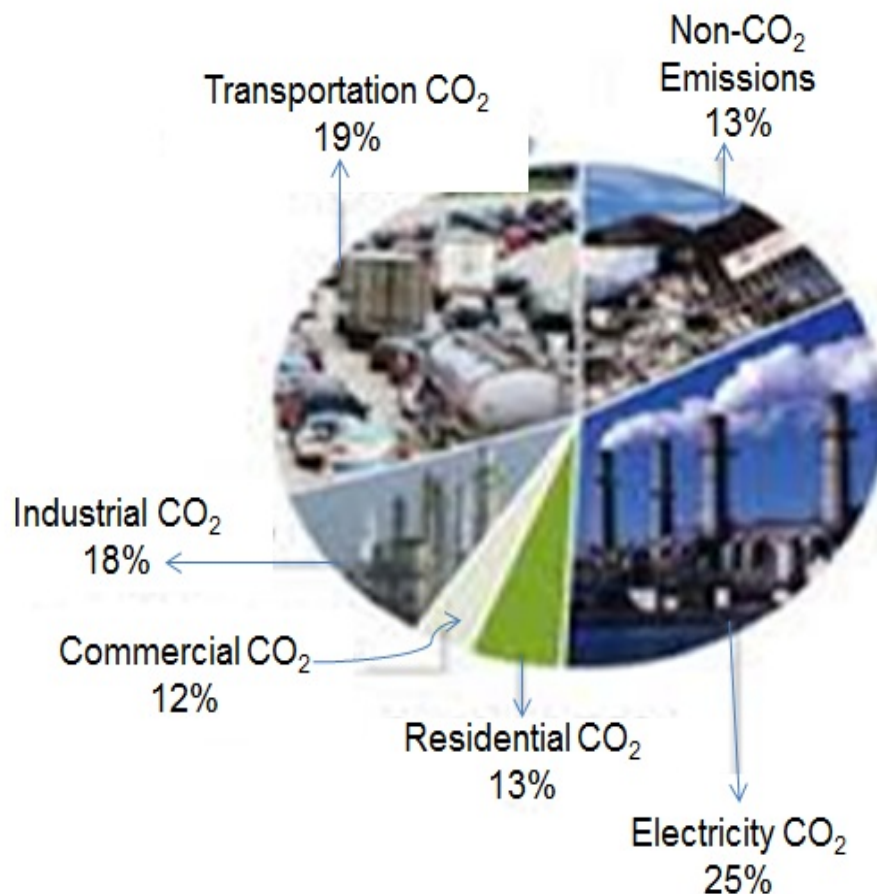


Figure 1.1. Contribution of carbon emission sectors globally [1].

As shown in Figure 1.1, the worldwide carbon emanation is increasing and much quicker than in any timescale of the complete human history. More than 80 percent of today's vitality requests depend on fossil powers. Out of this, around 40 per cent of fossil vitality is utilized for transportation as it were, making transport at the moment

the most noteworthy carbon emitter after coal fuelled establishments. This outflow has been perceived to be capable for upgrading worldwide warming and activating progressively fluctuating climate designs, counting annihilating surges, dry season and storms. The exceptionally essential thoughts of economic vitality and portability, from sun oriented control to a shrewd framework, from electric cars to versatile phones, may not have been realized without the advancement of electrochemical vitality capacity and change by implies of Fuel Cells and Batteries

## **1.2 Energy storage devices**

The extraordinary dominant part of the present lithium-particle batteries commonly uses dynamic materials of lithium cobalt oxide,  $\text{LiCoO}_2$  and crystalline graphite. Although financially, this has demonstrated to be effective in cell science, there is a general prerequisite for new positive and negative anode materials to encourage creation of the up and coming age of these vitality stockpiling gadgets. These materials will improve the presentation of current applications (for example mobile phones, PCs, iPods, individual gadgets and so forth.) just as permitting the entrance of new advertise openings, for example, control apparatuses, reinforcement control applications, electric vehicles and hybrid cars.

Over the past years  $\text{TiO}_2$  has attracted much attention due to its potential applications in environmental clean-up, energy production and storage. Since  $\text{TiO}_2$  is an abundant, low-cost and environmental friendly it has been confirmed to be the safe anode material in lithium ion batteries due to its Li-insertion potential (1.5-1.8V versus  $\text{Li}^+/\text{Li}$ ) in comparison with commercialized carbon anode materials [1,2,3]. The growth mechanism for  $\text{TiO}_2$  nanotubes mechanism is still not well understood, their comprehensive studies attract enhanced attention [4]. Hence, it becomes up vital not exclusively to synthesize such solid-state and molecular systems yet additionally to show their properties at a suitable size and time scale.  $\text{TiO}_2$  has several polymorphs. However, rutile and anatase are of interest due to their high stability as compared to other polymorphs [5].

For battery applications a high surface area as well as good electronic properties are important factors, this can be achieved through synthesis of the  $\text{TiO}_2$  as nanoclusters (nanotubes and nanospheres) [6]. The various polymorphs crystalline structures of  $\text{TiO}_2$ , namely anatase, brookite and rutile have been widely investigated for battery applications [7]. The anatase lattice belongs to a tetragonal body centred space group

named *I41/amd*. When the  $\text{TiO}_2$  is lithiated and the ratio of lithium rises above 0.5 ( $\text{Li}_{0.5}\text{TiO}_2$ ) the symmetry of the unit cell will decrease to an orthorhombic *Pmn21* space group. Due to this decrease in symmetry the unit cell will experience an increase in volume of about 4%. Generally, large volume expansion during lithiation is one of the reasons for capacity fading in batteries. However, the anatase structure has been reported to be better than the other structures in capacity to take up lithium ions [8]. Both bulk and nanostructured  $\text{TiO}_2$  have been investigated as anode materials. The process in the battery anode is based on the reduction of titanium from  $\text{Ti}^{4+}$  to  $\text{Ti}^{3+}$  and lithium insertion into the  $\text{TiO}_2$ . Lithium can be inserted reversibly into  $\text{TiO}_2$  to form  $\text{Li}_{0.5}\text{TiO}_2$ , since this gives a theoretical specific capacity of 168 mAh/g [9].

## 1.3 Literature Review

### 1.3.1 $\text{TiO}_2$ Nanotubes

Lithium-ion batteries (LIBs) are considered, the most promising energy storage devices for mobile electric vehicles, electronics and renewable energy systems operating on intermittent energy sources such as wind and solar [10]. Usually LIBs are connected in series or in parallel to deliver the user specified electrical characteristics. The growth mechanism for  $\text{TiO}_2$  nanotubes is still not well-understood and its structure is shown in Figure 1.3. Comprehensive theoretical studies have been carried out [11]. In 1995 the nanotubes of more complex structure based on the metal oxides were synthesized for the first time [12]. To date, considerable amount of information on such nanotubes has been accumulated, the method for their synthesis has been developed, and ways of modifying their properties and creation of new oxide nanostructures have been defined [13]. Hence, theoretical simulations of the nanotube stability, chemical and physical properties, play a key role [12] and stimulates further, more detailed study of known nanomaterials pointing to the synthesis of the new ones.

It was once proven that angle-dependent reactive ballistic deposition of amorphous nanostructured  $\text{TiO}_2$  films prepared directly on a Cu current collector, besides extra binder and conductive agents, constitutes an outstanding model system. This allows for the controlled and reproducible deposition and systematic study of the effect of various material properties along with morphology, surface area, and porosity on energy density and rate capability for dimensionally stable  $\text{TiO}_2$  anodes utilized in lithium ion batteries [17].

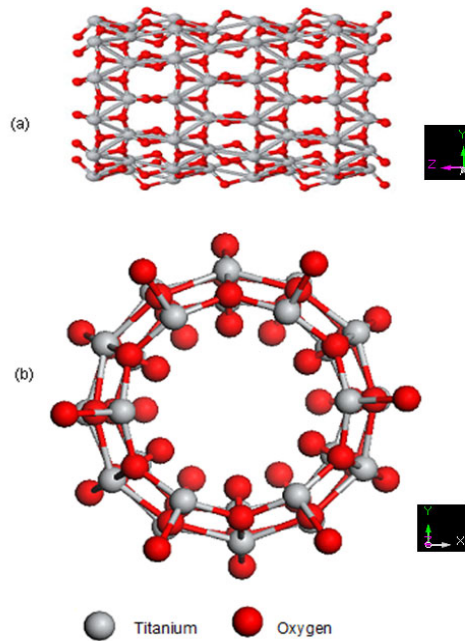


Figure 1.2. (a) A side and (b) cross sectional view of optimized 6-layer (6, 0) TiO<sub>2</sub> with a [101] orientation of the axis.

### Synthesis of TiO<sub>2</sub> nanotubes and nanoporous

The formation mechanism of TiO<sub>2</sub> nanotubular (TNT) and TiO<sub>2</sub> nanoporous (TNP) is shown in Figure 1.3. Well-known two-steps anodization method was applied to obtain highly ordered TNT and TNP structure. TNT is synthesized in ethylene glycol (EG) based electrolyte through the first step anodization using Ti-foil (Figure 1.3a). The top surface of the TNT is always with some kind of oxide layer (Figure 1.3b) irrespective of anodizing time. The oxide layer can be extracted with ultrasonic agitation and TNT with clear top end can be achieved (Figure 1.3c).

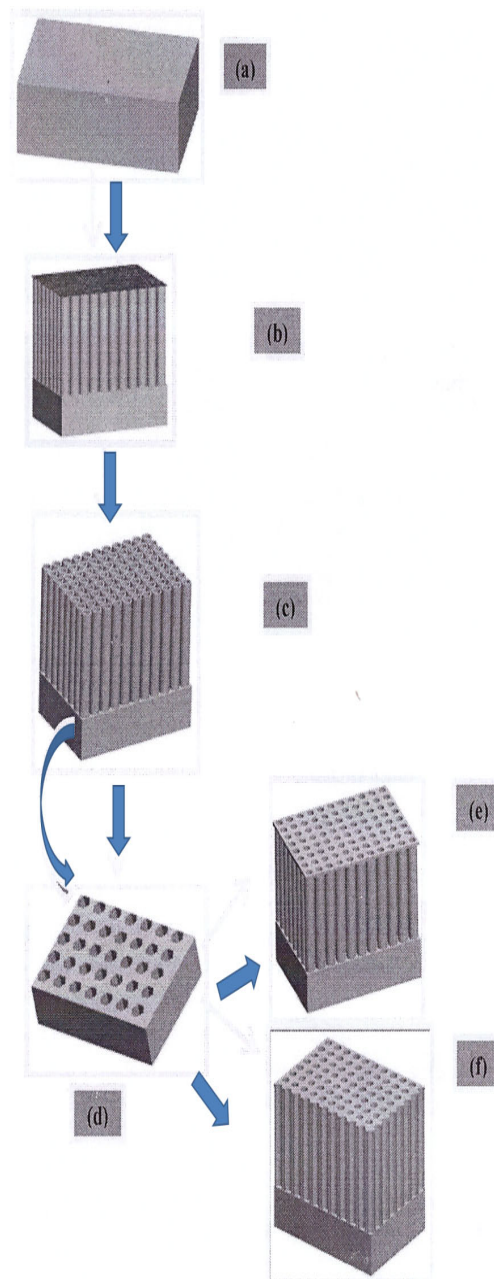


Figure 1.3. Schematic of fabrication process of obtaining TiO<sub>2</sub> nanotubes with nanoporous layers on top and complete titania nanoporous (TNP) structure via two-steps anodization: (a) Ti-foil, (b) First anodization and formation of TNTs with oxide layer on top, (c) TNTs with clear top end, (d) Ti-substrate after separation of TNTs, (e) TNTs covered with thin nanoporous layer, (f) complete TNP structure with uniform and parallel nanochannels [14].

TNT can be easily peeled-off from under lying patterned Ti-sheet by applying N<sub>2</sub> stream. Honeycomb-like patterned Ti-substrate is available for further anodization after separation of TNT from underlying Ti-foil (Figure 1.3.d). The second-step anodization in EG-based hydro-fluoric acid containing aqueous electrolytes produced TNT covered with a thin nano-porous layer on top surface (Figure 1.3.e), while the



second-step anodization in glycerol-based electrolyte led to highly uniform and ordered TNP morphology (Figure 1.3f).

### **1.3.2 TiO<sub>2</sub> flakes**

Anatase titanium dioxide is the most promising negative electrode material for Li-ion batteries due to its safety against overcharging and stable voltage plateau at 1.78 V [15]. However, the low electrical conductivity, poor rate capability and poor cycling performance caused by the structural changes during the lithiation process have limited its applications. A simple spreading method was used to produce novel TiO<sub>2</sub> flakes. In particular, the porous TiO<sub>2</sub> flakes exhibit larger reversible charge/discharge capacity, better rate capability and excellent cycling stability compared to anatase titanium dioxide nano-particles [16]. The thermal reaction process of the flakes was investigated by thermogravimetric differential thermal analysis (TG/DTA) [17]. The phase, structure, morphology and size distribution were examined by X-ray diffraction (XRD), high-resolution transmission electron microscopy (TEM) and scanning electron microscopy (SEM) [17]. The surface area and pore sizes were monitored by physisorption measurements. The relations between crystal structure, surface area, pore volume and electrochemical properties of anatase TiO<sub>2</sub> flakes were examined. The nano-sized grains of TiO<sub>2</sub> flakes, the pore volume and the surface area are all key factors contributing to the enhanced electrochemical properties [17].

#### **Synthesis of TiO<sub>2</sub> flakes**

Many synthetic methods were developed for TiO<sub>2</sub> flakes, but these processes are complex, time-consuming and difficult to be applied in large-scale synthesis. To reduce the complexity and the price of precursors of conventional synthesis process such as non-ionic surfactant template method and sol-gel method, [18,19] a simple spreading method can be used to make novel TiO<sub>2</sub> flakes. In particular, the porous TiO<sub>2</sub> flakes exhibit larger reversible charge/discharge capacity, better rate capability and excellent cycling stability compare to anatase TiO<sub>2</sub> nano-particles.

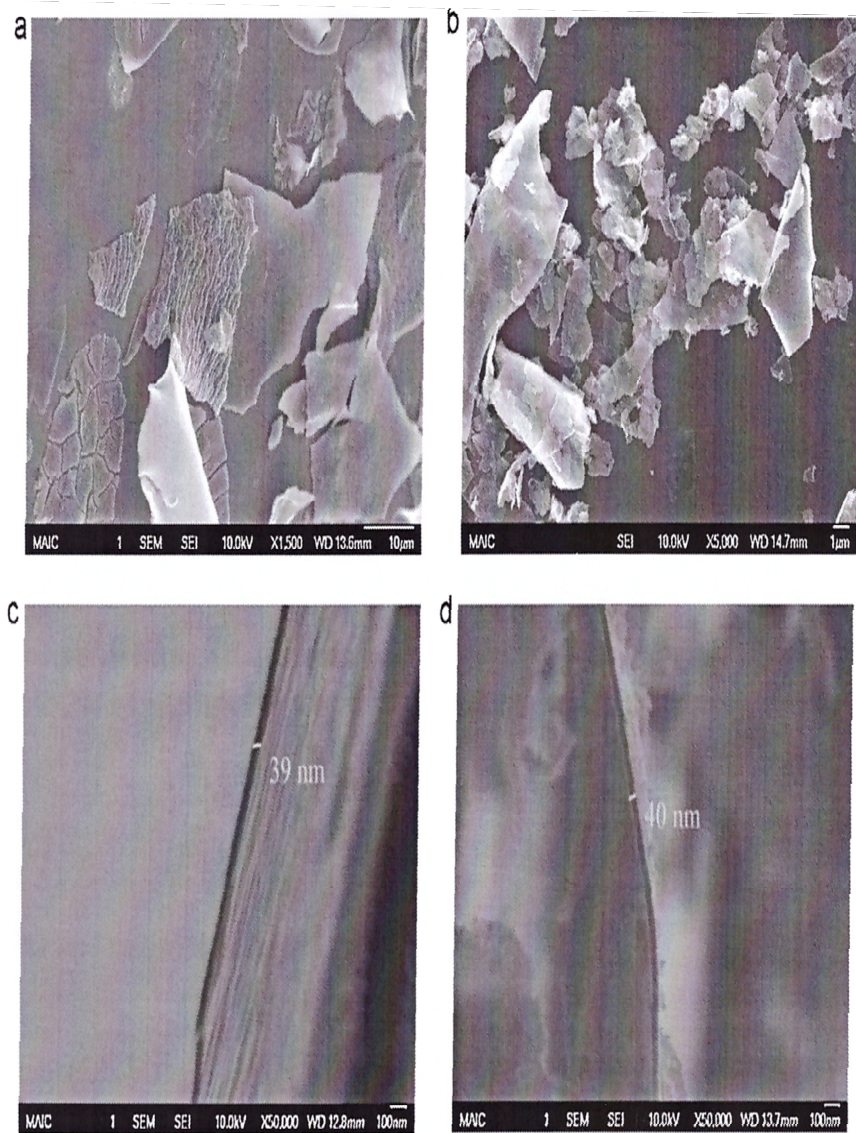


Figure 1.4. Scanning electron microscope (SEM) images of TiO<sub>2</sub> samples. (a) TiO<sub>2</sub> Flakes, (b) calcined TiO<sub>2</sub> Flakes, (c) edge of TiO<sub>2</sub> Flakes and (d) edge of calcined TiO<sub>2</sub> Flakes [20].

SEM images for TiO<sub>2</sub> flakes morphologies are shown in Figure 1.4 for different particle sizes. The grain size of TiO<sub>2</sub> flakes and calcined TiO<sub>2</sub> flakes are determined to be 4 nm and 9 nm respectively.

### 1.3.3 TiO<sub>2</sub> (B)

The TiO<sub>2</sub> (B) maximum intercalation amount of lithium ion is about 0.85 Li per Ti at 25°C [21]. TiO<sub>2</sub>(B) is the least dense polymorph of TiO<sub>2</sub>, and has a theoretical capacity of 335 mAh g<sup>-1</sup> which makes it a superior intercalation host for lithium compared with rutile and anatase [22]. It was demonstrated that bulk layered protonated titanates could be transformed to a metastable monoclinic modification of TiO<sub>2</sub> (TiO<sub>2</sub>(B)) under

annealing. This modification of TiO<sub>2</sub> has lower density than anatase or rutile and a monoclinic unit cell. Density ranges from (3.64 and 3.76 g.cm<sup>-3</sup>) which are smaller than the densities of anatase and rutile (3.9 and 4.25 g cm<sup>-3</sup>) [21]. Particles with higher surface areas are likely to result in electrodes with higher electrode/electrolyte contact areas. Coupled with the shorter diffusion paths within the smaller particles, this will lead to more facile intercalation in the order, tubes > wires > bulk material [2]. Reduced strain of intercalation and contributions from charge storage at the surface may also contribute to increased Li capacity, especially in the case of tubes which exhibit the highest surface area as well as wall thicknesses for intercalation [23].

### **Synthesis of TiO<sub>2</sub> (B)**

TiO<sub>2</sub> (B) is a metastable monoclinic modification of TiO<sub>2</sub> and was first synthesized by Marchand *et al.* [24] and [25]. Very recently, the use of TiO<sub>2</sub> (B) as photocatalyst has gained attention again due to its excellent photocatalytic activity which was reported by Zhu *et al.* [26]. In their work, they found that the unique structure of TiO<sub>2</sub> (B) nanofibers with a shell of anatase nanocrystals showed an excellent activity for the degradation of organic dye sulforhodamine B compared with that of P25. This exciting result makes us aware that further studies on TiO<sub>2</sub> (B) should be vital for extending the photocatalytic research field of TiO<sub>2</sub>. However, up to now, the synthesis of TiO<sub>2</sub>(B) is still a great challenge, and no facile synthesis method has been reported and the most common method for the synthesis of TiO<sub>2</sub>(B) now involves two steps: first, synthesis of H<sub>2</sub>Ti<sub>3</sub>O<sub>7</sub> by a hydrothermal treatment between the high concentration of NaOH aqueous solution and titanium compound, and subsequently with the thermal dehydration of H<sub>2</sub>Ti<sub>3</sub>O<sub>7</sub> [26], which is apparently complicated and time consuming. Thus, to find a new facile route to synthesize TiO<sub>2</sub>(B) is in urgent request.

#### **1.3.4 Bulk anatase TiO<sub>2</sub>**

3D structure of anatase TiO<sub>2</sub> consists of strongly distorted edge sharing TiO<sub>6</sub> octahedra with the space group of *I*<sub>41</sub>/*amd* as shown in Figure 1.5. The anatase TiO<sub>2</sub> can be measured as a stacking of 1D zigzag chains consisting of distorted edge-sharing octahedra. The purple spheres in Figure 1.6 depict the possible positions of lithium ions in anatase. Filling all sites leads to the stoichiometry of LiTiO<sub>2</sub>, but this is unlikely in a reality. Upon Li insertion, anatase converts into a two-phase mixture of tetragonal Li<sub>0.05</sub>TiO<sub>2</sub> (space group *I*<sub>41</sub>/*amd*) and the Li-rich orthorhombic Li<sub>0.5</sub>TiO<sub>2</sub>

(*Imma*) [27]. The overall orthorhombic distortion of the atomic positions in the transition from anatase to lithium titanate is insignificant and leads to more regularly shaped  $\text{TiO}_6$  octahedra in lithium titanate than in anatase.

Among different existing  $\text{TiO}_2$  structural polymorphs (anatase, rutile, brookite, and  $\text{TiO}_2(\text{B})$ ), studied in electrochemical cells vs.  $\text{Li}^+/\text{Li}$ , anatase has most interesting properties with a capacity of about 0.6 lithium ion in  $\text{Li}_x\text{TiO}_2$  at 1.78 V vs.  $\text{Li}^+/\text{Li}$ . This was confirmed separately using chemical lithiation with n-butyllithium which leads to a lithium uptake of 0.7 lithium per  $\text{TiO}_2$  [28]. *Ex-situ* X-ray diffraction upon lithium insertion demonstrated the formation of  $\text{Li}_{0.5}\text{TiO}_2$ , which crystallizes in an orthorhombic cell having an *Imma* space group, through a two phase transition [29]. Further studies claimed that good reversibility can be achieved with nanostructured anatase  $\text{TiO}_2$  either as mesoscopic or nanotubes [30,31,32]. The main effect of decreasing the crystallite size is to broaden the energy levels reachable in the materials, thus leading to a broader voltage window at which the electrochemical reaction takes place [33]. Compared to conventional graphite based systems which are used in prototype lithium-ion,  $\text{TiO}_2$  nanotubes offer some enhancements to cycle life, rate capability and safety characteristics. The lower operating voltage adversely affects the battery energy density. Armstrong *et al* [2] have briefly described lithium insertion into  $\text{TiO}_2$ -B nanowires and nanotubes have also been alluded to recently.

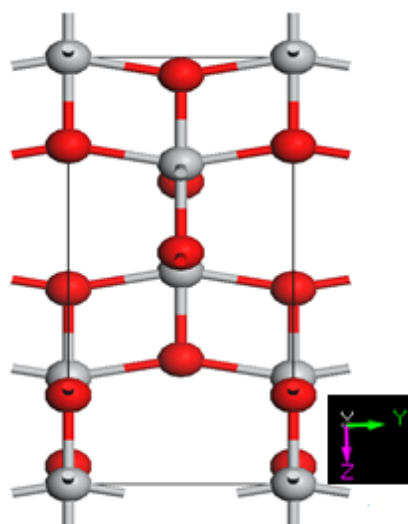


Figure 1.5. A unit cell of anatase  $\text{TiO}_2$  with tetragonal and space group of  $I4_1/amd$ , grey and red balls represent Ti and O atoms respectively.

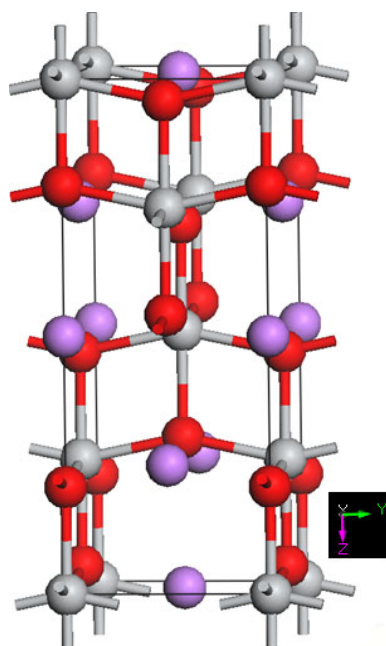


Figure 1.6. Schematic image of Li ions (purple spheres) inserted into anatase bulk TiO<sub>2</sub> structure.

### Synthesis of bulk anatase TiO<sub>2</sub>

TiO<sub>2</sub> nanoparticles can be synthesized using various methods such as sulphate process [34], chloride process [34], impregnation [35], co-precipitation [36], hydrothermal method [37], direct oxidation of TiCl<sub>4</sub> [38], metal organic chemical vapour deposition method, etc. [39]. Sol-gel method [40] is one of the most convenient ways to synthesize various metal oxides due to low cost, ease of fabrication and low processing temperatures. It is widely used to prepare TiO<sub>2</sub> for films, particles or monoliths. In general, the sol gel process involves the transition of a system from a liquid “sol” (mostly colloidal) into a solid “gel” phase. The homogeneity of the gels depends on the solubility of reagents in the solvent, the sequence of addition of reactants, the temperature and the pH. The precursors normally used for the synthesis and doping of nanoparticles are organic alkoxides, acetates or acetylacetonates as well as inorganic salts such as chlorides.

### 1.3.5 Brookite

Brookite, is one of the third natural form together with rutile and anatase polymorphs of TiO<sub>2</sub>, has a complex structure. It has eight formula units in the orthorhombic cell

with space group  $Pbca$ . Brookite formation may be pictured as the joining of distorted  $TiO_6$  octahedral sharing three edges.

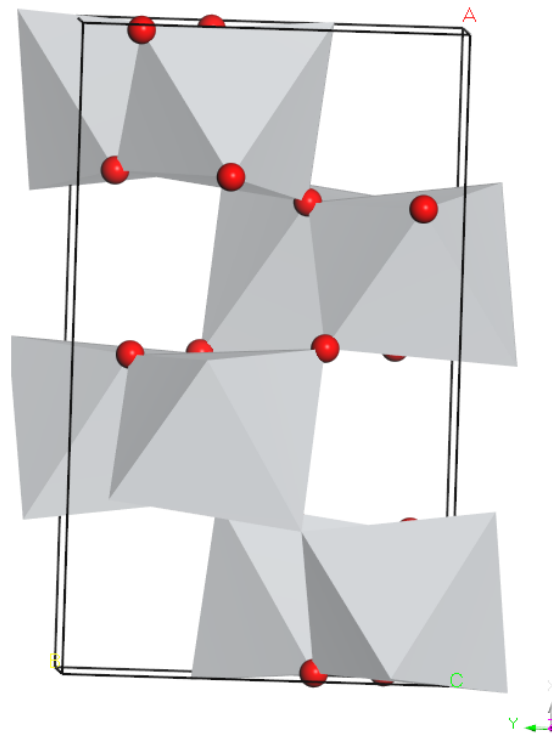


Figure 1.7. Unit cell of brookite  $TiO_2$  (oxygen and titanium atoms are represented by red sphere and grey octahedral site, respectively).

### 1.3.6 Rutile

Rutile  $TiO_2$  has a tetragonal structure which contains six atoms per unit cell as shown in Figure 1.8. This structure consists of a stacking of oxygen octahedra centered on titanium atoms. Band-structure calculations indicate that the valence band of rutile is mainly composed of the outermost p electrons from the oxygen atoms, while the lowest conduction band is mostly composed of the excited states of the titanium atoms. The symmetry of these bands is such that a direct band gap with dipole forbidden transitions at the  $\Gamma$  point is predicted [41,42]. Rutile structure poses the highest stability compared to other polymorphs [43].

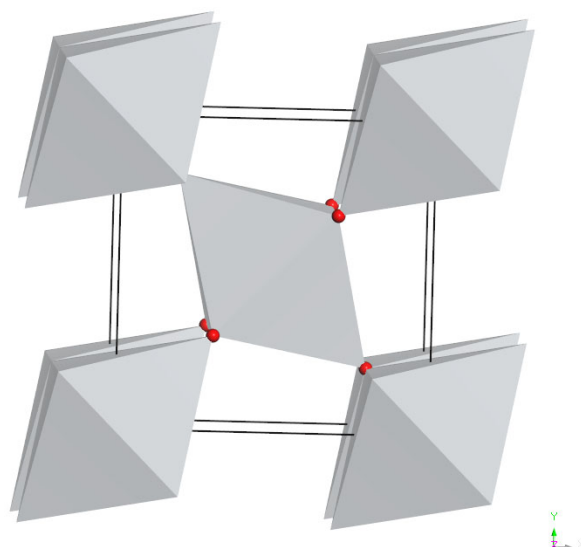


Figure 1.8. Unit cell of rutile  $\text{TiO}_2$  (oxygen and titanium atoms are represented by red sphere and grey octahedral site, respectively).

### 1.3.7 $\text{TiO}_2$ trigonal bipyramid (TB)

Ma *et. al.* recently reported the chemistry for a new class of unprecedented microporous  $\text{TiO}_2$  crystalline phases [44], which feature a special  $[\text{TiO}_5]$  trigonal bipyramid building block, a large pore size (5–7 Å), and high thermal stability. Hence, these microporous materials are potential anode materials for Li-ion batteries. Figure 1.9 shows the different phases of  $\text{TiO}_2$  (TB).

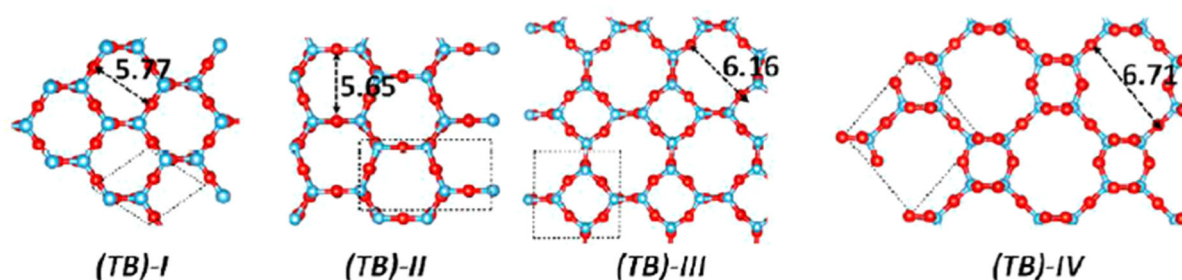


Figure 1.9.  $\text{TiO}_2$  (TB) phases consist of a  $[\text{TiO}_5]$  trigonal bipyramid structure unit.

### 1.3.8 $\text{TiO}_2$ nanospheres

There has been an expanding enthusiasm for manufacture of empty inorganic nanostructures attributable to their significant applications in optical, electronic, magnetic, catalytic, and sensing gadgets from photonic crystals, drug-delivery carriers, and nano-reactors [45,46,47]. The inner nanospace of these nanostructures, when coupled with chemical functionality of boundary materials, creates both aesthetic beauty and scientific attractions [48]. Among the many investigations in this area,

polymeric colloidal particles have been frequently utilized as templates to support the materials of interest via layer-by-layer technique. Recently, sacrificial metal templates have been introduced to prepare metal nanoshells that have higher standard reduction potentials [49].

### Synthesis of TiO<sub>2</sub> nanospheres

Hollow TiO<sub>2</sub> nanospheres in the diameter range of 10 to 20 micrometers had been synthesised in ionic liquids. In addition to this, smaller TiO<sub>2</sub> nanospheres with mesoporous core-shell structures have also been prepared with a combination of wet (solvent used: EtOH/H<sub>2</sub>O) and solid-state reactions [50].

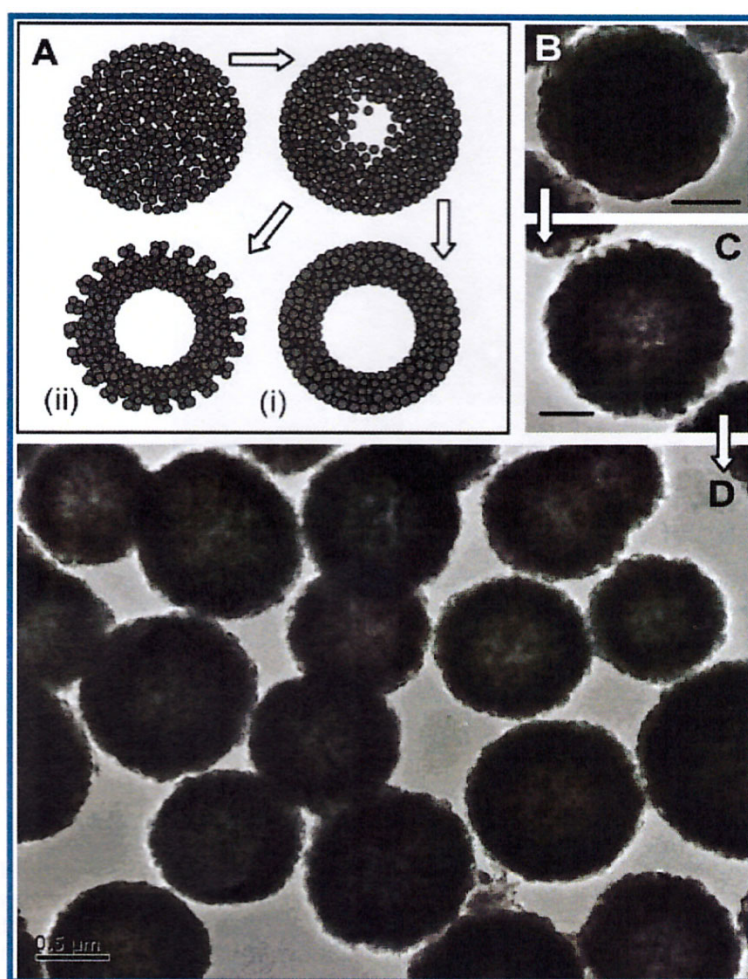


Figure 1.10. (A) Schematic illustration (cross-sectional view) of the ripening process and two types (i and ii) of hollow structures. Evolution (TEM images) of TiO<sub>2</sub> nanospheres synthesized with 30 mL of TiF<sub>4</sub> (1.3 mM) at 180°C with different reaction times: (B) 2h (scale bar=200nm), (C) 20h (scale bar=200nm), (D) 50h (scale bar=500nm) [51].

There is another simple “one pot” method that had also been developed to prepare hollow anatase TiO<sub>2</sub> nanospheres via Ostwald ripening in aqueous mediums [51].



Inner nanospace and highly organised crystallites in the shell and surface region can be created with a wide range of controlling parameters. As shown in Figure 1.10, an abrupt core-surface interface within the TiO<sub>2</sub> spheres has been further attained.

## 1.4 Motivation

On the theoretical side, most calculations are still limited to employing the main electronic structure methods such as Hartree-Fock (HF) or density functional theory (DFT), and the usage of highly correlated methods for large systems are not realistic. However, even within DFT methods, the results may sometimes suffer from incomplete treatment of electron correlation leading to underestimation of band gaps of TiO<sub>2</sub> polymorphs [52]. Usually, DFT provides acceptable results for the ground-state properties, which are in good agreement with experiment. However, DFT quality results for large systems, including the nanostructures, can be achieved by applying an approximate self-consistent-charge density-functional tight-binding (SCC-DFTB) methods [53,54]. Therefore, SCC-DFTB [55,56] serves as computationally efficient method to investigate electronic, structural and thermodynamic properties of TiO<sub>2</sub> polymorphs.

## 1.5 Specific Objectives

The objectives of this study are to:

1. derive potentials (Slater-Koster files) using SCC-DFTB
2. validate the potentials on bulk TiO<sub>2</sub> polymorphs viz., rutile brookite and anatase
3. generate Li<sub>x</sub>TiO<sub>2</sub> anatase nanostructures with various Li ion concentrations
4. use derived potentials to investigate:
  - electronic, structural and mechanical properties of various polymorphs
  - the effect of Li/Na content on the volume of bulk and nanospheres
  - the effect of temperature on TiO<sub>2</sub> bulk and nanostructures
  - predict properties of newly discovered TiO<sub>2</sub> TB polymorphs.

## 1.6 Outline of the study

In the current study, the density functional based tight binding (DFTB) approach and density functional plane wave pseudopotential method will be applied to determine some electronic and structural properties.

Chapter 1, we introduce the study and the content of this dissertation with literature background of  $\text{TiO}_2$  and the motivation of the study. In this chapter we also state the objectives and the outline of this study.

Chapter 2, we explain the theories behind the methods used in our study in detail i.e. the density functional theory (DFT), and density functional based tight binding (DFTB) approach.

Chapter 3, we derive Ti-O, Li-Ti-O and Na-Ti-O Slater-Koster potentials via DFTB+ parameterization, and validate the potentials by discussing structural, mechanical and electronic properties of bulk rutile and brookite  $\text{TiO}_2$ . These results are compared to available experimental results.

Chapter 4, we apply Li-Ti-O and Na-TiO potentials, discuss structural, mechanical and electronic properties of bulk anatase  $\text{TiO}_2$ . These results are compared to available experimental results. Additionally, we also discuss molecular dynamics properties of bulk and  $\text{TiO}_2$  nanostructures. These results are also compared to available experimental results.

Chapter 6, we use our potentials on new  $\text{TiO}_2$  (TB)-I and  $\text{TiO}_2$  (TB)-II structures (bulk and nanospheres). We also calculate structural, mechanical and electronic parameters.

Chapter 7, we make conclusions, recommendations, contributions and limitations of this study. Finally, the bibliography which gives the insight to the analysis of the work listed.

# Chapter 2: Methodology

## 2.1 Density-Functional based Tight-Binding (DFTB)

### 2.1.1 Introduction

In this chapter a very brief review of DFT is given in order to highlight its crucial aspects to the formulation of the DFTB method.

The Hohenberg-Kohn (HK) theorems [57] have made the electronic density acceptable as a basic variable to electronic-structure calculations. However, development of practical DFT methods only became relevant after W. Kohn and L. J. Sham published their famous set of equations called Kohn-Sham (KS) equations [58].

The use of the electronic density within the KS scheme allows a significant reduction of the computational demand involved in quantum calculations. Furthermore, the KS method paved the way for studying systems that could not be investigated by conventional *ab initio* methods (which use the wave function as basic variable).

Even though DFT methods have been successfully applied for systems of increasing complexity, methods which can include approximations to reduce further the computational demand, without compromising the reliability of results, are still required.

Slater and Koster started the application of tight-binding (TB) to the calculation of electronic structures [59]. The main idea behind this method is to describe the Hamiltonian eigenstates with an atomic-like basis set and replace the Hamiltonian with a parameterized Hamiltonian matrix whose elements depend only on the internuclear distances (this requires the integrals of more than two centers to be neglected) and orbital symmetries. Although the Slater–Koster method was conceived for the calculation of band structures in periodic systems, it was later generalized to an atomistic model, capable of treating finite systems as well. The transition to atomistic has three important main requirements, as discussed by Goringe *et al.* [60]

First, the elements of the Hamiltonian matrix must have a functional dependence on the interatomic distance. In the case of band structures one just has to know the matrix elements for discrete values of distance. This requirement was solved by Froyen and Harrison, [61] who proposed that the interatomic distance was related to the Hamiltonian elements by  $1/r^2$ .

The second requirement is to obtain an expression for the total energy and not only for the band energy. In 1979 Chadi [62] proposed that the total energy could be described as a sum of two contributions and in the same period he also put forward the method to surface energy minimizations of semiconductors,

$$E = E_{bs} + E_{rep} \quad 2.1$$

where  $E_{bs}$  (band-structure energy) is the sum over the energies of all occupied orbitals obtained by diagonalization of the parameterized Hamiltonian matrix, and  $E_{rep}$  is the repulsive contribution, obtained by the sum of the atomic-pair terms,

$$E_{rep} = \sum_{\alpha,\beta}^N U_{\alpha,\beta} \quad 2.2$$

in which  $N$  is the number of atoms in the system.

The third and last requirement is the possibility to derive the atomic forces from the total energy. This is especially important for geometry optimization and molecular dynamics. By assuming differentiability of  $U_{\alpha,\beta}$  in equation (2.2), the only problem is to derive  $E_{bs}$ , which depends on the parameterization method chosen for the Hamiltonian matrix.

The DFTB method fulfills these three requirements with the additional advantage of completely avoiding any empirical parameterization, since the Hamiltonian and overlap matrices are calculated using atom-like valence-orbitals which are derived from DFT. Therefore, the DFTB method can be considered as a simplification of the Kohn–Sham method.

## 2.1.2 The Kohn–Sham Method

Hohenberg and Kohn theorems [57] have proven that the electronic energy of a system can be totally determined from its electronic density through the variation principle, but they did not propose any procedure to perform this calculation. This was done about one year later, by Kohn and Sham [58], with the publication of their equations known as Kohn-Sham (KS) equations.

The solution of Kohn and Sham begins from the idea of using mono-electronic orbitals to calculate the kinetic energy in a simple, yet reasonably precise, way leaving a residual correction that could be calculated apart. Thus, one starts with a reference system of  $M$  non-interacting electrons subjected to the external potential  $v_s$ , with Hamiltonian

$$\hat{H}_s = - \sum_i^M \frac{1}{2} \nabla_i^2 + \sum_i^M v_s(\vec{r}_i) = \sum_i^M \hat{h}_s \quad 2.3$$

Where

$$\hat{h}_s = - \frac{1}{2} \nabla_i^2 + v_s(\vec{r}_i) \quad 2.4$$

in which there are no electron–electron repulsion terms and for which the electronic density is exactly the same as in the corresponding system of interacting electrons. By introducing the single particle orbitals  $\psi_i$  all electronic densities physically acceptable for the system of non-interacting electrons can be written in the form

$$\rho(\vec{r}_i) = \sum_i^M |\psi_i(\vec{r})|^2 \quad 2.5$$

Therefore, the HK functional can be written as:

$$F_{HK}[\rho] = T_s[\rho] + J[\rho] + E_{xc}[\rho] \quad 2.6$$

where  $T_s$  represents the kinetic-energy functional for the reference system of  $M$  non-interacting electrons, given by

$$T_s[\rho] = \sum_i^M \langle \psi_i | -\frac{1}{2} \nabla_i^2 | \psi_i \rangle \quad 2.7$$

where  $J$  represents the classic Coulomb interaction functional

$$j[\rho] = \frac{1}{2} \iint \frac{\rho(\vec{r})\rho(\vec{r}')}{|\vec{r} - \vec{r}'|} d\vec{r}d\vec{r}' \quad 2.8$$

and the remaining interactions are grouped in  $E_{xc}$ , the exchange-correlation functional, which contains the difference between the exact kinetic energy  $T$  and  $T_s$ , besides the non-classic part of the electron-electron interactions  $V_{ee}$ , *i.e.*

$$E_{xc}[\rho] \equiv T[\rho] - T_s[\rho] + V_{ee}[\rho] - J[\rho] \quad 2.9$$

After combining equations (2.6), (2.7) and (2.8) within the second HK theorem, the chemical potential can be written as

$$\mu = v_{KS}(\vec{r}) + \frac{\delta T_s[\rho]}{\delta \rho(\vec{r})} \quad 2.10$$

with the  $v_{KS}$  effective potential

$$\begin{aligned} v_{KS}(\vec{r}) &= v_{ext}(\vec{r}) + \frac{\delta J_s[\rho]}{\delta \rho(\vec{r})} + \frac{\delta E_{xc}[\rho]}{\delta \rho(\vec{r})} \\ &= v_{ext}(\vec{r}) + \int \frac{\rho(\vec{r}')}{|\vec{r} - \vec{r}'|} d\vec{r}' + v_{xc}(\vec{r}) \end{aligned} \quad 2.11$$

where  $v_{ext}$  is the external potential, normally due to the atomic nuclei, and the exchange-correlation potential  $v_{xc}$  is defined as

$$v_{xc}(\vec{r}) = \frac{\delta E_{xc}[\rho]}{\delta \rho(\vec{r})} \quad 2.12$$

Equation (2.10), restricted by  $\int \rho(\vec{r})d\vec{r} = M$ , is exactly the same equation that would be obtained for a system of  $M$  non-interacting electrons submitted to the external potential  $v_{ext} = v_{KS}$ . Thus, for a given  $v_{KS}$  a suitable value of  $\rho$  can be calculated for equation (2.10.) by solving the  $M$  monoelectronic equations

$$\left[ -\frac{1}{2}\nabla^2 + v_{KS}(\vec{r}) \right] \psi_i = \epsilon_i \psi_i \quad 2.13$$

and by using the calculated  $\psi_i$  in equation (2.10)

Equations (2.5) and (2.11, 2.12, 2.13) are the so-called Kohn-Sham equations. Since  $v_{KS}$  depends on  $\rho$  through  $v_{xc}$  the KS equations must be solved iteratively using a self-consistent procedure similar to the one depicted in Figure 2.1 An electronic density model  $\rho_0$  is normally chosen to start the iterative procedure. In principle, any positive function normalized for the number of electrons would be applicable, but a good initial estimate of  $\rho$  can significantly accelerate convergence.

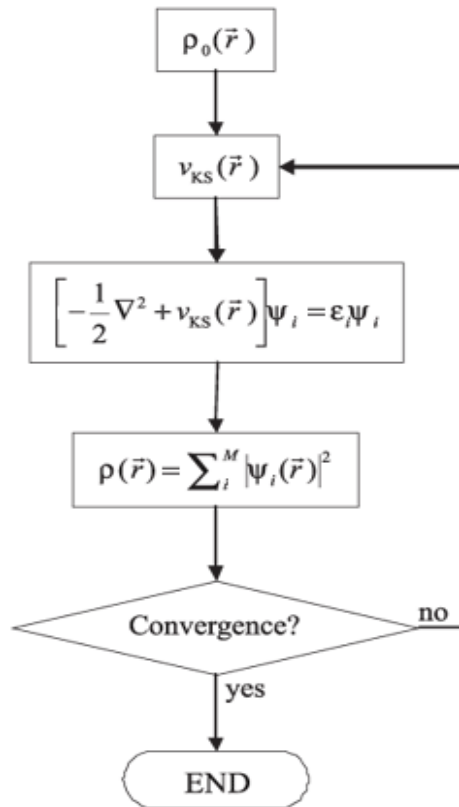


Figure 2.1. Flow-chart of a typical DFT calculation within the Kohn-Sham method [63].

At the end of the iterative procedure, the total energy can be calculated, which is given in the KS method by the following expression:

$$\begin{aligned}
E[\rho] = & \sum_i^M n_i \left\langle \psi_i \left| -\frac{1}{2} \nabla_i^2 + v_{ext}(\vec{r}) + \frac{1}{2} \int \frac{\rho(\vec{r}')}{|\vec{r} - \vec{r}'|} d\vec{r}' \right| \psi_i \right\rangle \\
& + E_{xc}[\rho] + \frac{1}{2} \sum_{\beta}^N \sum_{\alpha \neq \beta}^N \frac{Z_{\alpha} Z_{\beta}}{|\hat{R}_{\alpha} - \hat{R}_{\beta}|}
\end{aligned} \tag{2.14}$$

The most difficult part of the KS scheme is to calculate  $v_{ext}$  in equation (2.12). The existence of an exact density functional is assured by the first HK theorem, but the exact form of the  $E_{xc}$  functional remains unknown. However, many approximations of this functional have been described in the scientific literature over the last decades. In practice, the approximation chosen for  $E_{xc}$  and the way by which the KS orbitals are represented define the different DFT methods.

### 2.1.3 DFT as Basis for a Tight-Binding Method

Following Foulkes and Haydock [64] the electronic density is written as a reference density  $\rho_0$  plus a small fluctuation  $\delta\rho$ ,

$$\rho(\vec{r}) = \rho_0(\vec{r}) + \delta\rho(\vec{r}) \tag{2.15}$$

This electronic density is then inserted in equation (2.14):

$$\begin{aligned}
& E[\rho_0 + \delta\rho] \\
= & \sum_i^M n_i \left\langle \psi_i \left| -\frac{1}{2} \nabla^2 + v_{ext}(\vec{r}) + \int \frac{\rho'_0}{|\vec{r} - \vec{r}'|} d\vec{r}' + v_{xc}[\rho_0] \right| \psi_i \right\rangle \\
& - \frac{1}{2} \iint \frac{\rho'_0(\rho_0 + \delta\rho)}{|\vec{r} - \vec{r}'|} d\vec{r} d\vec{r}' - \int v_{xc}[\rho_0](\rho_0 + \delta\rho) d\vec{r} \\
& + \frac{1}{2} \iint \frac{\delta\rho'(\rho_0 + \delta\rho)}{|\vec{r} - \vec{r}'|} d\vec{r} d\vec{r}' + E_{xc}[\rho_0 + \delta\rho] + E_{nn}
\end{aligned} \tag{2.16}$$

where  $\rho'_0 = \rho_0(\vec{r})$  and  $\delta\rho' = \delta\rho(\vec{r}')$  are defined as short-hand notations. The second term in equation (2.16.) corrects the double counting in the Coulomb term; the third



term corrects the new exchange-correlation contribution; and the fourth term results from splitting the Coulomb energy into one part related to  $\rho_0$  and another related to  $\delta\rho$ .  $E_{nn}$  is the nuclear repulsion.

Afterwards,  $E_{xc}[\rho_0 + \delta\rho]$  is expanded in a Taylor series up to the second-order term:

$$\begin{aligned}
E_{xc}[\rho_0 + \delta\rho] &= E_{xc}[\rho_0] \\
&+ \int \left. \frac{\delta E_{xc}}{\delta\rho} \right|_{\rho_0} \delta\rho d\vec{r} \\
&+ \frac{1}{2} \iint \left. \frac{\delta^2 E_{xc}}{\delta\rho\delta\rho'} \right|_{\rho_0} \delta\rho\delta\rho' d\vec{r}d\vec{r}'
\end{aligned} \tag{2.17}$$

$$\begin{aligned}
&E \\
&= \sum_i^M n_i \left\langle \psi_i \left| -\frac{1}{2}\nabla^2 + v_{ext}(\vec{r}) + \int \frac{\rho'_0}{|\vec{r} - \vec{r}'|} d\vec{r}' + v_{xc}[\rho_0] \right| \psi_i \right\rangle
\end{aligned}$$

Substitution of equation (2.17) into (2.16) and use of the definition  $(\delta E_{xc}/\delta\rho)_{\rho_0} = v_{xc}[\rho_0]$  results in

$$\begin{aligned}
&-\frac{1}{2} \iint \frac{\rho'_0\rho_0}{|\vec{r} - \vec{r}'|} d\vec{r}d\vec{r}' + E_{xc}[\rho_0] - \int v_{xc}[\rho_0]\rho_0 d\vec{r} + E_{nn} \\
&+ \frac{1}{2} \iint \left( \frac{\delta\rho\delta\rho'}{|\vec{r} - \vec{r}'|} + \left. \frac{\delta^2 E_{xc}}{\delta\rho\delta\rho'} \right|_{\rho_0} \right) d\vec{r}d\vec{r}'
\end{aligned} \tag{2.18}$$

From equation (2.18) it is possible to define four important terms. The first is a reference Hamiltonian  $\hat{H}^0$  depending only upon  $\rho_0$

$$\hat{H}^0 = -\frac{1}{2}\nabla^2 + v_{ext}(\vec{r}) + \int \frac{\rho'_0}{|\vec{r} - \vec{r}'|} d\vec{r}' + v_{xc}[\rho_0] \tag{2.19}$$

The sum in the first line of equation (2.18.) is analogue to  $E_{bs}$  in equation (2.1). The terms in the second line of equation (2.18) define the repulsive contribution

$$\begin{aligned}
E_{rep}[\rho_0] &= -\frac{1}{2} \iint \frac{\rho'_0\rho_0}{|\vec{r} - \vec{r}'|} d\vec{r}d\vec{r}' + E_{xc}[\rho_0] - \int v_{xc}[\rho_0]\rho_0 d\vec{r} \\
&+ E_{nn}
\end{aligned} \tag{2.20}$$

Finally, the last term in equation (2.18) includes the corrections related to the fluctuations in the electronic density. This term is defined as

$$E_{2nd}[\rho_0, \delta\rho] = \frac{1}{2} \iint \left( \frac{\delta\rho\delta\rho'}{|\vec{r} - \vec{r}'|} + \left. \frac{\delta^2 E_{xc}}{\delta\rho\delta\rho'} \right|_{\rho_0} \right) d\vec{r}d\vec{r}' \quad 2.21$$

Therefore, equation (2.18) can be rewritten as

$$E = \underbrace{\sum_i^M n_i \langle \psi_i | \hat{H}^0 | \psi_i \rangle}_{E_{bs}} + E_{rep}[\rho_0] + E_{2nd}[\rho_0, \delta\rho] \quad 2.22$$

In order to obtain a good estimate of the reference electronic density  $\rho_0$  is written as a superposition of atom-like densities centered on the nuclei  $\alpha$ ,

$$\rho_0(\vec{r}) = \sum_{\alpha}^N \rho_0^{\alpha}(\vec{r}_{\alpha}), \quad \vec{r}_{\alpha} = \vec{r} - \vec{R}_{\alpha} \quad 2.23$$

with this approximation it is assured that  $E_{rep}$  does not depend on the electronic-density fluctuations. Furthermore, due to the neutrality of  $\rho_0^{\alpha}$  the Coulomb contributions become negligible for long distances. Therefore,  $E_{rep}$  can be expanded as

$$\begin{aligned} E_{rep} &= \sum_{\alpha}^N E_{rep}[\rho_0^{\alpha}] \\ &+ \frac{1}{2} \sum_{\beta}^N \sum_{\alpha \neq \beta}^N \left( E_{rep}[\rho_0^{\alpha} + \rho_0^{\beta}] - E_{rep}[\rho_0^{\alpha}] \right. \\ &\quad \left. - E_{rep}[\rho_0^{\beta}] \right) \\ &+ (\text{interactions of 3 and more centers}) \end{aligned} \quad 2.24$$

The contributions of 3 and more centers are rather small and can be neglected. These approximations can also be justified by Coulomb screening, *i.e.*, since  $\rho_0^{\alpha}$  is the electronic density of a neutral atom, the electron-electron interaction terms with more than two centers are cancelled by the nucleus-nucleus interactions.

Due to the screening of terms of more than two centers, one can assume the two-center contributions to be short ranged. However, the repulsion energy does not decay to zero for long interatomic distances. Instead, it decays to a constant value given by the atomic contributions:

$$\lim_{R_{\alpha\beta} \rightarrow \infty} E_{rep}[\rho_0] = \sum_{\alpha}^N E_{rep}[\rho_0^{\alpha}] \quad 2.25$$

Thus,  $\sum_{\alpha}^N E_{rep}[\rho_0^{\alpha}]$  is assumed in order to make  $E_{rep}$  dependent only on two-center contributions:

$$E_{rep}[\rho_0] \approx \frac{1}{2} \sum_{\alpha, \beta}^N U[\rho_0^{\alpha}, \rho_0^{\beta}] \quad 2.26$$

Although it would be possible to calculate  $E_{rep}$  for known values of  $\rho_0^{\alpha}$  it is more convenient to adjust  $E_{rep}$  to *ab initio* results. Thus,  $E_{rep}$  is fitted to the difference between the DFT energy and  $E_{bs}$  as a function of the interatomic distance  $R_{\alpha\beta}$  using a suitable reference structure, *i.e.*

$$E_{rep}[\rho_0] \equiv E_{rep}(R_{\alpha\beta}) = \{E_{DFT}(R_{\alpha\beta}) - E_{bs}(R_{\alpha\beta})\}_{\text{ref. struct.}} \quad 2.27$$

The value of  $E_{bs}$  can be obtained by diagonalization of the Hamiltonian matrix, which leads to

$$E_{bs} = \sum_{i=1}^M n_i \varepsilon_i \quad 2.28$$

The value of  $E_{rep}$  is usually fitted to a polynomial function or to a series of splines. Based on the considerations discussed so far, the DFTB model can be derived.

## 2.2 The role of DFTB in materials modelling

Success The Density Functional based Tight Binding (DFTB) method inhabits an important place in the hierarchy of techniques available for the atomistic modeling of materials as shown in Figure 2.2. The uses of empirically derived forcefields are

dominated by technological problems for large scale simulations. However, since they are adapted to a finite set of equilibrium situations (mostly experimental data and *ab initio* results for equilibrium configurations), they usually apply well to systems that are within the parameterization space, but often fail in other situations. Forcefields are not transferable to different chemical situations or to calculations of spectroscopic data which rely quantitatively on detailed knowledge of the electronic structure.

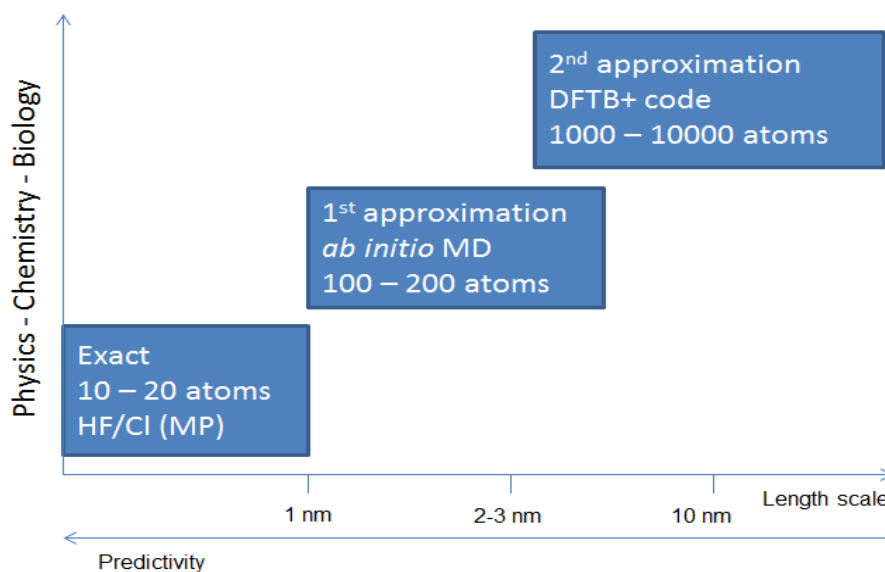


Figure 2.2. Hierarchy for some of the method for the atomistic modeling of materials.

A method based on quantum mechanics is therefore highly anticipated for large-scale applications. Such methods can be found in density-functional theory (DFT) for small to medium sized systems. Despite the general appeal of the DFT approach, accurate DFT calculations on more than hundreds of atoms for longer trajectory times remain expensive.

For the predictable future, the computational demands for describing structural, electronic, and dynamic properties of large and complex materials with technologically relevant size, simulation time, and statistics demand approximate solutions. In this context, empirical tight-binding (TB) methods have been developed and used in solid-state physics. Due to their conceptual simplicity, in most cases even neglecting self-consistency, they more readily address size problems. Although the TB approach is based on quantum mechanics, it lacks reliability and transferability due to the parameterization of the electronic Hamiltonian with respect to a finite set of equilibrium

structures and properties. Additionally, there is serious weakness in having no well-defined procedure for constructing the required data from an atomic basis (wavefunctions and potentials) in a way which could include any desired chemical element.

While minimizing both, the computational cost and the number of parameters, this method offers a high degree of transferability as well as universality for both ground-state and excited-state properties. DFTB operates with the same accuracy and efficiency for organic molecules, solids, clusters, insulators, semiconductors, and metals, even biomolecular systems are investigated.

### 2.2.1 The Standard DFTB Model without Self-Consistency

In the standard DFTB scheme, the second-order correction term,  $E_{2nd}$  of equation (2.22), is neglected. Therefore, the calculation of the total energy does not depend on the electronic-density fluctuations  $\delta\rho$  and, accordingly, it does not have to be solved iteratively.

In DFTB the KS orbitals are represented with a linear combination of atomic orbitals (LCAO) centered on the nuclei. Denoting the basis functions by  $\Phi_v$  and the expansion coefficients by  $C_{iv}$  one can write the KS orbitals in the form

$$\psi_i(\vec{r}) = \sum_v^N C_{iv} \Phi_v(\vec{r} - \vec{R}_\alpha) \quad 2.29$$

from this LCAO model, one obtains the secular problem

$$\sum_v^N C_{iv} (H_{\mu v}^0 - \varepsilon_i S_{\mu v}) = 0, \quad \forall \mu, v \quad 2.30$$

where the elements  $H_{\mu v}^0$  of the Hamiltonian matrix and  $S_{\mu v}$  of the overlap matrix are defined as follows:

$$H_{\mu v}^0 = \langle \Phi_\mu | \hat{H}^0 | \Phi_v \rangle; \quad S_{\mu v} = \langle \Phi_\mu | \Phi_v \rangle; \quad \forall \mu \in \alpha, v \in \beta \quad 2.31$$

The second term of equation (2.22) can be transformed, with equations (2.29) and (2.11), into

$$\begin{aligned} \sum_i^M n_i \langle \psi_i | \hat{H}^0 | \psi_i \rangle &= \sum_i^M n_i \sum_{\mu, \nu}^N C_{i\mu} C_{i\nu} \langle \Phi_\mu | \hat{T} + v_{KS}[\rho_0] | \Phi_\nu \rangle \\ &= \text{tr}(P \cdot H^0) \end{aligned} \quad 2.32$$

in which the elements of the density matrix  $P$  are defined as follows

$$P_{\mu\nu} = \sum_i^M n_i C_{i\mu} C_{i\nu} \quad 2.33$$

In order to restrict the LCAO to valence orbitals only, it is necessary to assure the orthogonality of the basis functions with respect to the core basis-functions of the remaining atoms (by using atomic orbitals as basis functions the orthogonality between the core and valence functions within the same atoms is already assured).

Denoting  $|\Phi\rangle$  as a non-orthogonalized basis-function and  $|\Phi_c^\beta\rangle$  as the core basis-functions of atom  $\beta$ , the corresponding orthogonalized basis-function of  $|\Phi\rangle$  is obtained by:

$$|\Phi_\mu\rangle = |\Phi_\mu\rangle - \sum_{\beta \neq \alpha} \sum_c |\Phi_c^\beta\rangle (\Phi_c^\beta | \Phi_\mu\rangle), \quad \mu \in \alpha \quad 2.34$$

By using this orthogonalization procedure, equation (2.32) is transformed into

$$\begin{aligned} &\sum_i^M n_i \langle \psi_i | \hat{H}^0 | \psi_i \rangle \\ &= \sum_i^M n_i \sum_{\mu, \nu}^N C_{i\mu} C_{i\nu} \left( \Phi_\mu \left| \hat{T} + v_{KS} \right. \right. \\ &\quad \left. \left. - \sum_{\beta}^N \sum_c |\Phi_c^\beta\rangle \varepsilon_c^\beta (\Phi_c^\beta | \right| \Phi_\nu \right), \quad \mu, \nu \notin \{\beta\} \end{aligned} \quad 2.35$$

where  $\varepsilon_c^\beta$  denotes the eigenvalue of the state  $c$  in atom  $\beta$ . The effective potential  $v_{KS}$  and the core correction in equation (2.35) can be interpreted as pseudo-potential ( $V_{pp}$ ). Writing  $v_{KS}$  as the sum of potentials  $V_\alpha$  centered on the atoms,

$$v_{KS}[\rho_0] = \sum_{\alpha}^N V_{\alpha}(\vec{r}_{\alpha}), \quad \vec{r}_{\alpha} = \vec{r} - \vec{R}_{\alpha} \quad 2.36$$

and using this definition in equation (2.35), the effective potential is transformed into a pseudo-potential for all atoms in the system, except for atoms to which  $\Phi_{\mu}$  and  $\Phi_{\nu}$  belong. Therefore, the pseudo-potential appears in the three-center terms and in the two-center terms whose valence orbitals belong to the same atom (so called crystal field terms). The pseudo-potential contributions are considerably smaller than the contributions of the full potentials and are neglected. Thus, the Hamiltonian matrix elements are defined as

$$H_{\mu\nu}^0 = \left( \Phi_{\mu} \left| -\frac{1}{2} \nabla_{\nu}^2 + V_{\alpha} + (1 - \delta_{\alpha\beta}) V_{\beta} \right| \Phi_{\nu} \right), \mu \in \{\alpha\}, \nu \in \{\beta\} \quad 2.37$$

where  $\delta_{\alpha\beta}$  is the Kronecker's delta. This approach, the *potential superposition*, has been used since the 1980's for the calculation of DFTB parameters. In 1998, Elstner *et al.* [56] presented an alternative approach to derive the DFTB equations through a second order expansion of the DFT total energy with respect to the *electron density*. As result the Hamiltonian matrix elements are calculated as density superpositions, which is identical to equation (2.37.) except for the contribution of the exchange correlation potential. Indeed, due to the non-linear nature of  $v_{xc}$ , the effective potential cannot be described as a simple sum of reference potentials within this approach, instead one obtains

$$H_{\mu\nu}^0 = \left( \Phi_{\mu} \left| -\frac{1}{2} \nabla^2 + V_{KS}[\rho_0^{\alpha} - \rho_0^{\beta}] \right| \Phi_{\nu} \right), \mu \in \{\alpha\}, \nu \in \{\beta\} \quad 2.38$$

Both approaches are physically motivated and their results are similar, which is not surprising if the potential difference between equations (2.37) and (2.38) is explicitly calculated. Both approaches have been used extensively in the past, the potential

superposition being more popular for standard DFTB calculations, and the density superposition more widely used for SCC-DFTB.

The  $\Phi_v$  basis functions and the reference atom-like densities  $\rho_0^\alpha$  are obtained by solving the Schrödinger equation

$$\left[ \hat{T} + V_{KS}[\rho_0^\alpha] + \left( \frac{r}{r_0} \right)^2 \right] \Phi_v(\vec{r}) = \varepsilon_v \Phi_v(\vec{r}) \quad 2.39$$

for the free atom within a self-consistent DFT method, as shown in figure 1. The contraction potential  $\left( \frac{r}{r_0} \right)^2$  in equation (2.39) constrains the wave functions, resulting in better basis sets for the study of condensed-phase systems and free molecules as well. The value for the parameter  $r_0$  is normally chosen between  $1.85r_{cov}$  and  $2r_{cov}$  with  $r_{cov}$  being the atomic covalent radius [65].

In practice, the Hamiltonian matrix elements are calculated as follows: For the diagonal elements the energy level of the free atom is chosen, which ensures correct dissociation limits. Due to the orthogonality of the basis functions the off-diagonal elements of the intra-atomic blocks are exactly zero. The interatomic blocks are computed as given in equation (2.37) or (2.38), depending on the choice of potential generation. Within the density superposition approach the Hamiltonian matrix elements unfold as follows:

$$H_{\mu\nu}^0 = \begin{cases} \varepsilon_\mu^{\text{free atom}}, & \mu = \nu \\ \langle \Phi_\mu | \hat{T} + V_{KS}[\rho_0^\alpha - \rho_0^\beta] | \Phi_\nu \rangle, & \mu \in \{\alpha\}, \nu \in \{\beta\}, \alpha \neq \beta \\ 0, & \text{otherwise} \end{cases} \quad 2.40$$

It should be noted that the Hamiltonian elements  $H_{\mu\nu}^0$  depend only on atoms  $\alpha$  and  $\beta$  and, therefore, only the two-center matrix elements are explicitly calculated, as well as two-center elements of the overlap matrix. According to equation (2.40.) the free atom eigenvalues form the diagonal of the Hamiltonian matrix, which assures the correct limit for free atoms.

By using  $\Phi_v$  and  $\rho_0^\alpha$  the Hamiltonian and overlap matrix elements can be calculated and tabulated as a function of the distance between atomic pairs. Thus, it is not



necessary to recalculate any integrals during, e.g., a geometry optimization or molecular dynamics simulation.

Lastly, an analytic expression for atomic forces can be derived from the total energy with respect to the atomic space-coordinates,

$$\vec{F}_\alpha = - \sum_i^M \sum_{\mu,v}^N C_{i\mu} C_{iv} \left[ \frac{\partial H_{\mu\nu}^0}{\partial \vec{R}_\alpha} - \varepsilon_i \frac{\partial S_{\mu\nu}}{\partial \vec{R}_\alpha} \right] - \frac{\partial E_{rep}}{\partial \vec{R}_\alpha} \quad 2.41$$

By this approach, the DFTB method covers all three requirements for an atomistic tight-binding approach.

### 2.2.2 The Self-Consistent Charge Correction: SCC-DFTB

The non-self-consistent DFT scheme described so far is very suitable to study systems in which the polyatomic electronic density can be well represented by a sum of atom-like densities, *i.e.* homonuclear covalent systems or highly ionic systems. However, the uncertainties in the standard DFTB increase when the chemical bonds in the system are controlled by a more delicate charge balance between atoms, especially in the case of heteronuclear molecules and polar semiconductors. In order to have a better description of electronic systems and better transferability of DFTB in the cases where long-range Coulomb interactions are significant, the method has been improved, giving rise to the self-consistent charge correction DFTB (SCC-DFTB) [56]. In this new scheme, the electronic density is corrected through inclusion of the second-order contributions  $E_{2nd}$  in equation (2.22.), which are neglected in standard DFTB.

In order to include the density fluctuations in a simple yet efficient way according to a tight-binding approach,  $\delta\rho$  is written as the superposition of atom-like contributions  $\delta\rho_\alpha$ , which fast decay along the distance from the corresponding atomic center,

$$\delta\rho = \sum_\alpha^N \delta\rho_\alpha \quad 2.42$$

where the atom-like contributions can be simplified with the monopole approximation:

$$\delta\rho_\alpha \approx \Delta q_\alpha F_{00}^\alpha Y_{00} \quad 2.43$$

Here  $\Delta q_\alpha$  is the Mulliken charge, difference between the atomic Mulliken population  $q_\alpha$  [66] and the number of valence electrons of the neutral free atom  $q_\alpha^0$  ( $\Delta q_\alpha = q_\alpha - q_\alpha^0$ ),  $F_{00}^\alpha$  denotes the normalized radial dependence of the density fluctuation in atom  $\alpha$  approximated to spherical by the angular function  $Y_{00}$ . In other words, the effects of charge transfer are included, but changes in the shape of the electronic density are neglected. Equation (2.21) then becomes

$$E_{2nd} \approx \frac{1}{2} \sum_{\alpha,\beta}^N \Delta q_\alpha \Delta q_\beta \underbrace{\iint \left( \frac{1}{|\vec{r} - \vec{r}'|} - \frac{\delta^2 E_{xc}}{\delta\rho\delta\rho'} \Big|_{\rho_0} \right) F_{00}^\alpha F_{00}^\beta Y_{00}^2 d\vec{r} d\vec{r}'}_{\gamma_{\alpha\beta}} \quad 2.44$$

in which the notation  $\gamma_{\alpha\beta}$  was introduced merely for convenience or simplicity.

In order to solve equation (2.44),  $\gamma_{\alpha\beta}$  must be analyzed. In the limit case where the interatomic separation is very large ( $|\vec{R}_\alpha - \vec{R}_\beta| = |\vec{r} - \vec{r}'| \rightarrow \infty$ ) one finds, by GGA-DFT, that the exchange-correlation term goes to zero and  $\gamma_{\alpha\beta}$  describes the interaction of two normalized spherical electronic densities, basically reducing to  $\frac{1}{|\vec{R}_\alpha - \vec{R}_\beta|}$ , thus,

$$E_{2nd} \approx \frac{1}{2} \sum_{\alpha,\beta}^N \frac{\Delta q_\alpha \Delta q_\beta}{|\vec{R}_\alpha - \vec{R}_\beta|} \quad 2.45$$

In the opposite case, for which the interatomic distance tends to zero ( $|\vec{R}_\alpha - \vec{R}_\beta| = |\vec{r} - \vec{r}'| \rightarrow 0$ ),  $\gamma_{\alpha\beta}$  describes the electron-electron interaction within the atom  $\alpha$  and can be related with the chemical hardness  $\eta_\alpha$  [67], or Hubbard parameter  $\gamma_{\alpha\alpha} = 2\eta_\alpha = U_\alpha$ . Typically, the atomic hardness can be calculated using the difference between ionization potential  $I_\alpha$  and electron affinity  $A_\alpha$  of atom  $\alpha$ :  $2h_\alpha = I_\alpha - A_\alpha$ . Due to practical problems, in particular related to the non-existence of various anions and accordingly missing experimental validation of the electron affinity of the corresponding elements, it is more convenient to exploit DFT to obtain these parameters. Application of Janak's theorem [68] relates the atomic hardness to the derivative of the HOMO energy with respect to the occupation number of the HOMO

$\eta_\alpha = \frac{\partial \varepsilon_{\alpha, \text{HOMO}}}{\partial n_{\alpha, \text{HOMO}}} = \frac{1}{2} U_\alpha$  and hence the energy change with respect to electron change within the HOMO. This approach offers the possibility to treat the charge contribution shell- or even orbital-wise, which is important for the calculation of certain elements with sp and d bonding contributions, in particular for transition metals. Orbital hardness values  $\eta_\xi = \frac{\partial \varepsilon_\xi}{\partial n_\xi}$  have been reported in the literature for elements from H to Xe [69]. In the following, we concentrate on the atomic SCC procedure, which implies that all sums over charges run over the atomic index  $\alpha$ . For orbital-dependent SCC the summation index for the charge would run over the shell index  $\xi$ . Within the monopole approximation,  $U_\alpha$  can be calculated, using a DFT procedure, as the second derivative of the total atomic energy of atom  $\alpha$  with respect to its atomic charge:

$$E_{2nd} \approx \frac{1}{2} \frac{\partial^2 E_\alpha \rho_0}{\partial q_\alpha^2} \Delta q_\alpha^2 = \frac{1}{2} U_\alpha \Delta q_\alpha^2 \quad 2.46$$

In order to obtain a well-defined and useful expression for systems in all scales, and still keep consistence with the afore approximations, an analytical expression was developed [56] to approximate the density fluctuations with spherical electronic densities. In accordance with Slater-type orbitals (Gaussian-type orbitals can also be employed) used to solve the KS equations [55,70], it is assumed an exponential decay of the normalized spherical electronic density:

$$\rho_0(\vec{r}) = \frac{\tau_\alpha^3}{8\pi} e^{-\tau_\alpha |\vec{r} - \vec{R}_\alpha|} \quad 2.47$$

Omitting the second-order contributions of  $E_{xc}$  in equation (2.44) one obtains:

$$\gamma_{\alpha\beta} = \iint \frac{1}{|\vec{r} - \vec{r}'|} \frac{\tau_\alpha^3}{8\pi} e^{-\tau_\alpha |\vec{r} - \vec{R}_\alpha|} \frac{\tau_\beta^3}{8\pi} e^{-\tau_\beta |\vec{r}' - \vec{R}_\beta|} d\vec{r} d\vec{r}' \quad 2.48$$

Integration over  $\vec{r}'$  gives:

$$\gamma_{\alpha\beta} = \int \left[ \frac{1}{|\vec{r} - \vec{R}_\alpha|} - \left[ \frac{\tau_\alpha}{2} + \frac{1}{|C|} \right] e^{-\tau_\alpha |\vec{r} - \vec{R}_\alpha|} \right] \frac{\tau_\beta^3}{8\pi} e^{-\tau_\beta |\vec{r} - \vec{R}_\beta|} d\vec{r} \quad 2.49$$

Setting  $|R = |\vec{R}_\alpha - \vec{R}_\beta|$ , after some coordinate transformations one gets

$$\gamma_{\alpha\beta} = \frac{1}{R} - s(\tau_\alpha, \tau_\beta, R) \quad 2.50$$

Where  $s$  is a short-range function with exponential decay, so that

$$\lim_{R \rightarrow 0} s(\tau_\alpha, \tau_\beta, R) = \frac{5}{16} \tau_\alpha + \frac{1}{R} \quad 2.51$$

Once it was assumed that the second-order contribution can be approximated by the Hubbard parameter when  $R = 0$ , according to equation (2.46), the exponents of equation (2.51) are obtained:

$$\tau_\alpha = \frac{16}{5} U_\alpha \quad 2.52$$

This result can be interpreted by noting that harder elements tend to have localized wave functions. The chemical hardness of a spin-depolarized atom is calculated by the energy derivative of the highest occupied atomic orbital with respect to its occupation number, equation (2.46), using a fully self-consistent *ab initio* method. Therefore, the influence of second-order contributions of the exchange-correlation energy is included in  $\gamma_{\alpha\beta}$  for short distances, where it is important. The fact that, within GGA, the exchange-correlation energy vanishes for large interatomic distances is taken into account. In the case of periodic systems, the long-range part can be calculated using the standard Ewald summation, whereas the short-range part  $s$  decays exponentially and can be summed over a small number of unit cells. Thus, equation (2.50) is a well-defined expression for extended and periodic systems.

Finally, the total energy within SCC-DFTB is written as

$$E_{SCC} = \sum_i^M n_i \langle \psi_i | \hat{H}^0 | \psi_i \rangle + \frac{1}{2} \sum_{\alpha, \beta}^N \gamma_{\alpha\beta} \Delta q_\alpha \Delta q_\beta + E_{rep} \quad 2.53$$

with  $\gamma_{\alpha\beta} = \gamma_{\alpha\beta}(U_\alpha, U_\beta, |\vec{R}_\alpha - \vec{R}_\beta|)$ . Here the contribution due to the Hamiltonian  $\hat{H}^0$  is exactly the same as in the standard DFTB scheme. Note that the first term in equation (2.53) does only simplify to the sum of MO energies, the convenient notation for DFTB,

if all charges are zero. Like in the non-self-consistent method, the wave functions  $Y_i$  are expanded in a LCAO model, equation (2.29), and equation (2.53) gives:

$$E_{SCC} = tr(P \cdot H^0) + \frac{1}{2} \sum_{\alpha, \beta}^N \gamma_{\alpha\beta} \Delta q_{\alpha} \Delta q_{\beta} + E_{rep} \quad 2.54$$

The charge fluctuations are calculated by Mulliken population analysis [66]:

$$q_{\alpha} = \frac{1}{2} \sum_i^M n_i \sum_{\mu \in \alpha}^N \sum_v^N (C_{i\mu} C_{iv} S_{\mu v} + C_{iv} C_{i\mu} S_{v\mu}) \quad 2.55$$

and secular equations similar to those in equation (2.30) can be obtained, with modified elements in the Hamiltonian matrix:

$$\begin{aligned} H_{\mu v}^0 &= \langle \Phi_{\mu} | \hat{H}^0 | \Phi_v \rangle \\ &+ \frac{1}{2} S_{\mu v} \sum_{\xi}^N (\gamma_{\alpha\xi} + \gamma_{\beta\xi}) \Delta q_{\xi} \\ &= H_{\mu v}^0 + H_{\mu v}^1, \quad \forall \mu \in \{\alpha\}, v \in \{\beta\} \end{aligned} \quad 2.56$$

The matrix elements  $H_{\mu v}^0$  and  $S_{\mu v}$  are identical to those defined in the standard DFTB method, in equation (2.31) Since the atomic charges depend on the monoatomic wave functions  $\psi_i$  it is necessary to use a self-consistent procedure. Once the elements  $S_{\mu v}$  extend to some neighboring atoms, multi-particle interactions are introduced. The second-order correction is achieved by introducing the element  $H_{\mu v}^1$ , which depend on the Mulliken charges.

Identically to the standard DFTB, the repulsive potential is fitted according to equation (2.27) using a suitable reference system.

As the self-consistent charge correction allows for the explicit treatment of charge-transfer effects, the transferability of  $E_{rep}$  is considerably better, in comparison with the non-self-consistent scheme.

As in the standard DFTB, a simple analytic expression for the atomic forces can be derived accordingly:

$$\vec{F}_\alpha = - \sum_i^M n_i \sum_{\mu,\nu}^N C_{i\mu} C_{i\nu} \left[ \frac{\partial H_{\mu\nu}^0}{\partial \vec{R}_\alpha} - \left( \varepsilon_i - \frac{H_{\mu\nu}^1}{S_{\mu\nu}} \right) \frac{\partial S_{\mu\nu}}{\partial \vec{R}_\alpha} \right] - \Delta q_\alpha \sum_\xi^N \frac{\partial \gamma_{\alpha\xi}}{\partial \vec{R}_\alpha} \Delta q_\xi - \frac{\partial E_{rep}}{\partial \vec{R}_\alpha} \quad 2.57$$

DFTB schemes have been successfully used in a wide range of applications, from molecular compounds [71,72] to systems in solid state [73,74,75,76].

### 2.2.3 Weak Forces: Dispersion-Corrected SCC-DFTB

London interactions, also called dispersion forces, are defined as attractive forces between nonpolar molecules, due to their mutual polarizability [77]. London dispersion forces are several orders of magnitude weaker than typical covalent or ionic interactions and also about 10 times weaker than hydrogen bridge interactions. Therefore, dispersion forces have negligible effect in short-range interactions and can be understood as the long-range component of van der Waals forces.

Despite their weak nature, London interactions affect many fundamental processes in chemistry, physics, and biology. They influence the formation of molecular crystals, the structure of biological molecules such as proteins and DNA, adsorption processes,  $\pi - \pi$  stacking interactions, among others.

However, as explained above, both the standard and self-consistent DFTB methods treat only short-range atomic potentials and terms with more than two centers are neglected. Therefore, the Hamiltonian matrix elements fall off quickly and become negligible at interatomic distances typically found in the region of the van der Waals minimum. Hence, DFTB completely disregards van der Waals interactions, especially dispersion forces.

Two treatments meant to include dispersion interactions *a posteriori* have been proposed [78,79]. In both cases the dispersion energy  $E_{disp}$  is calculated separately using empirical potentials and then added to the DFTB total energy expression. Since van der Waals forces are totally absent in DFTB, the addition of  $E_{disp}$  does not introduce any double-counting errors to the energy.

Since both treatments are somewhat similar, we describe that used in the present work [79]. This correction was implemented in an experimental version of the deMon code [80] and makes use of the UFF force field [81], already available in deMon. The dispersion interaction  $U_{\alpha\beta}$  between atoms  $\alpha$  and  $\beta$  at a distance  $R$  is given in Lennard-Jones-type form, which includes two parameters: van der Waals distance ( $R_{\alpha\beta}$ ) and well depth ( $d_{\alpha\beta}$ ):

$$U_{\alpha\beta}(R) = d_{\alpha\beta} \left[ -2 \left( \frac{R_{\alpha\beta}}{R} \right)^6 + \left( \frac{R_{\alpha\beta}}{R} \right)^{12} \right] \quad 2.58$$

The  $R_{\alpha\beta}$  and  $d_{\alpha\beta}$  parameters are reported in the original paper [81] and are available from H to Lw in the periodic table of elements. In UFF the van der Waals term is set to zero according to an adjacency criteria; however, this imposes an inflexible topology of the system, which is not desirable in a quantum-mechanical method. To overcome this problem, equation 58 is used only when  $U_{\alpha\beta}$  is attractive (London interactions are never repulsive), *i.e.*  $R < 2^{-1/6}R_{\alpha\beta}$ . In addition, a short-range potential is derived using the polynomial

$$U_{\alpha\beta}^{\text{short-range}}(R) = U_0 - U_1 R^n - U_2 R^{2n} \quad 2.59$$

where  $U_0$ ,  $U_1$ , and  $U_2$  are calculated to make the interaction energy and its first and second derivatives match equation (2.58) at  $R = 2^{-1/6}R_{\alpha\beta}$ . The best value suggested for  $n$  is 5, which gives the following  $U_0$ ,  $U_1$  and  $U_2$  parameters [79]:

$$U_0 = \frac{396}{25} d_{\alpha\beta} \quad 2.60$$

$$U_1 = 2^{5/6} \frac{672}{25} \frac{d_{\alpha\beta}}{R_{\alpha\beta}^5} \quad 2.61$$

$$U_2 = -2^{2/3} \frac{552}{25} \frac{d_{\alpha\beta}}{R_{\alpha\beta}^{10}} \quad 2.62$$

Therefore, the dispersion potential for the DFTB method can be written as

$$\begin{aligned}
& U_{\alpha\beta}(R) \\
= & \begin{cases} d_{\alpha\beta} \left[ -2 \left( \frac{R_{\alpha\beta}}{R} \right)^6 + \left( \frac{R_{\alpha\beta}}{R} \right)^{12} \right], \forall R \geq 2^{-1/6} R_{\alpha\beta} \\ \frac{396}{25} d_{\alpha\beta} - 2^{5/6} \frac{672}{25} \frac{d_{\alpha\beta}}{R_{\alpha\beta}^5} + 2^{2/3} \frac{552}{25} \frac{d_{\alpha\beta}}{R_{\alpha\beta}^{10}}, \forall R < 2^{-1/6} R_{\alpha\beta} \end{cases} \quad 2.63
\end{aligned}$$

and the dispersion energy is given by

$$E_{disp} = \frac{1}{2} \sum_{\alpha, \beta}^N U_{\alpha\beta}(R) \quad 2.64$$

This term is then added to the total DFTB energy calculated either using standard DFTB (section 2.2) or the SCC scheme (section 2.2.2).

## 2.3 CASTEP code

Success of the total energy method applications largely depends on good understanding of the underlying technology, of its strong points and its limitations. The theoretical background to Cambridge Sequential Energy Package (CASTEP) approach can be split into two groups, one that includes features common to all *ab initio* codes for solid state applications, and another that is fairly specific to CASTEP. The first group includes such concepts as adiabatic approximation and density functional theory, while the latter group refers to ideas of pseudopotentials, plane wave basis set, k-points sampling, etc. [63] The first principle calculations allow researchers to investigate the nature and origin of the electronic, optical, and structural properties of a system without the need for any experimental input, with the exception of the atomic number of mass of the constituent atoms.

### 2.3.1 Plane-Wave Basis Sets

The plane-wave basis sets are abundantly used in the calculations involving boundary conditions. Plane-wave basis sets are coupled with an “effective core potential” or pseudopotential in practical performance, such that they (plane-wave) are only used for valence charge density. The plane-wave basis is more efficient than the Gaussian-type basis because it is guaranteed to converge to the target wavefunction, while there is no such guarantee in the Gaussian-type. A wavefunction is needed for each



individual electron, since there is infinite number of electrons. However, the basis set required for the expansion of each wavefunction is also infinite. Bloch's theorem, which starts with periodicity of the crystal lattice, can handle this problem. Bloch's theorem defines the crystal momentum  $k$  as good quantum number and also gives the boundary condition for the single particle wavefunction,  $\varphi_k$ . Bloch's theorem is often stated in an alternative form: the following equation

$$\varphi_k(r + R_L) = e^{ik \cdot R_L} \varphi_k(r) \quad 2.65$$

is equivalent to the statement that all eigenfunctions  $\varphi_{k_i}$  of a single-particle Schrodinger equation with periodic potential can be written as a periodic function  $u_{k_i}$  modulated by a plane wave vector  $\mathbf{k}$  [82].  $\mathbf{R}_L$  is a direct lattice vector.

$$\varphi_{k_j}(r) = e^{ikr} u_{k_j}(r) \quad 2.66$$

Due to its periodicity  $u_{k_i}$  can be expanded as a set of plane wave basis

$$\varphi_{k_j}(r) = \sum_G C_{j,G} e^{iG \cdot r} \quad 2.67$$

where  $G$  are reciprocal lattice vectors. The functions  $u_{k_j}$  are periodic and can be expanded in a set of plane waves. Thus the electronic wavefunction with the exponential prefactor is

$$\varphi_{k_j}(r) = \sum_G C_{j,k+G} e^{i(k+G)r} \quad 2.68$$

where  $C_{j,k+G}$  coefficient of the periodic plane waves. Since this is the case with an infinite number of basis functions, it is necessary to accurately recreate the real wavefunction. The number of wavefunctions used is controlled by the largest wave vector in the expansion in (2.69), This is equivalent to imposing a cut-off on the kinetic energy as the kinetic energy of an electron with wavevector  $\mathbf{k}$  is given by

$$E_K = \frac{\hbar^2 |K + G|^2}{2m} \quad 2.69$$

Hence it is the only plane wave that is stable

$$E_K = \frac{\hbar^2 |K + G|^2}{2m} < E_{cut} \quad 2.70$$

are included in the basis. The plane wave set at a finite cutoff energy will lead to an error in the computed total energy; hence the energy must be increased until the calculated energy has converged. It is highly advisable and wise to use much denser  $k$  points to reduce errors and ensure convergence. Before making use of the plane wave expansion of the wavefunction we write the Kohn-Sham equation of density functional theory in the following way [63]:

$$\sum \left[ \frac{\hbar^2}{2m} |K + G|^2 \delta_{GG} + V_{eff} \right] C_{j,K+G} \quad 2.71$$

Where

$$V_{eff}(r) = V_{ext}(r) + V_H[n(r)] + V_{XC}[n(r)] \quad 2.72$$

$V_{ext}(r)$ ,  $V_H[n(r)]$ , and  $V_{XC}[n(r)]$  are Fourier transforms of the external potential of the nuclei, Hartree and exchange-correlation potentials respectively.

### 2.3.2 Pseudopotentials

The plane-wave pseudopotential method is a technique that can be used to calculate, with accuracy, the variation self-consistent solution to the density functional theory. Pseudopotentials are applied in atomic physics and neutron scattering. Many physical and chemical properties depend on the distribution of valence electrons, while the core electrons do not participate in a chemical bonding. The core electrons are strongly localized around the nucleus, and their wavefunctions overlap less with the core electron's wavefunction of the next neighboring atoms. Hence, the distribution of core electrons is basically the same, irrespective of which chemical environment the atom is in. Therefore, the core electrons are declared "frozen" and the core electron distribution is kept in the crystal environment. This is of good advantage since few electrons have to be treated and few eigenstates of the Kohn-Sham equations have to be calculated. Secondly, the total energy scale is largely reduced by the removal of core electrons from the calculation which makes the calculation of the energy differences between atomic configurations numerically much more stable. Hence the introduction of pseudopotential approximation is an attempt to eradicate the

unsolvable complicated effects of the core electrons in motion and their nuclear with an effective potential, or pseudopotential [83,84,85] . Thus the Schrodinger equation now contains a modified effective potential term instead of the coulombic potential term for core electrons. In the pseudopotential approach, only valence electrons are dealt with explicitly [86].

### 2.3.3 Ultrasoft pseudopotentials

Ultrasoft pseudopotentials were developed by Vanderbilt [88] in 1990. Many of the modern pseudopotential calculations use this generalization of the Kleinman-Bylander. The main goal of pseudopotentials is to create pseudofunctions that are as “smooth” as possible, and yet accurate. This approach is a radical departure from norm-conserving pseudopotentials discussed above. Ultrasoft pseudopotentials attain much smoother pseudo wavefunctions as the name states. In this approach, the pseudo wavefunctions are required to be equal to all electron wave functions outside the radius, as with the norm-conserving pseudopotentials, but inside the radius are allowed to be as soft as possible; the norm-conserving constraint is removed to accomplish this, however, this introduces some complications. However the ultrasoft pseudopotential reduces the planewave cutoff needed in the calculations, particularly because large values of radius can be used in their schemes. The complications that result are two-fold. First of all, since the pseudo-wavefunctions are equal to the all-electron wavefunctions (and therefore have the same norm) in the interstitial, but do not have the same norm inside  $TC$  they are necessarily not normalized. Secondly, the pseudo charge density is not obtained by computing  $\sum \varphi^* \varphi$  as with norm-conserving pseudopotentials; this will lead to the wrong total charge. A third, but less important, complication is that by relaxing the norm conservation, the resulting pseudopotentials can become less transferable. However, Vanderbilt pseudopotentials were proposed for use in large scale calculations, for which the cost of generating pseudopotentials is negligible compared with the cost of the calculations. The electron density is subdivided into a smooth part that extends throughout the unit cell and a hard part localized in the core region. Ultrasoft pseudopotentials have an advantage over the norm-conserving pseudopotential.

## 2.4 Molecular Dynamics

The procedure for performing a total-energy pseudopotential calculation using the molecular-dynamics technique is shown in Figure 2.3. The procedure requires an initial set of trial wave functions from which the Hartree potential and the exchange-correlation potential can be calculated. The equations of motion for the electronic states are integrated, and the wave functions are orthogonalized and normalized. The charge density generated by the new set of wave functions is then calculated. This charge density is used to construct a new set of Hamiltonian matrices, and a further set of wave functions is obtained by integration of the equation of motions and orthonormalization of the resultant wave functions. These iterations are repeated until the wave functions are stationary.

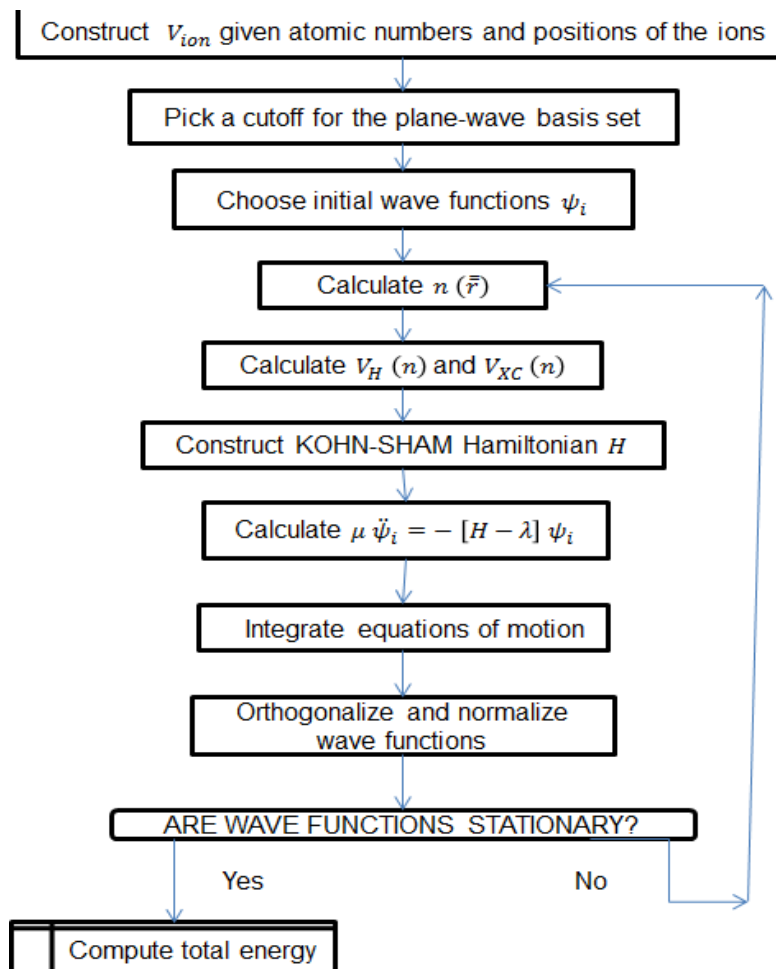


Figure 2.3. Flow chart describing the computational procedure for the calculation of the total energy of a solid with molecular dynamics [63].

## 2.5 Theoretical Background of the Calculated Properties

### 2.5.1 Density of States.

The density of states (DOS) of a system describes the number of states per interval of energy at each energy level that are available to be occupied. In other words, the density of states, denoted by  $g(E)$ , indicates how densely packed quantum states in a particular system. Unlike isolated systems, like atoms or molecules in gas phase, the density distributions are not discrete like a spectral density but continuous. A high DOS at a specific energy level means that there are many states available for occupation. A DOS of zero means that no states can be occupied at that energy level. In general a DOS is an average over the space and time domains occupied by the system. Integrating the density of states over a range of energy will produce a number of states.

$$N(E) = \int_E^{\Delta E} g(E)dE \quad 2.73$$

Thus  $g(E)dE$  represents the number of states between  $E$  and  $dE$ .

The density of states allows integration with respect to the electron energy to be used instead of the integration over the Brillouin zone. The density of the states is also a useful mathematical concept for visual analysis of the electronic structure.

### 2.5.2 Optical Properties

Optical properties of materials are defined as the interaction of the material with the electromagnetic radiation in the visible region. These interactions of photons with the electronic or crystal structure of a material result to a number of different optical phenomena [87]. The photons may transfer their energy to the material i.e. absorption; photons may give their energy, but photons of identical energy are immediately emitted by the material i.e. reflection; photons may not interact with the material i.e. transmission; and lastly, velocity of photons may change, during transmission i.e. refraction. Metals and non-metals have different band structures. Metals consist of partially filled high-energy conduction bands and non-metals consist of various energy band structures. All four optical phenomena (absorption, reflection, transmission and refraction) are important for these materials.

Table 2.1. Critical K-points in the first Brillouin zone.

Symbol	Description
$\Gamma$	Center of the Brillouin zone
Hexagonal	
A	Center of a hexagonal face
H	Corner point
K	Middle of an edge joining two rectangular faces
L	Middle of an edge joining a hexagonal face
M	Center of a rectangular face
Face-centered cubic	
K	Middle of an edge joining two hexagonal faces
L	Center of a hexagonal face
U	Middle of an edge joining a hexagonal and a square face
W	Corner point
X	Center of square face
Body-centered cubic	
H	Corner point joining four edges
N	Center of a face
P	Corner point joining three edges
Simple cube	
M	Center of an edge
R	Corner point
X	Center of a face

### 2.5.3 Elasticity

Elastic properties relate to different fundamentals of solid-state properties, such as equation of state. Elastic constants have vital information regarding the strength of the materials against an externally applied strain and also act as stability criteria to study structural transformations [88]. Mechanical stability of homogeneous crystals has long been a subject of extensive theoretical and computational investigation [89]. Born

initiated the systematic study of crystal stability under load [90]. The well-known Born stability criteria are a set of conditions on the elastic constants ( $C_{ij}$ ) which are related to the second-order change in the internal energy of a crystal under formation. But, Hill and Milstein suggested that the convexity of the internal energy in a crystal under stress is coordinate dependent and hence the ranges of Born stability are strongly sensitive to the choice of coordinates [91]. Wang et al have suggested that the Born conditions are only valid for the mechanical stability of unstressed systems and not valid for the stressed systems [90].

Barron and Klein also indicated that the normal definition of the elastic constants derived from the Helmholtz free energy cannot be directly applied to the study of the stress-strain relationship of a stressed state [92]. Wang and co-workers [90] demonstrated, however, that elastic constants cannot be used as stability criteria for a stressed system. They suggested the use of elastic stiffness coefficients as stability criteria for isotropic stress. For anisotropic stress, they obtained a more general form from path-dependent finite displacements. The stability criteria have been strongly formulated in terms of elastic stiffness coefficients ( $C_{ij}$ ) which govern the proper relations of stress and strain at finite strain by considering both the internal and the external work done during the process of deformation [92]. This strongly suggests that the stability analysis depends mainly on a proper generalization of the zero-stress constants valid for arbitrary stress. Bulk modulus is also one of the most important parameters that characterize the physical property of a material system, because it also measures the degree of stiffness or the energy required to produce a given volume deformation, while shear modulus describes the resistance to shape change caused by shearing force; Young's modulus reflects the resistance of materials against uniaxial tensions [93]. The Bulk modulus depicts the bonding characters in the material and it is usually used as an indicator for material strength and hardness and is the inverse of compressibility [94]. Pugh introduced the ratio of bulk to shear modulus of polycrystalline phases ( $B/G$ ) by considering that shear modulus represents the resistance to plastic deformation, while the bulk modulus represents the resistance to fracture. A high ( $B/G$ ) value is associated with ductility, while a low ( $B/G$ ) value is related to brittleness. The critical value separating ductility and brittleness is 1.75 [95]. Basically, elastic constants of a material describe its response to the external applied strain or the stress required to maintain a given deformation and provides useful

information of the strength of the material, as characterized by Bulk modulus ( $B$ ), shear modulus ( $C$ ), Young's modulus ( $E$ ) Poisson's ratio ( $\nu$ ) and Shear anisotropy factor ( $A$ ). Quadratic dependence of the crystal energy ( $E$ ) on the strain is expected for small deformations [95].

### 2.5.3.1 Elastic Stability Criteria

For a specific lattice, both stress and strain have three tensile and three shear components, giving six components in total. According to the theory of elasticity, a 6×6 symmetry matrix with 36 elements is needed to describe the relationship between stress and strain, such that  $\sigma_i = C_{ij}\varepsilon_j$  for small stresses,  $\sigma$  and strain,  $\varepsilon$ . For a tetragonal structure, only six elastic constants, corresponding to  $C_{11}$ ,  $C_{12}$ ,  $C_{13}$ ,  $C_{33}$ ,  $C_{44}$  and  $C_{66}$ , are independent. Therefore, the strain dependence of stress can be expressed as

$$\begin{pmatrix} \sigma_x \\ \sigma_y \\ \sigma_z \\ \tau_{yz} \\ \tau_{xz} \\ \tau_{xy} \end{pmatrix} = \begin{pmatrix} C_{11} & C_{21} & C_{31} & 0 & 0 & 0 \\ C_{12} & C_{22} & C_{32} & 0 & 0 & 0 \\ C_{13} & C_{23} & C_{33} & 0 & 0 & 0 \\ 0 & 0 & 0 & C_{44} & 0 & 0 \\ 0 & 0 & 0 & 0 & C_{55} & 0 \\ 0 & 0 & 0 & 0 & 0 & C_{66} \end{pmatrix} \times \begin{pmatrix} \varepsilon_{xx} \\ \varepsilon_{yy} \\ \varepsilon_{zz} \\ \gamma_{yz} \\ \gamma_{xz} \\ \gamma_{xy} \end{pmatrix} \quad 2.74$$

Where  $\sigma$  and  $\tau$  represent tensile and shear stress while  $\varepsilon$  and  $\gamma$  represent tensile and shear strain, respectively [95].

Basically, elastic constants of a material describe its response to the external applied strain or the stress required to maintain a given deformation and provides useful information of the strength of the material, as characterized by Bulk modulus ( $B$ ), shear modulus ( $G$ ), Young's modulus ( $E$ ), Poisson's ratio ( $\nu$ ) and Shear anisotropy factor ( $A$ ). Quadratic dependence of the crystal energy  $E$  on the strain is expected for small deformations. The elastic moduli for hexagonal crystal are given as follows

$$B_v = \frac{2}{9} \left( C_{11} + C_{12} + C_{13} + \frac{1}{2} C_{33} \right) \quad 2.75$$

$$G_T = \frac{1}{30} (C_{11} + C_{12} + 2C_{33} - 4C_{13} + 12C_{44} + 12C_{66}) \quad 2.76$$

Similarly, young's modulus can be calculated by:



$$E_x = \frac{[C_{33}(C_{11} + C_{12}) - 2C_{13}^2](C_{11} - C_{12})}{C_{11}C_{33} - C_{13}^2} \quad 2.77$$

$$\nu = \frac{C_{13}}{(C_{11} + C_{12})} \quad 2.78$$

While the anisotropy is calculated as follows:

$$A_1 = \frac{2C_{44}}{(C_{11} + C_{12})} = \frac{C_{44}}{C_{66}}, A_2 = \frac{C_{33}}{C_{11}}, A_3 = \frac{C_{12}}{C_{13}} \quad 2.79$$

For an elastically isotropic hexagonal crystal, the three anisotropy ratios ( $A_1$ ,  $A_2$  and  $A_3$ ) must be simultaneously equal to unity [96] as given above,  $E_x$  represents the Young's modulus along the [100] and [010] directions, whereas  $E_z$  on the other hand represents Young's modulus along the [001] direction. Young's modulus  $E$  is defined as the ratio between stress and strain and is used to provide a measure of the stiffness of the solid, i.e. the larger the value of  $E$ , the stiffer the material. Poisson's ratio ( $\nu$ ) refers to the ratio of transverse contraction strain to longitudinal extension strain during stretching, thus reflecting the stability of the crystal against shear. Hence, higher the Poisson's ratio is the better ductility the crystalline metal has at low temperatures. It is acknowledged that the bulk modulus  $B_0$  is a measure of resistance to volume changed by applied pressure. The elastic anisotropy  $A$  has an important implication in engineering science since it is highly correlated with the possibility of inducing microcracks in materials [97]. If the material is completely isotropic, the value of  $A$  will be equal to unity, whereas values smaller or larger than 1 measure the degree of elastic anisotropy. Thus the macroscopically measurable quantities obtained for materials are the shear modulus  $G$ , which represents the isotropic response for shearing, Young's modulus  $E$  corresponding to the stress–strain ratio in the case of tensile forces, bulk modulus  $B_0$ , Poisson's ratio  $\nu$  and the anisotropy constant  $A$ , which are all important for technological and engineering applications.

The requirements for mechanical stability in a hexagonal structure lead to the following restrictions on the elastic constants [98]:

$$C_{11} > 0, C_{11} - C_{22} > 0, C_{44} > 0, C_{11} + C_{22} - \frac{2C_{13}^2}{C_{33}} > 0 \quad \text{and}$$

$$C_{66} = \frac{C_{11} - C_{12}}{2} > 0$$

In hexagonal crystals, there exist five independent elastic constants,  $C_{11}$ ,  $C_{12}$ ,  $C_{13}$ ,  $C_{33}$  and,  $C_{44}$ .  $C_{11}$  and,  $C_{13}$  correspond to longitudinal modes along the [100] and [001]

directions, respectively,  $C_{44}$  and  $C_{66} = \frac{C_{11}-C_{12}}{2}$  can be determined from the speed of sound of transverse modes propagating along the [001] and [100] directions, respectively [99].  $C_{13}$ , is present in the combination with four other moduli in the velocity of modes propagating in less-symmetrical directions, such as [011]. Orthorhombic crystals have nine independent elastic constants,  $C_{11}, C_{12}, C_{13}, C_{22}, C_{23}, C_{33}, C_{44}, C_{55}$  and  $C_{66}$  [100]. Elastic moduli derived from these elastic constants are [101]

$$B_V = \frac{1}{9}(C_{11} + C_{22} + C_{33}) + \frac{2}{9}(C_{12} + C_{13} + C_{23}) \quad 2.80$$

$$B_R = [(S_{11} + S_{22} + S_{33}) + 2(S_{12} + S_{13} + S_{23})^{-1}] \quad 2.81$$

$$G_R = 15[4(S_{11} + S_{22} + S_{33}) - 4(S_{12} + S_{13} + S_{23}) + 3(S_{44} + S_{55} + S_{66})]^{-1} \quad 2.82$$

$$B_H = \frac{1}{2}(B_R + B_V) \quad 2.83$$

$$G_H = \frac{1}{2}(G_R + G_V) \quad 2.84$$

$$E_X = \frac{9B_X G_X}{G_X + 3B_X} \quad 2.85$$

Where  $X$  is the Voigt, Reuss or Hill, and  $S_{ij}$  is the inverse matrix of the elastic constants matrix  $C_{ij}$ , which is given by [102]:

$$S_{11} = \frac{(C_{11}C_{33} - C_{23}^2)}{(C_{11}C_{22}C_{33} + 2C_{12}C_{13} + C_{23} - C_{11}C_{23}^2 - C_{22}C_{13}^2 - C_{33}C_{12}^2)} \quad 2.86$$

$$S_{12} = \frac{(C_{13}C_{23} - C_{12}C_{33})}{(C_{11}C_{22}C_{33} + 2C_{12}C_{13}C_{23} - C_{11}C_{23}^2 - C_{22}C_{13}^2 - C_{33}C_{12}^2)} \quad 2.87$$

$$S_{13} = \frac{(C_{12}C_{23} - C_{22}C_{13})}{(C_{11}C_{22}C_{33} + 2C_{12}C_{13}C_{23} - C_{11}C_{23}^2 - C_{22}C_{13}^2 - C_{33}C_{12}^2)} \quad 2.88$$

$$S_{22} = \frac{(C_{11}C_{33} - C_{13}^2)}{(C_{11}C_{22}C_{33} + 2C_{12}C_{13}C_{23} - C_{11}C_{23}^2 - C_{22}C_{13}^2 - C_{33}C_{12}^2)} \quad 2.89$$

$$S_{23} = \frac{(C_{12}C_{13} - C_{11}C_{23})}{(C_{11}C_{22}C_{33} + 2C_{12}C_{13}C_{23} - C_{11}C_{23}^2 - C_{22}C_{13}^2 - C_{33}C_{12}^2)} \quad 2.90$$

$$S_{33} = \frac{(C_{11}C_{22} - C_{12}^2)}{(C_{11}C_{22}C_{33} + 2C_{12}C_{13}C_{23} - C_{11}C_{23}^2 - C_{22}C_{13}^2 - C_{33}C_{12}^2)} \quad 2.91$$

$$S_{44} = \frac{1}{C_{44}} \quad 2.92$$

$$S_{55} = \frac{1}{C_{55}} \quad 2.93$$

$$S_{66} = \frac{1}{C_{66}} \quad 2.94$$

Then, we can obtain other mechanical properties for orthorhombic systems such as Poisson coefficient, compressibility and Lamé constants using the following equations [103]:

$$U_x = \frac{1}{2} \left[ \frac{B_x - (2/3)G_x}{B_x + (1/3)G_x} \right] \quad 2.95$$

$$\mu_x = \frac{E_x}{[2(1 + \nu_x)]} \quad 2.96$$

$$\lambda_x = \frac{\lambda_x E_x}{[(1 + \nu_x)(1 - 2\nu_x)]} \quad 2.97$$

For orthorhombic crystal, the mechanical stability conditions are given by [104]

$$C_{11} + C_{12} + C_{33} + 2C_{12} + 2C_{13} + 2C_{23} > 0, \quad C_{22} + C_{33} - 2C_{13} > 0, \quad C_{11} > 0, \quad C_{22} > 0, \\ C_{33} > 0, \quad C_{44} > 0, \quad C_{55} > 0, \quad C_{66} > 0$$

Lastly the tetragonal crystals have six independent elastic constants ( $C_{11}, C_{12}, C_{13}, C_{33}, C_{44}, C_{66}$ ) [105]. The corresponding elastic moduli derived from these elastic constants are:

$$B = \frac{1}{9}(2C_{11} + C_{33} + 4C_{13} + 2C_{12}), \quad = \frac{1}{15}(2C_{11} + C_{33} - C_{12} - 2C_{13} + 6C_{44} + 3C_{66})$$

$$E = C_{33} - 2\nu C_{13}, \quad \nu = \frac{C_{13}}{C_{11} + C_{12}} \quad \text{and} \quad A_1 = \frac{2C_{66}}{C_{11} - C_{12}}$$

On a basal plane (the plane perpendicular to the principal axis (c axis) in a tetragonal or hexagonal structure).

$$A_2 = \frac{4C_{44}}{C_{11} + C_{33} - 2C_{13}}, \text{ on } (010) \text{ plane.}$$

The corresponding necessary conditions for mechanical stability criterion are [106]:

$$C_{44} > 0, \quad C_{66} > 0, \quad C_{11} > 0, \quad C_{33} > 0, \quad C_{11} - C_{12} > 0, \quad (C_{11} + C_{33} - 2C_{13}) > 0, \\ (2C_{11} + C_{33} + 2C_{12} + 4C_{13}) > 0.$$

In metals and alloys (a partial or complete solid solution of one or more elements in a metallic matrix) behaving like isotropic media, the young's modulus is proportional to the bulk modulus when the poisson's ratio is close to 1/3.

## 2.6 Generation of TiO<sub>2</sub> nanotubes

In 1991 Lijima [107] discovered carbon nanotubes. However the molecular geometry and the exciting properties of these nanotubes have not only stimulated the field of nanotechnology but have also initiated enormous efforts in physics, chemistry, and materials science. These one-dimensional (1D) nanostructures provide exceptional electronic properties, such as high electron mobility or quantum confinement effects, a very high specific surface area, and even show a very high mechanical strength [108,109]. The disadvantage in this area is how to precisely control the sizes, dimensionalities, compositions and crystal structures at the nanoscale level, which may serve as a powerful tool for the tailoring of physical/chemical properties of materials in a controllable way. However, with the Medea® software package [110] it is possible to control the size of nanotubes. TiO<sub>2</sub> nanostructures have received attention for their Li<sup>+</sup> storage properties in rechargeable batteries.

Materials design software (Medea®) was used to generate TiO<sub>2</sub> nanotube structures. These nanotubes were generated from the bulk structure, by cutting it along Miller index surfaces {101} with various orientations as shown in Figure 2.4. After cleaving the surface, the next step is to select and freeze atoms which will not form part of the slab for building a nanotube. Thus, freezing these atoms (thin balls and sticks in the diagram) simply contributes in controlling which atoms will be used to generate the nanotube. All the frozen atoms will not be part of the slab which will be wrapped to form a nanotube. Atoms placed at any position in the surface can be used to construct

the slab as long as they make the right stoichiometry of the system under investigation. Also any number of layers can be used as long as they form the correct stoichiometry of the system. The number of layers used determines and contributes to the number of walls that the nanotube will be made up of. When creating the slab, the frozen atoms are eliminated from forming part of the slab as shown in Figure 2.4.

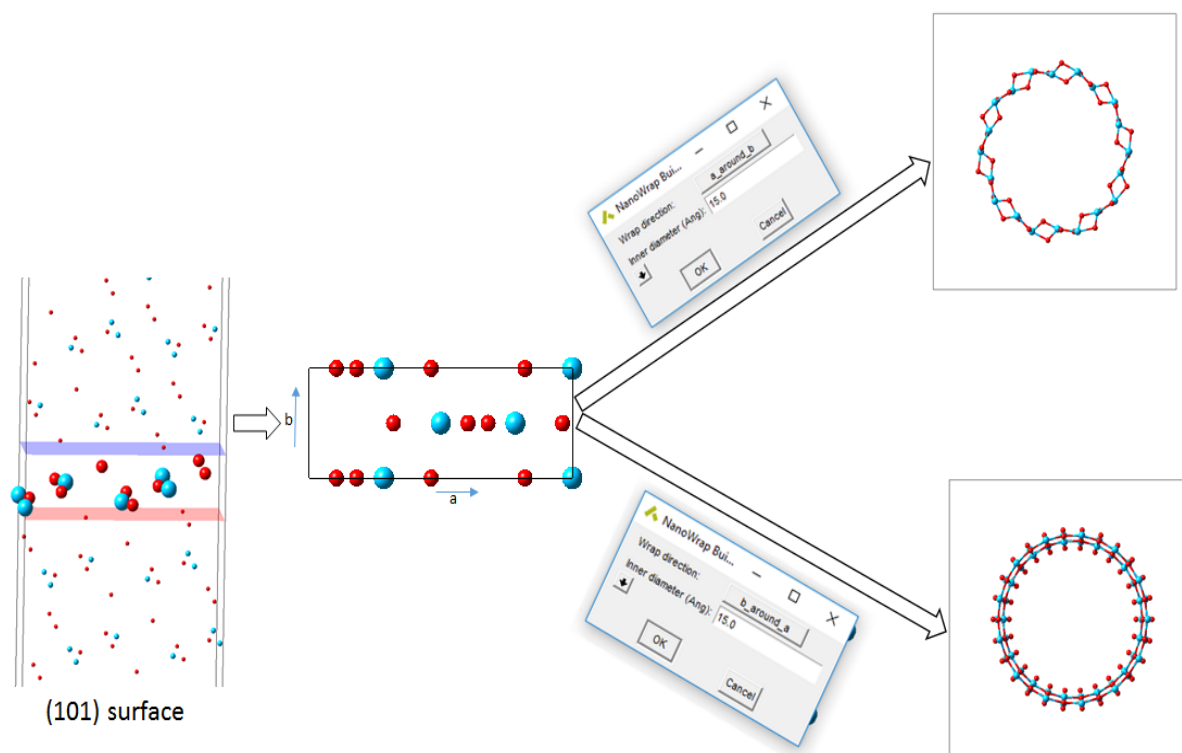


Figure 2.4. Generation of TiO<sub>2</sub> nanotubes with various wrapping direction.

The selected atoms which form the slab are wrapped around to form a nanotube. Figure 2.4 also depicts how a nanotube with a 15Å diameter was created from the slab.

## 2.7 Generation of nanospheres

The BIOVIA Materials Studio 2019 (19.1.0.2353) package was used to create the TiO<sub>2</sub> nanospheres of the rutile and anatase phases. Materials Studio is a molecular modelling package that can be used to study and analyze models of molecular structures and provides the ability to build and represent molecular structures with enhanced graphics. The **Build Nanostructure** utility of the **Build** utility within Materials Studio was used to create nanoparticles used in this study. This was carried out by initially creating the optimized bulk TiO<sub>2</sub> crystals unit cell. These lattices were used to create the bulk crystal with a perfect lattice. Subsequently, spheres of anatase

and tetragonal bipyramid (TB) were cut from the bulk lattice and some of the surface oxygen and titanium atoms were removed to ensure balance charge and the stoichiometry are shown in Figure 2.5.

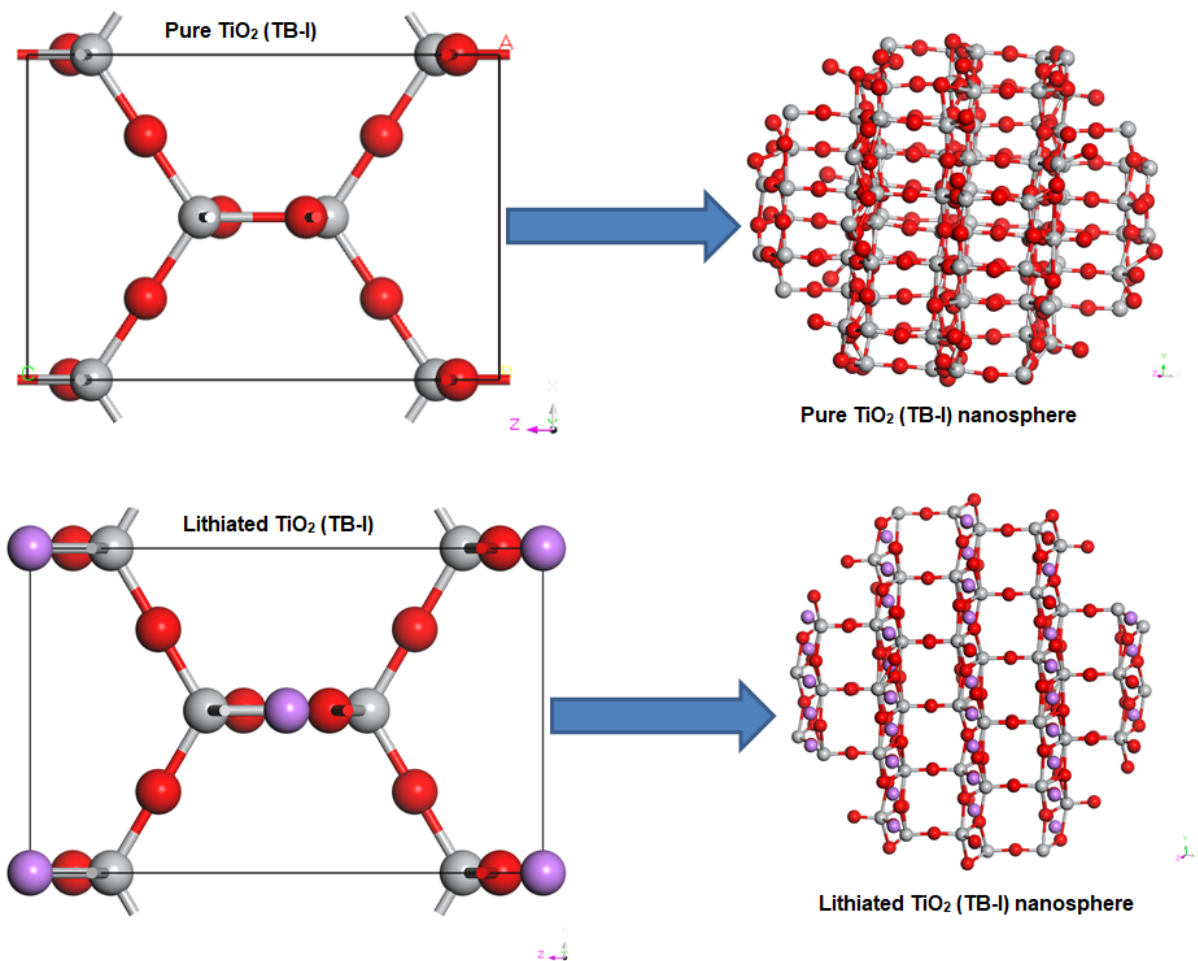


Figure 2.5 Image of nanosphere structures generated from bulk TiO<sub>2</sub> (pure and lithiated respectively). Ti, O and Li atoms are in grey, red and purple spheres respectively.

# Chapter 3: Derivation of DFTB potentials with validation using the rutile and brookite structures

## Overview

The DFTB potentials used in this chapter were derived using DMol3 and SCC-DFTB computer codes. We will briefly explain how such potentials were derived and present Ti-O, Li-Ti-O and Na-Ti-O potential interactions. Structural properties such as lattice parameters and mechanical properties of the rutile and brookite polymorphs will be discussed as a means of validating such potentials. We will also compare the calculated results with experiments where possible.

## 3.1 Several considerations when parameterizing

### 3.1.1 DFT and DFTB calculations

In order to generate data required by the fitting process energy calculations (and force calculations if requested) are performed twice. One calculation is a DFT calculation, for which the DFTB+ Parameterization task uses DMol<sup>3</sup>. The other calculation uses DFTB+ with the Slater-Koster files that were generated from an electronic part.

For heavy elements the DFT calculations, for both the repulsive part (DMol<sup>3</sup>) and the electronic part, need to include relativistic effects. For the DFTB+ electronic fitting the Zero Order Regular Approximation (ZORA) formalism is used. These relativistic calculations are activated for elements with an atomic number greater than 36 (Kr).

### 3.1.2 The fitting process

Once the energies and forces have been derived from both the DFT and DFTB calculations for all the sample systems it is possible to fit the coefficients of the polynomials for the repulsive terms to this data. This uses a standard least-squares fitting technique. The polynomial coefficients for all of the Slater-Koster files are generated in a single fitting calculation.

The fitting process is performed a number of times; for different orders of the polynomials and for different values of the cutoff radii around which the polynomials are based. The best fit from all these trials is used for the final set of Slater-Koster files.

### **3.1.3 Slater-Koster library file generation**

Once the polynomial coefficients have been calculated, the Slater-Koster files containing just the electronic part are updated to include the repulsive part. These are then used to generate fully-functional Slater-Koster files. All of the individual files are packaged up, together with some auxiliary data, into a single Slater-Koster library file. This form can be used by other DFTB+ tasks.

### **3.1.4 Data coverage**

As with any fitting process, both the quantity and quality of the data provided as input to the fitting process is crucial to the quality of the final Slater-Koster library. The quality of the data is handled by using appropriate parameters for the DFT and DFTB calculations and ensuring that the sample structures provided for these calculations are representative of the target systems (or their fragments) for the final library.

### **3.1.5 Degrees of freedom and number of trials**

For each element pair, the number of degrees of freedom in the fitting process corresponds to the number of terms in the polynomial. This is increased for the variation allowed in the degree of the polynomial and the cutoff radius.

Because all the element-pairs have their polynomial coefficients fitted in a single operation, the number of degrees of freedom is multiplied by the number of element pairs. The total number of data points for the fitting must be significantly higher than the total number of degrees of freedom. Additionally, it is also important to ensure that there are sufficient contributions for each of the individual element-pairs.

### **3.1.6 Element-pair coverage**

To ensure that there is sufficient data for the fitting, the sample structures together with their methods of variation are analyzed to determine which element pairs will have varying distances (in the desired range of cutoffs). For each structure the number of different conformations is divided by the number of varying element pairs for the



structure, and this gives a contribution that the structure can provide to the data for each of the element-pairs it contains. The contributions for each element-pair are summed over all the sample structures. This total contribution must then compare favourably with the number of degrees of freedom in the fitting procedure for a single element pair.

## 3.2 Parameterization

The density-functional-based tight-binding method (DFTB) [111] is an efficient quantum mechanical simulation method, which is an approximation to the density functional theory (DFT). This method is based on a second-order expansion of the Kohn-Sham total energy in the DFT with respect to charge density fluctuations. While being typically orders of magnitude faster than its *ab initio* counterpart, it provides results for many chemical problems with reasonable accuracy and precision.

The altogether determined unique DFTB technique gives a fantastic hypothetical structure which can be methodically expanded when higher precision is required. The achievement of the stable structure can be made from a decision by the immense measure of various deliberate augmentations which had been made after some time (e.g., charge self-consistency for portraying charge move, [56] incorporation of collinear and non-collinear turn, [112] time-subordinate [113] and GW [114] formalism to ascertain energized state properties, Green-work strategy to depict electron transport, [115] and so forth.

Normal in all extraordinary DFTB augmentations, the reality is that, the "most significant" some portion of the total energy is determined inside an inexact quantum mechanical methodology, while the rest, involving the core—core repugnance and the twofold tallying terms, is considered as a fitted semi old style communication vitality (the supposed repulsive energy) between partaking molecules, depending upon the arrangement of the nuclear cores in the framework. At the point when thoroughly done, the fitted potentials can even make up for parts of the mistake presented with the approximations in the quantum-precisely determined pieces of the DFTB energy. This division and the approximations in the quantum-precisely determined part permits counts on compound frameworks regularly a few sets of extent quicker and utilizing significantly less memory when contrasted with *ab initio* estimations, while as yet keeping up a sensible exactness.

In any case, the parametrization procedure for an expansive scope of chemical species is a challenging work, frequently taking a day or long periods of important research time. To bring down the obstruction of stretching out DFTB to new concoction frameworks, a few attempts have been made [116,117]. Unfortunately, the fitting structure appears to have a few restrictions. To begin with, it is just viewed as sub-atomic frameworks, making parametrizations for solids and surfaces rather tedious. Moreover, it does not appear to have incorporated any methods for mass fit information creation, i.e., does not appear to be fit for producing huge vivacious informational collections with sensibly minimal human intercession. This is not an issue when the fit is done against test information. However it keeps up a piece of the "parametrization boundary" by making the use of DFT adding machine references and filtering off-balance reference information substantially more troublesome than would normally have been appropriate. In conclusion, it is worked around a fixed spline portrayal of the repulsives, which gives a constrained adaptability. In this section, we portray a complete computerized fitting procedure for making horrible pair possibilities. It was created by attempting to improve the fitting technique quite far, while keeping its appropriateness to practically any sort of substance circumstance where one expects sensible portrayal by DFTB. We planned our calculation to manage an enormous assortment of horrible capacity shapes and to fit it to lively properties of particles as well as crystalline frameworks. Our calculation contains intelligent parts for the center fitting procedure as well as characterizing and building fit and test frameworks and making enormous arrangement of cluster fits with different evolving metaparameters (parameters influencing the parametrization, e.g., to begin with picked shorts or polynomial degrees). The relevance of the calculation has been exhibited by making poor cooperations for titanium-natural science, and crystalline titanium-oxide mixes. As will be indicated later, the acquired sets are of practically identical quality to the present best handcrafted ones for those frameworks, while fundamentally diminishing the human effort engaged with their creation.

### **3.2.1 Automatic parametrization scheme**

The density-functional-based tight-binding method is an efficient scheme for quantum mechanical atomistic simulations. While the most relevant part of the chemical energies is calculated within a DFT (DMol3), a fitted correction function—the repulsive

energy—is used to achieve results as close to *ab initio* counterparts as possible as shown in Table 3.5. We have developed an automatic parametrization scheme to ease the process of the repulsive energy fitting, offering a more systematic and much faster alternative to the traditional fitting process. Density functional theory (DFT) code (DMol3) was used when deriving the potentials. The following conditions were applied DNP basis, pwc functional, and for fitting basis the lowest degree of cutoff polynomial was 3 and the highest ranges from 8 to 10. Other than driving DFT calculators in the fitting procedure automatically, the adaptability of our plan additionally permits the utilization of outside data (e.g., atomic elements directions or exploratory information) as a source of perspective. Results with a few components demonstrate that our methodology can deliver parameter sets practically comparable to handmade ones, yet requiring far less human effort and time.

In order to fit repulsive functions for the Ti—Ti and Ti—O interactions, we used a fit set including a titanium oxide systems (with a very low weight). The molecular fit paths were created by stretching bonds and displacing titanium atoms while the crystalline paths were created by uniformly changing the volume of the crystal lattices and by using crystals with displaced titanium atoms.

We used both energy and force targets in the fit. In a fit session of a few days, we were able to produce a set of Ti—Ti and Ti—O repulsive potentials which reproduce energy and geometrical data in the same quality as the reference handmade set. A detailed comparison is given in 3.3.1 and Chapter 4.

After creating the repulsives for the Ti—Ti and Ti—O interactions, we extended the set to a complete TiO<sub>2</sub> set, still using exponential basis functions for expressing the repulsive potentials. Although this peculiar shape is the numerically most convenient way to confine the range of the Ti—Ti repulsive well below the second-neighbour distance and gives good results for various systems, it may be an interesting question for future investigations whether it is a precise representation of the underlying physics.

### **3.3 Validation of DFTB Slater-Koster potentials**

In the previous subsection 3.2 we derived Slater-Koster potentials successfully. These potentials are going to be validated in this chapter. We will predict structural,

mechanical and electronic properties of rutile and brookite TiO<sub>2</sub> phases. Moreover, these two TiO<sub>2</sub> phases are going to be lithiated. We will also compare our DFTB results with theoretical as well as experimental data.

### 3.3.1 Methodology

The density-functional-based tight-binding method (DFTB) [111] is an efficient quantum mechanical simulation method which was used to fully optimize rutile TiO<sub>2</sub>.

The DFT based *ab-initio* simulations were performed with the Cambridge Serial Total Energy Package (CASTEP) code [118] for mechanical properties. A plane wave basis set was used for expanding electronic states in the pseudopotential approximation and the used energy cutoff was set to 340 eV. The ultrasoft pseudopotentials [119,120] from the CASTEP database for the computations were employed. Exchange-correlation effects were taken into account using the generalized gradient approximation (GGA) in the efficient formulation of Perdew, Burke and Ernzerhof [121,122]. Reciprocal space integration in the Brillouin zone for rutile was performed by summation over (6 × 6 × 8) k-points respectively with a Monkhorst-Pack grid [123]. With the computational parameters applied (smearing: 0.1 eV, number of stains: 4 and maximum displacement: 4 × 10<sup>-4</sup> Å), a very high level of convergence of elastic parameters was achieved.

The LiTiO<sub>2</sub> parametrization set of Slater-Koster parameters we derived for all Li-Ti-O interatomic interactions was employed. The supercell models of 1×2×1 brookite structure had the size of up to 64 atoms.

## 3.4 Structural properties

### 3.4.1 Rutile

The rutile octahedron shows a slight orthorhombic distortion, such that its symmetry is lower than orthorhombic. The Ti-Ti distances in anatase are larger than those in rutile. In the rutile structure, there are 10 neighbouring octahedrons in contact with each octahedron and two sharing edge oxygen pairs and eight sharing corner oxygen atoms as shown in Figure 3.1. Among the various polymorphs of TiO<sub>2</sub>, rutile is generally considered to be the most stable bulk phase, while at the nanoscale, anatase and brookite are considered to be more stable due to their lower surface energy, although there are some contradictions in the literature [5,124].

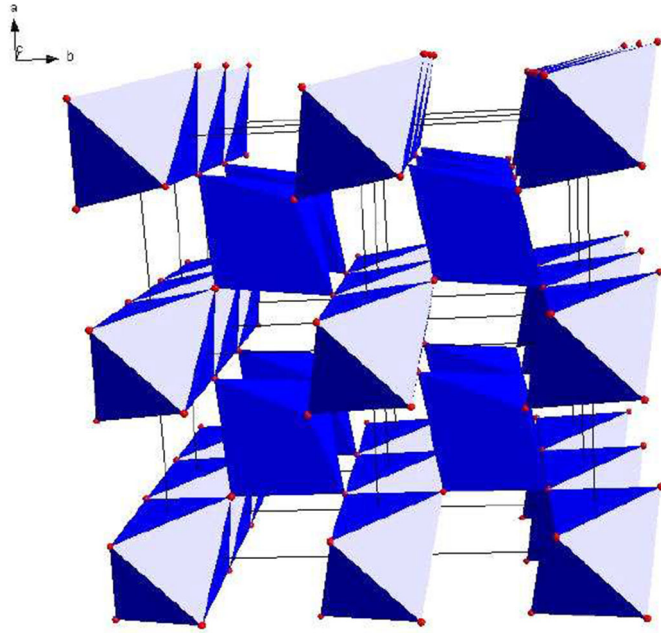


Figure 3.1. The atomic structure of rutile  $\text{TiO}_2$  with channels. Red spheres denote oxygen.

The bulk lattice parameters obtained from the full geometry optimization and some available experimental data are listed in Table 3.1. After full rutile  $\text{TiO}_2$  geometry optimization, the obtained values of the equilibrium lattice parameters together with experimental data and other theoretical results were compared. Our results were found to be in agreement with the one obtained by other scientists using various methods. The calculated equilibrium lattice parameters were within 4% of the experimental values.

Table 3.1. Lattice parameters (a, b and c) and volume (V) of rutile  $\text{TiO}_2$  calculated with DFTB compared with other theoretical and experimental data.

	DFTB (This work)	Matsui Potential [125]	DFT-GGA+D+U [126]	DFT-GGA [126]	Experimental [127]
a (Å)	4.671	4.510	4.870	4.618	4.594
c (Å)	2.998	3.020	2.954	2.948	2.958
V (Å <sup>3</sup> )	67.96	61.43	67.96	62.487	62.42

### 3.4.2 Brookite

To explore the structural properties of brookite  $\text{TiO}_2$ , geometry optimization was performed using DFTB+ code. Brookite  $\text{TiO}_2$  displays orthorhombic symmetry as compared to anatase and rutile structures which are tetragonal.

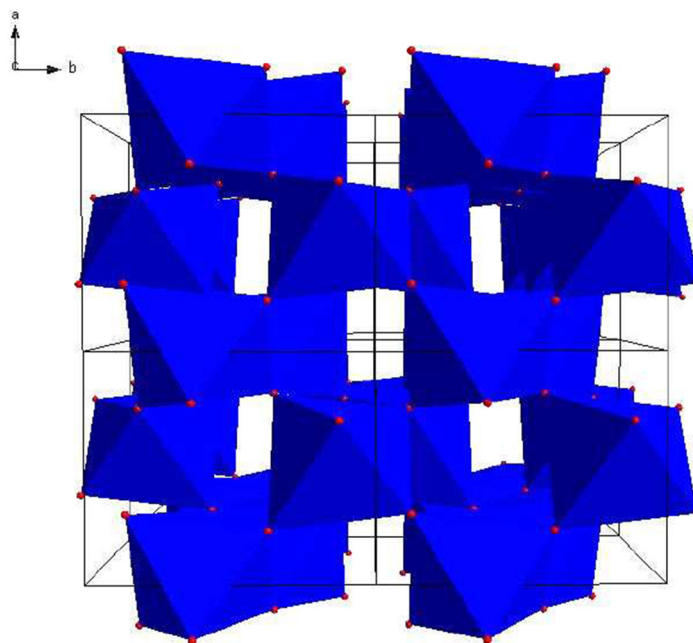


Figure 3.2. The atomic structure of brookite  $\text{TiO}_2$  with channels. Red sphere denote oxygen.

Brookite was formed by  $\text{TiO}_6$  octahedrons sharing 3 edges and 3 corners offering channels along the  $c$ -axis for the lithium ions (**Figure 3.2**). The octahedral site which has a larger space than the tetrahedral site is generally known to be energetically preferable site during lithium ions insertion. Thus, lithium ion insertion results in a slight distortion of the lattice, leading to anisotropic lattice expansion [128]. The DFTB calculated lattice parameters and volume, in Table 3.2 were in good agreement with DFT and experimental results.

Table 3.2. Lattice parameters (a, b and c) and volume (V) of brookite TiO<sub>2</sub> calculated with DFTB compared with the LDA, GGA and experimental.

	[129]				Exp. [130]
	DFTB (This work)	(GGA)RPBE	(GGA)PW91	LDA	
A (Å)	9.256	9.327	9.252	9.098	9.180
b (Å)	5.472	5.565	5.500	5.396	5.457
c (Å)	5.178	5.209	5.177	5.088	5.158
V (Å <sup>3</sup> )	262.26	270.37	263.41	249.74	258.40

## 3.5 Mechanical properties

### 3.5.1 Rutile

The elastic constants ( $C_{ij}$ ) are vital for understanding the mechanical properties of a solid material. The reaction of crystal lattice to external stress within the elastic limit is characterized elastic constants. In Table 3.3 the elastic constants and elastic modulus of the rutile titanium dioxides are reported. The mechanical moduli, i.e. shear modulus (G), bulk modulus (B), and Young's modulus (E) were calculated using the Voigt Reuss–Hill approximation from the elastic constants. The VRH approximation provides reasonable mechanical moduli for bulk polycrystalline material. The  $C_{ij}$  elastic constants were found to be in reasonable agreement with the results calculated and measured previously, except for  $C_{33}$  which is underestimated. According to Pugh's criterion [131], materials with Pugh modulus ratio greater than 0.57 show brittleness, whereas those with the ratio less than 0.57 show ductility; hence the DFTB calculated G/B in Table 3.3 indicates ductility.

Table 3.3. Elastic constants  $C_{ij}$ (GPa), bulk modulus B(GPa), shear modulus G(GPa), Young's modulus E(GPa), Pugh modulus ratio G/B and Possion's ratio (M) for the bulk rutile TiO<sub>2</sub>.

Name	DFTB	CASTEP	[132]	PBE [133]	Exp. [134]
C <sub>11</sub>	252.28	286.69	292	262	268
C <sub>33</sub>	335.36	497.15	471	458	484
C <sub>44</sub>	99.32	125.56	114	135	124
C <sub>66</sub>	214.71	228.69	236	221	190
C <sub>12</sub>	232.73	185.62	192	176	175
C <sub>13</sub>	155.82	161.44	174	146	147
B <sub>VRH</sub>	214.3	227.25	212	205	212
G <sub>VRH</sub>	69.3	119.12	113		
E <sub>VRH</sub>	304.20				
G/B	0.32	0.52			
M		0.277			

There are six elastic constants C<sub>11</sub>, C<sub>12</sub>, C<sub>13</sub>, C<sub>33</sub>, C<sub>44</sub> and C<sub>66</sub> according to symmetry of the tetragonal structure. The calculated elastic constants C<sub>ij</sub> for the rutile TiO<sub>2</sub> structure satisfy the Born stability criteria for a tetragonal structure: (C<sub>11</sub>-C<sub>12</sub>)>0, C<sub>ij</sub>>0(ij=11, 33, 44 and 66), are listed by Born et al. [135]. We noted that the independent elastic constants for the rutile TiO<sub>2</sub> were all positive and satisfy the necessary stability conditions, suggesting elastic stability. As a result, the crystal structures of TiO<sub>2</sub> polymorphs were stable. This is in good agreement with the experimental and calculated results found by Ding et al. [136], Zhu et al. [137]. The percentage difference between DFTB and experimental bulk moduli was found to be 2.4%. However, there were some discrepancies in C<sub>33</sub> parameters using DFTB. These parameters were underestimated.

### 3.5.2 Brookite

The DFTB calculated elastic constants, bulk modulus, shear modulus, Young's modulus, Pugh modulus ratio G/B and Possion's ratio of the bulk TiO<sub>2</sub> brookite polymorph are shown in Table 3.4 along with our calculated DFT CASTEP results and other theoretical data. From the values of the elastic constants the intrinsic mechanical stability of the structure can be deduced, since the condition for mechanical stability



of an orthorhombic crystal is depicted in equation [2.5.3]. The calculated elastic constants of brookite crystal do satisfy such stability criteria, indicating that they are inherently stable. Overall, we found a reasonable agreement between our DFTB and DFT computed and theoretical values reported by Ding and Xiao [136], except for  $C_{33}$  which is underestimated by DFTB. The Pugh modulus ratio using DFTB is in good agreement with the one from CASTEP. However, other  $C_{ij}$  parameters were underestimated. The magnitude of G/B ratio allude to the ductility of brookite  $TiO_2$ .

Table 3.4. Elastic constants  $C_{ij}$ (GPa), bulk modulus B(GPa), shear modulus G(GPa), Young's modulus E(GPa), Pugh modulus ratio G/B and Possion's ratio for bulk  $TiO_2$  brookite.

Name	DFTB	CASTEP	PBESol [136]
$C_{11}$	237.27	319.23	306.95
$C_{22}$	301.17	319.24	320.77
$C_{33}$	230.56	316.47	305.92
$C_{44}$	82.33	104.96	105.38
$C_{55}$	82.10	101.71	94.89
$C_{66}$	123.44	104.63	87.02
$C_{12}$	157.01	175.52	168.08
$C_{13}$	118.01	157.46	168.33
$C_{23}$	126.27	145.22	
$B_{VRH}$	172.1	212.18	
$G_{VRH}$	78.8	93.00	
$E_{VRH}$	243.43	0.44	
G/B	0.46		
M		0.309	

### 3.6 Electronic properties (Rutile and brookite)

In this section we consider electronic properties of rutile and brookite polymorphs. The DFTB calculated bandgap energies of such polymorphs are given in Table 3.5 and that of rutile is 3.095 eV and it agrees with previously reported theoretical and experimental values which fall in the range 3.01-3.37 eV, and are related to direct and indirect

bandgaps. Similarly, the DFTB calculated brookite bandgap is 3.113 eV and also compare with results in literature which are in the range 3.13-3.56 eV [141].

Table 3.5. Results band gap energies for TiO<sub>2</sub> polymorphs (rutile and brookite). The results are compared with available experimental data and other computational results.

Structures	Our DFTB Bandgap value using dispersion correction (eV)	Other Bandgaps (eV) [138] [139] [140]
Rutile	3.095	3.01-3.37
Brookite	3.113	3.13-3.56

The DFTB calculated results are deduced from the total and partial density (PDOS) in Figures 3.3, 3.4. and also identify the electronic contributions from s, p and d orbitals in rutile and brookite TiO<sub>2</sub>. The valence band from -18 to 0 eV shows a strong hybridization between O 2p and Ti 3d electrons while the conduction band from 0 to 21 eV is mostly contributed by Ti 3d electrons with a small contribution from the O 2p electrons. Both of Ti 3d and O 2p states are involved in electron transition from the valence to conduction band across the band gap in both rutile and brookite TiO<sub>2</sub> phase.

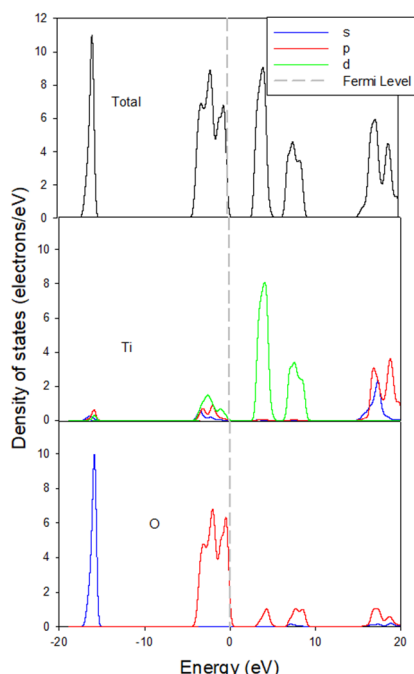


Figure 3.3. The total and partial density of states (DOS) of rutile TiO<sub>2</sub> computed from DFTB.

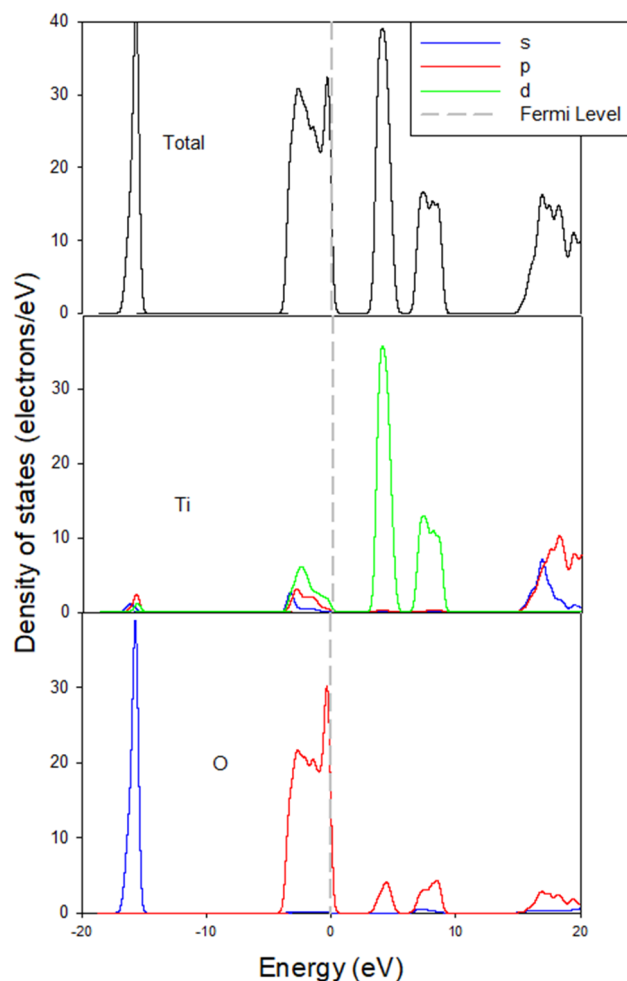


Figure 3.4. The total and partial density of states (DOS) of brookite  $\text{TiO}_2$  computed from DFTB. The band gaps of the rutile and brookite  $\text{TiO}_2$  are also reflected in the DFTB calculated band structures shown in Figure 3.5 and Figure 3.6 which are also compared with results in literature.

It is, however, well known that the underestimated or overestimated band gaps can be due to the choice of exchange-correlation function in DFT. In order to overcome the well-known deficiency regarding energy gap underestimation, dispersion correction within DFTB+ was employed. Hence, we obtained results which were in good agreement with previously calculated outcomes as shown in Table 3.5.

When using dispersion correction, the DFTB+ uses universal force field (UFF) based Lennard-Jones dispersion corrections. UFF is moderately accurate for predicting geometries and conformational energy differences of organic molecules, main group inorganics, and metal complexes [81].

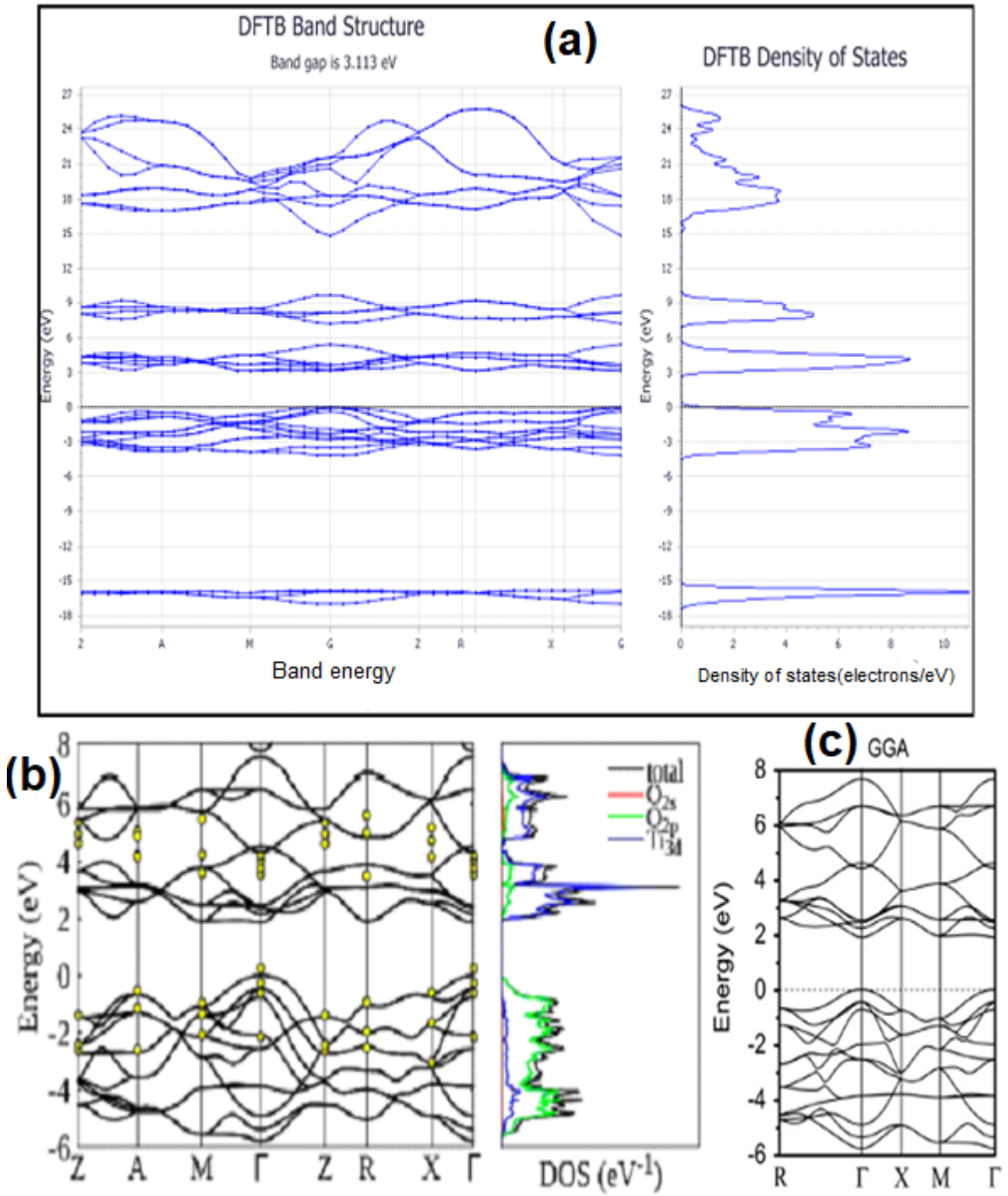


Figure 3.5. Band structure and the corresponding DOS of brookite obtained with (a) DFTB+ (This work), (b) DFT-GGA [141] and (c) DFT-GGA [139].

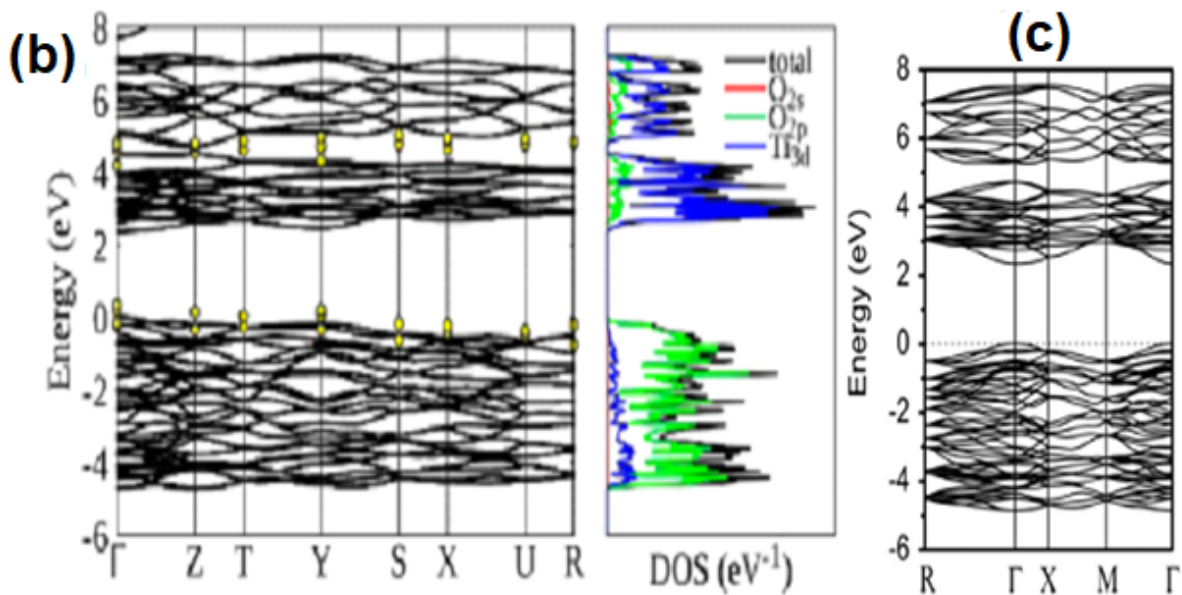
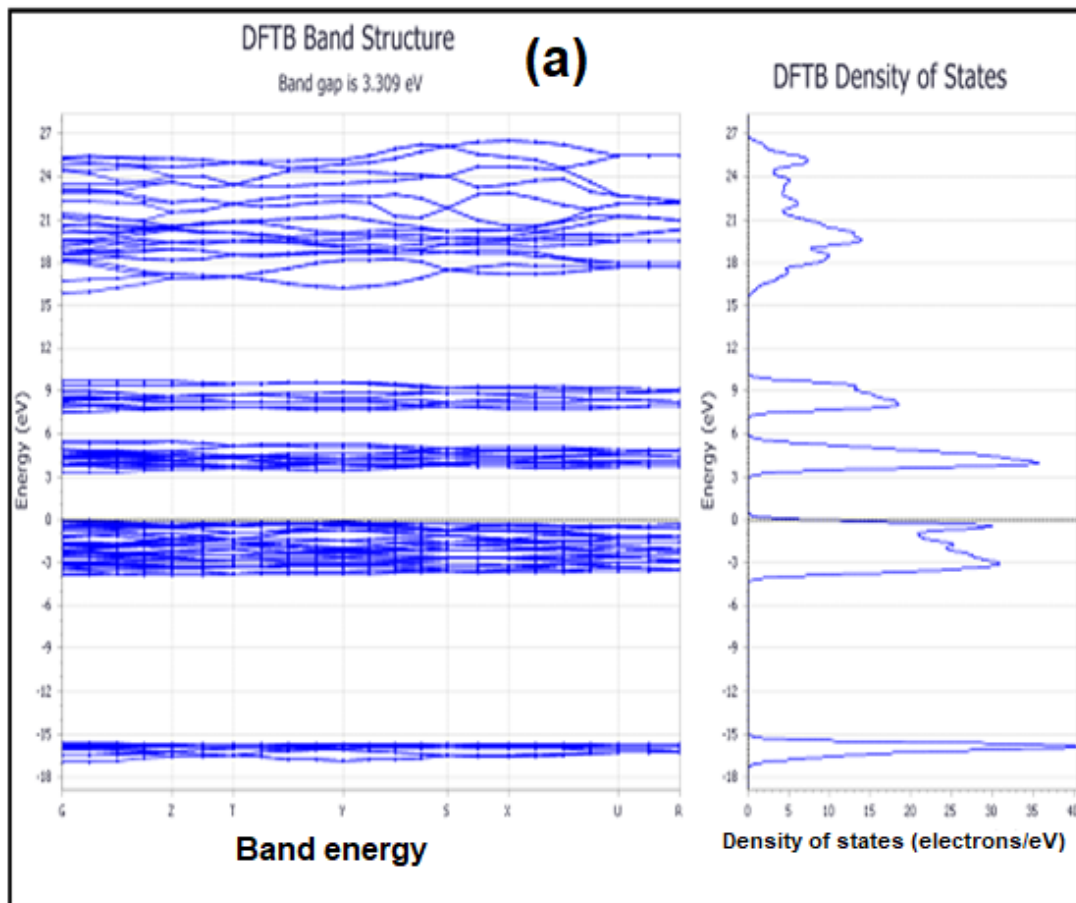
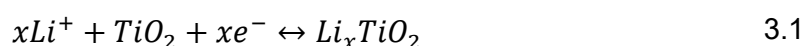


Figure 3.6. Band structure and the corresponding DOS of rutile obtained with (a) DFTB+, (b) DFT-GGA [141] and (c) DFT-GGA [139].

### 3.7 Lithiation

Recently, a number of reports have indicated that nanosized rutile  $\text{TiO}_2$  possesses significantly improved lithium intercalation capability [63,142]. Rutile  $\text{TiO}_2$  is known to be a very stable phase, though in its bulk crystalline form, it can only accommodate negligible amounts of Li ( $<0.1$  Li per  $\text{TiO}_2$  unit) at room temperature. Overall, the lithium reaction associated with the  $\text{TiO}_2$  polymorphs [143,144] can be expressed through equation 3.1 as



Despite various polymorphs of  $\text{TiO}_2$  (i.e., rutile, brookite, and anatase) yielding relatively disparate electrochemical properties, it should be conceivable to finely tune  $\text{TiO}_2$  performance as a function of crystalline structure, size, and morphology [145].

#### 3.7.1 Rutile preferable sites

Available lithium insertion sites (I and II) in rutile  $\text{TiO}_2$  are shown in Figure 3.7. It is known that a more stable site can be deduced from the interception of the Fermi level with the DOS plot; where an interface at a lower portion of the DOS allude to a relatively stable site. Figures 3.8 and 3.9 show the total DOS for lithium located in sites I and II of  $\text{TiO}_2$  respectively. Although it is difficult to differentiate how the Fermi level cuts the DOS in the two configurations, the magnified portions of the DOS in Figure 3.10 indeed affirm that site I is more preferable. This is further substantiated

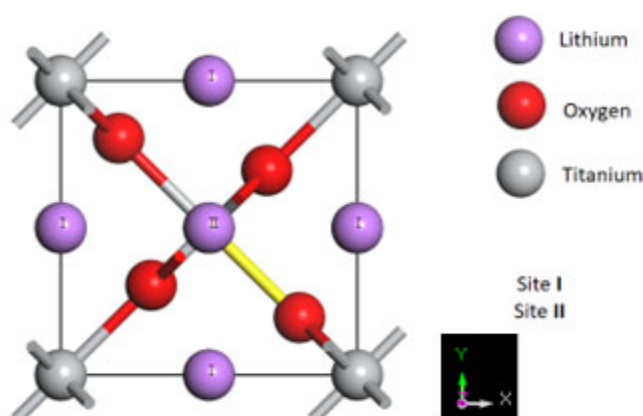


Figure 3.7. The lithium rutile phase in the  $\text{LiTiO}_2$  sample indicating two possible Li positions. Ti, O and Li atoms are in grey, red and purple spheres respectively.

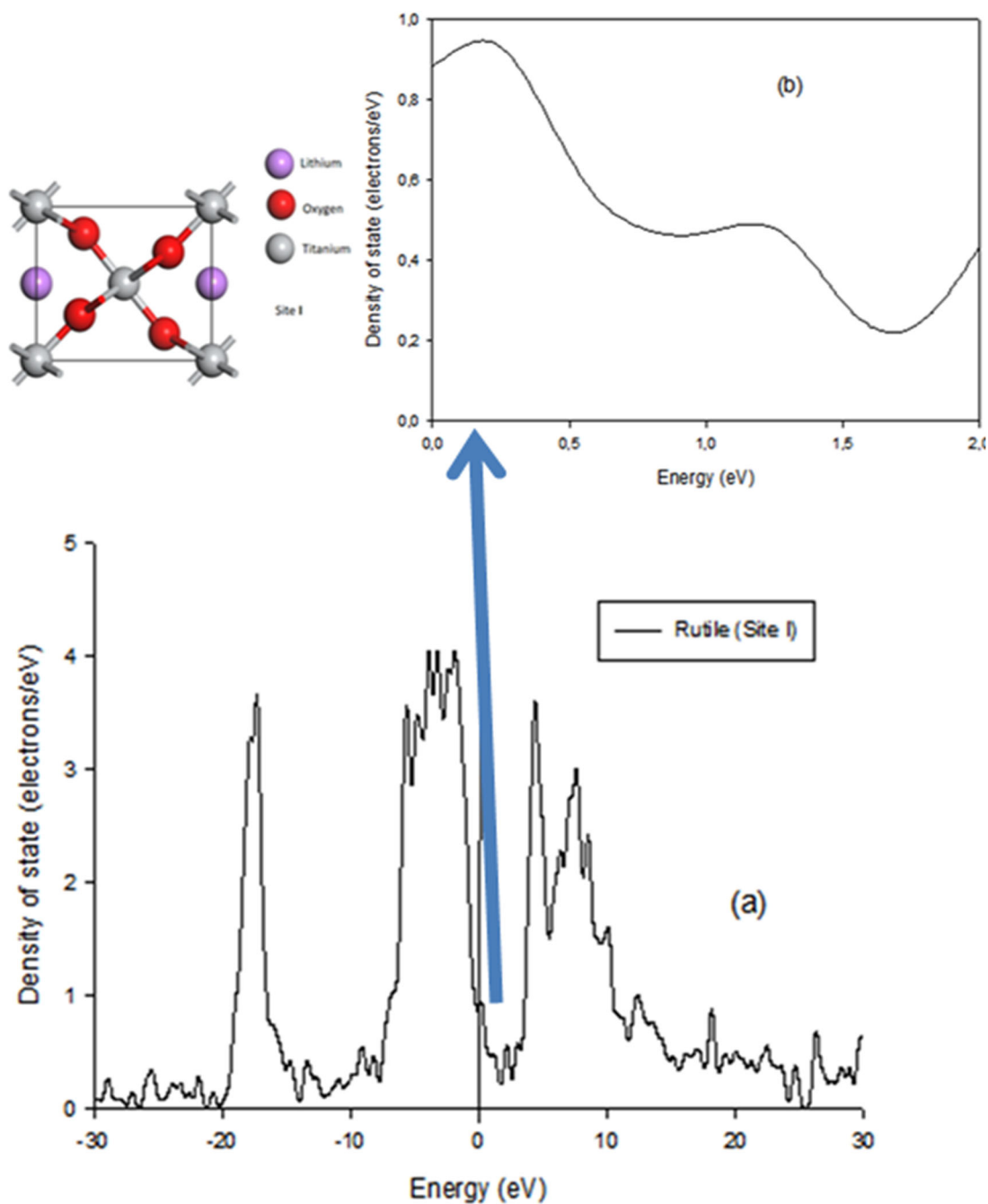


Figure 3.8. (a) The total DOS, (b) the lithium rutile phase in the  $\text{Li}_x\text{TiO}_2$  sample indicating possible Li ion position (I) and insert of the energy at the Fermi level.

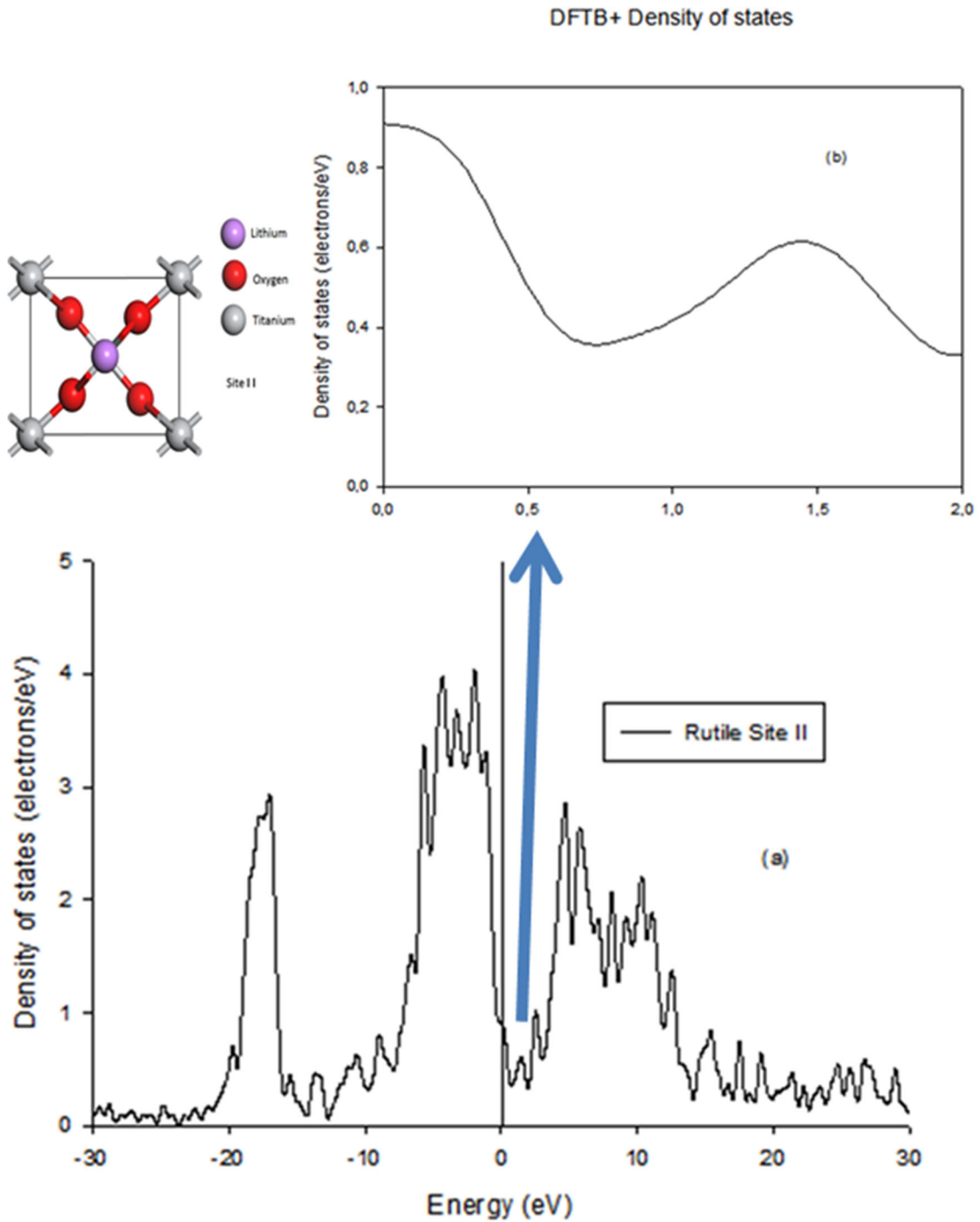


Figure 3.9. (a) The total DOS, (b) the lithium rutile phase in the  $\text{Li}_x\text{TiO}_2$  sample indicating possible Li ion position (II) and insert of the energy at the Fermi level.

by total energies related to lithium insertions in sites I and II of  $\text{TiO}_2$ , as depicted in Table 3.6, where site I is associated with a lower energy.



### DFTB+ Density of States

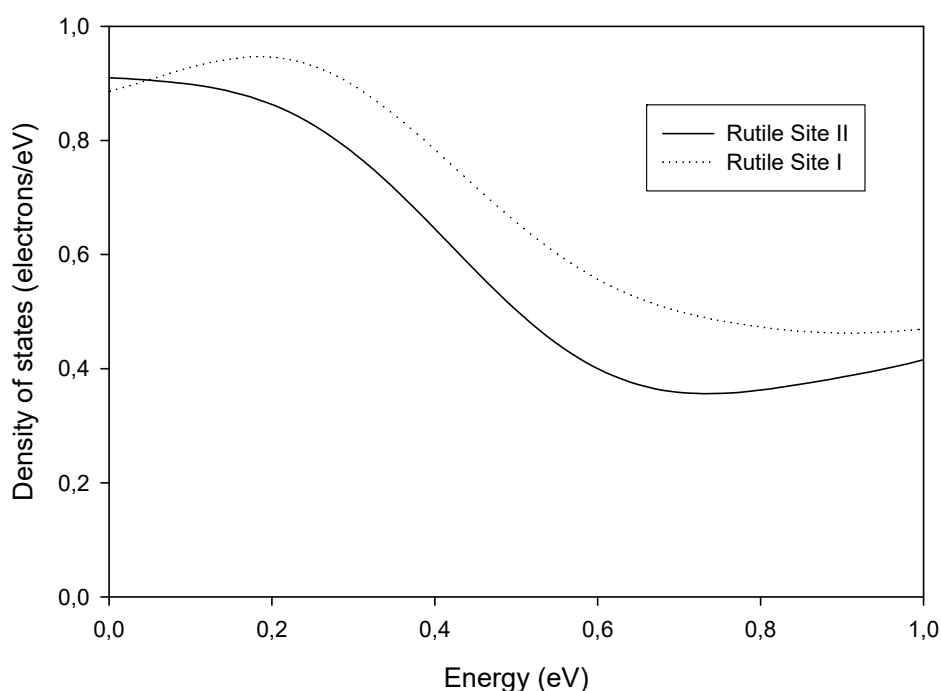


Figure 3.10. DOS of the rutile  $\text{TiO}_2$  with two different sites calculated using the DFTB+.

Table 3.6 Relative energies and lattice parameters for the most stable Li intercalation sites in rutile  $\text{TiO}_2$ .

Total Energy(kcal/mol)	a(Å)	b(Å)	c(Å)	x(M/Ti)	Atoms	Volume(Å <sup>3</sup> )	Density(g/cm <sup>3</sup> )	Site
-15462	4.377	3.628	3.280	0.5	7	52.08	5.206	I
-14860	4.351	3.661	3.282	0.5	7	52.28	5.296	II

### 3.7.2 Rutile – Lithiated induced structural change

The large change in unit cell volume as shown in Figure 3.11, causes mechanical failure of the original rutile crystallites due to abundant strains induced during lithium insertion. This separation of crystallites may clarify the huge irreversible capacity loss of micro-sized rutile observed in the cycling tests [146]. All lattice parameters increase in concentration ranges 0 to 0.125 Li/Ti and 0.25 to 0.5 Li/Ti. Hence, our results are in agreement with experimental data, especially the transition from tetragonal to orthorhombic symmetry above 0.1 Li/Ti (Figure 3.11). However, there was a slight decrease in *a* and *b* lattice parameters. Furthermore, the expected large (anisotropic) diffusion coefficient of Li ions along *c*-direction is observed, experimentally reported to be approximately  $10^{-6} \text{ cm}^2\text{s}^{-1}$  at room temperature [147,148].

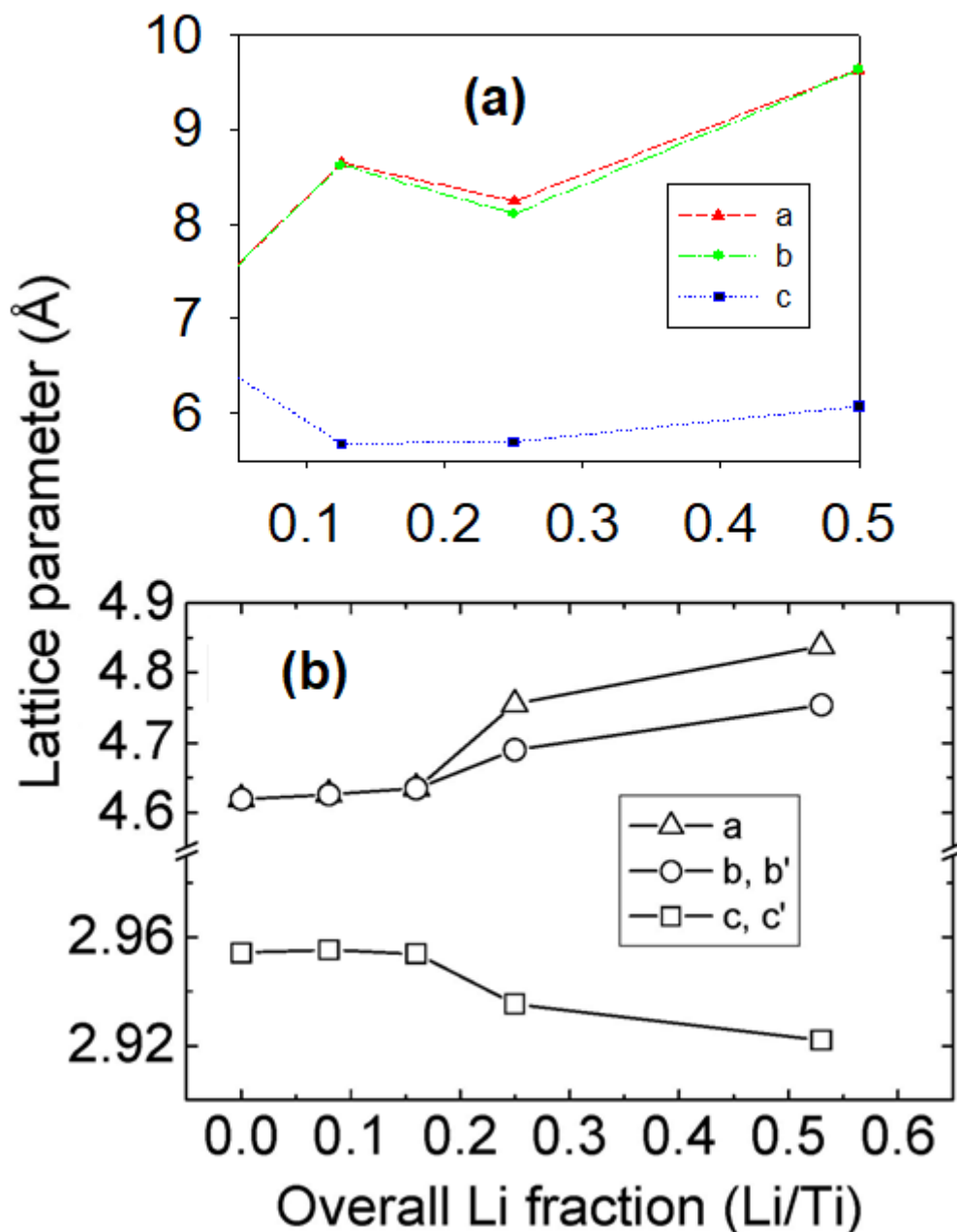


Figure 3.11. (a) The rutile system used consists of a primitive cell built up of  $2 \times 2 \times 2$  unit cells (16 Ti and 32 O atoms) and (b) experimental lattice parameters changes of a single Li ion in a primitive cell.

The change in volume during lithium intercalation of rutile is shown in Figure 3.12. We observed an increase in volume during lithiation which is in agreement with experimental results. However, there was an insignificant decrease in volume between 0.125 and 0.25 Li/Ti concentrations. This change might be due to transformation of rutile phase.

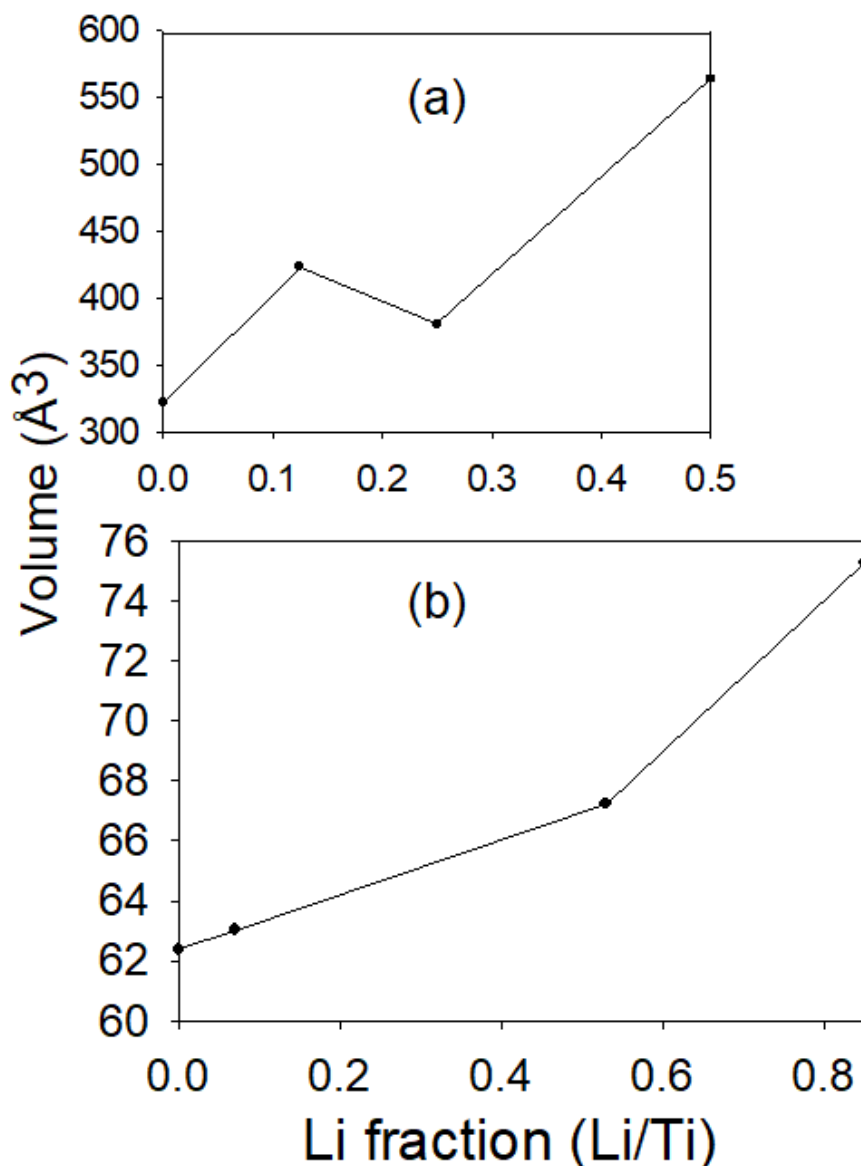


Figure 3.12. (a) The system used consists of a primitive cell built up of  $2 \times 2 \times 4$  unit cells (32 Ti and 64 O atoms) and (b) experimental volume changes of a single Li ion in a primitive cell.

### 3.7.3 Brookite - Lithiated induced structural change

We created a brookite  $1 \times 2 \times 1$  supercell containing 16  $\text{TiO}_2$  units  $[(\text{LiTiO}_2)_{16}]$ . The lithium atomic coordinates were fixed as 8c (0.403, 0.345, 0.449), the occupancy was set to 1.0. The Ti-Ti and O-O distances within a  $\text{LiTi}_{32}\text{O}_{64}$  brookite are 4.296Å and 3.551Å, versus 5.129Å and 3.460Å, respectively in Li ion free crystal. Volume changes

and a significant deformation of the lithiated brookite  $\text{TiO}_2$  structure were observed as compared to their initial structures.

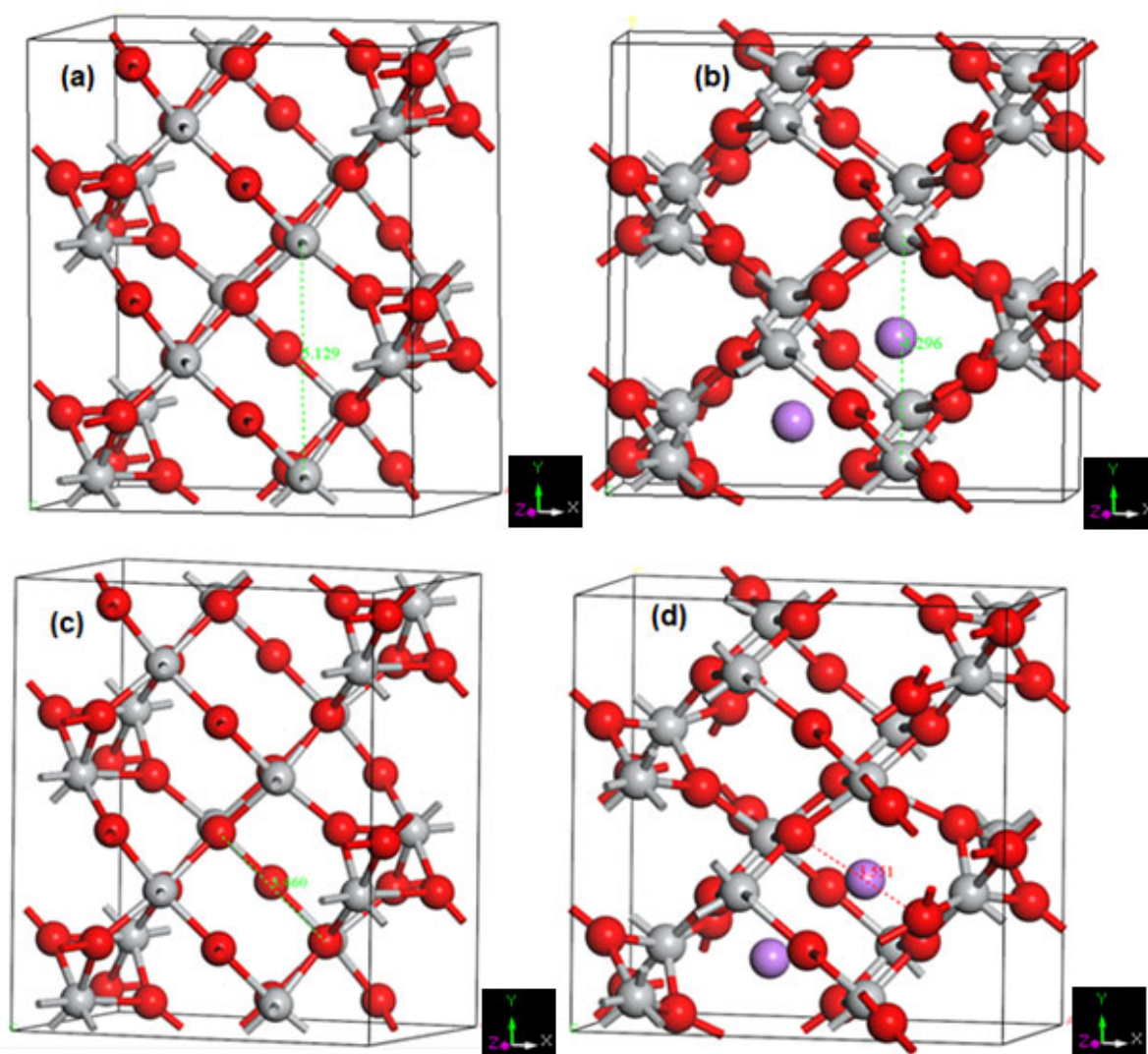


Figure 3.13. (a) and (b) Ti-Ti bond length before and after lithiation, (c) and (d) O-O bond length before and after lithiation respectively. Ti, O and Li atoms are in grey, red and purple spheres respectively.

Li-uptake by polycrystalline brookite is insignificant at room temperature while the intercalation behaviour at raised temperatures, the brookite intercalate more Li ions concentrations [149]. The insertion properties of lithium ions in the brookite phase  $\text{TiO}_2$  have been rarely pronounced [150] which would result from the difficulties in studying and preparing brookite phase  $\text{TiO}_2$  materials. Moreover, the bulk state of brookite  $\text{TiO}_2$  has been proved to be a poor insertion anode due to the structure restrictions of lithium ion diffusion, leading to minor attention.

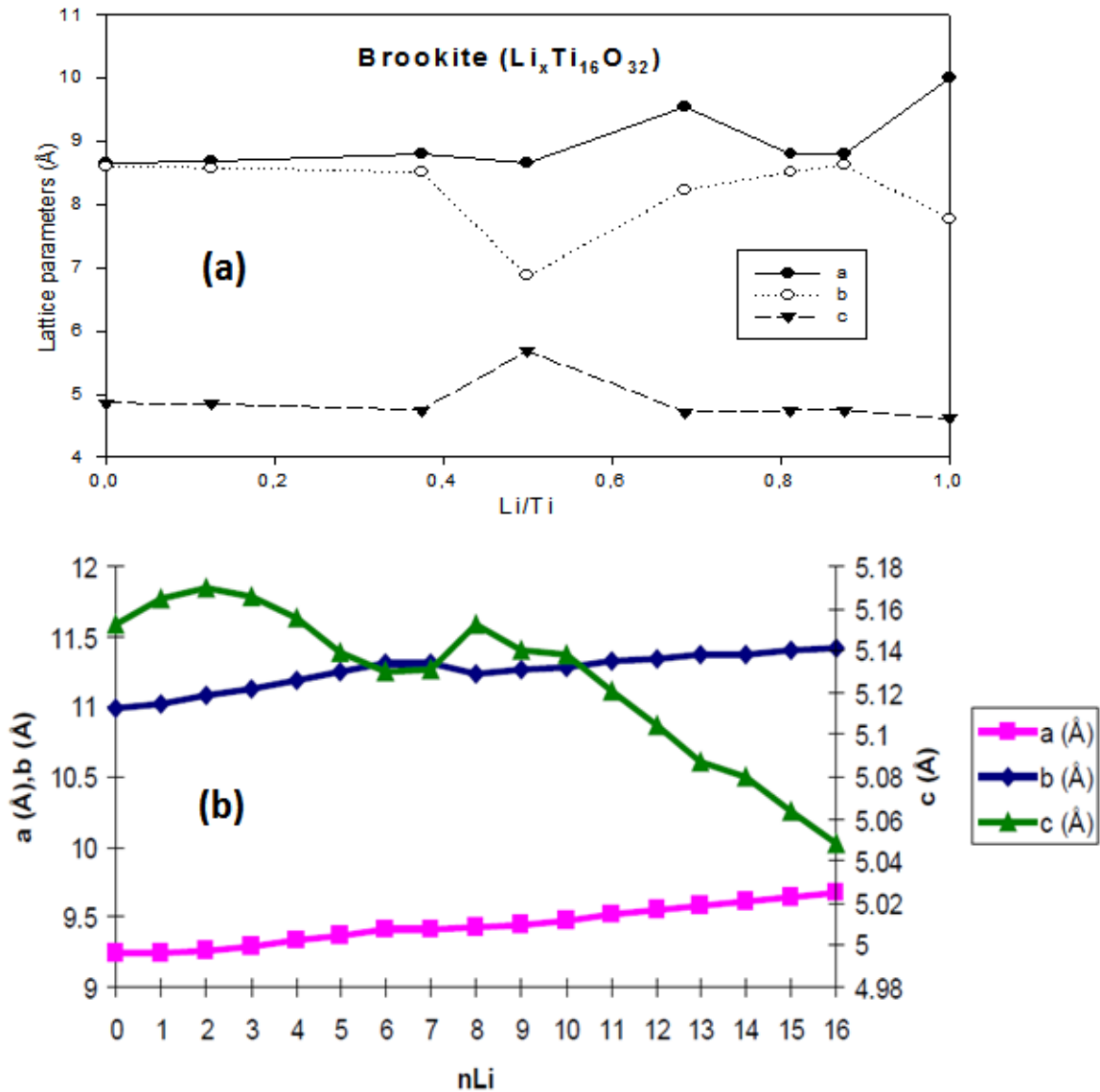


Figure 3.14. (a) Lattice parameters change of a unit cell of brookite  $\text{Li}_n\text{Ti}_{16}\text{O}_{32}$  as a function of Li/Ti ratio and (b) from literature the cell parameters (a, b, c) of brookite during the Li intercalation [151].

In Figure 3.14(a), lattice parameters (a and b) are in agreement the results from literature [151]. However, c parameter decreases from 0 to 0,4 and 0,5 to 1,0 concentrations which is similar the observation by Muhamed [151] as shown in the figure above.

### 3.8 Summary

In this chapter we have used a new fitting mechanism to create repulsive potentials for the DFTB method in an automatic way using least-squares fitting on automatically generated reference data. The derived potentials of  $\text{TiO}_2$  were also validated, by predicting the lattice parameters of bulk rutile and compare them the previously

calculated ones. The obtained structural and mechanical properties using DFTB+ approach which are in good agreement with either prior reported experimental or theoretical work. The choice of lithium intercalation site in bulk TiO<sub>2</sub> rutile was determined by performing DFTB+ full geometry optimization. The minimum energies of lithiated rutile at different sites were compared. Their density of states were also compared, to the energetically favoured lithiation site. The octahedral positions appear to be favoured. We also used DFTB+ derived potentials to highlight the structural and electronic properties of TiO<sub>2</sub> polymorphs. Brookite crystal lattice parameters were calculated and are in good agreement with previously theoretical results. The predicted elastic constants of brookite crystal do satisfy these stability criteria, indicating that brookite is inherently stable. Volume changes and a significant deformation of the lithiated brookite TiO<sub>2</sub> structure have been observed when contrasted with their underlying structures. Hence, brookite is not a good anode candidate for lithium ion batteries.

# Chapter 4: Structural and electronic properties of anatase TiO<sub>2</sub> polymorph

## 4.1 Introduction

Since, we have derived and validated our Slater-Koster potentials for TiO<sub>2</sub> successfully in Chapter 3. In this chapter we apply these potentials to calculate structural, mechanical and electronic properties of bulk anatase TiO<sub>2</sub> phases and their lithiated and sodiated versions. We will also extend such predictions to larger anatase systems such as nanotubes and nanospheres; which depicts the advantages of the semi-empirical DFTB method over the DFT approach. Molecular dynamics calculations, which allow introduction of temperature, will, in addition, be carried on the bulk and nanotubes of anatase TiO<sub>2</sub>.

## 4.2 Methodology

The quantum-chemical calculations were implemented within the Density Functional based Tight Binding (DFTB) method [111,152] as implemented in BIOVIA Materials Studio. The Li<sub>x</sub>TiO<sub>2</sub> and Na<sub>x</sub>TiO<sub>2</sub> parametrization set of Slater-Koster parameters we derived for all Li-Ti-O and Na-Ti-O interatomic interactions were employed.

Bulk anatase structures (pure, lithiated and sodiated) and nanotubes were simulated with the 4 × 4 × 2 and 1 × 1 × 6 Monkhorst-Pack [45] grids for *k*-point sampling, respectively. The equilibrium lattice parameters were obtained after full geometry optimization calculations having different lattice parameters and volumes. Therefore, as a general rule, the steepest descents algorithm was used for the first 10-100 steps, after which the ABNR algorithm was used for nanotubes and nanospheres to complete the optimization to convergence (Appendix A and Appendix B).

## 4.3 Structural properties (bulk)

Anatase TiO<sub>2</sub> has tetragonal crystal structure, in which the slightly distorted TiO<sub>6</sub> octahedral in Figure 4.1 could be considered as a building block. The octahedral has two longer equivalent apical Ti—O bonds (Ti—O1 and Ti—O4) with bond length  $D_{ap}$  and four equivalent equatorial Ti—O bonds (Ti—O2, Ti—O3, Ti—O5 and Ti—O6) with bond length  $D_{eq}$ . It is shown that  $D_{ap}$  is larger than  $D_{eq}$  in Table 4.1 the apical axis are softer than equatorial in TiO<sub>6</sub> octahedral.

Table 4.1. Titanium—Oxygen compound handmade parametrization (tiorg), automatically created one (auto) and the one that we created. Atom pairs denote distance in Å.

Ti <sub>2</sub> O <sub>4</sub> (dibridged with end O atoms in cis position)			
properties	Our results	tiorg [153]	auto [153]
Ti—Ti	2.817	2.800	2.635
Bridging Ti—O	1.846	1.887	1.812
TiO <sub>2</sub> anatase			
Shortest Ti—Ti	3.031	2.996	3.082
Shortest Ti—O	1.901	1.921	1.957

The unit cell contains four TiO<sub>2</sub> formula units of anatase. At ambient conditions we obtain a=3.888 and c=9.405 Å which are in good agreement with literature.

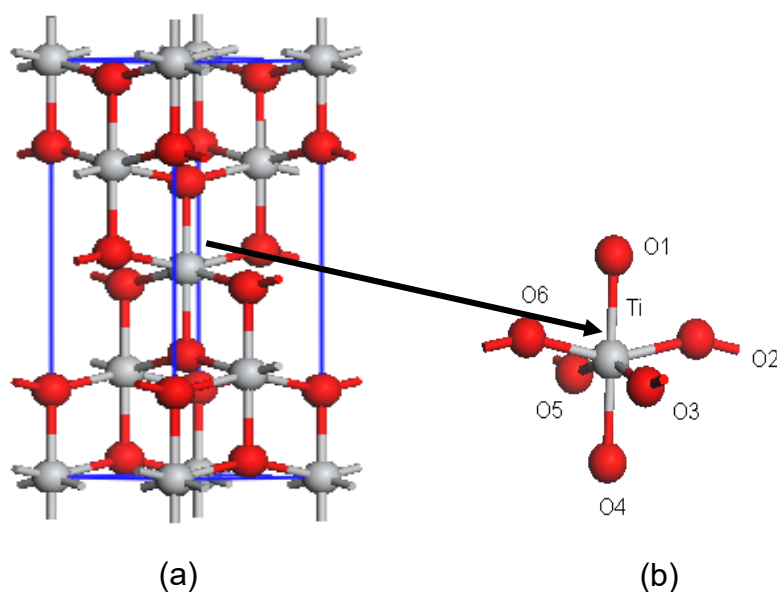


Figure 4.1 (a) The tetragonal crystal cell of anatase, (b) The atomic structure of TiO<sub>6</sub> octahedron in anatase TiO<sub>2</sub>. Grey and red spheres denote titanium and oxygen, respectively.



Table 4.2. Lattice parameters (a, b and c) and volume (V) of anatase TiO<sub>2</sub> calculated with DFTB method compared with the theoretical and experimental values.

	DFTB	Tight binding [126]	DFT [154]	Experimental [130]
a (Å)	3.888	3.782	3.785	3.784
b (Å)	3.888	3.782	3.785	3.784
c (Å)	9.405	9.502	9.512	9.515
V (Å <sup>3</sup> )	141.6	136.0	136.3	136.2

After full anatase TiO<sub>2</sub> geometry optimization, the calculated lattice parameters were compared with experimental data and other theoretical results, and were found to be in agreement. Both, the calculated equilibrium lattice parameters and volumes are within 4% of the computational and experimental values.

#### 4.4 Mechanical and electronic properties (bulk)

In order to gain insights into mechanical properties of a solid material, the elastic constants ( $C_{ij}$ ) are very important. These components will reduce to six elements  $C_{11}$ ,  $C_{12}$ ,  $C_{13}$ ,  $C_{33}$ ,  $C_{44}$  and  $C_{66}$  according to the symmetry of the tetragonal structure as shown in Table 4.3. In this study DFTB and CASTEP methods were used to determine mechanical properties. The percentage difference between  $C_{11}$  and  $C_{66}$  on using the DFTB and CASTEP codes is within 13%. However,  $C_{13}$ ,  $C_{33}$  and  $C_{44}$  were underestimated by DFTB as compared to DFT (CASTEP, VASP) and the Morse potential methods. The exchange-correlation functions which were used in each method are GGA-PBEsol, GGA-PBE functional respectively. When using CASTEP, the predicted bulk modulus and shear modulus (143.5 GPa and 62.9 GPa) agree reasonably with experimental results (178 GPa and 71.03 GPa) respectively [132,136,155]. Moreover, the percentage differences between bulk and shear moduli are within 10%. We have observed that the DFTB method tends to underestimate mechanical parameters as shown in Table 4.3 and Table 3.4. In Figure 4.2, we show the electronic density of states for anatase TiO<sub>2</sub> using DFTB as compared to the one using VASP code, cited in literature. The valence band edge of both materials is dominated by O 2p, and the conduction band edge is formed from Ti 3d. This implies

that excess electrons in these materials will be centred on the d states of cations, whereas electron holes are centred on 2p states of oxygen, which is consistent with the findings by Landmann *et.al.* [156] and Scanlon *et.al.* [157].

Table 4.3. Elastic constants  $C_{ij}$  (GPa), bulk modulus B (GPa), shear modulus G (GPa), Young's modulus E(GPa), Pugh modulus ratio G/B and Poisson's ratio for anatase bulk  $\text{TiO}_2$ .

Name	DFTB(This work)	CASTEP(This work)	CASTEP [136]	VASP [158]	Morse potential [155]
$C_{11}$	388.15	353.21	355.86	309.4	377
$C_{33}$	228.07	237.34	207.41	195	191
$C_{44}$	47.45	81.59	74.75	75	72
$C_{66}$	52.26	59.71	60.62	55	57
$C_{12}$	104.31	153.83	155.05	131	145
$C_{13}$	93.75	146.69	147.74	134	153
$B_{VRH}$	143.5	199.99	201	177	181
$G_{VRH}$	62.9	76.08	71.03	65	64.3
$E_{VRH}$	202.54		189.93	178	
G/B	0.44	0.38			
M		0.331			

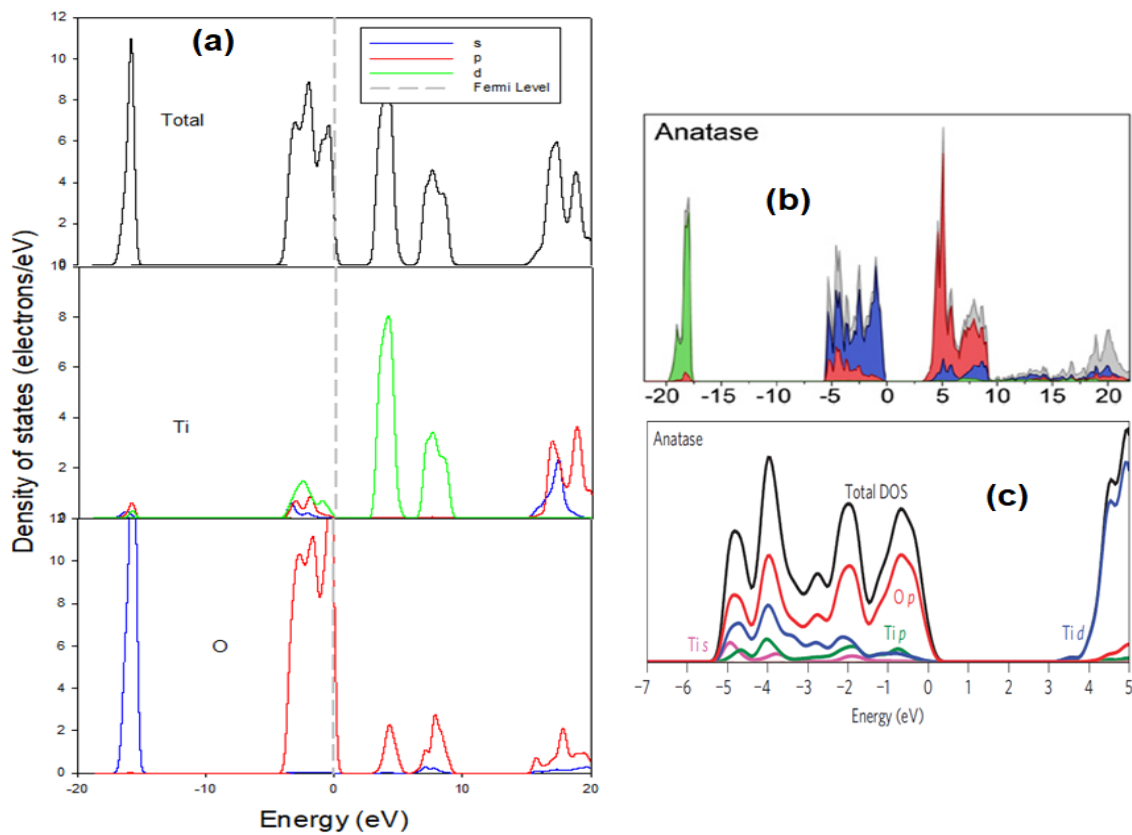


Figure 4.2. Comparison of the total and partial electronic density of states of anatase  $\text{TiO}_2$  calculated using the (a) DFTB (b) and (c) VASP (HSE06 hybrid density functional) [156] [157].

For comparison, the band structures calculated by DFTB+ and GW methods are shown in Figure 4.2. The optical band gap for anatase is reported as  $\sim 3.60\text{eV}$  when using VASP (HSE06) [157] and  $\sim 3.2\text{ eV}$  [138] experimentally. The calculated band gap energy for anatase ( $3.183\text{ eV}$ ) using DFTB+ method was found to be in agreement with an experimental and computational data [156] [157]. Overall, these findings show the accuracy and reliability DFTB results as compared with other methods.

## 4.5 Lithiation (bulk)

The anatase phase of  $\text{TiO}_2$  is a functioning material towards lithium intercalation, with a theoretical capacity of  $335\text{ mAh g}^{-1}$ . Notwithstanding, the typically estimated capacity of  $168\text{ mAh g}^{-1}$ , derived from the rate of  $1\text{ C}$ , is mentioned in literature [159,160]. Approximately  $0.6\text{ mol Li}^+$  can be inserted per mol  $\text{TiO}_2$  at  $1.78\text{ V}$  (versus  $\text{Li/Li}^+$ ) [16]. In spite of these points of interest,  $\text{TiO}_2$  experiences low electronic conductivity and  $\text{Li}^+$  diffusivity [161], which will restrict the rate capability and its wide practical application.

### 4.5.1 Preferable sites

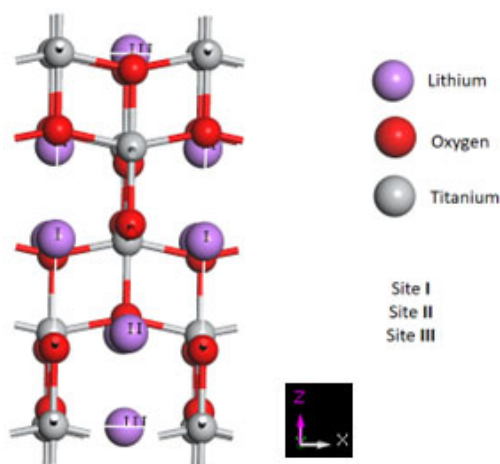


Figure 4.3. The anatase  $\text{LiTiO}_2$  structure indicating three possible Li positions, I, II, and III; Ti, O and Li atoms are indicated in grey, red and purple spheres respectively.

In order to identify positions that could be occupied by Li in anatase  $\text{TiO}_2$ , three different sites, I, II, and III were considered as depicted in Figure 4.3. Generated lithiated structures were geometrically optimized and total energies were calculated.

Table 4.4. Relative energies and lattice parameters for the most stable Li intercalation sites in anatase TiO<sub>2</sub>.

Total								
Energy(kcal/mol)	a(Å)	b(Å)	c(Å)	x(Li/Ti)	Atoms	Volume(Å <sup>3</sup> )	Density	Site
-26966.21	3.595	3.595	7.215	0.25	13	93.24	5.815	III
-26966.14	3.595	3.595	7.215	0.25	13	93.24	5.815	II
-26965.95	3.595	3.595	7.215	0.25	13	93.24	5.815	I

Energies related to the location of Li at three sites in anatase TiO<sub>2</sub> are shown in Table 4.4, and it was noted that Li (III) site corresponds to the lowest total energy (−26966.21 kcal/mol), and whereas those of the Li (II) (-26966.14 kcal/mol ) and Li (I) (-26965.95 kcal/mol) site are reflected at higher energies. It is further observed that, on the whole, the magnitudes of the total energies for the sites, are close to each other.

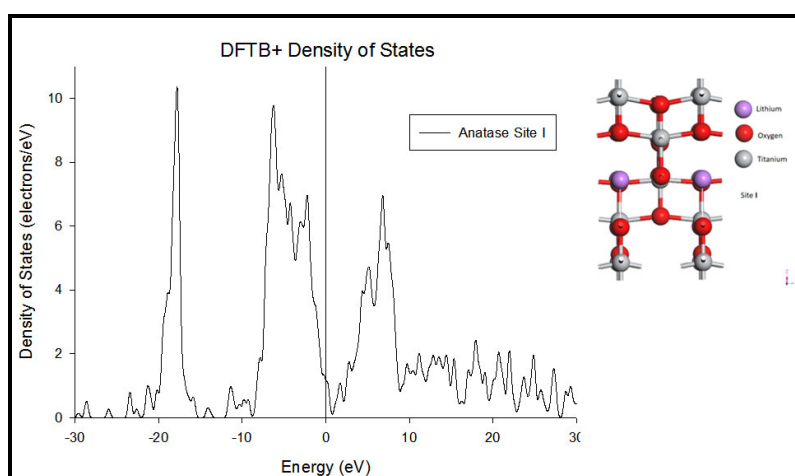


Figure 4.4. The lithium anatase phase in the Li<sub>x</sub>TiO<sub>2</sub> sample indicating possible Li position(I).

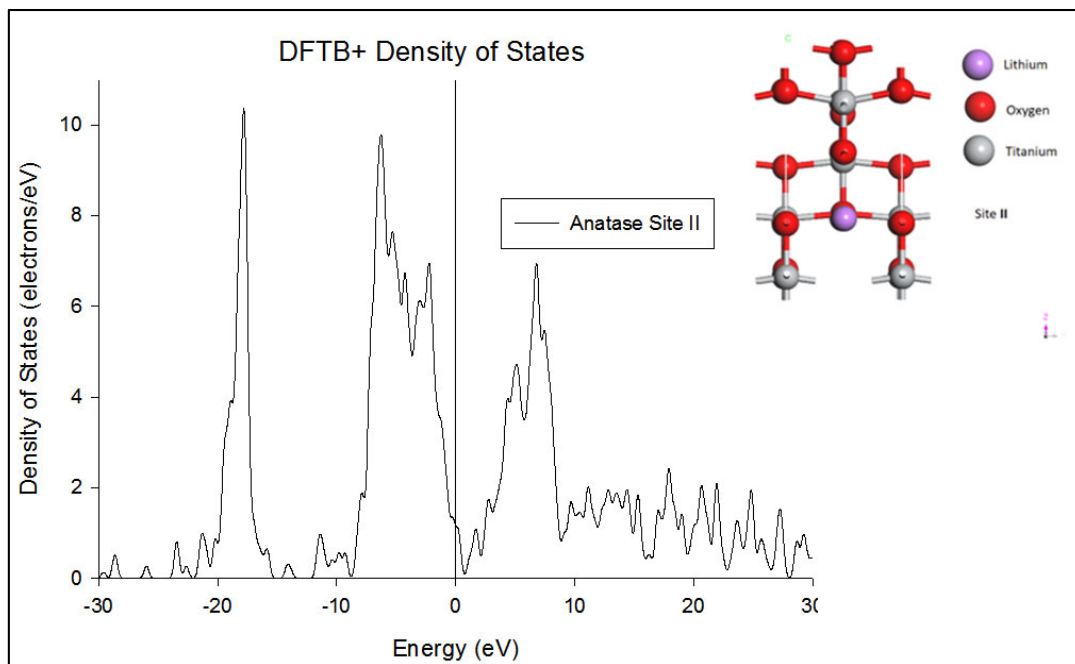


Figure 4.5. The lithium anatase phase in the  $\text{Li}_x\text{TiO}_2$  sample indicating possible Li position(II).

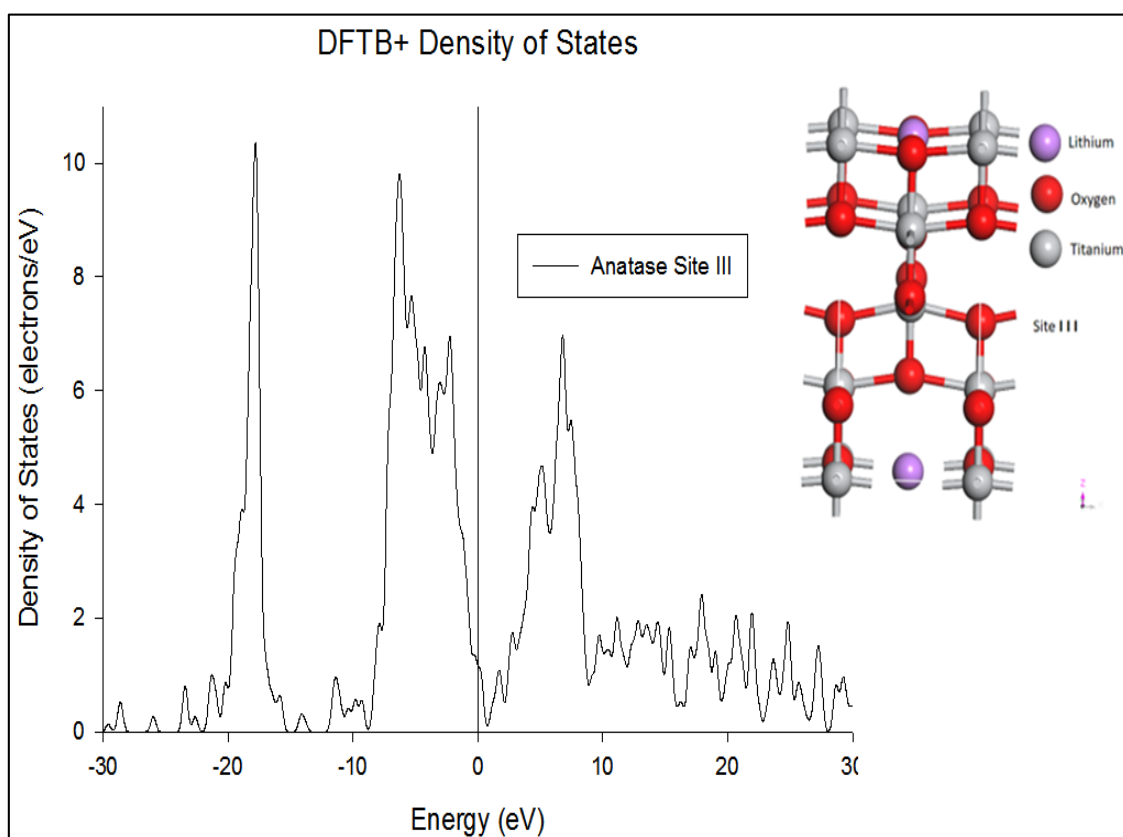


Figure 4.6. The lithium anatase phase in the  $\text{Li}_x\text{TiO}_2$  sample indicating possible Li position (III).

Such closeness in stability is further confirmed by the density of states (DOS) in Figure 4.4, Figure 4.5 and Figure 4.6, where the interception of Fermi level on the DOS for the three sites appears similar. However, the magnified diagram of the DOS highlights the stability better. It is apparent that the interception occurs at a lower value for the Li (III) site and the curves corresponding to the Li (I and II) sites are almost overlapping and intercept the Fermi level at higher energies (Figure 4.7). The lithiated  $\text{TiO}_2$  in which the DOS cut at the lowest point on the fermi level will be the most stable structure. Hence, from these DOS structures the most stable lithiation sites were found to be (I) for anatase.

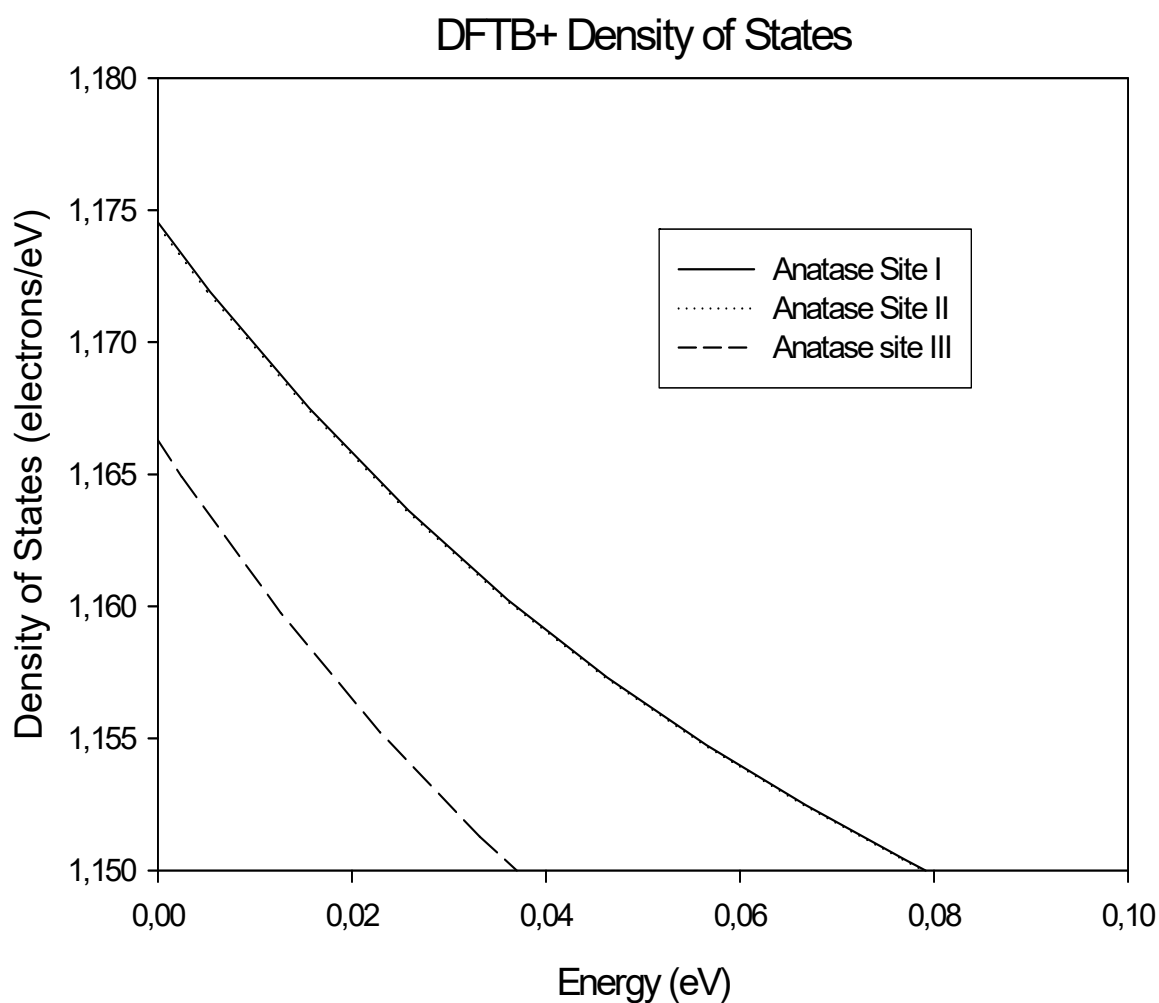


Figure 4.7. DOS of the anatase  $\text{TiO}_2$  with three different sites calculated using the DFTB+.

## 4.5.2 Change in volume and lattice parameters for various (Li/Ti and Na/Ti)

During  $\text{Li}^+$  insertion, anatase undergoes a phase transformation from a tetragonal to an orthorhombic phase, which is characterized by a spontaneous phase separation into lithium-poor  $\text{Li}_{0.01}\text{TiO}_2$  and lithium-rich  $\text{Li}_{0.5}\text{TiO}_2$  phases [15].

The extent to which anatase  $\text{TiO}_2$  can store Li renders it a good anode candidate for lithium ion battery [162]. The proposed maximum Li that can be inserted in  $\text{TiO}_2$  anatase varies in literature, from Li/Ti 0.5 to 1, depending on the temperature and experimental techniques employed. The total orthorhombic distortion of atomic positions during the transformation from anatase to lithium titanate is insignificant and leads to more regularly shaped  $\text{TiO}_6$  octahedra in lithium titanate than in anatase.

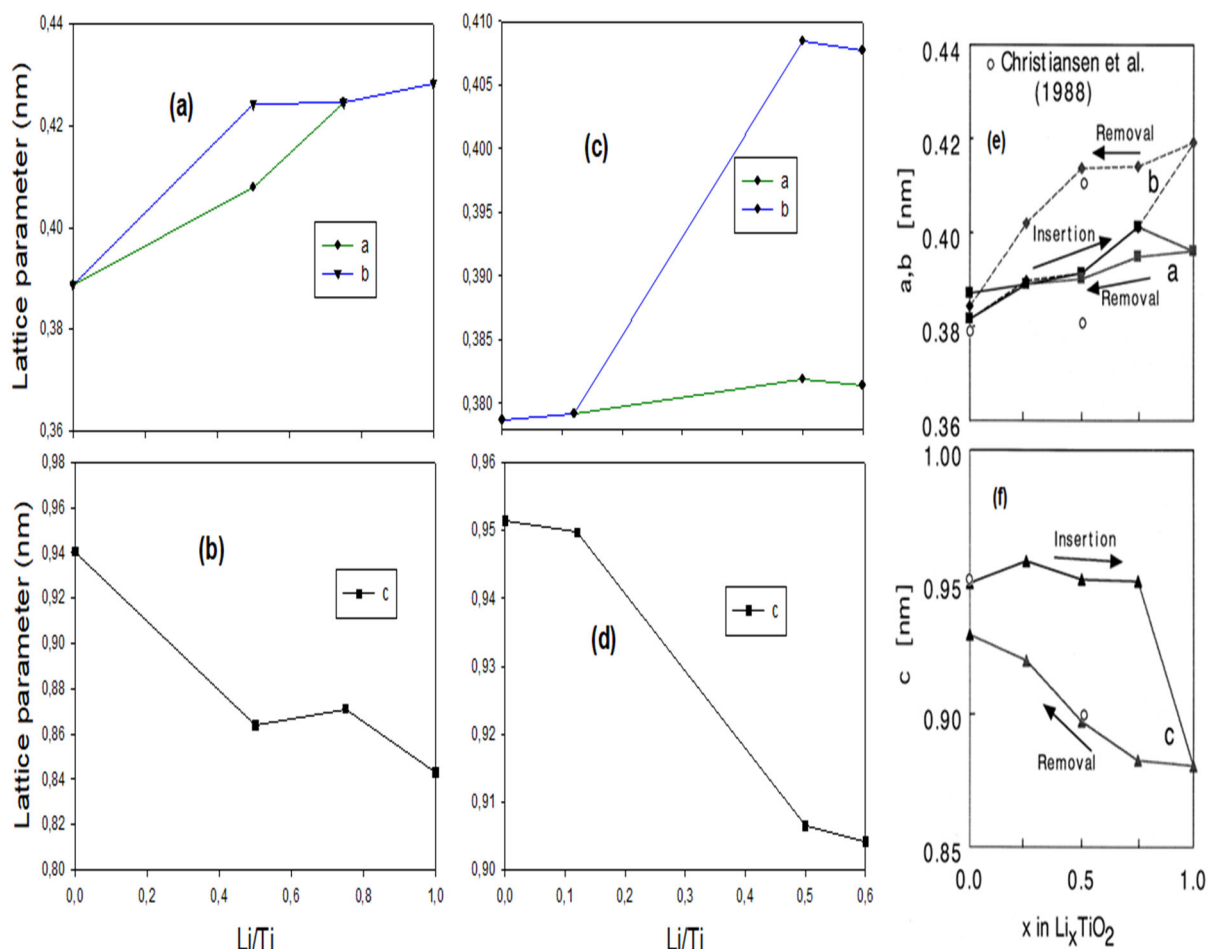


Figure 4.8. (a) and (b) DFTB calculated lattice parameters change of a unit cell of  $\text{Li}_n\text{TiO}_2$  as a function of Li/Ti ratio (c) and (d) Lattice parameters of a unit cell of  $\text{Li}_n\text{TiO}_2$  as a function of Li concentration during intercalation [163], (e) and (f) cell dimensions of  $\text{Li}_x\text{TiO}_2$  as a function of x lithium [164].

In the current DFTB calculations, the change in symmetry is accompanied by a decrease of the unit cell along the z axis and an increase along the y axis up to Li/Ti 0.50, as shown in Figure 4.8 (a) and (b). Such lattice parameter changes are consistent with those observed in literature Figure 4.8 (c),(d) [169] and Figure 4.8 (e),(f) [170]. In addition, the DFTB geometry optimized anatase TiO<sub>2</sub> structures, without and with Li ions, are characterized by a non-discrete distribution of interatomic distances shown in Figure 4.9. On lithiating anatase, the Ti-Ti bond length decreases from 6.187Å and 4.909Å whereas O-O bond length increases from 3.410Å and 3.578Å.

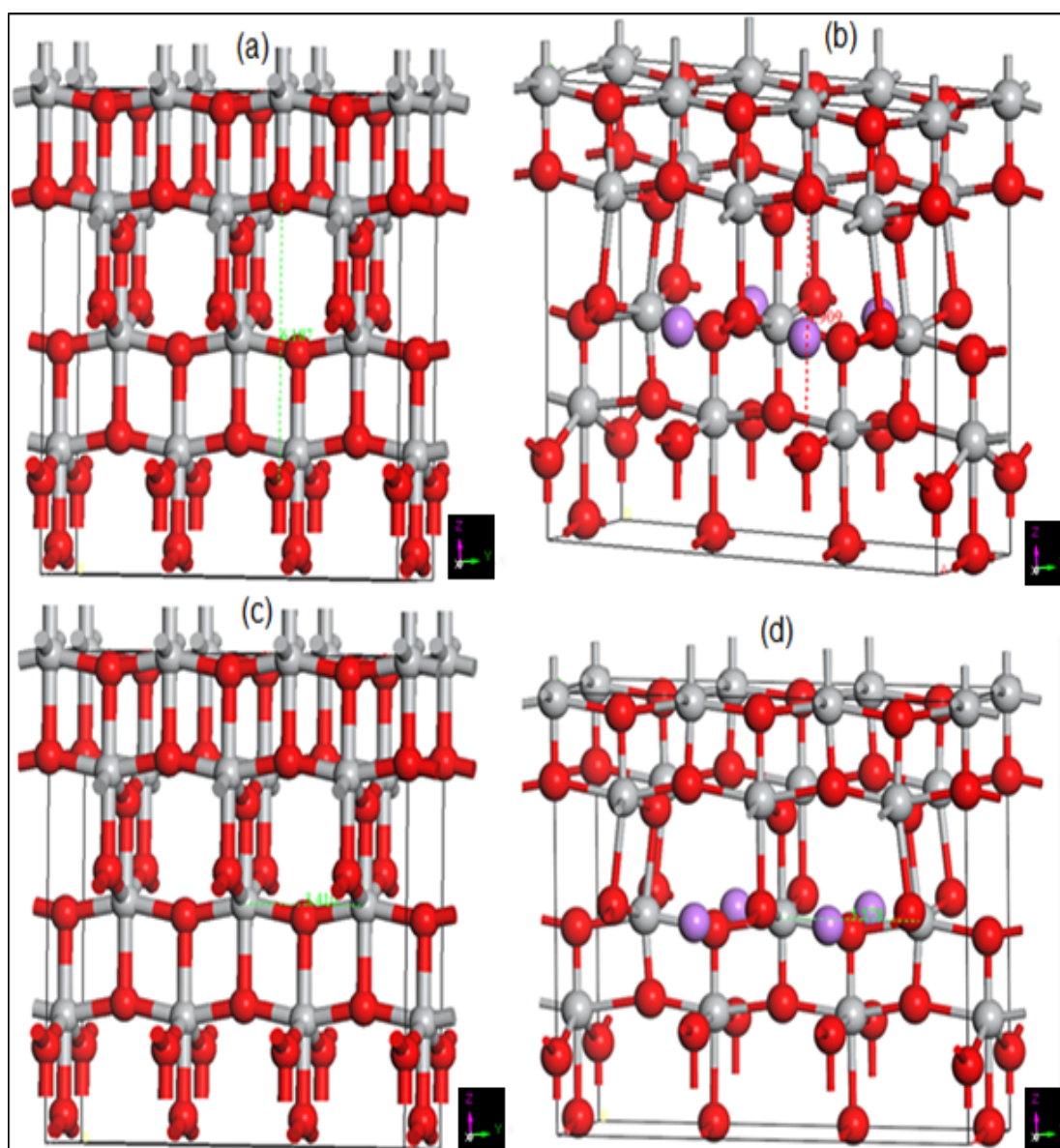




Figure 4.9. (a) and (b) O-O bond length before and after lithiation, (c) and (d) Ti-Ti bond length before and after lithiation. Ti, O and Li atoms are in grey, red and purple spheres respectively.

Based on changes of lattice parameters and bond lengths we now consider the overall reduced volume change of the anatase with lithiation. Indeed, trends of the DFTB calculated volume change, as reflected in Figure 4.10 (a), are closer to the experimental results, as shown in Figure 4.10 (b) and (c). In both DFTB and experimental results a large change of the cell volume was observed at  $x=0.75$ .

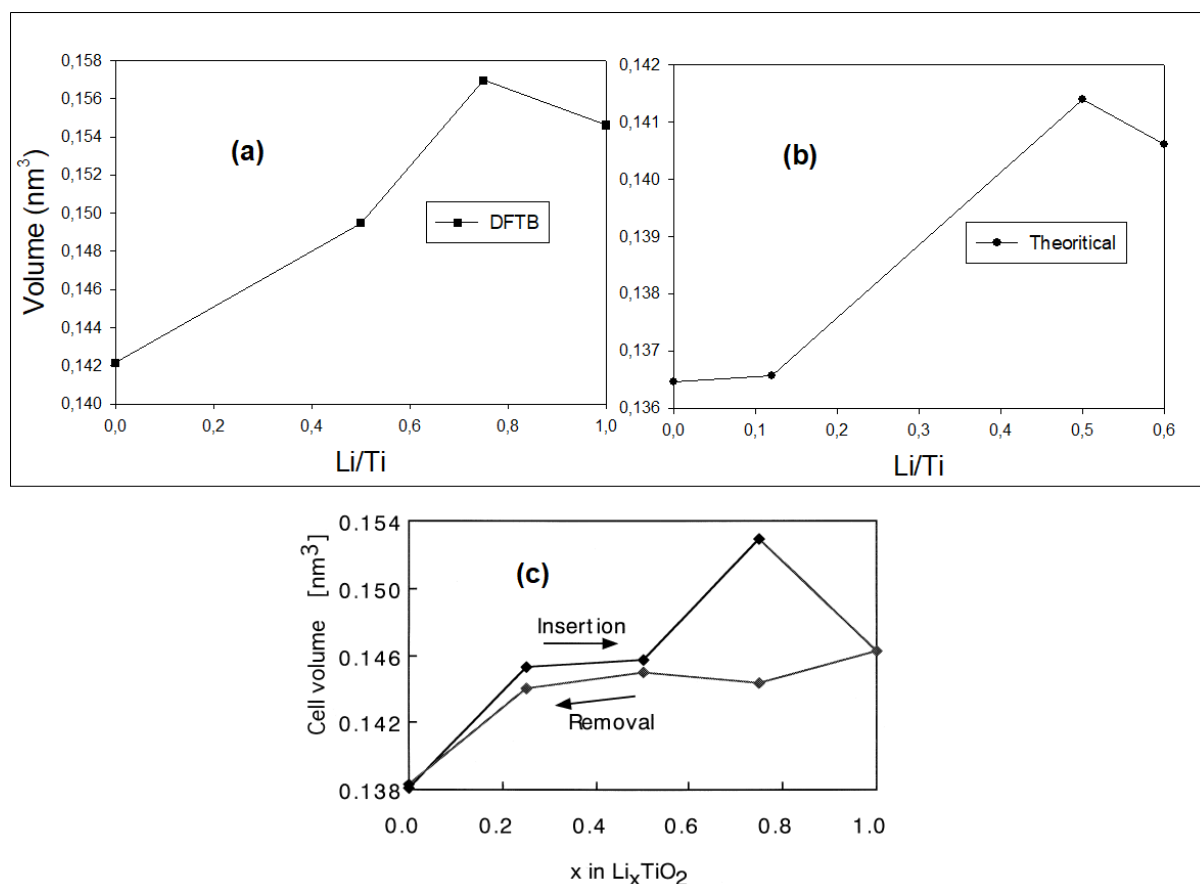


Figure 4.10. (a) Volume change of a unit cell of  $\text{Li}_x\text{TiO}_2$  as a function of Li/Ti ratio, (b) Volume change of a unit cell of  $\text{Li}_x\text{TiO}_2$  as a function of Li concentration during intercalation, (c) Cell volume of  $\text{Li}_x\text{TiO}_2$  plotted [164] against lithium x (experimental work).

Wagemaker *et al* found that the changes of unit cell induced by Li ion intercalation usually result in decreasing the c-axis and increasing the b-axis but the total volume changes for the Li ion insertion is less than 4% due to the low total Li content [163].

We now proceed to apply our derived DFTB model to sodiated anatase  $\text{TiO}_2$  polymorph. To better understand the structural properties analysis of the sodiated

anatase, the table and figure highlighting the structural relationship between the lattice parameters of sodiated bulk  $\text{Na}_x\text{TiO}_2$  is shown in

Table 4.5 and Figure 4.11. The volume of bulk  $\text{Na}_x\text{TiO}_2$  increased slightly from 0.25 to 0.5 Na ions concentrations. From 0.5 to 0.75 Na ions, we observed rapid increase in volume and from 0.75 to 1.0 Na ions there was sudden decrease in volume. This trend in volume is similar to the one during lithiation of bulk anatase  $\text{TiO}_2$ .

Table 4.5. Lattice parameters and energies of  $\text{Na}_x\text{TiO}_2$ .

<b>Na/Ti</b>	<b>a (Å)</b>	<b>b (Å)</b>	<b>c (Å)</b>	<b>Energy(kcal/mol)</b>
0.25	5.156	5.156	7.654	-20713
0.5	4.210	5.500	8.901	-23032
0.75	4.868	4.868	10.12	-24796
1.0	4.885	4.885	9.842	-26943

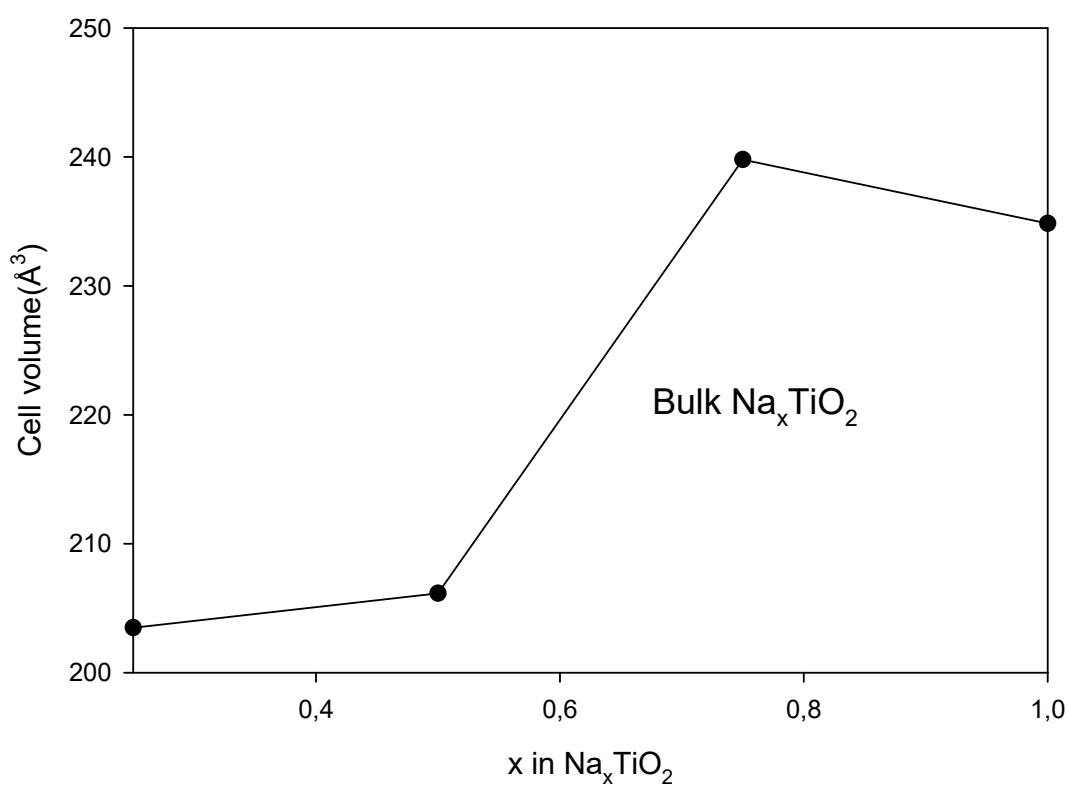


Figure 4.11. Predicted cell volume of  $\text{Na}_x\text{TiO}_2$  plotted against sodium concentrations.

It can therefore be surmised that our derived DFTB model is able to reproduce known complex structural changes in bulk lithiated anatase  $\text{TiO}_2$ , and can therefore be reliably employed to predict properties of larger structures with intriguing nano-architectures related to lithiated anatase.

## 4.6 Anatase $\text{TiO}_2$ Nanotubes

### 4.6.1 Generating nanotubes with various diameters

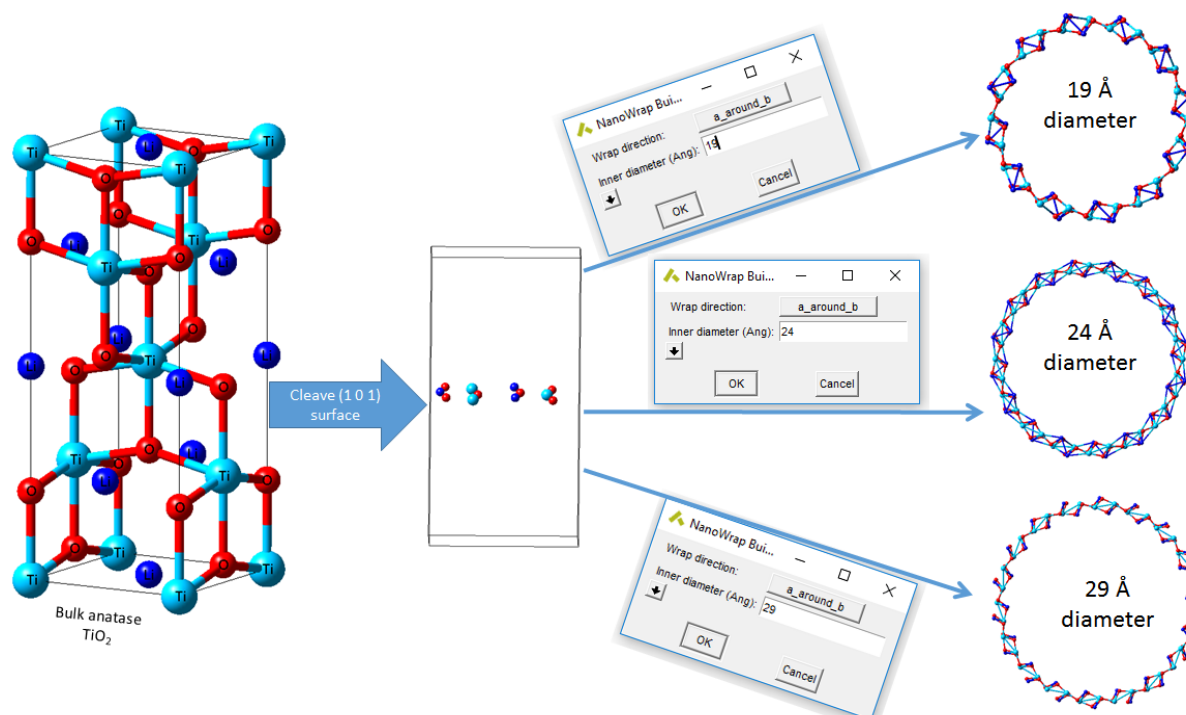


Figure 4.12. Anatase  $\text{LiTiO}_2$  nanotubes with diameter range (19-29Å) generated from bulk anatase.

In this section various  $\text{LiTiO}_2$  nanotubes with larger diameter (19Å-29Å) are generated and discussed.  $\text{LiTiO}_2$  nanotube generated from {101} surface with diameter ranging from 15Å-30Å are shown in Figure 4.12. These nanotubes are generated by cleaving the {101} surface and wrapping it into nanotubes with different diameters. Nanotubes generated

from {101} surface are composed of different number of atoms corresponding to the size of the diameter. Prior studies have shown that the anatase polymorph of TiO<sub>2</sub> grown along the (101) direction may expose more reactive facets; therefore, 3D motifs should undergo faster [165,166] reversible lithium intercalation and deintercalation. Thus, nanotubes with diameter 19Å have 96 atoms while 24Å and 29Å are composed of 128 and 144 atoms, respectively. The nanotubes are wrapped along around b. Application of nanostructured TiO<sub>2</sub>, in precise anodic TNT, increases energy/power densities due to the higher surface area, shorter ion diffusion path lengths between electrodes, which also lead to improvement of electron transfer and better accommodation of volumetric changes during the charge/discharge cycles [167,10,168,169].

#### 4.6.2 Band gap energies of pure TiO<sub>2</sub> nanotube with various diameters

The band gaps of anatase TiO<sub>2</sub> nanotubes were predicted using DFTB+ code as shown in Table 4.6. These results are in good agreement with results that was calculated by Evarestov *et al.* using *ab initio* method [12].

Table 4.6. Energy gaps of anatase TiO<sub>2</sub> nanotube with different diameters.

	This work				<i>Ab initio</i> [12]
Diameter (Å)	8.00	10.00	12.00	14.00	5 — 40
Band gap (eV)	4.0099	4.1049	4.1048	4.0000	4.76 — 5.40

For *ab initio* simulations on TiO<sub>2</sub> nanotubes (SW NTs), Evarestov *et al.* [12] have applied the formalism of line symmetry groups describing one-periodic (1D) nanostructures with rotohelical symmetry. Both types of NTs can be formed by rolling up the stoichiometric nanosheets of anatase TiO<sub>2</sub> phase. Optimized parameters of the atomic and electronic structure of corresponding nanotubes in Table 4.6 (*ab initio*) have been calculated using hybrid LCAO method as implemented in the CRYSTAL code. For TiO<sub>2</sub> nanotubes, certain qualitative similarities between the band gap energy functions exist despite the different chemical nature.

Compared to the common TiO<sub>2</sub> powder, the TiO<sub>2</sub> nanotube (TNT) is also a white colored powder. The optical band gap energy calculated from the ultraviolet–visible light absorption spectra by assuming indirect transition of TiO<sub>2</sub> is approximately

3.41—3.45 eV for chemically synthesized TNT [170], which is slightly larger than that of anatase (3.2 eV) and rutile (3.0 eV) crystals. This blue shift of the absorption edge wavelength is attributed to the quantum size effect of  $\text{TiO}_2$  semiconductor [171] in TNT because of very thin nanotube wall thickness of approximately 1—2 nm. Recent materials design strategy of  $\text{TiO}_2$  nanoparticles focuses on the developed visible light responsible for  $\text{TiO}_2$  photocatalyst [172] so that the enlarged band gap seems to be disadvantageous; nevertheless TNT exhibits unique and excellent photochemical properties which contribute enhanced environmental purification performance.

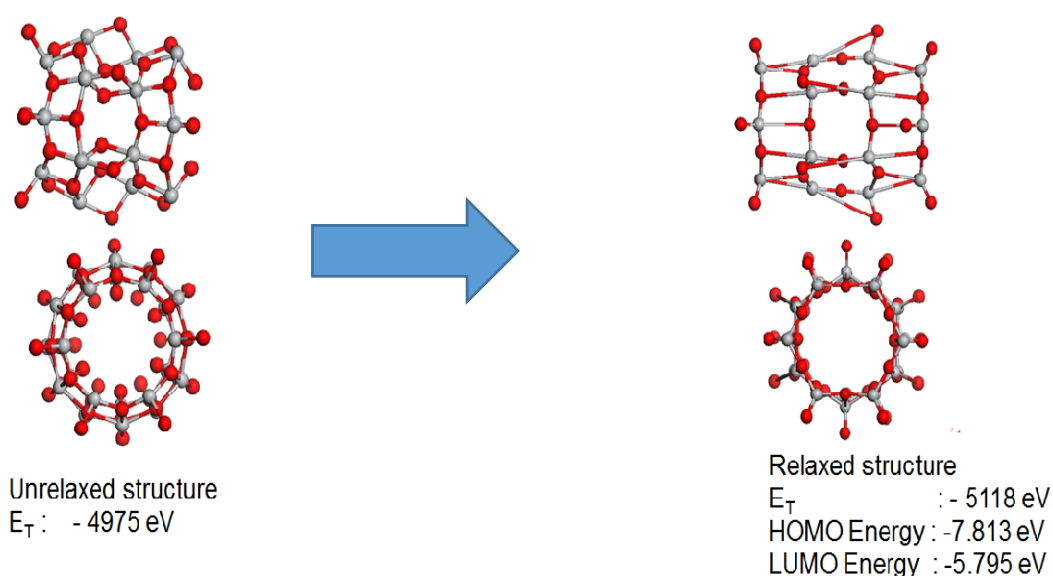


Figure 4.13. Unrelaxed and relaxed anatase  $\text{TiO}_2$  nanotube structure. Ti and O atoms are in grey and red spheres respectively.

Figure 4.13 shows the unrelaxed and relaxed structure of anatase  $\text{TiO}_2$  nanotube. It is observed that the energy of the unrelaxed structure has the energy which is higher than the relaxed structure; hence the relaxed structure is stable. Generally, we define a band gap as the difference between highest occupied molecular orbitals (HOMO) and lowest unoccupied molecular orbitals, therefore the band gap energy of 2.017 eV. This value shows that  $\text{TiO}_2$  nanotube is a semiconductor and the higher surface area exposable of a relaxed structure makes it a good material for Li insertion.

#### 4.6.3 Band gap energies of $\text{Li}_x\text{TiO}_2$ nanotubes with various diameters

To describe the electronic structure of anatase  $\text{LiTiO}_2$  the electronic density of states (DOS) and the band gap energy structures were analysed. The total DOS for all the three model of anatase  $\text{LiTiO}_2$  with 96 atoms, 128 atoms and 144 atoms using DFTB+ are shown in Figure 4.14. The band gap energies of the 19 Å, 24 Å and 29 Å were

found to be 3.448 eV, 3.454 eV and 3.463eV, respectively. Thus, as we increase the diameter of the nanotube the band gap energy also increases.

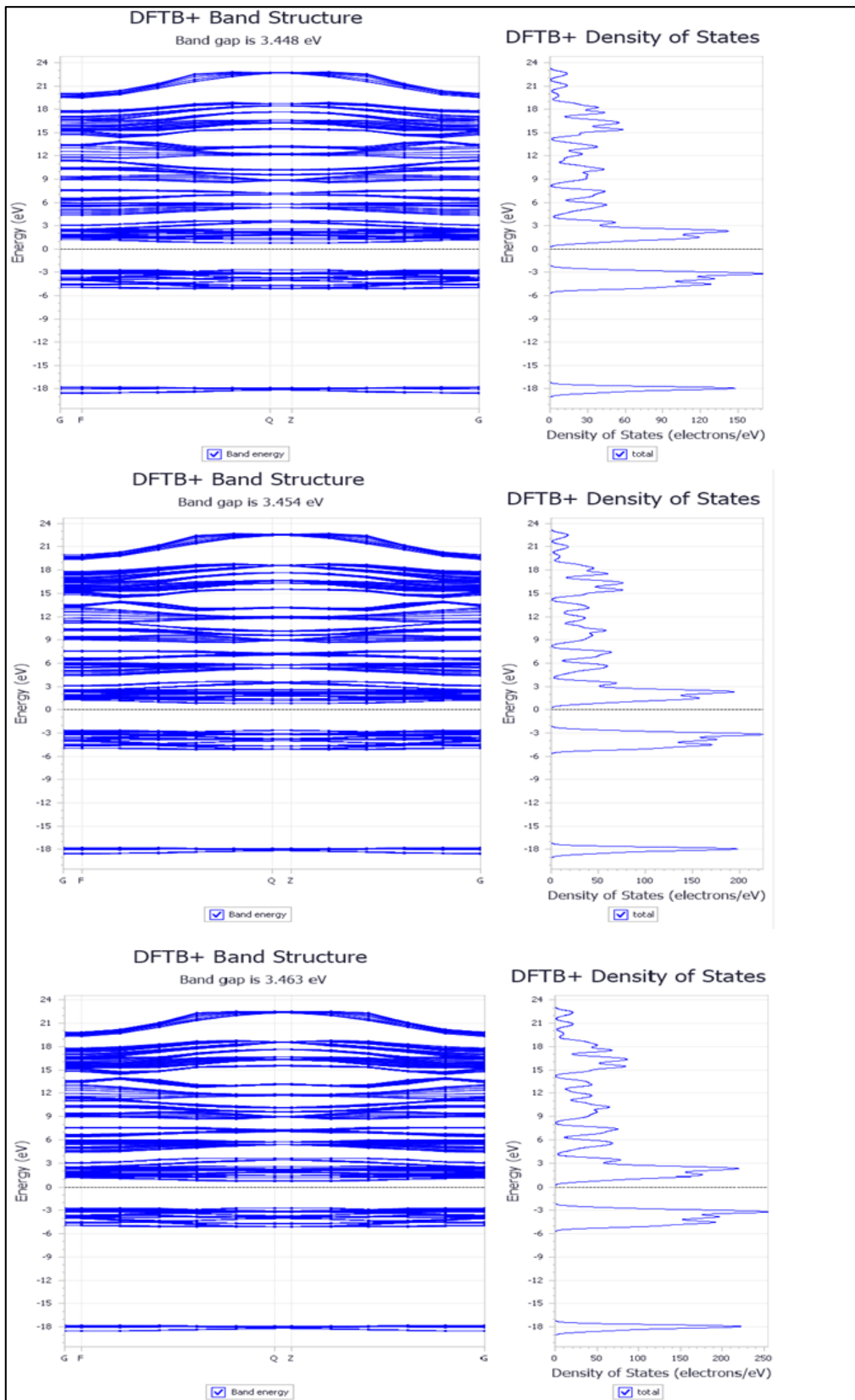


Figure 4.14. DFTB+ band structure and total density of states of a fully optimized  $\text{LiTiO}_2$  (19-29 Å).

## 4.7 Anatase $\text{TiO}_2$ Nanospheres

Recently, several  $\text{TiO}_2$  nano-structures, e.g., nanoparticles [21], nanorods [22], nanoplates [23], nanowires [24] and nanotubes [22] were investigated and compared for purposes of understanding their lithium ion storage capacity. Moreover,  $\text{TiO}_2$  nanospheres has attracted wide interest owing to their intrinsic electrical properties [173], their direct connection to the Ti metal substrate (direct back contact) and their beneficial geometric features.

Nanospheres were generated from lithiated and sodiated bulk anatase  $\text{TiO}_2$  using nanocluster builder within BIOVIA materials studio. These nanospheres were delithiated and desodiated to create nanospheres of various Li/Na concentrations. The number of atoms for nanospheres ranges from 386 to 509 atoms. To optimize nanospheres, two different algorithms were used. The steepest algorithm was used for the first 10-100 steps, after which the ABNR algorithm was applied until the nanospheres were fully optimized.

### 4.7.1 Structural change for various (Li/Ti and Na/Ti)

In this section we compare structural changes of anatase  $\text{TiO}_2$  nanosphere associated with insertion of different mobile ions, i.e. lithium and sodium. Geometry optimized  $\text{TiO}_2$  nanospheres with various concentrations of lithium are shown in Figure 4.15. The structural variation of the nanosphere is hardly noticeable, in the range  $\text{Li}_x\text{TiO}_2$  ( $x=0.1, 0.6, 0.9$  and  $1.0$ ); and this is confirmed by minimal changes in the RDFs as depicted in Figure 4.16. Furthermore, Table 5.7 shows a distinct volume change in the concentration range  $x= 0$  to  $0.1$ , and no observable change occurs above  $x= 0.1$ , except for some slight fluctuations. It was also experimentally observed that  $\text{TiO}_2$  nanospheres always maintain stable structure favourable to Li ion diffusion [173].

However, Figure 4.19 shows the structure of anatase  $\text{TiO}_2$  nanosphere responded differently to sodiation. It is observed that the nanosphere is significantly distorted at a low Na concentration, i.e.  $x=0.25$ . A higher degree of structural order is gradually introduced as the Na concentration is increased, until a fully crystalline pattern is noted at  $x=1.0$ . The structural transformation is further supported by the RDFs in Figure

4.19, where the height of a distinct peak at a radial distance of 3.5 Å is enhanced substantially, as the sodium concentration increases from  $x=0.5$  to  $x=1$ . Figure 4.20. In addition, a marked increase in volume is observed in that range.

Lastly, electronic properties associated with lithium and sodium insertions in  $\text{TiO}_2$  nanosphere are reflected in partial density of states. The DOS profiles for lithiated and sodiated anatase  $\text{TiO}_2$  nanospheres are shown in Figure 4.18 and Figure 4.23, where, the valence band mainly originated from O-2p and 2s electrons and Ti-3d is dominant in the conduction band. Whereas lithiation has minimal impact on the electronic structure, an increment in sodium concentration tends to shift the Ti-3d peaks toward Fermi energy level.

It can therefore be surmised that sodiation affects structural and electronic transformation of anatase  $\text{TiO}_2$  nanosphere, and in contrast lithiation appears to hardly change such properties (Figure 4.17 and Figure 4.21). This could be partly attributed to different properties of Li and Na, such as ionic radius and polarizability. Wei *et al.* observed similar structural changes (Figure 4.22) associated with a rhombohedral phase  $\text{Na}_x\text{TiO}_2$  showing high degree of disorder [174]. The volume change should be monitored, when sodiating the anode material. We have observed a gradual change in volume in Figure 4.21. This gradual change might mitigate the dendrite formation or failure of anode material. In summary, DFTB approach can handle larger number of atoms in nanospheres.



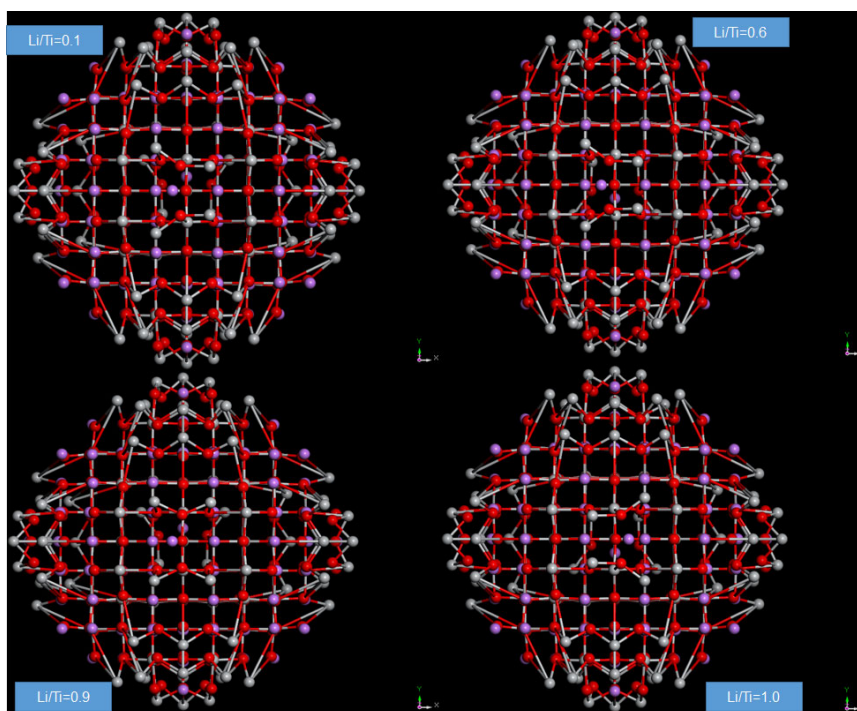


Figure 4.15. DFTB+ optimized structures for stoichiometric  $\text{Li}_x\text{TiO}_2$  ( $x=0.1, 0.6, 0.9$  and  $1.0$ ). Ti, O and Li atoms are in grey, red and purple spheres respectively.

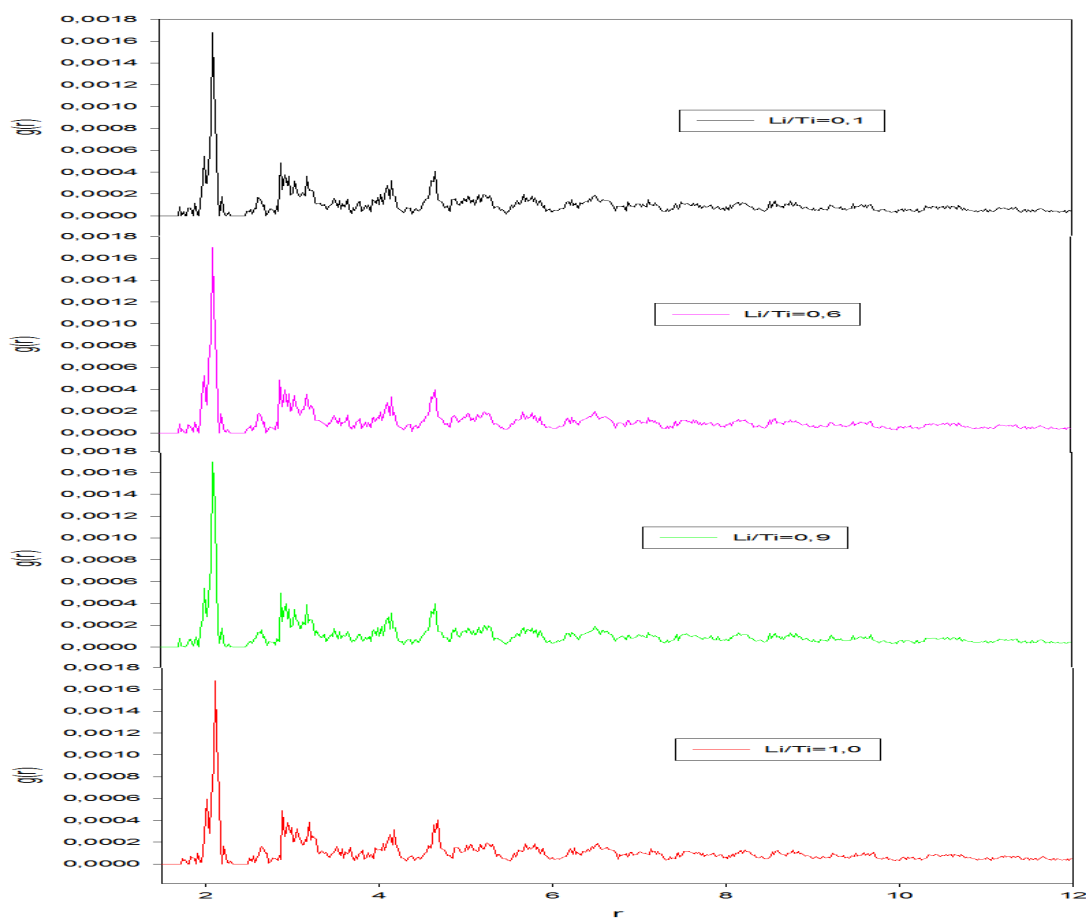


Figure 4.16. Radial distribution functions (RDFs) for anatase  $\text{Li}_x\text{TiO}_2$  ( $x=0.1 - 1$ ) nanospheres.

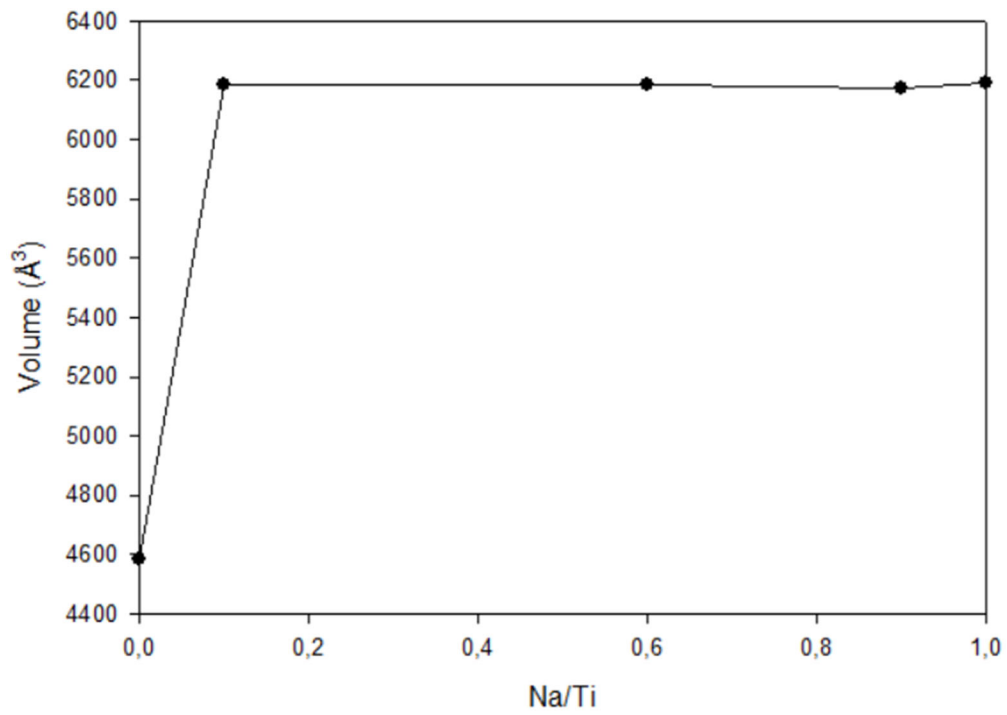


Figure 4.17. The energies and volumes of  $\text{Li}_x\text{TiO}_2$  nanospheres where  $x= 0.0, 0.1, 0.6, 0.9$  and  $1.0$ .

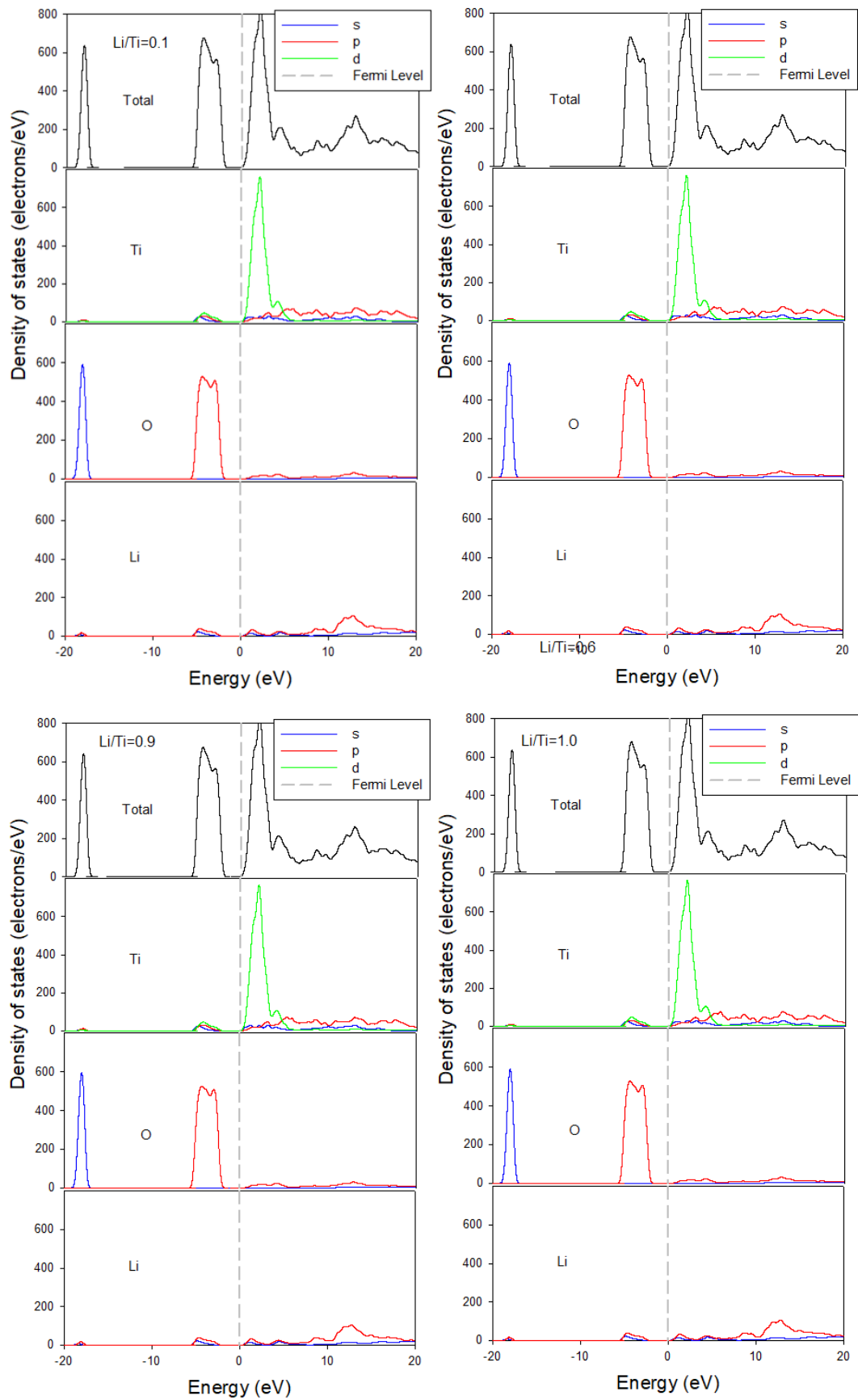


Figure 4.18. Partial density of states (PDOS) for anatase  $\text{Li}_x\text{TiO}_2$  nanosphere.

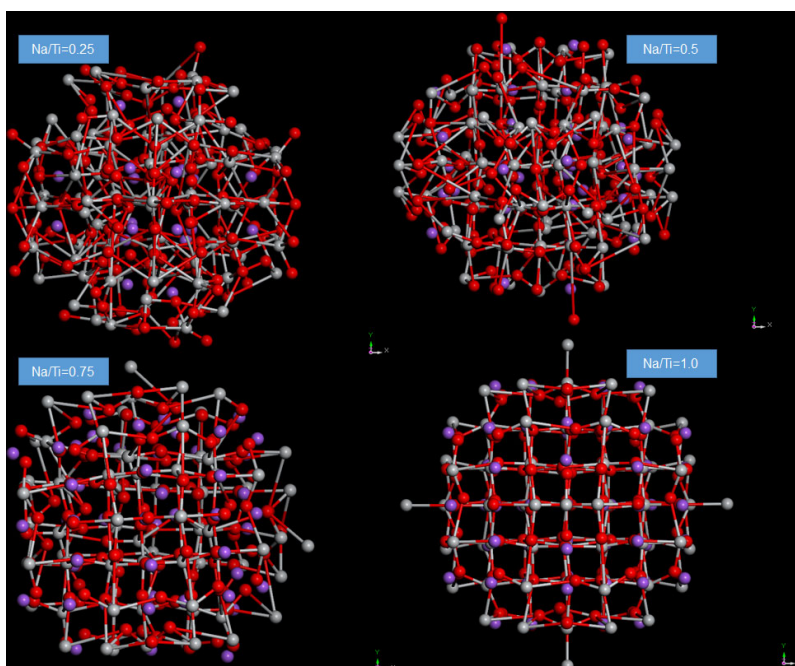


Figure 4.19. DFTB+ optimized structures for stoichiometric  $\text{Na}_x\text{TiO}_2$  ( $x=0.25, 0.5, 0.75$  and  $1.0$ ). Ti, O and Na atoms are in grey, red and purple spheres respectively.

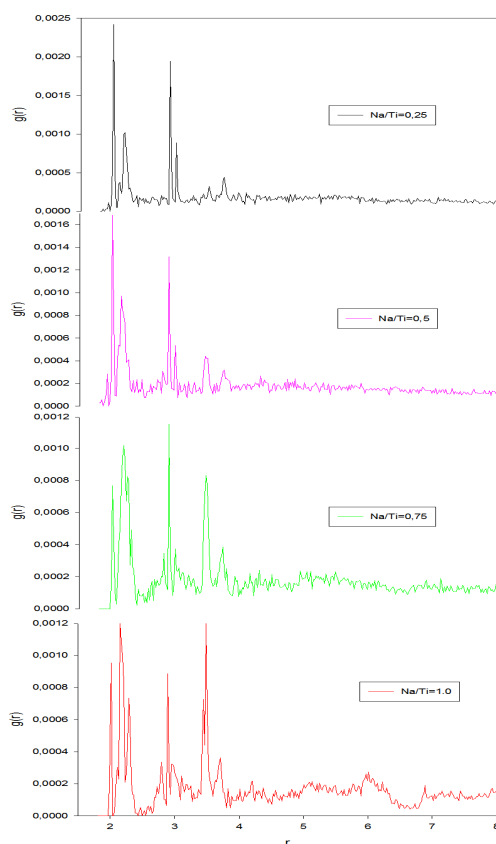


Figure 4.20. Radial distribution function (RDF) for anatase  $\text{Na}_x\text{TiO}_2$  nanosphere.

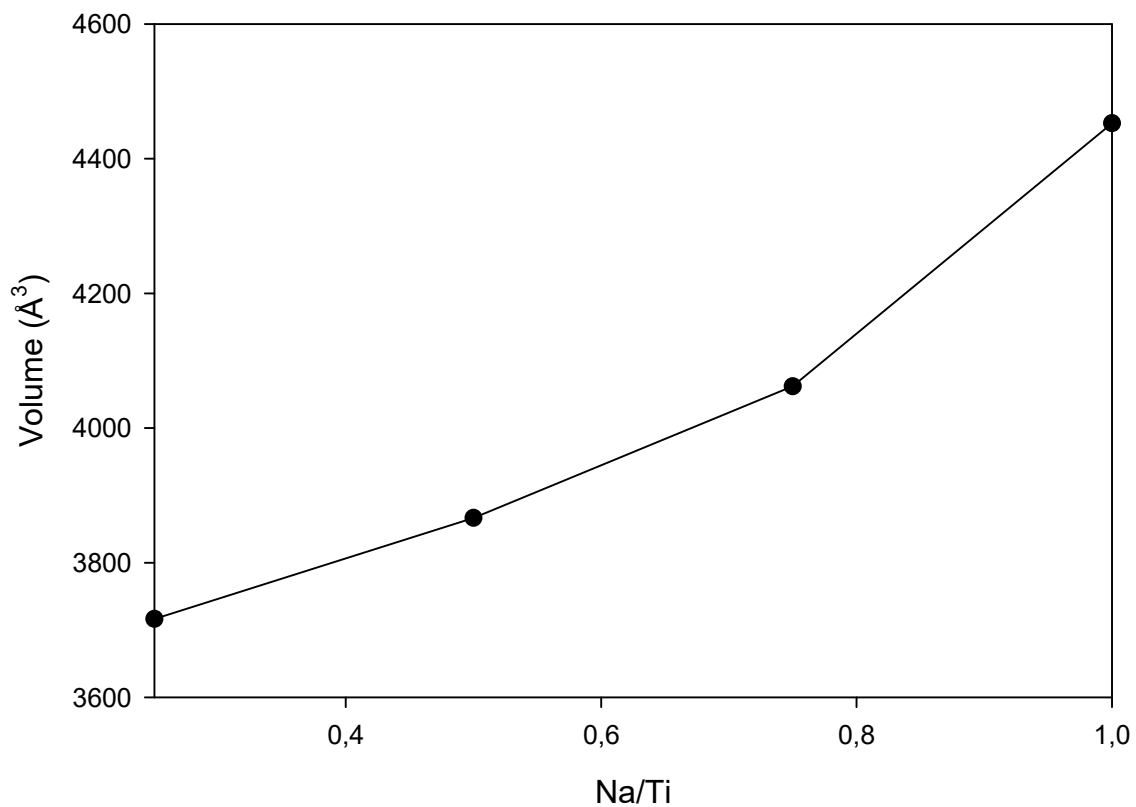


Figure 4.21. The graph for volumes of  $\text{Na}_x\text{TiO}_2$  nanospheres vs Na/Ti (from 0.0 to 1.0).

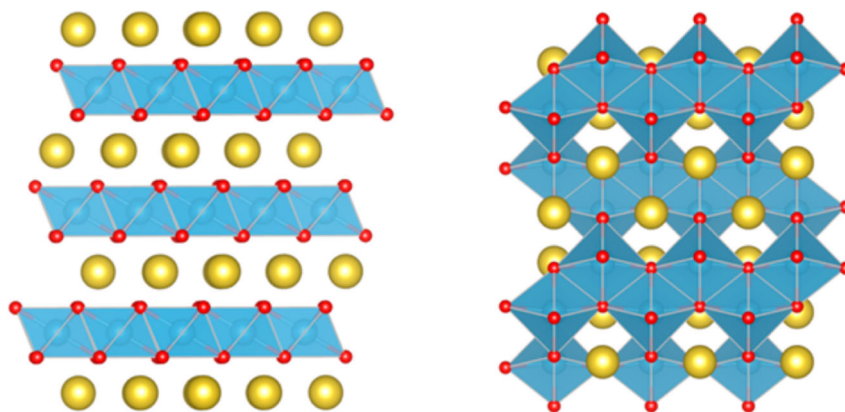


Figure 4.22. DFT optimized structures for stoichiometric  $\text{NaTiO}_2$ . Left panel: rhombohedral layered structure [175]. Right panel: tetragonal  $\text{LiTiO}_2$  structure [176].

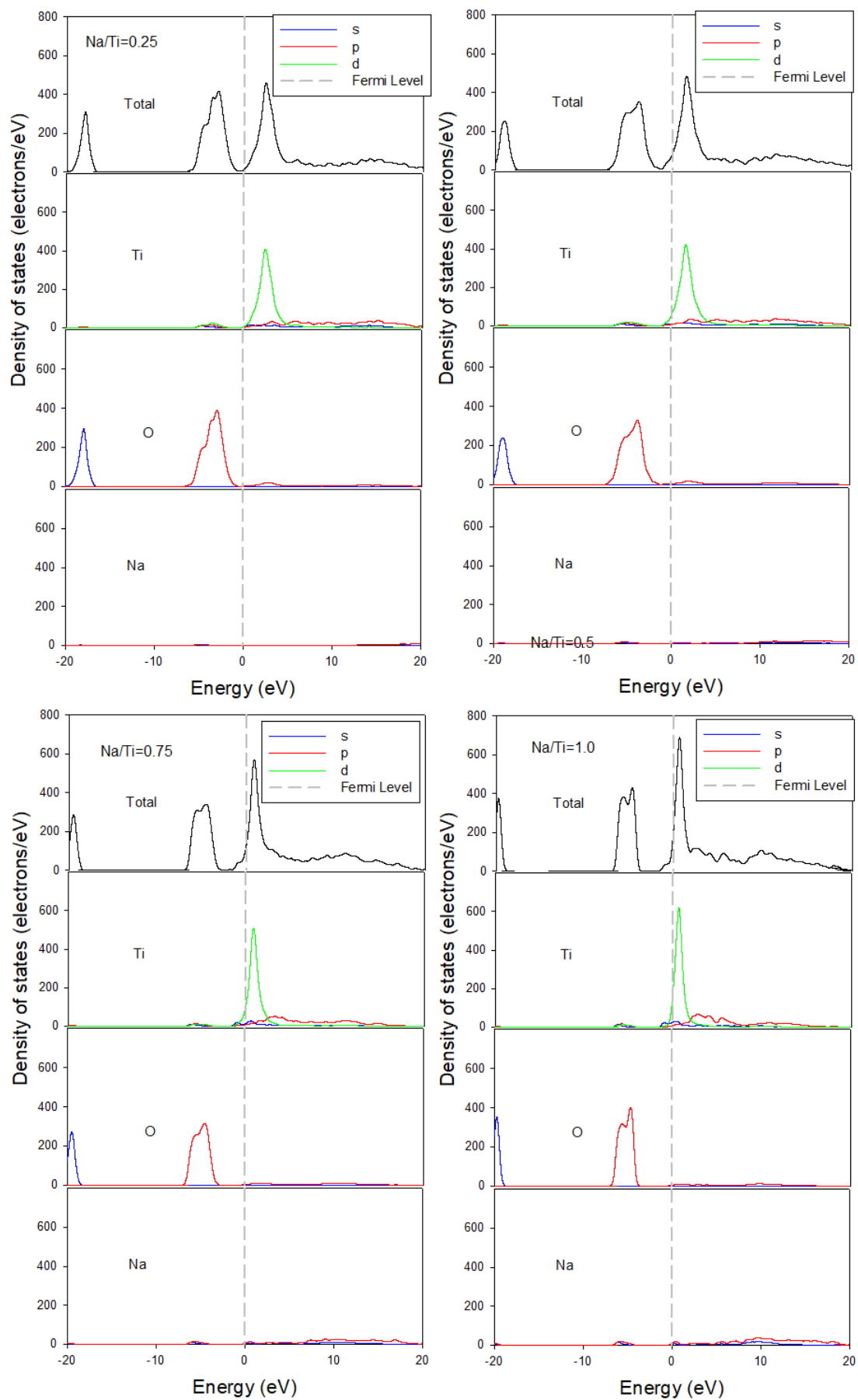


Figure 4.23. Partial density of states (PDOS) for anatase  $\text{Na}_x\text{TiO}_2$  (x=0.2 – 1) nanospheres.

## **4.8 Molecular dynamics of TiO<sub>2</sub> nanotubes)**

### **4.8.1 Methodology**

Molecular dynamics (MD) is a computational designed simulation in which atoms and molecules are granted to collaborate for a period of time by estimations of known physics, giving an aspect of the motion of the particles. Molecular dynamics simulation method is fundamental in explaining and predicting numerous properties of materials in solid and liquid phase. The extent of the success of the molecular dynamics technique is subject to the availability of computational power. The size of the simulation system and the time of simulation should be selected such that the calculation is completed within a reasonable time period. The timestep of the simulation should be chosen small enough to avoid any statistical errors associated with integrating the equations of motion, and the number of timesteps, that is, the total simulation time, should be chosen large enough to capture the phenomenon begin modelled. In this chapter we present canonical ensemble (NVT) results that have a number of thermodynamic control parameters in order to give back more acceptable experimental results for TiO<sub>2</sub> nanotubes.

Furthermore, the kinetic stability of some of bulk nanotubes was investigated using the DFTB approach in molecular dynamics (MD) mode. MD simulations of nanotubes were performed during 40 ps with the time step 1 fs as for NVT-ensembles at temperatures 300 K up to 1000 K, using an NHL thermostat with the decay constant 1 ps.

## **4.9 Molecular dynamics for anatase TiO<sub>2</sub> nanotube**

The molecular dynamics calculations were performed on the anatase TiO<sub>2</sub> nanotube at different temperatures using DFTB model within the NVT ensemble, as shown in Figure 4.24. The nanotube starts to deform at approximately 227 °C (500K). The bandgap was calculated from DOS, and its magnitude is underestimated compared to the experimental value (Figure 4.25), which can be attributed to the choice of exchange-correlation energy in Table 4.6. A change in the bandgap is noted at 500K, which is coincident with onset of structural changes of the nanotube. However an anomalous increase of the bandgap, followed by a marked reduction is noted from 700K to 900K, which is consistent with the diffuse reflectance studies [177]. Hence

it can be concluded that the DFTB model is good since it can reproduce high temperature properties of the nanotube well. Such nanotubes can withstand higher

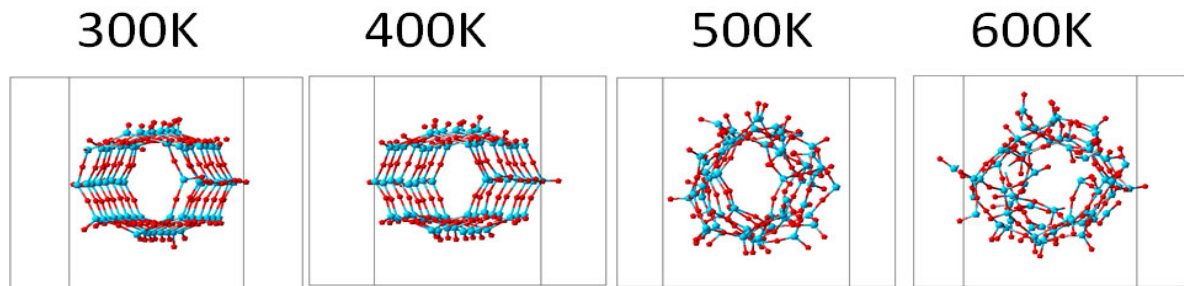


Figure 4.24. Structure of anatase  $\text{TiO}_2$  nanotube at different temperatures using MD NVT ensemble. Ti and O atoms are in blue and red spheres respectively.

temperature than the one at which lithium-ion batteries to operate. This renders these nanotubes a good candidate for use in storage devices as an anode material.

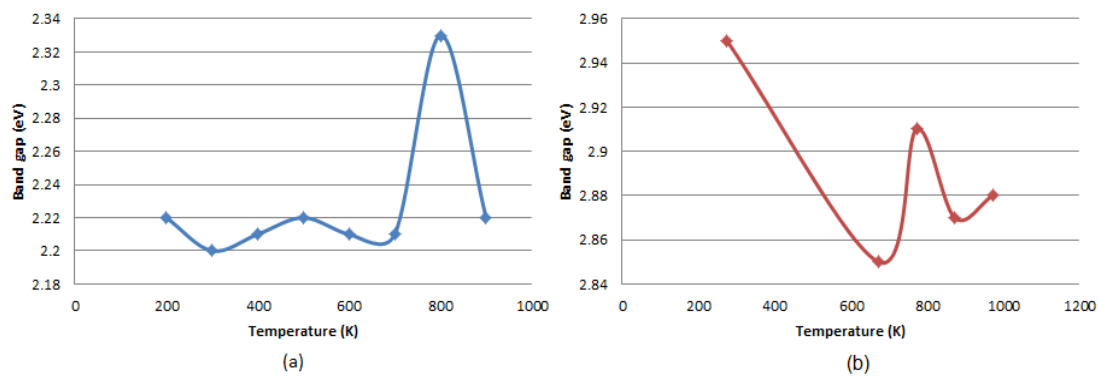


Figure 4.25. Bandgap vs. temperature for anatase  $\text{TiO}_2$  nanotube (a) using NVT ensemble molecular dynamics and (b) one obtained from diffuse reflectance experiments [177].

## 4.10 Summary

The computational calculations in this chapter were carried out using DFTB+ and the potential we validated. The obtained structural parameters at the level of DFTB approaches were found to be in good agreement with either previously reported theoretical or experimental work. Reliable band gap energy values and band structures were found to be consistent with previously reported results.

In order for  $\text{TiO}_2$  nanotubes and nanospheres to be fully optimized two different algorithms were used. It was clearly observed that the nanoparticles cannot reach convergence unless multiple algorithms were applied. We conclude that computational results for anatase NT- $\text{TiO}_2$  are sensitive to the choice of the algorithm.



Therefore, an appropriate choice of algorithms is very crucial to obtain reliable results. The valence band and conduction bands of the nanotube mainly consist of O2p and Ti3d states respectively, similar to that one of bulk TiO<sub>2</sub>. Depending on the nanotube radius and atomic arrangement in the nanotube wall, the valence band and conduction band modify in different manners to change the band gap.

We have determined the volume of lithiated and sodiated for bulk and nanosphere respectively. The change in volume during Li-ion intercalation into bulk anatase was found to be insignificant as compared to that of sodiated bulk. Similarly, the change in volume for lithiated nanosphere was minimal as compared to sodiated nanosphere.

DFTB+ molecular dynamics (MD) calculations were performed using NVT ensemble to TiO<sub>2</sub> systems. The band gap energy of bulk anatase TiO<sub>2</sub> was found to be decreasing as the temperature increases. For TiO<sub>2</sub> nanotube, the band gap energy trend was in strong agreement with the experimental results.

We have applied the DFTB and CASTEP program module embedded in Materials Studio in the frame of density functional theory to calculate bulk modulus and elastic constants of anatase TiO<sub>2</sub>. Anatase was found to be ductile, which is very good for energy storage devices. In the next chapter we are going to apply these codes to determine properties of complex TiO<sub>2</sub> (TB) microporous crystal structure that can accommodate Na-ion during insertion.

# Chapter 5: Structural and electronic properties of TiO<sub>2</sub> (TB-I) and (TB-II) polymorphs

## 5.1 Introduction

The increasing demand for portable and non-polluting electricity sources requires the development of new battery technologies with enhanced energy densities. TiO<sub>2</sub>-based materials are being increasingly more proposed as promising anodes for lithium-ion batteries, due to their low cost, mild weight, and nontoxicity. A range of polymorphs have been investigated with nanoporous and different nanoscale morphologies often supplying expanded performance [178,179].

The anode is a necessary and an important component in LIBs; therefore, the research and improvement on the modern state of affairs of anode materials are some of the most important factors to determine the performance of this device. An ideal anode material should meet the following necessities [180,181]: (1) excessive unique surface area and large uncovered surface providing extra lithium insertion channels, (2) low quantity trade in the course of Li ion intercalation/de-intercalation process, which is essential for good biking stability, (3) giant pore size and short paths for fast lithium ion diffusion with high speed, which is critical for exact charge capability, (4) low internal resistance which leads to two quick charging and discharging, (5) low intercalation potential for Li, (6) low price and (7) environment friendliness.

Recently, new TiO<sub>2</sub> structures with stable and larger channels have been persistently investigated in experiments. To date, porous TiO<sub>2</sub> such as TiO<sub>2</sub> membranes (mean pore size, around 9 Å) [182,183] and TiO<sub>2</sub> xerogels (mean pore size, ~15 Å) [184] have, however, either intergranular or amorphous pores, being not thermally stable beyond 400 °C. [183,184]. Whether titania could have large porous crystalline phases (e.g., >5 Å) is unknown.

In this chapter, we propose that TiO<sub>2</sub> (TB) crystals structures are highly promising anode materials for LIBs and SIBs based on DFTB calculations. These structures possess larger 1D channels as compared with other TiO<sub>2</sub> polymorphs such as rutile brookite and anatase. Our DFTB calculations reveal that this distinctive microporous crystal structure can accommodate Li/Na ion during insertion per TiO<sub>2</sub> formula unit.

Moreover, the possible Li/Na insertion sites and volume changes also support the applicability of this TiO<sub>2</sub> (TB) compound as a SIB anode material.

## 5.2 Methodology

All calculations reported in this chapter were carried out using the plane wave DFTB program as implemented in BIOVIA Materials Studio 2019, where potentials were parameterized using DMol3 and DFTB codes. To validate our results CASTEP code was used to predict mechanical properties. The exchange-correlation functional utilized was GGA-PBE.<sup>14</sup> The plane wave cutoff energy utilized was 490 eV and a Monkhorst-Pack-scheme k-point mesh of (2 × 6 × 2) was used for First Brillouin-Zone sampling. For all the crystal structures, both lattice and atomic coordinates were fully optimized until the maximal force component below 0.01 eV/Å and the elastic strain of 0.003 for mechanical parameters. For the calculations of density of states (DOS) and charge difference, k-points of (4 × 6 × 4) were used.

Nanospheres were generated from lithiated and sodiated bulk TiO<sub>2</sub> (TB) using nanocluster builder. These nanospheres were delithiated and desodiated to create nanospheres of various Li/Na concentration. The number of atoms for nanospheres, ranges from 324 to 568 atoms. To optimize nanospheres, two different algorithms were used. The steepest was used for the first 10-100 steps, after which the ABNR algorithm was applied until our nanospheres were fully optimized.

## 5.3 Bulk TiO<sub>2</sub> TB-I

### 5.3.1 Structural and mechanical properties of TiO<sub>2</sub> (TB)-I

Table 5.1. Geometry lattice parameters for crystalline TiO<sub>2</sub> TB-I.

TiO <sub>2</sub> Structure	Space group	Lattice parameters (Å)	
		DFTB (This work)	DFT [44]
TB-I	<i>Imma</i> (74)	a=6.048	6.070
		b=3.887	3.820
		c=8.784	9.020

A new class of stable microporous structures constituted by the [TiO<sub>5</sub>] trigonal bipyramid (TB) building block, namely, TiO<sub>2</sub>(TB)-I, is presented in balls.

Figure 5.1. In Table 5.1, we list the lattice parameters (a, b, and c) of typical  $\text{TiO}_2(\text{TB})\text{-I}$  crystals, which possess the *Imma* symmetry. They display a 1D channel with large pore sizes, ranging from 5.6 to 6.7 Å [44]. The calculated equilibrium lattice constants (DFTB (a = 6.048 Å, b = 3.797 Å and c = 9.789 Å)) are in good agreement with the DFT calculated values (a = 6.07 Å, b = 3.82 Å, c = 9.02 Å [44]).

According to our knowledge so far, there are no calculated or experimental elastic constants,  $C_{ij}$ s, to compare with, except for some moduli of elasticity. We predicted mechanical parameters using DFTB and validated these with results from the DFT CASTEP code. For low symmetry phases the isotropic crystalline elastic constants, bulk ( $B_{\text{RVH}}$ ) and shear ( $G_{\text{RVH}}$ ) moduli can be calculated by applying the so-called Reuss Voigt-Hill averaging method and using the single elastic constants  $C_{ij}$  [185]. Calculated mechanical properties are presented in Table 5.2 and DFTB and DFT elastic constants are generally consistent. The DFTB bulk modulus for  $\text{TiO}_2(\text{TB})\text{-I}$  is 114.4 GPa and a DFT one is 102.6 GPa and its DFTB shear modulus is 28.2 GPa and the DFT calculated is 35.6GP; these results are in reasonable agreement. The bulk modulus is also in agreement with the experimental (120.3 GPa) results [44]. The variation can be attributed to the much estimation incorporated in the computations of the elastic constants. However, the methods used in predicting elastic constants appear satisfactory even though no data was available from the experiment or computational to compare our results with. All these results show that the applied DFTB method is reliable and authentic.

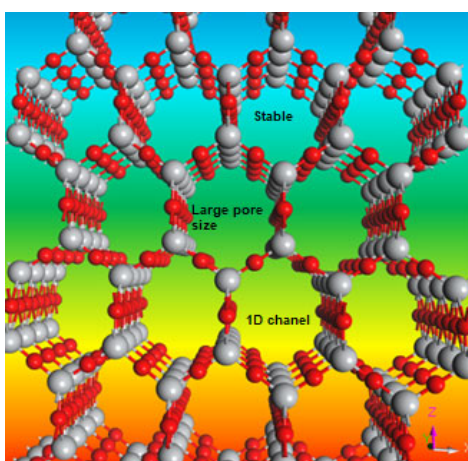


Figure 5.1. The crystal structures for  $\text{TiO}_2$  (TB)-I phase: Ti, grey balls; O, red balls.

One of the mechanical properties of the crystalline solid such as  $B_{RVH}/G_{RVH}$  (Pugh's modulus ratio [95]) is also critical. The Pugh's modulus ratio is usually used as an empirical rule to distinguish ductile ( $B_{RVH}/G_{RVH} > 1.75$ ) from brittle materials ( $B_{RVH}/G_{RVH} < 1.75$ ). The ductility is correlated with the  $B_{RVH}/G_{RVH} = 4.06$  and  $B_{RVH}/G_{RVH} = 2.88$  using DFTB and DFT methods respectively.

Table 5.2. Elastic constants  $C_{ij}$  (GPa), (Russ's, Voigt's and Hill's) bulk modulus  $B_{RVH}$  (GPa) and shear modulus  $G_{RVH}$  (GPa) for  $TiO_2(TB)$ -I together with the theoretical and experimental results at zero pressure.

	DFTB	DFT CASTEP	Exp. [44]
	<b>GPa</b>		
$C_{11}$	162.861	154.688	
$C_{12}$	66.386	52.982	
$C_{13}$	106.621	93.104	
$C_{22}$	272.611	205.659	
$C_{23}$	93.856	84.475	
$C_{33}$	111.055	112.577	
$C_{44}$	44.593	52.425	
$C_{55}$	14.136	38.165	
$C_{66}$	24.917	29.599	
$B_{RVH}$	114.4	102.6	120.3
$G_{RVH}$	28.2	35.6	

### 5.3.2 Structural and energy change of $TiO_2$ (TB)-I during lithium/sodium intercalation

Lithium-ion batteries (LIBs) are substantially highly-priced and much less appealing due to uneven distribution of lithium resources, regardless of their profitable applications, basically in portable electronics and frequently in cell devices over many years [186]. Therefore, the scientific activity has been shifted into creating non-lithium, so-called "post-lithium" batteries with lower prices and similar or even higher performance [187]. However, sodium-ion batteries (SIBs) have attracted interest as the most promising choice to LIBs, due to their operational mechanism being similar

to lithium [188]. Moreover, sodium has a larger ionic radius than Li, which makes it difficult to find appropriate electrode substances that can be de/intercalated with Na throughout the charge/discharge process, hence raising problems of cycling stability and price of such batteries. For commercially workable SIBs, therefore, it is imperative to enhance stable and high-performance electrode materials.

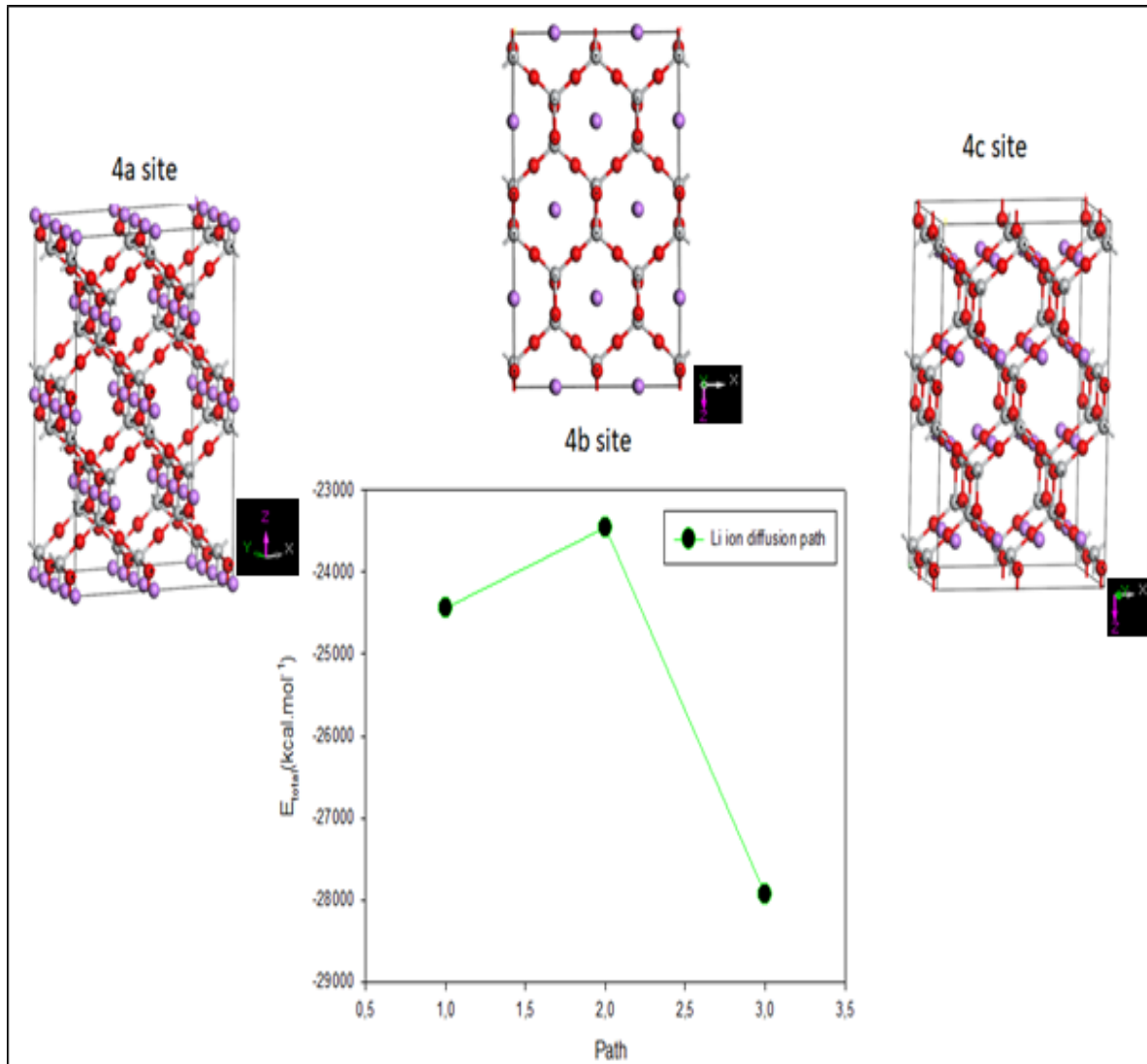


Figure 5.2. The total energy of fully lithiated  $\text{TiO}_2$  (TB)-I at various sites, 4a, 4b and 4c (Li-purple, O-red and Ti-grey).

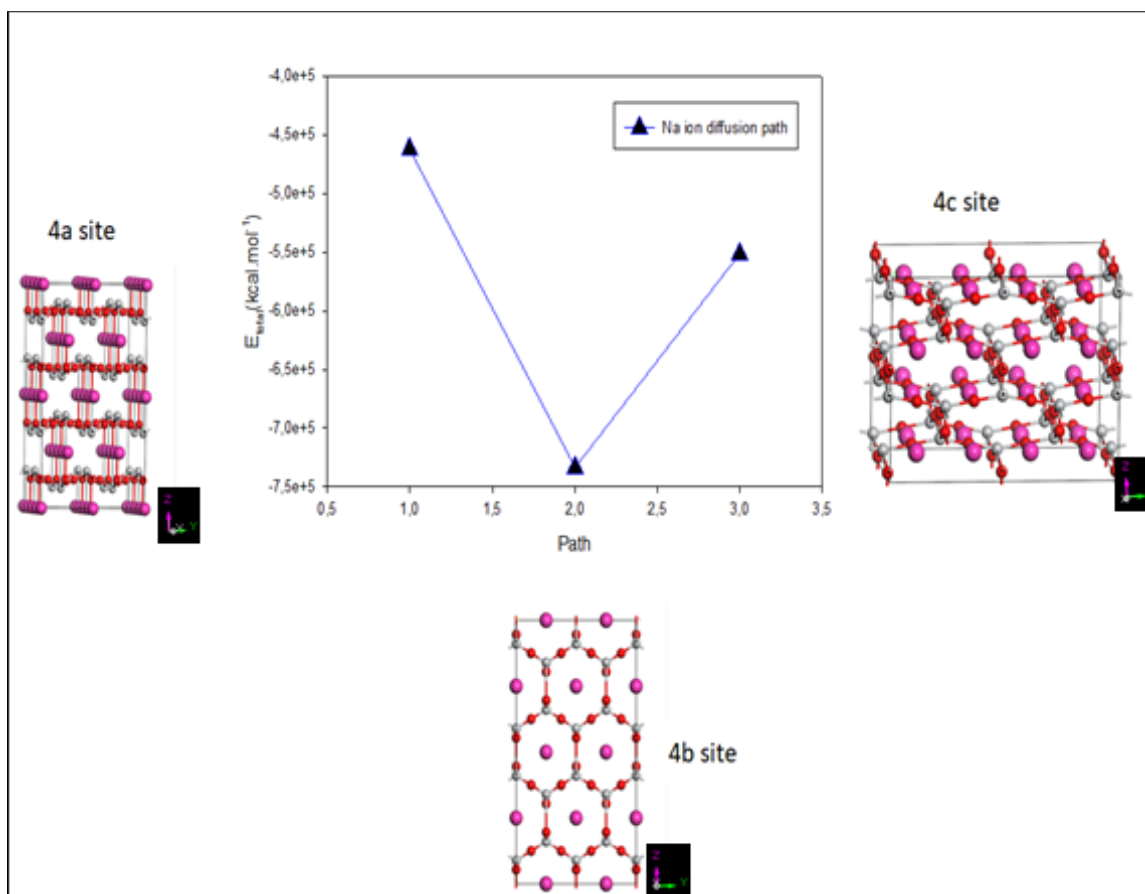


Figure 5.3. The total energy of fully sodiated  $\text{TiO}_2(\text{TB})\text{-I}$  at various sites 4a, 4b and 4c (Na-pink, O-red and Ti-grey).

It is known that the structure with the lowest energy is more stable. In Figure 5.2 and Figure 5.3, we present total energies for bulk  $4\text{LiTiO}_2(\text{TB})\text{-I}$  and  $4\text{NaTiO}_2(\text{TB})\text{-I}$  at various insertion sites. According to the calculated results, lithium ions prefer 4a and 4c sites in concurrence with *Ma et al.* [44] throughout the lithiation process, Li ions will diffuse into the channel and anchor to the middle of two bridge O anions, whilst leaving the channel area open. Importantly, these  $\text{TiO}_2(\text{TB})$  crystals after Li insertion exhibit a low volume enlargement (less than 7%) even at the  $\text{Li}:\text{TiO}_2 = 1:1$  ratio. However, sodium ions prefer the channel space (4b site) as compared to lithium ions. This is attributed to the fact that sodium has a larger ionic radius than Li, which makes it difficult to occupy 4a or 4c site. The results of sodiation are highly consistent with theoretical data, where the insertion sites of Na ions with larger ionic radius are shown to be possibly inside the 1D channel and to migrate through the channel [189].

The cell dimension profile for bulk  $\text{TiO}_2(\text{TB})\text{-I}$  structure lithiated and sodiated are presented in

Figure 5.4 and Figure 5.5 respectively. The lattice parameters for lithiation show similar trend, except for 4c site, whereby, a-parameter decreases at the beginning of lithiation and increases at the end. Moreover, the volume change was found to be insignificant. However, for sodiation, there was no trend found and the volume change was less than 35.0 %. Lithiated  $\text{TiO}_2$  (TB)-I are more energetically stable than sodiated ones (see Figure 5.6). The energy of lithiated  $\text{TiO}_2$  (TB)-I decreases with an increase in Li concentration. However, in the sodiated systems the energy started by decreasing and thereafter increases.

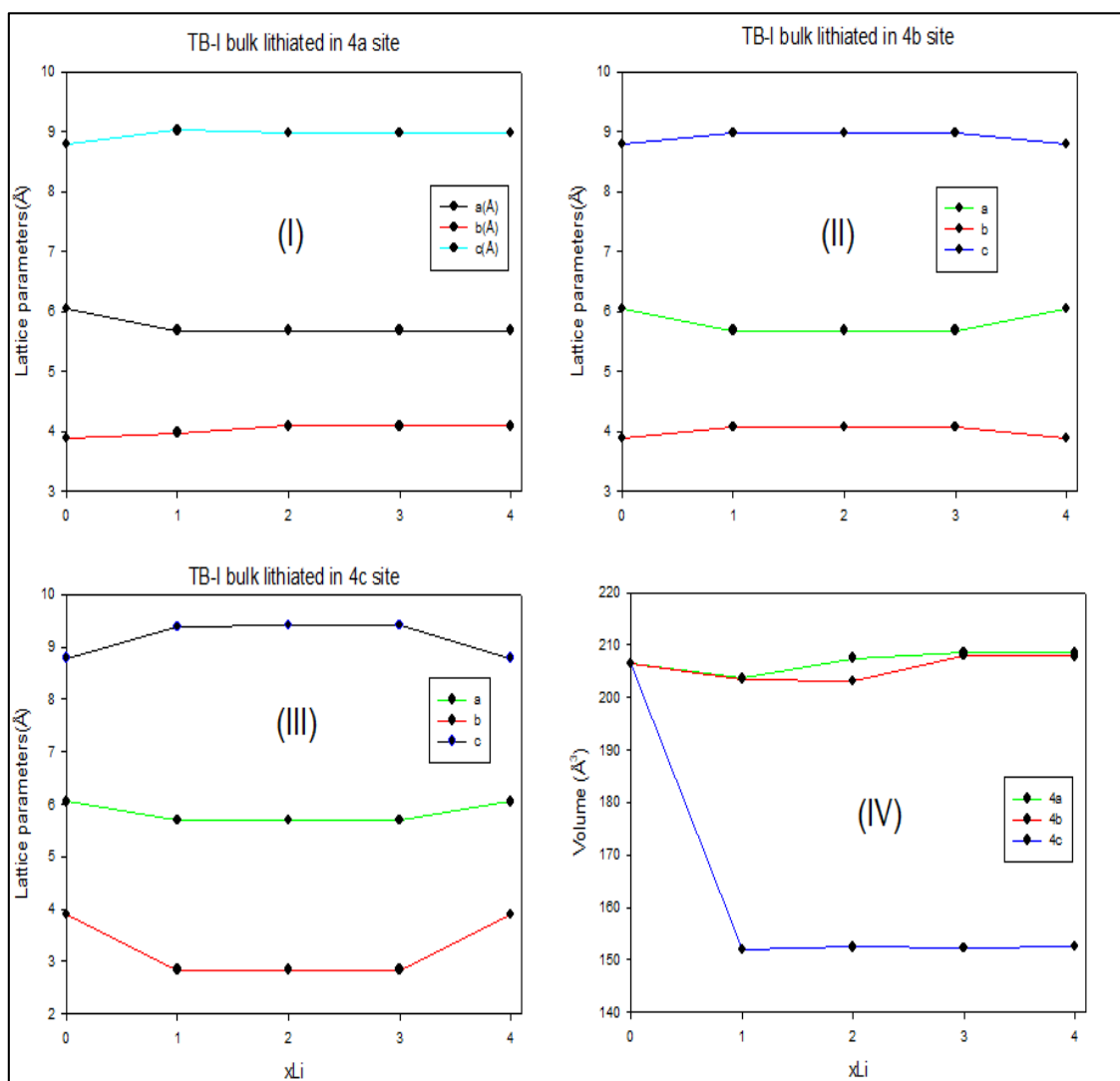


Figure 5.4. Cell dimensions of  $\text{Li}_x\text{Ti}_4\text{O}_2$  (TB)-I as a function of  $x$  lithium at (I) 4a, (II) 4b and (III) 4c site. (IV) Volume change for 4a, 4b and 4c sites.



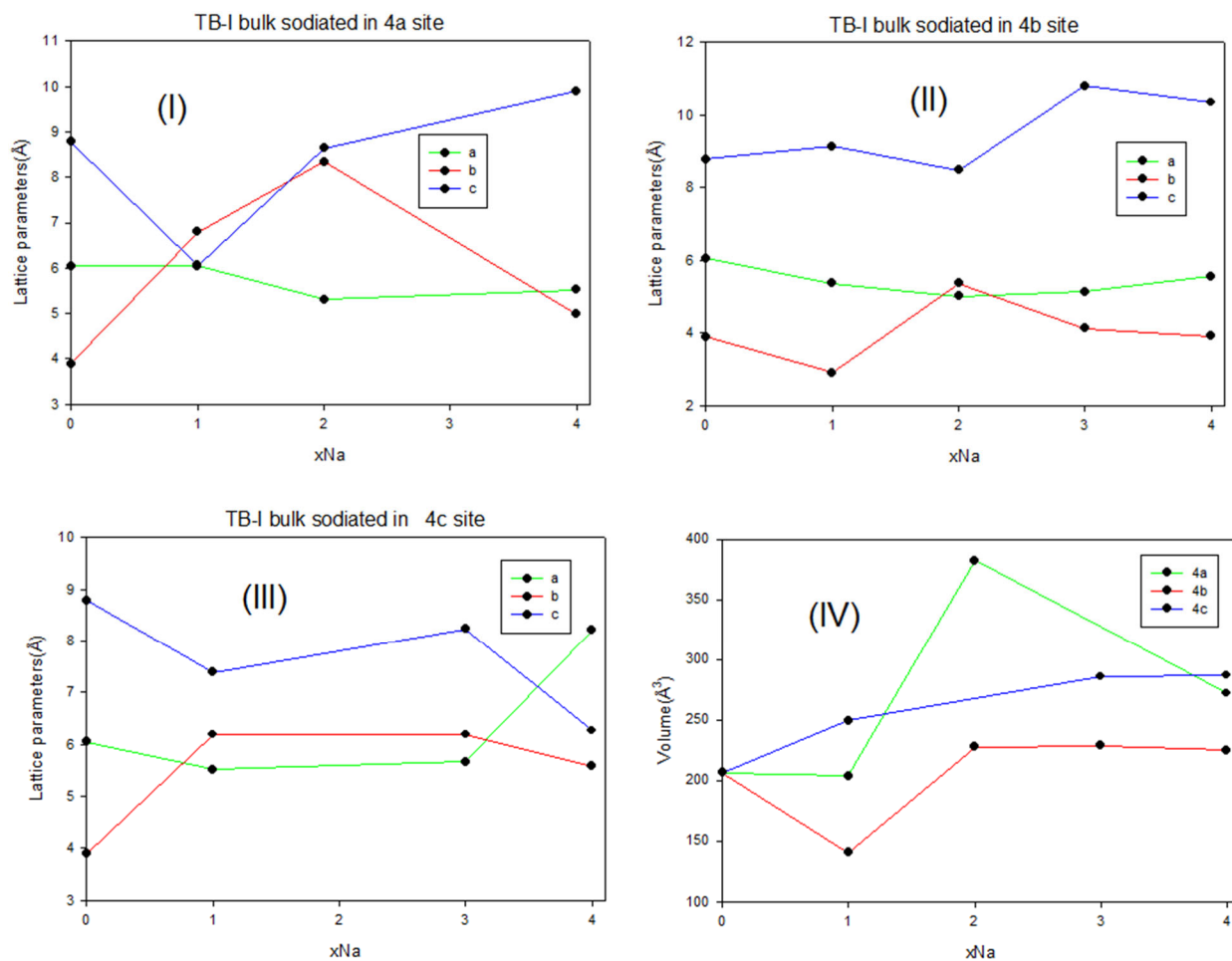


Figure 5.5. Cell dimensions of  $\text{Na}_x\text{Ti}_2\text{O}_4$  as a function of x sodium at (I) 4a, (II) 4b and (III) 4c site. (IV) Volume change for 4a, 4b and 4c sites.

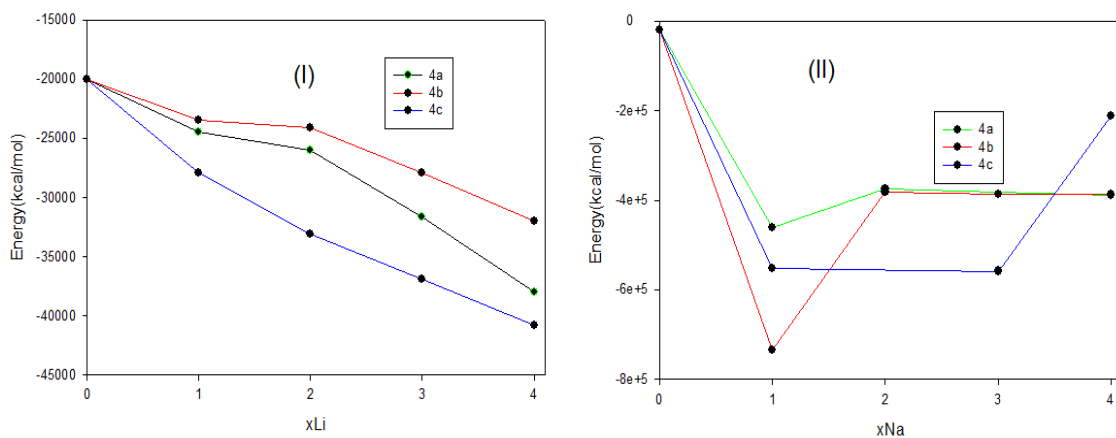


Figure 5.6. The total energy of various (I) lithium and (II) sodium concentrations into  $\text{TiO}_2$  (TB)-I at various sites.

## 5.4 Electronic properties of bulk $\text{Na}_x\text{TiO}_2$ TB-I

To describe the electronic structure of a  $\text{TiO}_2$  TB-I phase, the electronic partial density of states (PDOS) were analysed in Figure 5.7. PDOS profile depicts that the major contribution to the electronic properties are from Ti-3d and O-2p. In all Na ions concentrations, the valence band mainly originates from O-2p with lower Ti-3d contribution. The conduction band was dominated by Ti-3d with significant O-2p which is in line with DFT results of Choe *et. al.* [189], as shown in Figure 5.8; and in concurrence our bandgap reduces as Na concentration is increased.

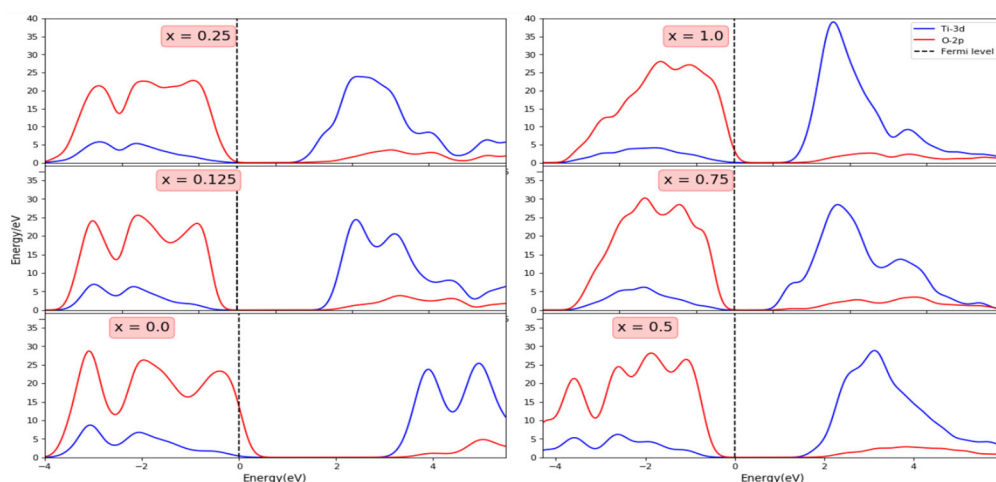


Figure 5.7. Partial density of states of  $\text{Na}_x\text{TiO}_2$  compounds in the TB-I phase at different values of Na content  $x$ , calculated with the DFTB method.

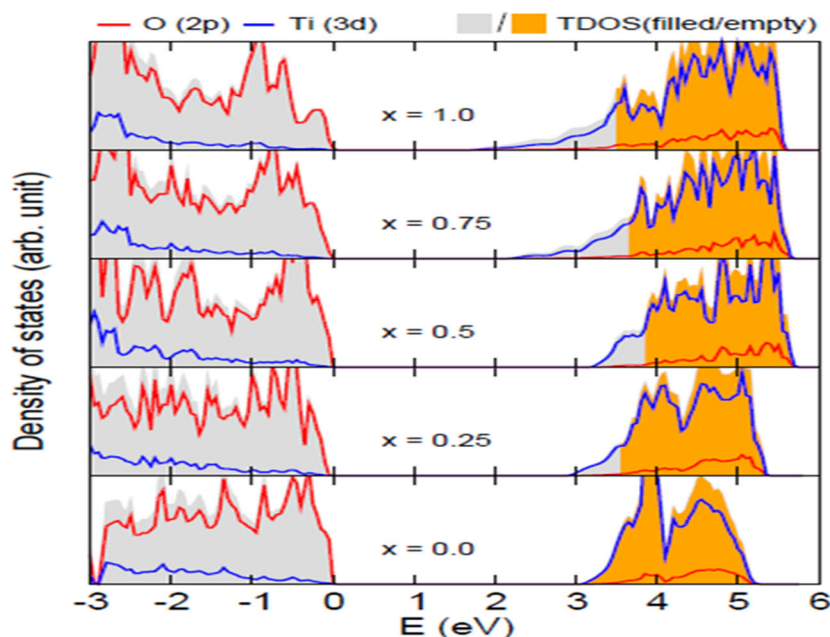


Figure 5.8. Projected density of states of  $\text{Na}_x\text{TiO}_2$  compounds in TB-I phase at different-Na  $x$  content, calculated with the PBEsol XC functional [189].

The TB-I phase partial density of states (PDOS) for  $\text{Li}_x\text{TiO}_2$  are displayed in Figure 5.9. It was found that the pristine  $\text{TiO}_2$  is an insulator with a wide bandgap of 3.306 eV using DFTB method, which is smaller than that of the previous PBE calculation (3.88 eV) [44]. Compared to other transition metal oxides, its valence band maximum (VBM) is predominantly composed of O-2p states, while the conduction band minimum (CBM) is composed of Ti-3d states. During lithiation of  $\text{TiO}_2$ , such features of VBM and CBM were altered. By increasing the Li content, the energy gap between the VBM and CBM decreases, and part of the CBM became occupied states, demonstrating that the lithiation changes the compound from an electron insulating to electron conducting material.

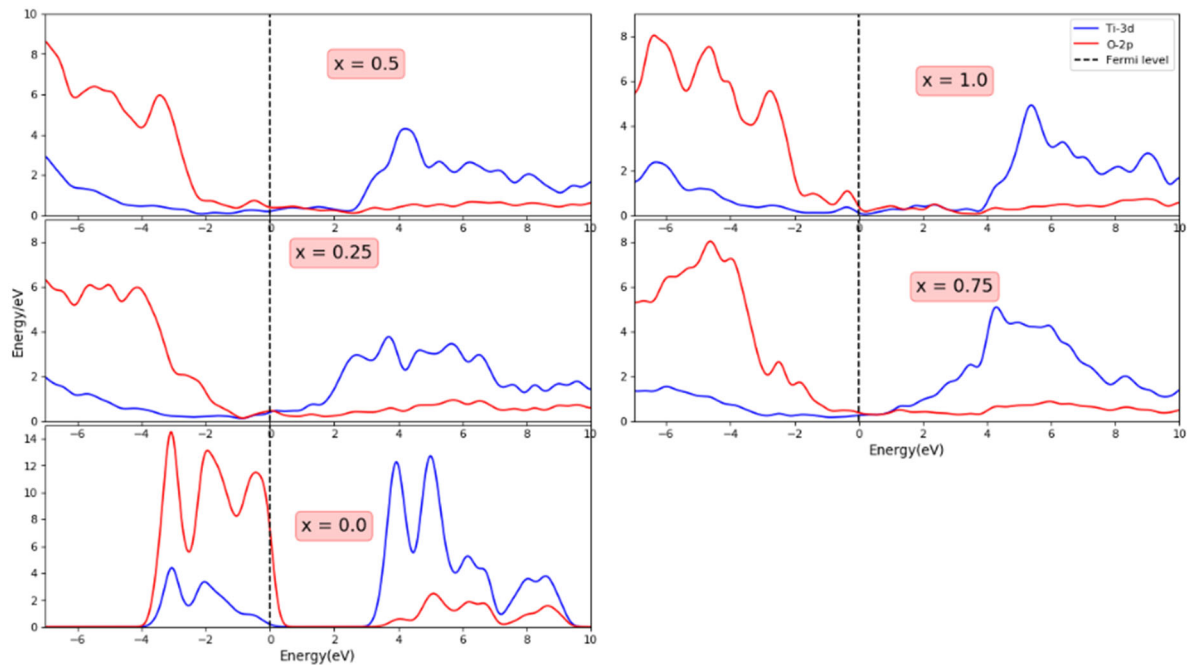


Figure 5.9. Partial density of states of  $\text{Li}_x\text{TiO}_2$  compounds in the TB-I phase at different values of Li content  $x$ , calculated with the DFTB method.

## 5.5 Lithiation of $\text{TiO}_2$ TB-I nanosphere

### 5.5.1 Lithiation and structural properties of $\text{TiO}_2$ (TB)-I nanospheres

Nanosizing  $\text{TiO}_2$  can significantly enhance electrode reaction kinetics of  $\text{TiO}_2$  during intercalation/deintercalation processes and increase lithium/sodium storage capacity of  $\text{TiO}_2$  (TB). Therefore, nanosizing  $\text{TiO}_2$  combined the mesoporous nanospheres structure is one effective way for the development of high-performance  $\text{TiO}_2$  anodes. The graph representing change in volumes during lithiation for 4a, 4b, and 4c site are

shown in Figure 5.10. It must be noted that, in the 4b site, the variation of the cell volume was larger because of the steepest slope as compared to that of 4a and 4c sites. However, the volumetric behaviour is favourable in 4a and 4c sites because it may prevent a rapid deterioration of the electrode due to the smaller total volume change.

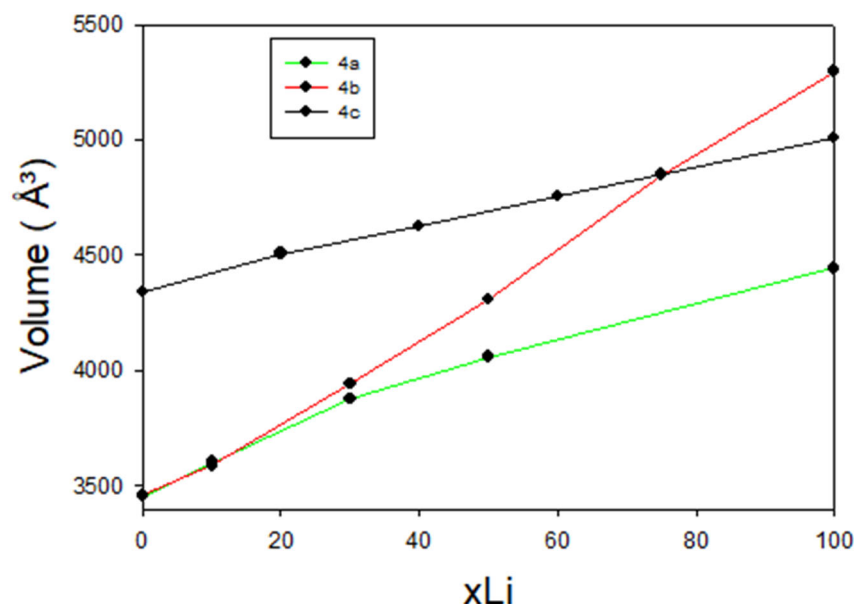


Figure 5.10. Volume profile of  $\text{TiO}_2$  (TB)-I nanosphere during lithiation.

Structures of  $\text{TiO}_2$  (TB) I nanospheres which were lithiated at the 4a site are shown in Figure 5.11. Structural transformation is noted with increasing lithium concentration, with most distortions occurring on  $\text{Li}_{20}\text{Ti}_{108}\text{O}_{216}$ , beyond which crystallinity is restored and a structure emerges and remains intact on  $\text{Li}_{100}\text{Ti}_{108}\text{O}_{216}$  and  $\text{Li}_{111}\text{Ti}_{108}\text{O}_{216}$ . Figure 5.12 depicts  $\text{TiO}_2$  (TB) I nanospheres which were lithiated at the 4b site and crystallinity is maintained up to  $\text{Li}_{20}\text{Ti}_{108}\text{O}_{216}$ . A transformation sets in on  $\text{Li}_{30}\text{Ti}_{108}\text{O}_{216}$  and results in a crystalline patterns for  $\text{Li}_{50}\text{Ti}_{108}\text{O}_{216}$ , and nanospheres tends to be more amorphous at higher lithium content.  $\text{TiO}_2$  (TB) I nanospheres which were lithiated at the 4c site are shown in Figure 5.13. There seems to be a transformation of the nanosphere from  $\text{Li}_0\text{Ti}_{140}\text{O}_{280}$  to  $\text{Li}_{20}\text{Ti}_{140}\text{O}_{280}$  beyond which a stable structure is noted and becomes more crystalline up to the highest concentration.

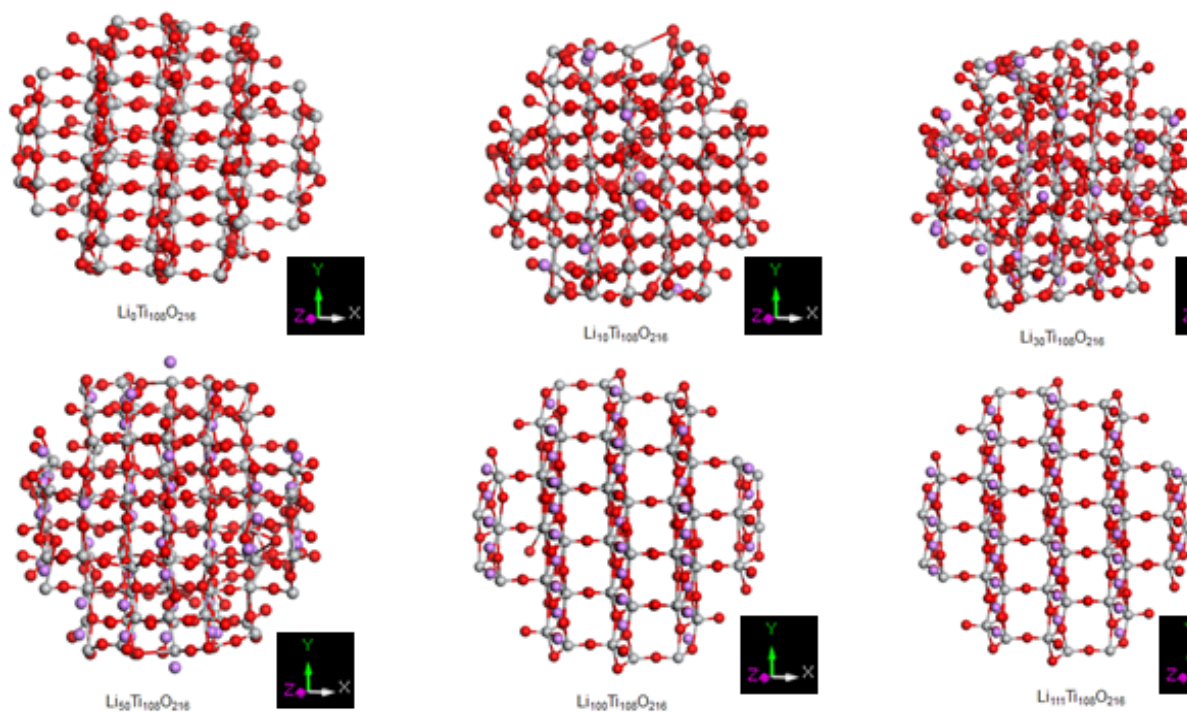


Figure 5.11.  $\text{TiO}_2$  (TB)-I nanospheres with various lithium ions concentration into 4a site. Ti, O and Li atoms are in grey, red and purple spheres respectively.

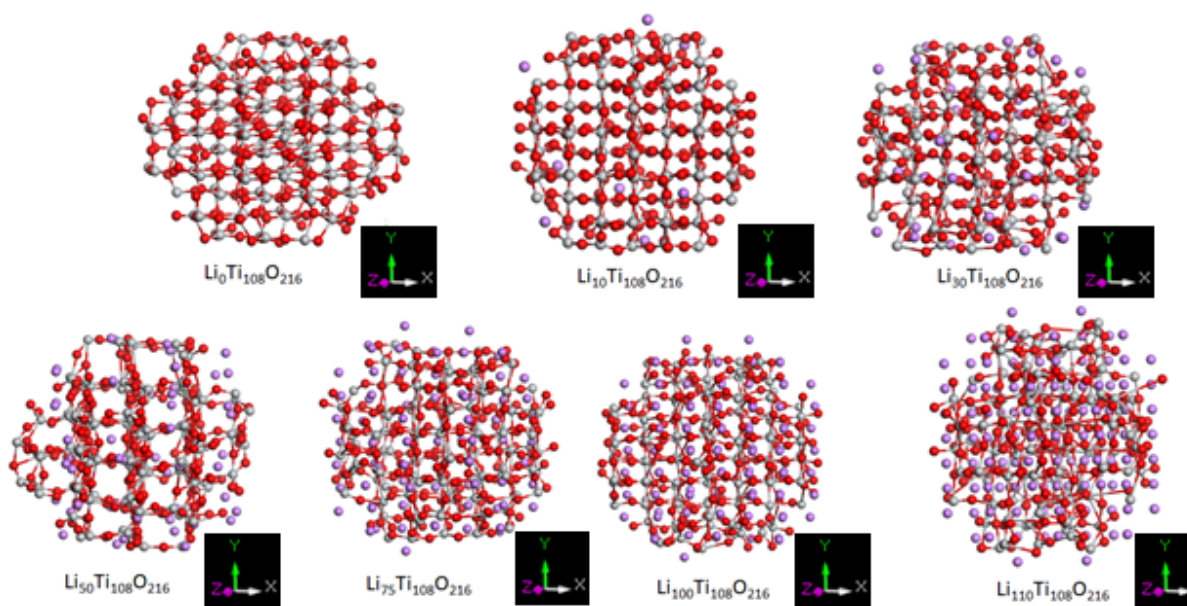


Figure 5.12.  $\text{TiO}_2$  (TB)-I nanospheres with various lithium ions concentration into 4b site. Ti, O and Li atoms are in grey, red and purple spheres respectively.

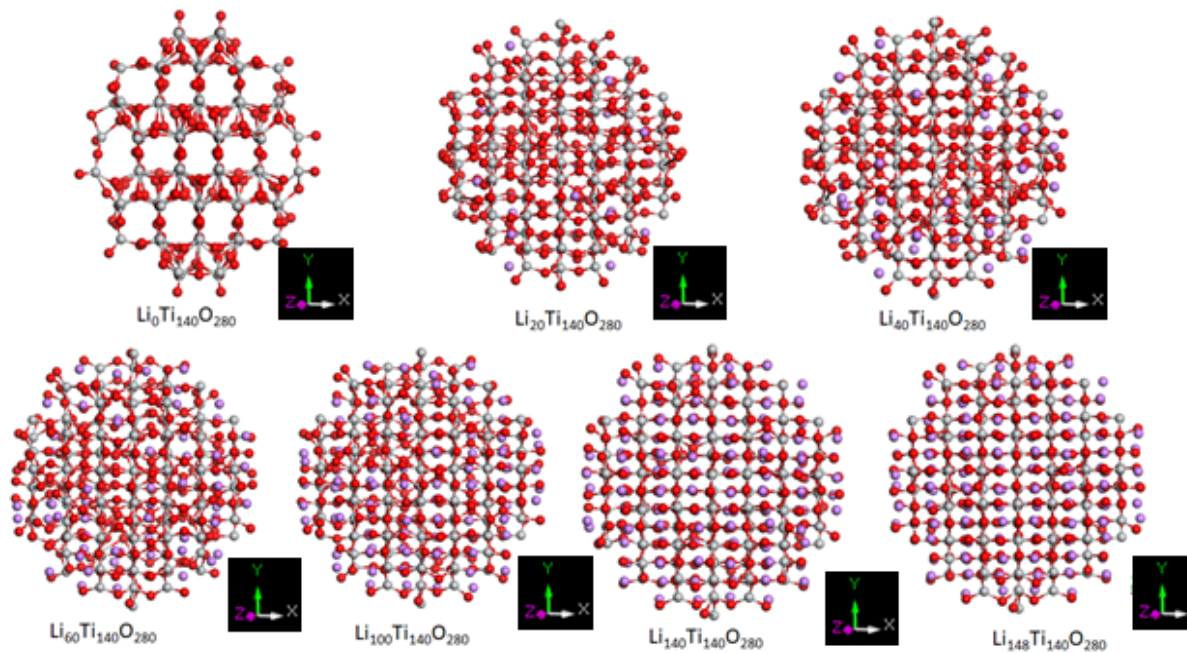


Figure 5.13  $\text{TiO}_2$  (TB)-I nanospheres with various lithium ions concentration into 4c site. Ti, O and Li atoms are in grey, red and purple spheres respectively.

### 5.5.2 Electronic properties of $\text{TiO}_2$ (TB)-I nanospheres

For a detailed overview of the electronic structure of  $\text{TiO}_2$  (TB)-I nanosphere (see Figure 5.14,

Figure 5.15 and Figure 5.16), the total and partial density of states (DOS) were calculated. On all three lithiated sites (4a, 4b and 4c), the valence band mainly originated from O-2s, O-2p states with some contribution from the Ti-3d. Ti-3d dominate the conduction band. Similarly, Choe *et al.* found the O-2p states to be prevalent in the valence band, while the conduction band is mainly composed of Ti 3d states [189]. From the 4a and 4b lithiated sites nanospheres, the pseudo gap moves toward Fermi level.

### 5.5.3 Summary on impact of lithiation for $\text{TiO}_2$ (TB)-I nanospheres

In  $\text{TiO}_2$  the (TB) I nanosphere, the volume changes with lithiation at 4a and 4c sites are nearly similar; whereas the volume change associated with the 4b site is relatively steep. Such variations appear to be consistent with nanosphere structural changes, where at the 4b site, the structure tends to be amorphous for high Li concentrations, whereas similar crystallinity is observed for those with lithiation at 4a and 4c sites. In

addition, the energetics of the bulk TiO<sub>2</sub> (TB) I indicated that the Li atoms are less stable at the 4b site than other sites. Electronic properties of TiO<sub>2</sub> (TB) I nanosphere,

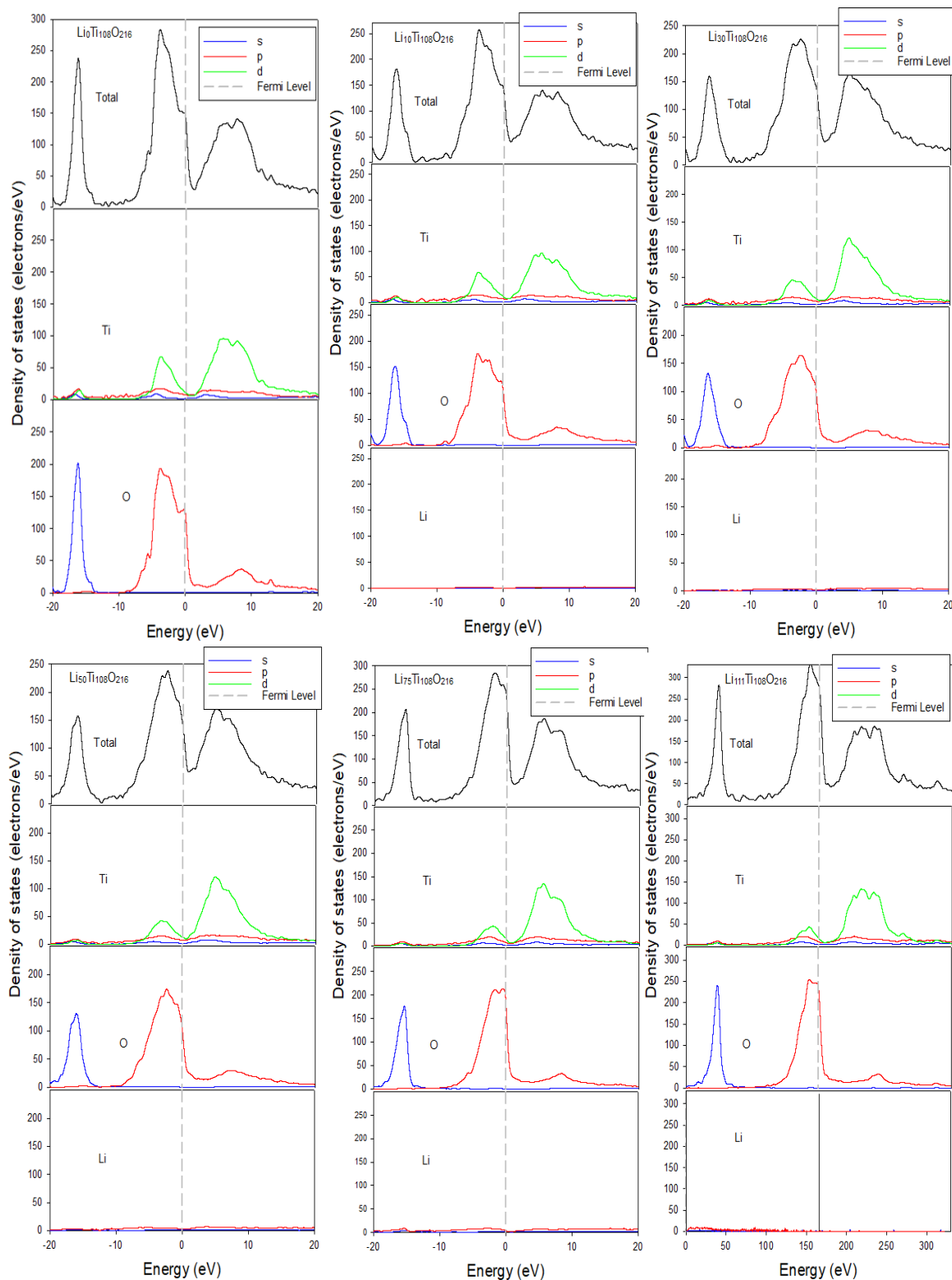


Figure 5.14. Partial density of states (PDOS) for TiO<sub>2</sub> (TB)-I nanospheres with various lithium ions concentration into 4a site.

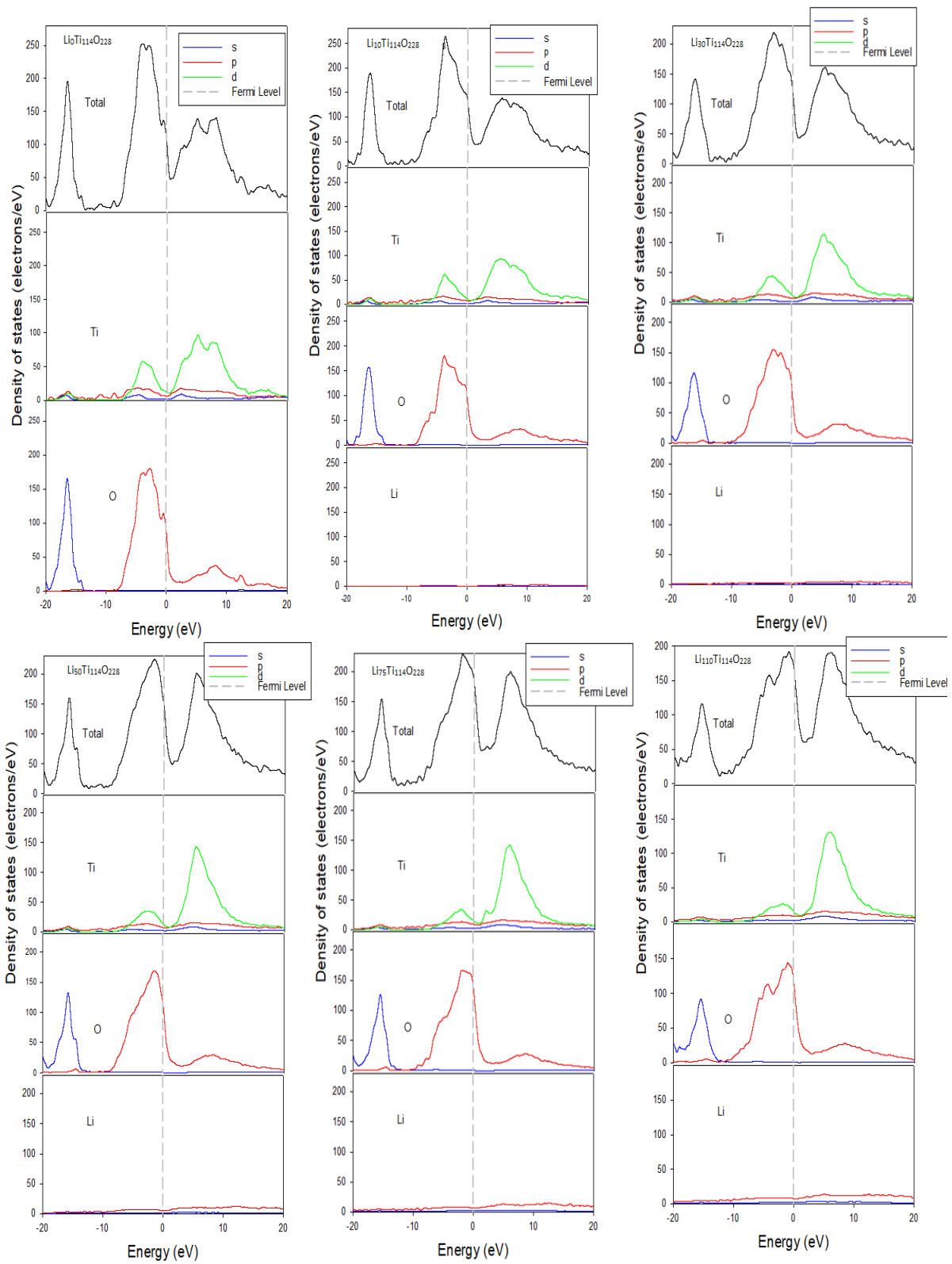


Figure 5.15. Partial density of states (PDOS) for  $\text{TiO}_2$  (TB)-I nanospheres with various lithium ions concentration into 4b site.



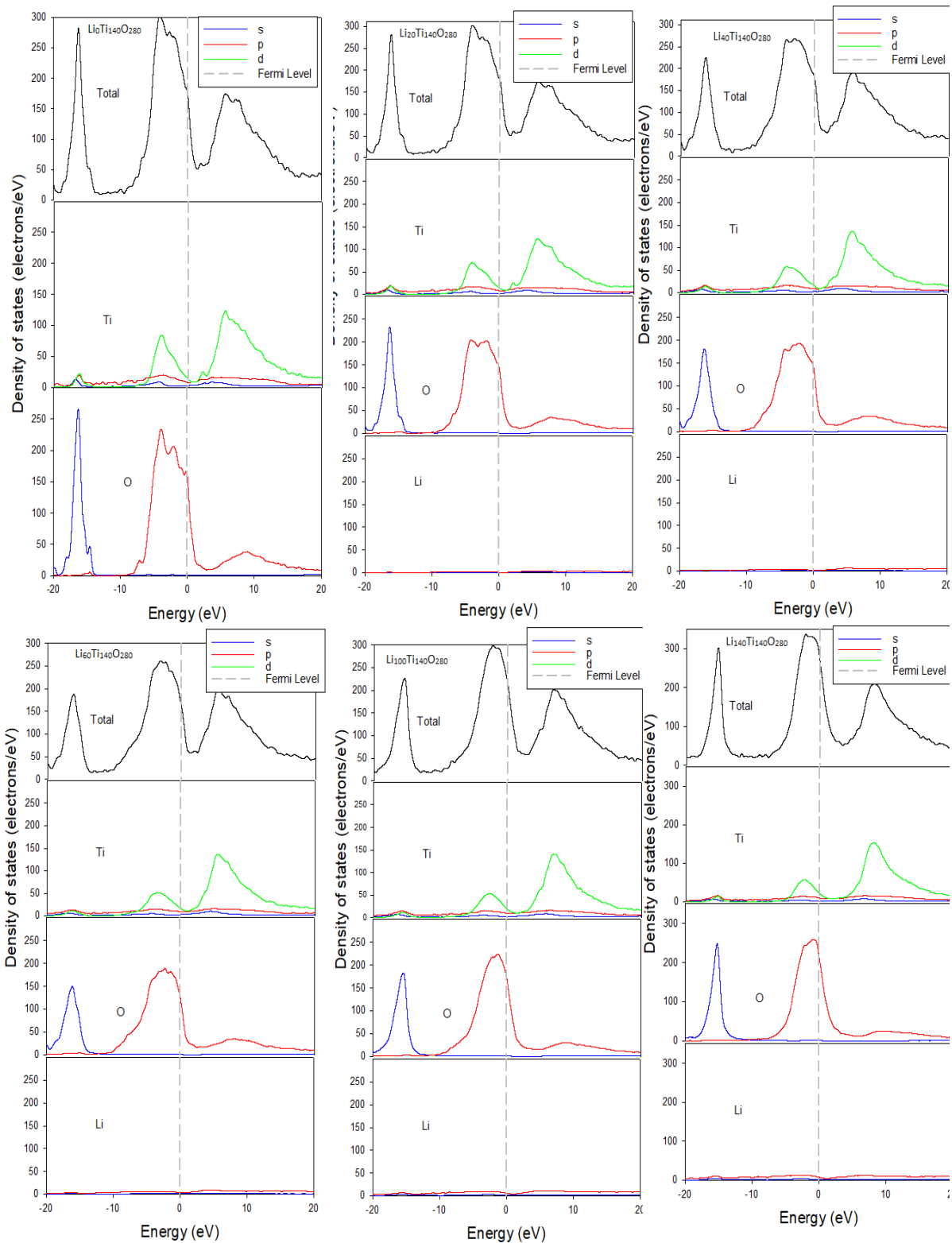


Figure 5.16. Partial density of states (PDOS) for  $\text{TiO}_2$  (TB)-I nanospheres with various lithium ions concentration into 4c site.

as depicted by the DOS, generally show that the Fermi level falls into a pseudogap, especially in the absence of lithiation. Upon lithiation the Fermi level appears to shave the top end of the valence band. The extent of that shaving appears similar for lithiation at all sites (4a, 4b and 4c). The shifting of the Fermi level into the pseudogap, which

normally alludes to stability, could perhaps be achieved by introducing temperature or pressure in the nanosphere; since all calculations are carried out at 0K in our DFTB calculations.

## 5.6 Structural properties of bulk TiO<sub>2</sub> (TB)-II during lithiation/sodiation

A conventional structure of the bulk TiO<sub>2</sub> (TB)-II is shown in Figure 5.17 and possesses a C<sub>mcm</sub> symmetry. The corresponding lattice parameters calculated by the DFTB method are depicted in Table 5.3, and are in good agreement with the DFT results [44].

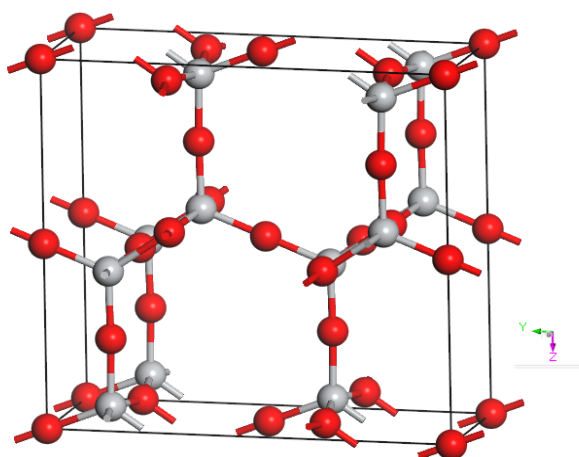


Figure 5.17. The crystal structure of TiO<sub>2</sub> (TB)-II polymorph. Ti and O atoms are in grey and red spheres respectively.

Table 5.3. Lattice parameters of TiO<sub>2</sub> (TB)-II.

TiO <sub>2</sub> Structure	Space group	Lattice parameters (Å)	
		DFTB(This work)	DFT [44]
TB-II	C <sub>mcm</sub> (63)	a= 3.82	3.82
		b=10.91	10.91
		c=10.00	10.03

In addition to structural properties, mechanical properties can also depict how well the derived DFTB model is reproducing the TiO<sub>2</sub> (TB-II) structural and thermodynamic

properties. Consequently, we have calculated elastic constants by the DFTB approach and in the absence of experimental and theoretical values we have compared them with those we calculated with the DFT Castep code. Generally, there is a good agreement between the two sets of results, except for  $C_{11}$  and  $C_{22}$  which are underestimated by DFT method. The calculated shear ( $G_{RVH}$ ) modulus of the  $TiO_2$  (TB-II) phase, shown in Table 5.4, is similar on employment of both the DFTB and DFT methods. On the other hand, the DFTB calculated bulk modulus (115.8GPa) is much closer to the experimental results (127.3GPa) [44], when compared to the DFT results (101.01 GPa). This further alludes to the reliability of the derived DFTB model on predicting properties of the  $TiO_2$  (TB-II) polymorph.

Furthermore, the elastic stability criterion for orthorhombic crystals under isotropic pressure is as follows  $C_{ii} > 0$  ( $i = 1, 4, 5, 6$ ),  $C_{11}C_{22} - C_{12}^2 > 0$ ,  $C_{11}C_{22}C_{33} + 2C_{12}C_{13}C_{23} - C_{11}C_{23}^2 - C_{22}C_{13}^2 - C_{33}C_{12}^2 > 0$  [33,34]. It is obvious that the calculated elastic constants of the orthorhombic  $TiO_2$  (TB-II) satisfy the elastic stability criterion, rendering the orthorhombic structure as mechanically stable. Although no available experimental and other theoretical data are employed to cross-check the present results, the current outcome can provide a useful reference for future studies

The variation of the three lattice parameters with lithium and sodium content at 8d sites are given in Figure 5.18(i) and (ii) respectively. The lithium insertion appears to effect minimal changes on all lattice parameters and consequently the volume. However, with an increase in the sodium content (Figure 5.18(ii)) the a lattice parameter increases up to  $xNa = 2$ , whilst b and c reduce; between  $xNa = 2$  and 5, a remains constant whilst b and c increase and reduce slightly respectively. In the range  $xNa = 5$  and 7 a reduction in a occurs when an increase in b and c are noted, whereas between  $xNa = 7$  and 8 a is constant, b reduces and c increases. On the whole, such trends in variations and fluctuations of the lattice parameters with sodiation are generally consistent with previously reported work [44]. The net effect is an increase in the volume between  $xNa = 0$  and 2, (which is mainly attributable to a relatively large increase in the a lattice parameter) and reduction from  $xNa = 2$  to 8. Except for this slight anomaly, our DFTB results yield results that are consistent with previous work.

Table 5.4. Elastic constants  $C_{ij}$ (GPa), (Russ's,Voigt's and Hill's), bulk modulus  $B_{RVH}$  and shear modulus  $G_{RVH}$  for  $TiO_2$  (TB)-II together with the theoretical and experimental.

	DFTB	DFT CASTEP	Exp. [44]
		GPa	
C <sub>11</sub>	262.48	183.81	
C <sub>12</sub>	91.61	75.91	
C <sub>13</sub>	85.10	73.51	
C <sub>22</sub>	122.53	93.80	
C <sub>23</sub>	102.47	100.91	
C <sub>33</sub>	135.58	131.82	
C <sub>44</sub>	13.51	11.47	
C <sub>55</sub>	30.53	34.04	
C <sub>66</sub>	34.84	34.75	
<b>B<sub>RVH</sub></b>	115.74	101.01	127.3
<b>G<sub>RVH</sub></b>	26.88	26.59	

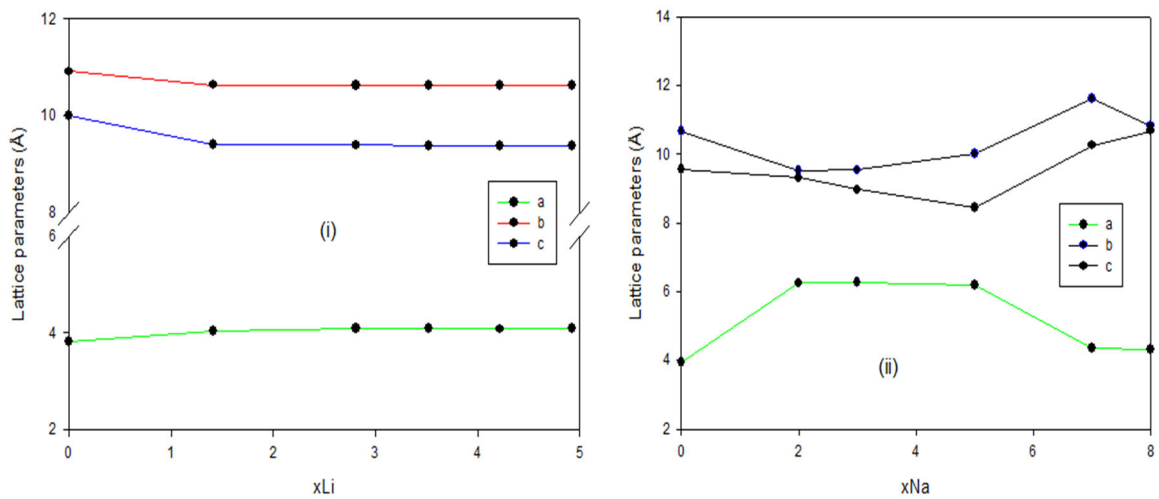


Figure 5.18. Cell dimensions of (i)  $\text{Li}_x\text{Ti}_4\text{O}_2$  and (ii)  $\text{Na}_x\text{Ti}_4\text{O}_2$  as a function of x lithium/sodium at 8d sites.

On the whole, the volume change in the  $\text{TiO}_2$  TB-II phase is considerably smaller compared to that in commercial graphite ( $\sim 300\%$ ). This offers the possibility of  $\text{TiO}_2$  (TB-II) as a fast charging anode material.

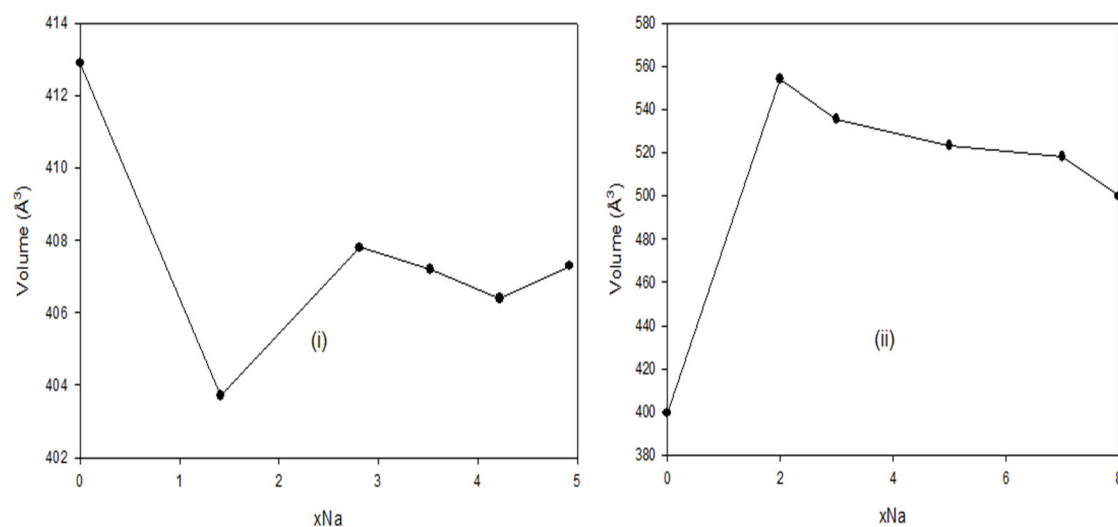


Figure 5.19. Volume profile of bulk  $\text{TiO}_2$  (TB-II) during lithiation (i) and sodiation (ii).

## 5.7 Electronic properties of bulk $\text{Na}_x\text{TiO}_2$ and $\text{Li}_x\text{TiO}_2$ TB-II

In order to understand the electronic properties of  $\text{TiO}_2$  TB-II phase, the partial density of states (PDOS) for the 3d electrons of Ti atom and 2p electrons of O atoms were investigated as the Na concentration was varied, using DFTB approach (Figure 5.20). In all cases, the valence band mainly originated from O-2p with smaller contribution of Ti-3d. The conduction band was dominated by Ti-3d with limited O-2p contributions which is similar to the sodiated TB-I phase which is depicted in Figure 5.8. In the PDOS, the bandgap reduces with increasing Na ion concentration from  $x=0$  to  $x=1$ , which is consistent with previous DFT results [197].

The variation of the PDOS for the bulk  $\text{TiO}_2$  TB-II phase with Li content,  $x$ , calculated using the DFTB method, is displayed in Figure 5.21. As noted previously, the pristine  $\text{TiO}_2$  is an insulator with a wide bandgap of 3.306 eV; which is smaller than that of the previous PBE calculation (3.91 eV) [44]. Compared to other transition metal oxides, its valence band maximum (VBM) is predominantly composed of O-2p states, while the conduction band minimum (CBM) is dominated by Ti-3d states. During lithiation which results in  $\text{Li}_x\text{TiO}_2$ , the features of VBM and CBM were altered. By increasing the Li content, the energy gap between the VBM and CBM decreases from  $x=0$  to  $x=0.5$ ,

and part of the bandgap is occupied by states, demonstrating that lithiation changes the compound from an insulator to an electron conducting material. However, the energy gap between the VBM and CBM increases from  $x=0.5$  to  $x=1.0$ , and part of the CBM remains occupied states.

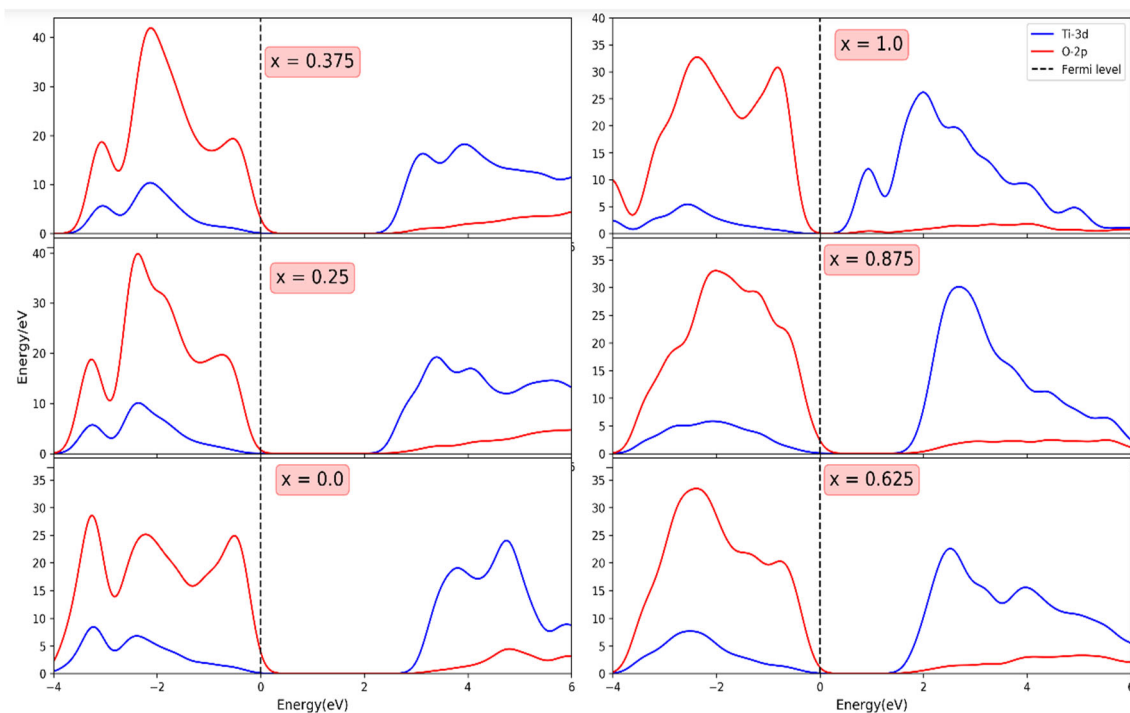


Figure 5.20. Partial density of states of  $\text{Na}_x\text{TiO}_2$  compounds in the TB-II phase at different values of Na content  $x$ , calculated with the DFTB method.

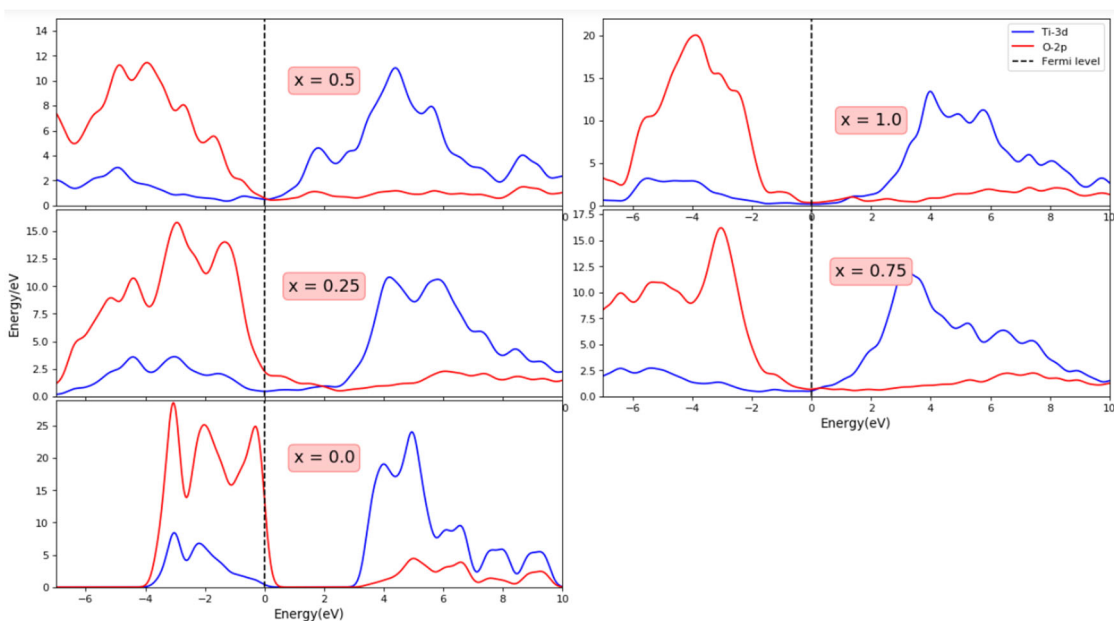


Figure 5.21. Partial density of states of  $\text{Li}_x\text{TiO}_2$  compounds in the TB-II phase at different values of Li content  $x$ , calculated with the DFTB method.

## 5.8 Structural properties of TiO<sub>2</sub> (TB)-II nanosphere during lithiation

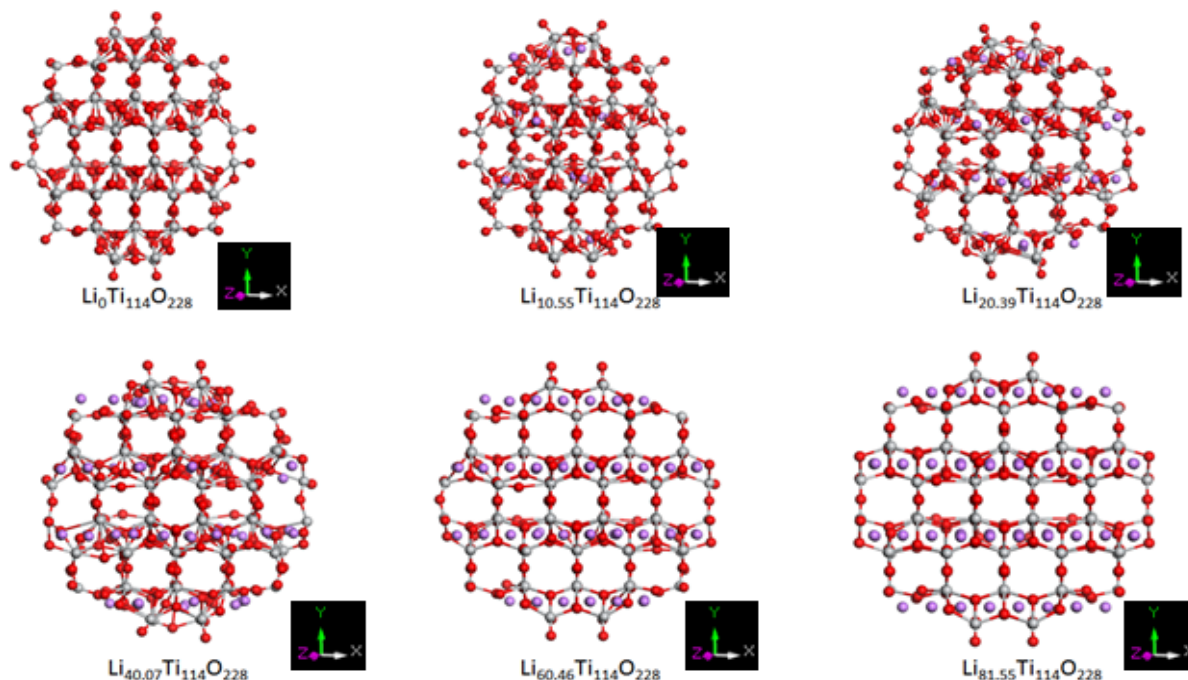


Figure 5.22. TiO<sub>2</sub> (TB)-II nanospheres with various lithium ions concentration into 8d site. Ti, O and Li atoms are in grey, red and purple spheres respectively.

The TiO<sub>2</sub> (TB) II nanospheres which were lithiated at 8d sites are shown in Figure 5.22. Well defined crystalline patterns are observed from Li<sub>0</sub>Ti<sub>114</sub>O<sub>228</sub> to Li<sub>81.55</sub>Ti<sub>114</sub>O<sub>228</sub> and large void spaces and connective electron pathways allow for fast ion transfer as well as avoiding aggregation with the effective buffers associated with volume changes. Slight structural transformation occurs at Li<sub>40.07</sub>Ti<sub>114</sub>O<sub>228</sub> and a new structure emerges beyond this and is maintained up to Li<sub>81.55</sub>Ti<sub>114</sub>O<sub>228</sub>. The volume change with lithiation of the nanosphere is shown in Figure 5.23. We have examined the correlation of the DOS and volume change for TiO<sub>2</sub> (TB-II) nanospheres. By computing the Li<sub>x</sub>TiO<sub>2</sub> (TB-II) nanostructures, we found that during the lithiation process, the volume increases rapidly from ~10 to 40 Li-ions, while gradually increasing between ~40 to 80 Li-ions concentrations. In the absence of

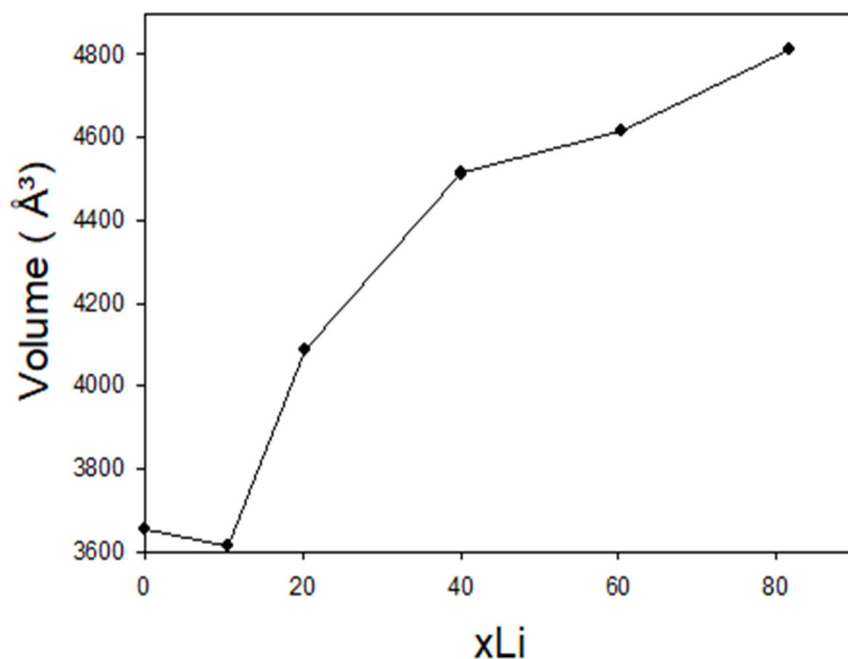


Figure 5.23. Volume profile for lithiated TiO<sub>2</sub> (TB)-II nanosphere

lithiation, the Fermi level intercepts the DOS curve close to a pseudogap (Figure 5.24). As the lithium content is increased, the shape of the O 2p state changes, especially above Li<sub>40.07</sub>Ti<sub>114</sub>O<sub>228</sub> and the Fermi level is slightly shifted away from the pseudogap. The extent of shifting from the pseudogap is not as much as in the (TB) I nanosphere. This could suggest a better stability of lithiated (TB) II phase than that of the (TB) I nanosphere in Figure 5.23. However, a distinct variation in the slope of the volume vs Li content appears at Li<sub>40.07</sub>Ti<sub>114</sub>O<sub>228</sub> and is consistent with associated structural change. The mild volume change of the TiO<sub>2</sub> (TB) II phase with lithiation was also observed in the bulk structure (Figure 5.19).

## 5.9 Summary

Hierarchically ordered porous TiO<sub>2</sub> with 2D structures have acquired exceptional interest mainly as negative electrodes in LIBs. These special porous structures provide a fast reactant transport via the larger pore diameters as properly as an excessive surface area which is acquired from the smaller pores performing as active sites for the adsorption/desorption of the reactants.

For both TiO<sub>2</sub> (TB)-I and TiO<sub>2</sub> (TB)-II, the calculated equilibrium lattice constants using DFTB method were found to be in good agreement with the calculated [44]. TiO<sub>2</sub> (TB)-I structure was found to be mechanical stable and ductile. The change in



volume during Li/Na ion insertion was significant for TiO<sub>2</sub> (TB)-I and it increased by not more than 18% in TiO<sub>2</sub> (TB)-I. However in (TB)-II phase the volume decreases, which are similar to what has been observed in literature [189]. Moreover, the possible Li/Na insertion sites and volume change also support the applicability of this TiO<sub>2</sub> (TB)-I compound as a SIB anode material.

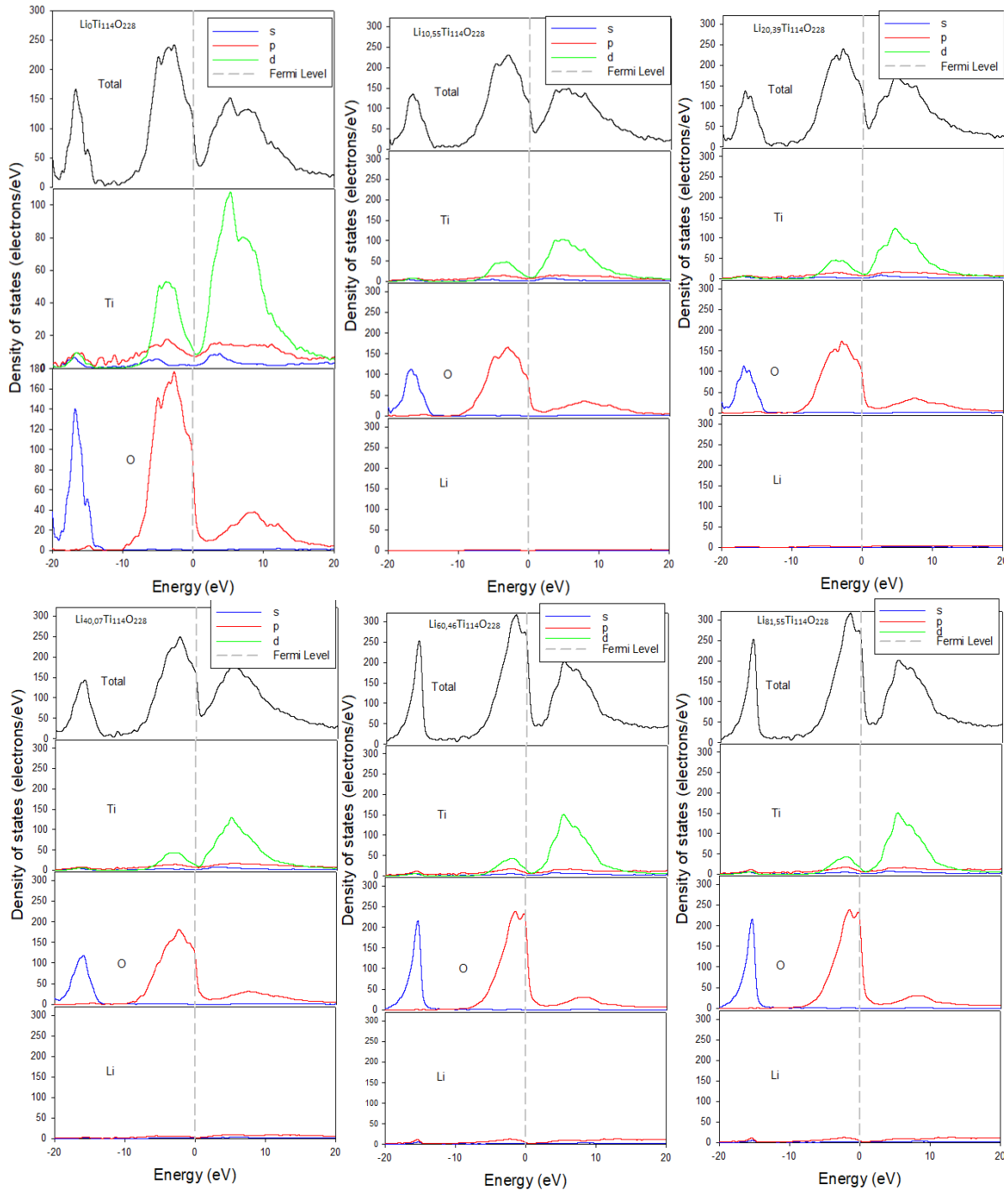


Figure 5.24. Partial density of states (PDOS) for  $\text{TiO}_2$  (TB)-II nanospheres with various lithium ions concentration into 8d site.

In conclusion, the ability of the DFTB model to calculate properties of bulk  $\text{TiO}_2$  (TB) I and II polymorphs has been reasonably validated for pristine, lithiated and sodiated structures. In addition, the DFTB model, by being able to comfortably handle larger structures than the DFT approach, has further been employed to predict suitability of nanostructured configurations in anode materials during charging and discharging of lithium ion batteries. Calculations on sodiation of nanospheres for both  $\text{TiO}_2$  (TB)-I and (TB)-II polymorphs were attempted and convergence could not be attained, consequently refinement of the DFTB models may be necessary to achieve this.

# Chapter 6: Conclusions and recommendations

## 6.1 Conclusion

In this thesis we have endeavored to study a promising energy storage anode  $\text{TiO}_2$ , using a state of the art semi-empirical approach, the self-consistent density functional tight binding method (SCC-DFTB), which is more accurate than the classical empirical methods since it takes electronic properties into consideration, whilst simultaneously being able to comfortably handle larger systems, such as nano-architectures, than those normally investigated by the widely used first principles density functional theory (DFT) methods. However, the latter technique was employed, in a limited way, to validate some of the results of the new  $\text{TiO}_2$  models that were derived by the DFTB method.

The main advantage of the SCC-DFTB over the conventional tight binding (NCC-DFTB) and other methods is the introduction of a Coulomb interaction between charge fluctuations. We derived parameters for Ti-O and O-O interactions in  $\text{TiO}_2$  using the SCC-DFTB parameterization procedure, and validated them on the well-known polymorphs of the bulk  $\text{TiO}_2$  namely, rutile, brookite and anatase. The resulting structural, such as lattice parameters, and electronic properties results were in good agreement with experimental values. In the calculations of electronic properties, the well-known deficiency regarding band gap energy underestimation or overestimation, were overcome by inclusion of the dispersion correction within DFTB+. When using dispersion correction, the DFTB+ uses universal force field (UFF) based Lennard-Jones dispersion corrections. UFF is moderately precise for predicting geometries and conformational energy differences. The band gap energies of the three  $\text{TiO}_2$  polymorphs were improved after using dispersion corrections. Most elastic constants of the three polymorphs were well reproduced except for a few such as  $C_{33}$  which tended to be underestimated, when compared with the experimental and theoretical results.

In order to enable lithiation and sodiation of  $\text{TiO}_2$ , parameters for Ti-Li, O-Li, Li-Li, Ti-Na, O-Na, Na-Na, Ti-O and O-O interactions were derived. The variations in structural properties for the bulk  $\text{TiO}_2$  polymorphs were calculated and compared with available results. Additionally, we also derived parameters for Ti-Na, O-Na, Na-Na, Ti-O and O-

O interactions and they were used to calculate properties of sodiated bulk anatase  $\text{TiO}_2$  and nanospheres with various concentrations of sodium ions. The change in volume during Li-ion intercalation into bulk anatase was found to be insignificant as compared to that of sodiated bulk. Similarly, the change in volume for lithiated nanosphere was minimal as compared to sodiated nanosphere.

For purposes of illustrating competitive advantages of the DFTB semi-empirical approach, we firstly studied nanostructures of the chemically most stable polymorph, namely anatase, where a larger number of atoms was involved compared to those routinely used in DFT calculations. This new SCC-DFTB set gave accurate values of band gap energies of the anatase  $\text{TiO}_2$  dioxide nanotubes with the diameter ranging from 8-14Å. Galvanostatic measurements showed that the  $\text{Li}^+$  storage capacity is higher for the nanotube electrode than the theoretical value for the bulk anatase  $\text{TiO}_2$  materials [190]. The corresponding SCC-DFTB structural parameters of this bulk anatase  $\text{TiO}_2$  are in good agreement with reference to DFT+U results. The molecular dynamics simulations between temperatures of 200-1000K successfully run for anatase  $\text{TiO}_2$  bulk and nanotube structures on the NVT ensemble.

Structural properties of the lithiated and sodiated  $\text{TiO}_2$  anatase nanospheres and structural transition with concentrations were predicted. The optimisation was not straightforward and a steepest descent and ABNR algorithm are proposed to efficiently study nanoclusters. It reduces the computational cost drastically. Similarly, the change in volume for lithiated nanosphere was minimal as compared to sodiated nanosphere. Furthermore, a structural transition was noted in the sodiated  $\text{TiO}_2$  anatase nanospheres, consistent with what was observed in literature.

The final application of our newly derived SCC-DFTB potentials was on the recently discovered state of the art trigonal bipyramid (TB)  $\text{TiO}_2$ , with (TB)-I and  $\text{TiO}_2$  (TB)-II polymorphs, which have enormous 1-D channels that provide suitable pathways for mobile ion transport in battery anodes. In both structures  $\text{TiO}_2$  (TB)-I and  $\text{TiO}_2$  (TB)-II, the calculated equilibrium lattice constants, using DFTB method, are in good agreement with those in literature [44]. Unlike the three  $\text{TiO}_2$  polymorphs just discussed, the calculated elastic constants are consistent (to within 5%) with those of the DFT results we carried out, and the predicted bulk modulus agrees with the experimental one. It was further noted that the (TB)-I polymorph was more

mechanically stable and ductile. The change in volume during Li/Na ion insertion was significant for TiO<sub>2</sub> (TB)-I while it increased by more than 27% in TiO<sub>2</sub> (TB)-II. Moreover, the possible Li/Na insertion sites and volume change also support the applicability of this TiO<sub>2</sub> (TB)-I compound as a SIB anode material.

Finally, the present study has shown that SCC-DFTB is successful for providing groundwork for the usage of SCC-DFTB potentials for theoretical studies of TiO<sub>2</sub> polymorphs. TiO<sub>2</sub> nanotubes and nanospheres studies that are normally computationally demanding are rendered feasible, including quantum chemical molecular dynamics simulations.

## 6.2 Recommendations

Structural, electronic, mechanical and temperature dependence of thermodynamic properties of some TiO<sub>2</sub> nanostructures have been studied extensively using first principles method. However, we would like to put forward some recommendations emanating from the current study. We have calculated bulk moduli, elastic constants and energy band gaps which are of great interest, since such properties will contribute significantly in the development of new anode materials for lithium-ion material. We hope that our calculations will stimulate more experimental and theoretical work on elastic constants and energy band gaps. The availability of such results will enable a meaningful validation of our predictions. Although anatase TiO<sub>2</sub> nanoparticles have been obtained in experimentally, our understanding of structure of such important polymorph of TiO<sub>2</sub> nanoparticles is limited. Therefore, the understanding about the atomic scale studies like those observed in present work could be quite valuable and further investigation of other surfaces (e.g. [0 0 1] Miller indices) of anatase TiO<sub>2</sub> in future. There are few reports of brookite as negative electrode material for lithium ion batteries. Molecular dynamics simulation can be performed at high temperatures for titanium dioxide nanostructures. Amorphisation and recrystallisation technique might also be employed, for TiO<sub>2</sub> nanostructures.

## 6.3 Contributions of the study

In this thesis, we present a new method, i.e., the Density Functional based Tight Binding (DFTB) method, which we used to develop potentials in order to predict properties of materials both accurately and quickly. Using a DFTB method, we

demonstrate that it is computationally possible to determine the lattice parameters and energies for large systems, i.e., without the help of any excellent empirical potentials, which are available only for few number of atoms and type of materials. This diverse advantage is vital when such empirical potentials are difficult to obtain, e.g., for multi-atom type materials. Steepest descent and ABNR algorithms are proposed to optimize efficiently TiO<sub>2</sub> nanoclusters. It reduces the computational cost drastically. We also can use these potentials to predict properties of new materials.

## **6.4 Limitations of the study**

This studies and its scope had restricted resources, for example, equipment, funding and time. Despite the fact that different conceivable outcomes exist, the scope was limited to exploring the properties of five titanium dioxide polymorphs and to intercalate these polymorphs. Only the Anatase TiO<sub>2</sub> was utilized to create the nanotubes and nanospheres while both TiO<sub>2</sub> (TB-I) and TiO<sub>2</sub> (TB-II) generated nanospheres. Sodiation was likewise confined to Bulk and nanosphere anatase. Furthermore, NVT MD was performed to demonstrate Li/Na particles migration at which the transformation of bulk Anatase TiO<sub>2</sub> happened. Finally, two trigonal bipyramid (TB) TiO<sub>2</sub> structures were lithiated and sodiated.

## Bibliography

- [1] A. N. Jansen, A. J. Kahaian, K. D. Kepler, P. A. Nelson, K. Amine, D. W. Dees, D. R. Vissers, M. M. Thackeray, "Development of a high-power lithium-ion battery," *J. Power Sources*, vol. 81–82, pp. 902–905, 1999.
- [2] A. R. Armstrong, G. Armstrong, J. Canales, P. G. Bruce, "TiO<sub>2</sub>-B nanowire as negative electrode for rechargeable lithium batteries," *J. Power Sources*, vol. 146, pp. 501–506, 2005.
- [3] M. A. Reddy, M. S. Kishore, V. Pralong, V. Caignaert, V. U. Varadaraju, B. Raveu, "Room temperature synthesis and Li insertion into nanocrystalline rutile TiO<sub>2</sub>," *Electrochem. Commun.*, vol. 8, pp. 1299–1303, 2006.
- [4] G. Mogilevsky, Q. Chen, H. Kulkarni, A. Kleinhammes, W. M. Mullins, Y. Wu, "Layered Nanostructures of Delaminated Anatase: Nanosheets and Nanotubes," *J. Phys. Chem. C*, vol. 112, pp. 3239–3246, 2008.
- [5] J. Muscat, V. Swamy, N.M. Harison, "First principles calculations of the phase stability of TiO<sub>2</sub>," *Phys. Rev. B*, vol. 65, pp. 224112–224127, June 2002.
- [6] C. Yu, X. Zang, J. Li, T. Lu, L. Pan D. Yang, "Enhanced electrochemical performances of anatase TiO<sub>2</sub> nanotubes bysynergetic doping of Ni and N for sodium-ion batteries," *Electrochimica Acta.*, vol. 254, pp. 130–139, 2017.
- [7] D. Deng, M. G. Kim, J. Y. Lee, and J. Cho, "Green energy storage materials: Nanostructured TiO<sub>2</sub> and Sn-based anodes for lithium-ion batteries," *Energy Environ. Sci.*, vol. 2, pp. 818–837, 2009.
- [8] J. Cho J. Kim, "Rate Characteristics of Anatase TiO Nanotubes and Nanorods for Lithium Battery AnodeMaterials at Room Temperature," *J. Electrochem. Soc.*, vol. 154, pp. A542–A546, 2007.
- [9] G. Oltean, C. -W. Tai, K. Edström, F. Björefors, L. Nyholm W. Wei, "High energy and power density TiO<sub>2</sub> nanotube electrodes for 3D Li-ion microbatteries," *J. Mater. Chem. A.*, vol. 1, pp. 8160–8169, 2013.

- [10] P. G. Bruce, B. Scrosti, J.M. Tarascon, "Nanomaterials for rechargeable lithium batteries," *Angew. Chem. Int. Ed.*, vol. 47, pp. 2930–2946, 2008.
- [11] F. Nunzi, F. De Angelis, "DFT Investigations of Formic Acid Adsorption on Single-Wall TiO<sub>2</sub> Nanotubes: Effect of the Surface Curvature," *J. Phys. Chem. C*, vol. 115, pp. 2179–2185, 2011.
- [12] R. A. Evarestov, A. B. Bandura, M. V. Losev, "Symmetry and stability of nanotube based on titanium dioxide," *Russ J. Gen. Chem.*, vol. 80, pp. 1152–1167, 2010.
- [13] K. M. Abraham, "Directions in secondary lithium battery research and development," *Electrochim. Acta.*, vol. 38, pp. 1233–1248, 1993.
- [14] G. Ali, C. Chen, S. H. Yoo, J. M. kum, S. O. Cho, "Fabrication of complete titania nanoporous structures via electrochemical anodization of Ti," *Nano. Research Let.*, vol. 6, pp. 1–10, 2011.
- [15] M. Wagemaker, W. J. H. Borghols, F. M. Mulder, "Large Impact of Particle Size on Insertion Reactions. A Case for Anatase Li<sub>x</sub>TiO<sub>2</sub>," *J. Am. Chem. Soc.*, vol. 129, pp. 4323–4327, 2007.
- [16] A. Matsuda, T. Matoda, T. Kogure, K. Tadanaga, T. Minami, M. Tatsumisago, "Formation and Characterization of Titania Nanosheets-Precipitated Coatings via Sol-Gel Process with Hot Water Treatment under Vibrations," *Chem. Mater.*, vol. 17, pp. 749–757, 2005.
- [17] M.-C. Yang, Y.-Y. Lee, B. Xu, K. Powers, Y. S. Meng, "TiO<sub>2</sub> flakes as anode materials for Li-ion-batteries," *J. Power Sources*, vol. 207, pp. 166–172, 2012.
- [18] A. Matsuda, T. Matoda, T. Kogure, K. Tadanaga, T. Minami, M. Tatsumisago, "Formation and characterization of titania nanosheet-precipitated coatings via Sol-Gel method with hot water treatment," *Chem. Mat.*, vol. 17, pp. 749–757, 2005.



- [19] T. Sasaki, S. Nakano, S. Yamauchi, M. Watanabe, "Fabrication of titanium dioxide thin flakes and their porous aggregate," *Chem. Mat.*, vol. 9, pp. 602–608, 1997.
- [20] M. -C. Yan, Y. -Y. Lee, B. Xu, K. Powers, Y. S. Meng, "TiO<sub>2</sub> as anode material for Li-ion-batteries," *J. Power Sources*, vol. 207, pp. 166–167, 2012.
- [21] G. Nuspl, K. Yoshizawa, T. Yamabe, "Lithium Intercalation in TiO<sub>2</sub> Modifications," *J. Mater. Chem.*, vol. 7, pp. 2529–2536, 1997.
- [22] G. Armstrong, A. R. Armstrong, J. Canales, P. G. Bruce, "TiO<sub>2</sub>(B) nanotubes as negative electrodes for rechargeable lithium batteries," *Electrochem. Solid-State Lett.*, vol. 9, pp. A139–A143, 2006.
- [23] A. R. Armstrong, G. Armstrong, J. Canales and P. G. Bruce, "Lithium-ion intercalation into TiO<sub>2</sub>(B) nanowires," *Adv. Mater.*, vol. 17, pp. 862–865, 2005.
- [24] R. Marchiand, L. Brohan, M. Tournoux, "TiO<sub>2</sub>(B) a new form of titanium dioxide and the potassium octatitanate K<sub>2</sub>Ti<sub>8</sub>O<sub>17</sub>," *Mater. Res. Bull.*, vol. 15, pp. 1129–1133, 1980.
- [25] M. Tournoux, R. Marchand, L. Brohan, "Layered K<sub>2</sub>Ti<sub>4</sub>O<sub>9</sub> and the open metastable TiO<sub>2</sub>(B) structure," *Prog. Solid State Chem.*, vol. 17, pp. 33–52, 1986.
- [26] D. J. Yang, H. W. Liu, Z. F. Zheng, Y. Yuan, J. C. Zhao, E. R. Waclawik, X. B. Ke, H. Y. Zhu, "An efficient photocatalyst structure: TiO<sub>2</sub>(B) nanofibers with a shell of anatase nanocrystals," *J. Am. Chem. Soc.*, vol. 131, pp. 17885–17893, 2009.
- [27] M. Wagemaker, R. Krol, A. P. M. Kentgens, A. A. Well, F. M. Mulder, "Two phase morphology limits lithium diffusion in TiO<sub>2</sub> (anatase)," *J. Am. Chem. Soc.*, vol. 123, pp. 11454–11461, 2001.

- [28] D. W. Murphy, M. Greenblatt, S. M. Zahurak, R. J. Cava, J. V. Waszczak, G. W. Hull, R. S. Hutton, "Lithium Insertion in Anatase : A new route to the Spinel  $\text{LiTi}_2\text{O}_4$ ," *Rev. Chim. Miner.*, vol. 19, pp. 441–449, 1982.
- [29] G. Sudant, E. Baudrin, D. Larcher, J. M. Tarascon, "Electrochemical lithium reactivity with nanotextured anatase-type  $\text{TiO}_2$ ," *J. Mater. Chem.*, vol. 15, no. 12, pp. 1263–1269, 2005.
- [30] S. J. Bao, Q. L. Bao, C. M. Li, Z. L. Dong, "Novel porous anatase  $\text{TiO}_2$  nanorods and their high lithium electroactivity," *Electrochem. Commun.*, vol. 9, no. 5, pp. 1233–1238, 2007.
- [31] H. G. Yang, H. C. Zeng, "Preparation of Hollow Anatase  $\text{TiO}_2$  Nanospheres via Ostwald Ripening," *J. Phys. Chem. B*, vol. 108, no. 11, pp. 3492–3495, 2004.
- [32] J. Li, Z. Tang, Z. Zhang, "Preparation and Novel Lithium Intercalation Properties of Titanium Oxide Nanotubes," *Electrochem. Solid-State Lett.*, vol. 8, pp. A316–A319, 2005.
- [33] S. H. Kang, J. B. Goodenough, L. K. Rabenberg, "Nanocrystalline Lithium Manganese Oxide Spinel Cathode for Rechargeable Lithium Batteries," *Electrochem. Solid-State Lett.*, vol. 4, no. 5, pp. A49–A51, 2001.
- [34] M. Howe.Grant , *Kirk-Othmer Encyclopedia of Chemical Technology*, M. Howe.Grant, Ed.: John Wiley & Sons Inc, 1997, ch. vol.24, p. 225.
- [35] M. I. Litter, J. A. Navio, "Comparison of the photocatalytic efficiency of  $\text{TiO}_2$ , iron oxides and mixed Ti(IV)-Fe(III) oxides: photodegradation of oligocarboxylic acids," *J. Photochem. Photobiol. A. Chem.*, vol. 84, pp. 183–193, 1994.
- [36] L. Palmisano, V. Augugliaro, A. Sclafani. M. Schiavello, "Activity of chromium-ion-doped titania for the dinitrogen photoreduction to ammonia and for the phenol photodegradation," *J. Phys. Chem.*, vol. 92, pp. 6710–6713, 1988.

- [37] Y. Wang, Y. Hao, H. Cheng, J. Ma, B. Xu, W. Li, S. Cai, "Hybrid polymer/nanocrystalline TiO<sub>2</sub> composites prepared via low-temperature in-matrix crystallization of titania," *J. Mater. Sci.*, vol. 34, pp. 2773–2779, 1999.
- [38] M. K. Akhtar, Y. Xiong, S. E. Pratsinis, "Vapor synthesis of titania powder by titanium tetrachloride oxidation," *AIChE J.*, vol. 37, pp. 1561–1570, 1991.
- [39] W. Li, S. Ismat Shah, C. P. Huang, O. Jung, C. Ni, "Structure and size distribution of TiO<sub>2</sub> nanoparticles deposited on stainless steel mesh," *Mater. Sci. Eng. B*, vol. 96, pp. 247–253, 2002.
- [40] C. -C. Wang, Z. Zhang, and J. Y. Ying, "Photocatalytic decomposition of halogenated organics over nanocrystalline titania," *NanoStructured Mater*, vol. 9, pp. 583–586, 1997.
- [41] N. Daude, C. Gout, and C. Jonanin, "Electronic band structure of titanium dioxide," *Phys. Rev. B*, vol. 15, pp. 3229-3235, 1977.
- [42] J. L. Jourdan, C. Gout, and J. P. Albert, *Solid State Commun.*, vol. 31, p. 1023, 1979.
- [43] J. Jaćimović, R. Gaál C. Vaju, A. Magrez, H. Berger, and L. Forró, "High-Pressure Study of Anatase TiO<sub>2</sub>," *Materials*, vol. 3, pp. 1509-1514, 2010.
- [44] S.-D. Huang, Y.-H. Fang, Z.-P. Liu S. Ma, "Microporous Titania Crystals with Penta-oxygen Coordination," *ACS Appl. Energy Mater*, vol. 1, p. 22–26, 2018.
- [45] F. Caruso, "Nanoengineering of particle surfaces," *Adv. Mater*, vol. 13, pp. 11–22, 2001.
- [46] W. Scharl, "Current Directions in Core-Shell Nanoparticle Design," *Adv. Mater*, vol. 12, pp. 1899–1908, 2000.
- [47] N. S. Sobal, U. Ebels, H. Mohwald, M. Giersig, "Synthesis of Core-Shell PtCo Nanocrystals," *J. Phys. Chem. B*, vol. 107, pp. 7351–7354, 2003.

- [48] T. Sun, B. Mayers, Y. Xia, "Metal nanostructures with hollow interiors," *Adv. Mater.*, vol. 15, pp. 641–646, 2003.
- [49] C. G. Goltner, "Investigation of the core-shell surface in gold@ silica nanoparticles: A silica imprinting method," *Angew. Chem. Int. Ed.*, vol. 38, pp. 3155–3160, 1999.
- [50] T. Nakashima, N. Kimuzuka, "Interfacial synthesis of hollow TiO<sub>2</sub> microspheres in ionic liquids," *J. Am. Chem. Soc.*, vol. 125, pp. 6386–6387, 2003.
- [51] H. G. Yang, H. C. Zeng, "Preparation of hollow anatase TiO<sub>2</sub> nanospheres via Ostwald ripening," *J. Phys. Chem. B*, vol. 108, pp. 3492–3495, 2004.
- [52] W. Kohn P. Hohenberg, "Inhomogeneous electron gas," *Phys. Rev. B*, vol. 136, pp. 864–871, 1964.
- [53] L. J. Sham W. Kohn, "Stimulated Emission of Radiation in a Single Mode," *Phys. Rev.*, vol. 140, pp. A1051–A1056, 1965.
- [54] J. C. Slater and G. F. Koster, "Simplified LCAO Method for the Periodic Potential Problem," *Phys. Rev.*, vol. 94, pp. 1498–1524, 1954.
- [55] D. Porezag, Th. Frauenheim, Th. Kohler, G. Seifert, R. Kaschner, "Construction of tight-binding-like potentials on the basis of density-functional theory: Application to carbon," *Phys. Rev. B*, vol. 51, pp. 12947–12957, 1995.
- [56] M. Elstner, D. Porezag, G. Jungnickel, J. Elsner, M. Haugk, Th. Frauenheim, S. Suhai, G. Seifert, "Self-consistent-charge density-functional tight-binding method for simulations of complex materials properties," *Phys. Rev. B*, vol. 58, pp. 7260–7268, 1998.
- [57] P. Hohenberg, W. Kohn, "Inhomogeneous electron gas," *Phys. Rev. B*, vol. 136, pp. 864–871, 1964.
- [58] W. Kohn, L. J. Sham, "Stimulated Emission of Radiation in a Single Mode," *Phys. Rev.*, vol. 140, pp. A1051–A1056, 1965.

- [59] J. C. Slater, G. F. Koster, "Simplified LCAO Method for the Periodic Potential Problem," *Phys. Rev.*, vol. 94, pp. 1498–1524, 1954.
- [60] C. M. Goringe, D. R. Bowler, E. Hernández, "Tight-binding modelling of materials," *Rep. Prog. Phys.*, vol. 60, pp. 1447–1512, 1997.
- [61] S. Froyen, Walter A. Harrison, "Elementary prediction of linear combination of atomic orbitals matrix elements," *Phys. Rev. B*, vol. 20, pp. 2420–2422, 1979.
- [62] D. J. Chadi, "Atomic and Electronic Structures of Reconstructed Si(100) Surfaces," *Phys. Rev. Lett.*, vol. 43, pp. 43–47, 1979.
- [63] M. C. Payne, M. P. Teter, D. C. Allan, T. A. Arias, J. D. Joannopoulos, "Iterative Minimization Techniques for ab initio Total-Energy Calculations: Molecular Dynamic and Conjugate Gradients," *Rev. Mod. Phys.*, vol. 64, pp. 1045–1097, 1992.
- [64] W. Matthew, C. Foulkes, "Tight-binding models and density-functional theory," *Phys. Rev. B*, vol. 39, pp. 12520–12536, 1989.
- [65] Th. Frauenheim, M. Seifert, M. Elsterner, Z. Hajnal, G. Jungnickel, D. Porezag, S. Suhai, R. Scholz, "A self-consistent charge density-functional based tight-binding method for predictive materials simulations in physics, chemistry, and biology," *Phys. Stat. Sol. B*, vol. 217, pp. 41–62, 2000.
- [66] R. S. Mulliken, "Electronic Population Analysis on LCAO-MO Molecular Wave Functions," *J. Chem. Phys.*, vol. 23, pp. 1833–1840, 1955.
- [67] R. G. Parr, R. G. Pearson, "Absolute hardness: companion parameter to absolute electronegativity," *J. Am. Chem. Soc.*, vol. 105, pp. 7512–7516, 1983.
- [68] J. F. Janak, "Proof that  $\partial E/\partial n_i = \epsilon$  in density-functional theory," *Phys. Rev. B*, vol. 18, pp. 7165–7168, 1978.

- [69] T. Mineva, T. Heine, "Orbital hardness tensors from hydrogen through xenon from Kohn–Sham perturbed orbitals," *Int. J. Quantum Chem.*, vol. 106, pp. 1396–1405, 2006.
- [70] G. Seifert, D. Porezag, Th. Frauenheim, "Calculations of molecules, clusters, and solids with a simplified LCAO-DFT-LDA scheme," *Int. J. Quantum Chem.*, vol. 58, pp. 185–192, 1996.
- [71] T. Heine, H. F. Dos Santos, S. Patchkovskii, H. A. Duarte, "Structure and Dynamics of  $\beta$ -Cyclodextrin in Aqueous Solution at the Density-Functional Tight Binding Level," *J. Phys. Chem. A*, vol. 111, pp. 5648–5654, 2007.
- [72] H. Hu, Z. Lu, M. Elstner, J. Hermans, W. Yang, "Simulating water with the self-consistent-charge density functional tight binding method: from molecular clusters to the liquid state," *J. Phys. Chem. A*, vol. 111, pp. 5685–5691, 2007.
- [73] J. Frenzel, A. F. Oliveira, H. A. Duarte, T. Heine, G. Seifert, "Structural and Electronic Properties of Bulk Gibbsite and Gibbsite Surfaces," *Anorg. Allg. Chem.*, vol. 631, pp. 1267–1271, 2005.
- [74] J. Frenzel, J. O. Joswig, G. Seifert, "Optical Excitations in Cadmium Sulfide Nanoparticles," *J. Phys. Chem. C*, vol. 111, pp. 10761–10770, 2007.
- [75] A. Kuc, A. Enyashin, G. Seifert, "Metal–Organic Frameworks: Structural, Energetic, Electronic, and Mechanical Properties," *J. Phys. Chem. B*, vol. 111, pp. 8179–8186, 2007.
- [76] R. Luschtinetz, A. F. Oliveira, J. Frenzel, J. O. Joswig, G. Seifert, H. A. Duarte, "Adsorption of phosphonic and ethylphosphonic acid on aluminum oxide surfaces," *Surf. Sci.*, vol. 602, pp. 1347–1359, 2008.
- [77] P. Muller, "GLOSSARY OF TERMS USED IN PHYSICAL ORGANIC CHEMISTRY," *Pure Appl. Chem.*, vol. 66, pp. 1077–1184, 1994.

- [78] M. Elstner, P. Hobza, T. Frauenheim, S. Suhai, E. Kaxiras, "Hydrogen bonding and stacking interactions of nucleic acid base pairs: A density-functional-theory based treatment," *J. Chem. Phys.*, vol. 114, pp. 5149–5155, 2001.
- [79] L. Zhechkov, T. Heine, S. Patchkovskii, G. Seifert, H. A. Duarte, "An Efficient a Posteriori Treatment for Dispersion Interaction in Density-Functional-Based Tight Binding," *J. Chem. Theory Comput.*, vol. 1, pp. 841–847, 2005.
- [80] A. M. Koester, R. Flores, G. Geudtner, A. Goursot, T. Heine, S. Patchkovskii, J. U. Reveles, A. Vela, D. R. Salahub, *deMon VS. 1.1*. Ottawa, Canada: NRC, 2004.
- [81] A. K. Rappe, C. J. Casewit, K. S. Colwell, W. A. Goddard, W. M. Skiff, "UFF, a full periodic table force field for molecular mechanics and molecular dynamics simulations," *J. Am. Chem. Soc.*, vol. 114, pp. 10024–10035, 1992.
- [82] N. W. Ashcroft, N. D. Mermin, Philadelphia: Saunders College Publishing, 1976.
- [83] J.S. Blakemore, *Solid State Physics*, 2nd ed.: Cambridge University Press, 1985.
- [84] J. C. Phillips, L. Kleinman, "New Method for Calculating Wave Functions in Crystal and Molecules," *Phys. Rev.*, vol. 116, pp. 287–294, 1959.
- [85] M. L. Cohen, V. Heine, "The Fitting of Pseudopotentials to Experiment Data and their Subsequent Application," *Sol. State Phys.*, vol. 24, pp. 37–248, 1970.
- [86] W. E. Pickett, "Pseudopotential Methods in Condensed Matter Applications," *Comp. Phys. Rep.*, vol. 9, pp. 115–197, 1989.
- [87] <http://www.sciencedaily.com>, "Science Daily," Mar. 16, 2008.
- [88] Z. Zhou, B. Joos, "Stability Criteria for Homogeneously Stressed Materials and the Calculation of Elastic Constants," *Phys. Rev. B*, vol. 54, pp. 3841–3850, 1996.

- [89] B. B. Karki, G. J. Ackland, J. Crain, "Elastic Instability in Crystal from ab initio Stress-Strain Relations," *J. Phys. Conden. Matt.*, vol. 9, pp. 8579–8586, 1997.
- [90] J. Wang, J. Li, S. Yip, S. R. Phillpot, D. Wolf, "Mechanical Instabilities of Homogeneous Crystals," *Phys. Rev. B*, vol. 52, pp. 621–627, 1995.
- [91] F. Milstein H. G. Hopkins, M. J. Sewell, "Mechanics of Solids ed (Oxford: Pergamon)," pp. 417–452, 1982.
- [92] T. H. K. Barron, M. L. Klein, "Second-Order Elastic Constants of a Solid under Stress," *Proc. Phys. Soc.*, vol. 85, pp. 523–532, 1965.
- [93] C. Kittel, *Introduction to Solid State Physics*, 5th ed. New York: John Wiley & Sons, 1976.
- [94] M. L. Cohen, "Calculation of Bulk Moduli of Diamond and Zinc-Blende Solids," *Phys. Rev. B*, vol. 32, pp. 7988–7991, 1985.
- [95] S. F. Pugh, "Relations Between Elastic Moduli and Plastic Properties of Polycrystalline Pure Metals," *Philos. Mag.*, vol. 45, pp. 823–843, 1954.
- [96] J. P. Perdew, Y. Wang, "Accurate and Simple Analytic Representation of the Electron Gas Correlation Energy," *Phys. Rev. B*, vol. 45, pp. 13244–13249, 1992.
- [97] H. Olijnyk, A. P. Jephcoat, "The  $E_{2g}$  Phonon and the Elastic Constant  $C_{44}$  in Hexagonal Van Der Waals Bonded Solids," *J. Phys. Conden. Matt.*, vol. 12, pp. 10423–10437, 2000.
- [98] S. Goumri-Said, M. B. Kanou, "Theoretical Investigations of Structural, Elastic, Electronic and Thermal Properties of Damiaoite  $PtIn_2$ ," *Comp. Mat. Sci.*, vol. 43, pp. 1056–1065, 2008.
- [99] Y. Qiao, H. Zhang, C. Hong, X. Zhang, "Phase Stability, Electronic Structure and Mechanical Properties of Molybdenum Disilicide: A First-Principles Investigation," *Phys. D: Appl. Phys.*, vol. 42, pp. 105407–105413, 2009.



- [100] S. O. Kasap, P. Capper, C. Koughia, "Handbook of Electronic and Photonic Materials," pp. 758–805, 2006.
- [101] S. K. R. Patil, S. V. Khare, B. R. Tuttle, J. K. Bording, S. Kodambaka, "Investigation of Mechanical Stability of Possible Structure of PtN Using First-Principles Computations," *Phys. Rev. B*, vol. 73, pp. 104110–104118, 2006.
- [102] P. Ravindran, I. Fast, P. A. Korzhavyi, B. Johansson, J. Wills, O. Eriksson, "Density Functional Theory for Calculation of Elastic Properties of Orthorhombic Crystals: Application to TiSi<sub>2</sub>," *J. App. Phys.*, vol. 84, pp. 4891–4904, 1998.
- [103] H.S Chen, *Anisotropy of Elasticity about Metal*. Beijing: Metallurgy Industry Press, 1996.
- [104] B. Mayer, H. Anton, E. Bott, M. Methfessel, J. Sticht, P. C. Schmidt, "Ab-Initio Calculation of the Elastic Constants and Thermal Expansion Coefficients of Laves Phases," *Interm.*, vol. 11, pp. 23–30, 2003.
- [105] K. Burke, J. P. Perdew, M. Levy, *In Modern Density Functional Theory: A Tool for Chemistry*, P. Politzer J. M. Seminario, Ed. Amsterdam: Eds. Elsevier, 1995.
- [106] D. C. Langreth, J. P. Perdew, "The Exchange Correlation Energy of a Metallic Surface," *Sol. State Comm.*, vol. 17, pp. 1425–1429, 1975.
- [107] S. Iijima, "Helical microtubules of graphitic carbon," *Nature*, vol. 56–58, p. 354, 1991.
- [108] C. M. Lieber, "One-dimensional nanostructures: chemistry, physics & applications," *Solid State Commun.*, vol. 107, pp. 607–616, 1998.
- [109] C. N. R. Rao, A. Muller, and A. K. Cheetham, *The Chemistry of Nanomaterials: Synthesis, Properties and Applications*. Weinheim, Germany: Wiley-VCH, 2006.
- [110] MedeA, "v2.8, Materials Design, Inc.," Angel Fire NM USA, 2012.
- [111] G. A. Seifert, "Tight-Binding Density Functional Theory: An Approximate Kohn–Sham DFT Scheme," *J. Phys. Chem.*, vol. 111, pp. 5609–5613, 2007.

- [112] C. Kohler, G. Seifert, T. Frauenheim, "Density-Functional based calculations for Fe( $n$ ), ( $n \leq 32$ )," *Chem. Phys.*, vol. 309, pp. 23–31, 2005.
- [113] T. Niehaus, "Approximate time-dependent density functional theory," *THEOCHEM*, vol. 914, pp. 38–49, 2009.
- [114] T. Niehaus, M. Rohlfing, F. D. Sala, A. D. Carlo, T. Frauenheim, "Quasiparticle energies for large molecules: A tight-binding-based Green's-function approach," *Phys. Rev. A*, vol. 71, pp. 022488–022508, 2005.
- [115] A. Pecchia, A. D. Carlo, "Incoherent electron-phonon scattering in octanethiols," *Rep. Prog. Phys.*, vol. 67, pp. 1497–1561, 2004.
- [116] J. M. Knaup, B. Hourahine, T. Frauenheim, "Initial Steps toward Automating the Fitting of DFTB  $E_{\text{rep}}(r)$ ," *J. Phys. Chem. A*, vol. 111, pp. 5637–5641, 2007.
- [117] M. Gaus, C. P. Chou, H. Witek, M. Elstner, "Automatized Parametrization of SCC-DFTB Repulsive Potentials: Application to Hydrocarbons," *J. Phys. Chem. A*, vol. 113, pp. 11866–11881, 2009.
- [118] M. D. Segall, P. L. D. Lindan, M. J. Probert, C. J. Pickard, P. J. Hasnip, S. J. Clark, M. C. Payne, "First-principles simulation: ideas, illustrations and the CASTEP code," *J. Phys. Condens. Matter*, vol. 14, pp. 2717–2744, 2002.
- [119] D. Vanderbilt, "Soft self-consistent pseudopotentials in a generalized eigenvalue formalism," *Phys. Rev. B*, vol. 41, pp. 7892–7895, 1990.
- [120] J. S. Lin, A. Qteish, M. C. Payne, V. Heine, "Optimized and transferable non-local separable *ab initio* pseudopotentials," *Phys. Rev. B*, vol. 47, pp. 4174–4180, 1993.
- [121] J. P. Perdew, Y. Wang, "Accurate and Simple Analytic Representation of the Electron Gas Correlation Energy," *Phys. Rev. B*, vol. 45, pp. 13244–13249, 1992.

- [122] P. Perdew, K. Burke, M. Ernzerhof, "PBE Generalized Gradient Approximation," *Phys. Rev. Lett.*, vol. 77, pp. 3865--3868, 1996.
- [123] H. J. Monkhorst, J. D. Pack, "The Monkhorst and Pack grids," *Phys. Rev. B*, vol. 13, pp. 5188–5191, 1976.
- [124] M. V. Dozzi, G. L. Chiarello, A. Di Paola, L. Palmisano, E. Selli M. Altomare, *Catal. Today*, vol. 252, pp. 184–189, 2015.
- [125] M. Akaogi M. Matsui, "Molecular dynamics simulation of the structural and physical properties of the four polymorphs of TiO<sub>2</sub>," *Molecular Simulation*, vol. 6, pp. 239-244, 1991.
- [126] J. K. Burdett, T. Hughbanks, G. J. Miller, J. W. Richardson, J. V. Smith, "Structural-electronic relationships in inorganic solids: Powder neutron diffraction studies of the rutile and anatase polymorphs of titanium dioxide at 15K and 295K," *J. Am. Chem. Soc.*, vol. 109, pp. 3639–3646, 1987.
- [127] R. Wyckoff, *Crystal Structures*, 2nd ed. New York: Interscience, 1964.
- [128] K. Yong M. Choi, "A facile strategy to fabricate high-quality single crystalline brookite TiO<sub>2</sub> nanoarrays and their photoelectrochemical properties," *Nanoscale*, vol. 6, pp. 13900–13909, 2014.
- [129] M. F. M. Taib, O. H. Hassan, M. Z. A. Yahya, A. M. M. Ali M. H. Samat, "Structural, electronic and optical properties of brookite phase titanium dioxide," *Mater. Res. Express*, vol. 4, pp. 2053-1591, 2017.
- [130] W. Y. Ching S. D. Mo, "Electronic and optical properties of three phases of titanium dioxide: Rutile, anatase, and brookite," *Phys. Rev. B*, vol. 51, pp. 13023–13032, 1995.
- [131] S. F. Pugh, "XCII. Relation between elastic moduli and the plastic properties of polycrystalline pure metals," *Philos Mag*, vol. 45, pp. 823-843, 1954.

- [132] E. Shojaee and M. R. Mohammadzadeh, "First principles elastic and thermal properties of TiO<sub>2</sub> :a phonon approach," *J. Phys.: Condens. Matter*, vol. 22, pp. 1-8, 2010.
- [133] "First principles computations of second-order elastic Constants (SOEC) and equations of state of rutile TiO<sub>2</sub>," *Physics Research International*, vol. 2011, pp. 1-7, 2011.
- [134] G. Steinle-Neumann, J. Meinhardt M. Iuga, "Ab-initio simulation of elastic constants for some ceramic materials," *Eur. Phys. J. B*, vol. 58, pp. 127–133, 2007.
- [135] K. Huang M. Born, *Dynamical Theory and Experimental I*. Berlin: Springer-Verlag, 1982.
- [136] Y. Ding and B. Xiao, "Anisotropic elasticity, sound velocity and thermal conductivity of TiO<sub>2</sub> polymorphs from first principles calculations.," *Computational Materials Science*, vol. 82, pp. 202–218, 2014.
- [137] J. -X. Yu, Y. -J. Wang, X. Chen, F. -Q. Jing J. Zhu, "First-principles calculations for elastic properties of rutile TiO<sub>2</sub> under pressure," *Chin. Phys. Soc.*, vol. 17, pp. 2216–2221, 2008.
- [138] D. Reyes-Coronado, G. Rodriguez-Gattorno, M. E. Espinosa-Pesqueira, C. Cab, R. d. Coss, G. Oskam, "Phase-pure TiO<sub>2</sub> nanoparticles: anatase, brookite and rutile," *Nanotechnology*, vol. 19, pp. 145605–145615, 2008.
- [139] M. Mohamad , B. Ul Haq, R.Ahmed, A. Shaari, N. Ali, R. Hussain, "Characterization of rutile, anatase and brookite polymorphs," *Materials Sciencein Semiconductor Processing*, vol. 31, pp. 405–414, 2015.
- [140] M. S. Hybertsen W. Kang, "Quasiparticle and Optical Properties of Rutile and Anatase TiO<sub>2</sub>," *Phys. Rev. B*, vol. 82, p. 085203/1–085203/ 11, 2010.
- [141] T. Zhu, S. -P. Gao, "The Stability, Electronic Structure, and Optical Property of TiO<sub>2</sub> Polymorphs," *J. Phys. Chem. C*, vol. 118, pp. 11385–11396, 2014.

- [142] M. Wagemaker, U. Lafont, E. M. Kelder, F. M. Mulder W. J. H. Borghols, "Impact of nanosizing on lithiated rutile TiO<sub>2</sub>," *Chem. Mater.*, vol. 20, pp. 2949-2955, 2008.
- [143] A. Stashans, S. Lunell, R. Bergström, A. Hagfeldt, and S.-E. Lindquist, "Theoretical study of lithium intercalation in rutile and anatase," *Phys. Rev. B: Condens. Matter Mater. Phys.*, vol. 53, p. 159–170, 1996.
- [144] C. L. Olson, J. Nelson, and M. S. Islam, "Defect Chemistry, Surface Structures, and Lithium Insertion in Anatase TiO<sub>2</sub>," *J. Phys. Chem. B*, vol. 110, p. 9995–10001, 2006.
- [145] G.-N. Zhu, Y.-G. Wang, and Y.-Y. Xia, "Ti-based compounds as anode materials for Li-ion batteries," *Energy Environ. Sci.*, vol. 5, p. 6652–6667, 2012.
- [146] Y. S. Hu, L. Kienle, Y. G. Guo, and J. Maier, "High lithium electroactivity of nanometer-sized rutile TiO<sub>2</sub>," *Adv. Mater.*, vol. 18, pp. 1421–1426, 2006.
- [147] F. Gligor and S. W. de Leeuw, "Lithium diffusion in rutile structured titania," *Solid State Ionics*, vol. 177, pp. 2741–2746, 2006.
- [148] M. V. Koudriachova, N. M. Harrison, and S. W. de Leeuw, "Density functional simulations of lithium intercalation in rutile," *Phys. Rev. B: Condens. Matter Mater. Phys.*, vol. 65, pp. 235423–235435, 2002.
- [149] D. Choi, S. Kerisit, K. M. Rosso, D. Wang, J. Zhang, G. Graff, J. Liu Z. Yang, "Nanostructures and lithium electrochemical reactivity of lithium titanites and titanium oxides: A review," *Journal of Power Sources*, vol. 192, pp. 588-598, 2009.
- [150] X. Yang et al., "Oriented Nanocrystal Arrays of Selectable Polymorphs by Chemical Sculpture," *Chem. Mater.*, vol. 21, pp. 3197–3201, 2009.
- [151] Mohamed Kamal Hassan Ali Matar,.: University College London, 2011, p. 192.
- [152] Th. Frauenheim, M. Seifert, M. Elsterner, Z. Hajnal, G. Jungnickel, D. Porezag, S. Suhai, R. Scholz , "A self-consistent charge density-functional based tight-

binding method for predictive materials simulations in physics, chemistry, and biology," *Phys. Stat. Sol. B*, vol. 217, no. 1, pp. 41–62, 2000.

- [153] DFTB. [Online]. [HTTP://www.dftb.org/parameters/download](http://www.dftb.org/parameters/download)
- [154] K. V. K. Rao, S. V. N. Naidu, L. Iyengar, "Thermal expansion of rutile and anatase," *J. Am. Ceram. Soc.*, vol. 53, pp. 124–126, 1970.
- [155] J. Gale, L. Dubrovinsky V. Swamy, "Atomistic simulation of the crystal structures and bulk moduli of TiO<sub>2</sub> polymorphs," *J. Phys. Chem. Solids*, vol. 62, pp. 887-895, 2001.
- [156] M. Landmann, E. Rauls, and W. G. Schmidt, "The electronic structure and optical response of rutile, anatase and brookite TiO<sub>2</sub>," *J. Phys.: Condens. Matter.*, vol. 24, pp. 195503-195508, 2012.
- [157] D. O. Scanlon et al., "Band alignment of rutile and anatase TiO<sub>2</sub>," *Nat. Mater.*, vol. 12, pp. 798-801, 2013.
- [158] H. Malik, R. Batool, R. Perveen, F. Saleemi, H. Rasheed, M. A. Saeed, C. Sao, M. Rizwan T. Mahmood, "Elastic, electronic and optical properties of anatase TiO<sub>2</sub> under pressure: A DFT approach," *Chin. J. Phys.*, vol. 55, pp. 1252–1263, 2017.
- [159] M. Mancini et al., "Mesoporous anatase TiO<sub>2</sub> composite electrodes: electrochemical characterization and high rate performances," *Journal of Power Sources*, vol. 189, pp. 585-589, 2009.
- [160] E. Paillard, E. Binetti, S. Krueger, M. Striccoli, M. Winter, S. Passerini D. Bresser, "Percolating networks of TiO<sub>2</sub> nanorods and carbon for highof TiO<sub>2</sub> nanorods and carbon for high powder lithium insertion electrodes," *Journal of Power Sources*, vol. 206, pp. 301-309.
- [161] J. Y. Shin, D. Samuelis, and J Maier, "Sustained lithium-storage performance of hierarchical, nanoporous anatase TiO<sub>2</sub> at high rates: emphasis on interfacial

- storage phenomena," *Advanced Functional Materials*, vol. 21, pp. 3464-3472, 2011.
- [162] L. Kavana, I. Exnarb, M. Grätzela S. Y. Huang, "Rocking Chair Lithium Battery Based on Nanocrystalline TiO<sub>2</sub> (Anatase)," *J. Electrochem. Soc.*, vol. 142, p. L142, 1995.
- [163] M. Wagemaker, G. J. Kearley, Ad A. van Well, H. Mutka, and F. M. Mulder, "Multiple Li Positions inside Oxygen Octahedra in Lithiated TiO<sub>2</sub> Anatase," *J. AM. CHEM. SOC.*, vol. 125, pp. 840-848, 2003.
- [164] T. Iwasaki, Y. Onodera, H. Hayashi, T. Nagasi, A. Chatterjee, K. Chiba T. Ebina, "Ab initio study on the topological Li insertion in titanium oxide," *Journal of Power Sources*, vol. 81–82, pp. 393–396, 1999.
- [165] J. S. Chen et al., "Constructing hierarchical spheres from large ultrathin anatase TiO<sub>2</sub> nanosheets with nearly 100% exposed (001) facets for fast reversible lithium storage," *J. Am. Chem. Soc.*, vol. 132, p. 6124–6130, 2010.
- [166] C. H. Jiang and J. S. Zhang, "Nanoengineering Titania for High Rate Lithium Storage: A Review," *J. Mater. Sci. Technol.*, vol. 29, p. 97–122, 2013.
- [167] R. Zazpe, M. Krbal, H. Sopha, J. Prikry, S. Ng, L. Hromadko, F. Bures, J. M. Macak F. Dvorak, "One-dimensional anodic TiO<sub>2</sub> nanotubes coated by atomic layer deposition: Towards advanced applications," *Applied Materials Today*, vol. 14, pp. 1–20, 2019.
- [168] I. Hanzu, T. Djenizian, P. Lavela, J. L. Tirado, P. Knauth G. F. Ortiz, "Alternative Li-ion battery electrode based on self-organized titania nanotubes," *Chem.Mater.*, vol. 21, pp. 63–67, 2009.
- [169] N.A. Kyeremateng, "Self-organised TiO<sub>2</sub> nanotubes for 2D or 3D Li-ion microbatteries," *ChemElectroChem*, vol. 1, pp. 1442–1466, 2014.
- [170] T. Sekino, "Direct diameter-controlled growth of multiwall," *Bull. Ceram. Soc. Jpn*, vol. 41, pp. 261–271, 2006.

- [171] Y. Wang, N. Herron, "Nanometer-sized semiconductor clusters: materials synthesis, quantum size effects, and photophysical properties," *J. Phys. Chem.*, vol. 95, pp. 525–532, 1991.
- [172] R. Asahi, T. Morikawa, T. Ohwaki, K. Aoki, Y. Taga, "Visible-light photocatalysis in nitrogen-doped titanium oxides," *Science*, vol. 293, pp. 269–271, 2001.
- [173] Y. F. Yuan, F. Chen, M. Zhu, G. C. Cai, S. M. Yin, J. L. Yang, S. Y. Guo, Y. Wu, "TiO<sub>2</sub> nanocrystalline-assembled mesoporous nanosphere as high-performance anode for lithium-ion batteries," *Mater Lett.*, vol. 240, pp. 96-99, 2018.
- [174] F. Mika, J. M. Benjamin, J. B. Olaf, W. C. Karena, P. Valérie, M. Antoine, I. L. Oleg, M. Jiwei, G. Henri, K. Shinichi, D. Damien, L. Wei, "A Reversible Phase Transition for Sodium Insertion in Anatase TiO<sub>2</sub>," *Chem. Mater.*, vol. 29, p. 1836–1844, 2017.
- [175] S. J. Clarke, A. J. Fowkes, A. Harrison, R. M. Ibberson, and M. J. Rosseinsky, "Synthesis, Structure, and Magnetic Properties of NaTiO<sub>2</sub>," *Chem. Mater.*, vol. 10, p. 372–384, 1998.
- [176] W. J. H. Borghols et al., "The Electronic Structure and Ionic Diffusion of Nanoscale LiTiO<sub>2</sub> Anatase," *Chem. Phys.*, vol. 11, p. 5742–5748, 2009.
- [177] R. P. Antony, T. Mathews, A. Dasgupta, S. Dash, A.K. Tyagi, B. Raj, "Rapid breakdown anodization technique for the synthesis of high aspect ratio and high surface area anatase TiO<sub>2</sub>," *J. Sol. State Chem.*, vol. 184, pp. 624–632, 2011.
- [178] "Particle size dependence of the lithium storage capability and high rate performance of nanocrystalline anatase TiO<sub>2</sub> electrode," *J. Power Sources*, vol. 166, pp. 239-243, 2007.
- [179] D. Choi, S. Kerisit, K. M. Rosso, D. Wang, J. Zhang, G. Graff, and J. Liu Z. Yang, "Nanostructures and lithium electrochemical reactivity of lithium titanates and titanium oxides," *J. Power Sources*, vol. 192, pp. 588-598, 2009.



- [180] E. Miele, F. De Angelis, E. Di Fabrizio, R. P. Zaccaria, C. Capiglia S. Goriparti, "Review on recent progress of nanostructured anode materials for Li-ion batteries," *Journal of Power Sources*, vol. 257, pp. 421–443, 2014.
- [181] F. Fang, Y. Zhao et al. L. Bai, "A sandwich structure of mesoporous anatase TiO<sub>2</sub> sheets and reduced graphene oxide and its application as lithium-ion battery electrodes," *RSC Advances*, vol. 4, pp. 43039–43046, 2014.
- [182] A. Voigt, R. Weber, M. Morbé P. Puhlfürß, "Microporous TiO<sub>2</sub> membranes with a cut off < 500 Da," *J. Membr. Sci.*, vol. 174, p. 123–133, 2000.
- [183] J. E. ten Elshof, D. H. A. Blank J Sekulić, "A microporous titania membrane for nano-filtration and pervaporation," *Adv. Mater.*, vol. 16, p. 1546–1550, 2004.
- [184] M. A. Anderson Q. Xu, "Sol-gel route to synthesis of microporous ceramic membranes: preparation and characterization of microporous TiO<sub>2</sub> and ZrO<sub>2</sub> xerogels," *J. Am. Ceram. Soc.*, vol. 77, p. 1939–1945, 1994.
- [185] R. Hill, "The Elastic Behaviour of a Crystalline Aggregate," *Proc. Phys. Soc.*, vol. A 65, pp. 349-354, 1952.
- [186] J. -M. Tarascon, M. Armand, "Issues and challenges facing rechargeable lithium batteries," *Nature*, vol. 414, pp. 359-367, 2001.
- [187] L. L. Shaw M. Sawicki, "Advances and challenges of sodium ion batteries as post lithium ion batteries," *RSC Adv.*, vol. 5, pp. 53129–53154, 2015.
- [188] S.-T. Myung, Y.-K. Sun J.-Y. Hwang, "Sodium-ion batteries: present and future," *Chem. Soc. Rev.*, vol. 46, pp. 3529–3614, 2017.
- [189] C.-J. Yu, K.-C. Ri, J.-S. Kim, U.-G. Jong, Y.-H. Kyeab, S.-N. Honga S.-H. Choe, "First-principles study of Na<sub>x</sub>TiO<sub>2</sub> with trigonal bipyramid structures: an insight into sodium-ion battery anode applications," *Phys.Chem.Chem.Phys.*, vol. 21, pp. 8408--8417, 2019.

- [190] K. Zhu, Q. Wang, J. Kim, A. A. Pesaran, A. J. Frank, "Pseudocapacitive Lithium-Ion Storage in Oriented Anatase TiO<sub>2</sub> Nanotube Arrays," *J. Phys. Chem. C*, vol. 116, p. 11895–11899, 2012.
- [191] B. L. Trout, B. R. Brooks J. -W. Chu, "A super-linear minimization scheme for the nudged elastic band method," *J. Chem. Phys.*, vol. 119, pp. 12708–12717, 2003.
- [192] K. S. Colwell, C.J. Casewit A. K. Rappe, "Application of a Universal force field to metal complexes," *Inorg Chem.*, vol. 32, pp. 3438–3450, 1993.
- [193] C. H. Sun, X. H. Yang, J. S. Chen, Z. Li, X. W. Lou, C. Li, S. C. Smith, G. Q. Lu, H. G. Yang, "Higher charge/discharge rates of lithium-ions across engineered TiO<sub>2</sub> surfaces leads to enhance battery performance.," *Chem. Commun.*, vol. 46, pp. 6129–6131, 2010.
- [194] J. S. Olsen L. Gerward, *J. Appl. Crystallogr.*, vol. 30, p. 259, 1997.
- [195] J. Li, S. Yip, S. R. Phillpot, D. Wolf J. Wang, "Mechanical Instabilities of Homogeneous Crystals," *Phys. Rev. B*, vol. 52, pp. 12627–12635., 1995.
- [196] S.-P. Gao T. Zhu, "The stability, electronic structure, and optical properties of TiO<sub>2</sub> polymorphs," *J. Phys. Chem. C*, vol. 118, pp. 11385–11396, 2014.
- [197] J. Park Y. Yoon, "The effects of nanostructures on the mechanical and tribological properties of TiO<sub>2</sub> nanotubes," *Nanotechnology*, vol. 29, pp. 165705-165710, 2018.
- [198] B. Zachau-Christianse, K. West, T. Jacobsen, and S. Atlung, "Lithium insertion in different TiO<sub>2</sub> modifications," *Solid State Ionics*, vol. 28-30, pp. 1176-1182, 1988.
- [199] K. Yoshizawa, and T. Yamabe G. Nusp, "Lithium intercalation in TiO<sub>2</sub> modifications," *J. Mater. Chem.*, vol. 7, pp. 2529-2536, 1997.

- [200] A. N. Enyashin, A. A. Rempel I. S. Popov, "Size dependent content of structural vacancies within TiO nanoparticles: Quantum-chemical DFTB study," *Superlattices and Microstructures*, vol. 113, pp. 459-465, 2018.
- [201] M. Grimsditch, E. S. Zoubolis, and A. Polian, "Elastic constants of Boron Nitride," *J. Appl. Phys.*, vol. 76, pp. 832-834, 1994.
- [202] S. Yip M. Tang, "Lattice Instability in  $\beta$ -SiC and Simulation of Brittle Fracture," *J. App. Phys*, vol. 76, pp. 2719–2725, 1994.
- [203] V. W. H. Baur, "Atomabstände und Bindungswinkel im Brookit, TiO<sub>2</sub>," *Acta Cryst.*, pp. 214–216, 1961.
- [204] D. Y. Kim, J. S. D. Almeida, M. Mattesini, M. M. E. Isaev, R. Ahuja L. Kóci, "Mechanical stability of TiO<sub>2</sub> polymorphs under pressure: ab initio calculations," *J. Phys.: Condens. Matter*, vol. 20, pp. 345218-345225, 2008.
- [205] T. Zhu, S. -P. Gao, "The Stability, Electronic Structure, and Optical Property of TiO<sub>2</sub> Polymorphs," *J. Phys. Chem. C*, vol. 118, pp. 11385–11396, 2014.

# Appendix A

## Steepest Descent Minimization Method

Steepest descent (SD) is one of the oldest and simplest methods. It is actually more important as a theoretical, rather than practical, reference by which to test other methods. However, 'steepest descent' steps are often incorporated into other methods (e.g., Conjugate Gradient, Newton) when round off destroys some desirable theoretical properties, progress is slow, or regions of indefinite curvature are encountered.

In the linear system  $Ax = b$  suppose the coefficient matrix  $A$  is symmetric and positive definite. Solving  $Ax = b$  is equivalent to minimizing the quadratic function

$$Q(x) = \frac{1}{2}x^T Ax - x^T b \quad \text{A.1}$$

The exclusive reliance on gradients by the steepest descents method is both its weakness and its strength. Convergence is slow near the minimum because the gradient approaches zero, but the method is extremely robust, even for systems that are far from harmonic. It is the method most likely to generate the true low-energy structure, regardless of what the function is or where the process begins. Therefore, the steepest descents method is often used when the gradients are large and the configurations are far from the minimum. This is commonly the case for initial relaxation of poorly refined crystallographic data or for graphically built models. In fact, as explained in the following sections, more advanced algorithms are often designed to begin with steepest descents as the first step.

## Appendix B

### Adopted Basis Newton-Raphson (ABNR)

M. Karplus and D.J. States developed the adopted basis Newton-Raphson method originally. A derivative method that is suited for large system such as proteins is the adopted basis Newton-Raphson algorithm [191]. Instead of calculating the full dimensional curvature (i.e., the full Hessian matrix) at each minimization step, this ABNR method limits its calculation. In the ABNR minimization the Newton-Raphson scheme is only applied in a small subspace of the molecule. So the whole displacement of the geometry is a combination of a steepest descent (SD) step plus a small contribution of Newton-Raphson (NR).

$$\Delta q_k = \Delta q_k^{SD} + \Delta q_k^{NR} \quad \text{B.1}$$

At the beginning of the minimization only the steepest descent component is employed ( $\Delta q_k^{NR} = 0$ ). After several SD steps, the last  $m$  geometry displacements can be used as basis  $\{\Delta q_{lk}\}_m$  of dimension  $m$  to obtain the NR step. So at step  $k$  the last  $m$  geometries are used  $q_l; l = k - 1, k - 2, \dots, k - m$

$$\Delta q_k^{NR} = \sum_{l=1}^m \Delta q_{lk} c_{lk} \text{ where } \Delta q_{lk} = q_{k-l} - q_k \quad \text{B.2}$$

This equation can be approximated in a Taylor expansion with respect to  $q_k$  and then the Newton-Raphson become

$$\sum_{l'=1}^m \sum_{l=1}^m \Delta q_{kl'} \cdot [g(q_{k-l}) - g(q_k)] c_{lk} = - \sum_{l'=1}^m \Delta q_{kl'} \cdot g(q_k) \quad \text{B.3}$$

## Appendix C

### Smart algorithm

Materials Studio uses smart minimization [192], which automatically combines appropriate features of several methods in a "cascade". Smart Minimizer starts with the steepest descent method and is followed by the conjugate gradient method. Steepest descent is the method most likely to generate a lower-energy structure, regardless of what the function is or where it begins. It will quickly reduce the energy of the structure during the first iteration, and is efficient for the first 10 - 100 steps. However, convergence will slow down considerably as the gradient approaches zero. It is often used when the gradients are very large, and the configurations are far from the minimum. The conjugate gradient method improves the line search direction by storing information from the previous iteration. It is the method of choice for systems that are too large for storing and manipulating a second derivative matrix. The time per iteration is longer than for steepest descents, but this is more than compensated for by efficient convergence. In Materials Studio you can set the level of accuracy (target minimum derivative) required for convergence. The atomic derivatives can be summarized as a root-mean-square (rms) value, the derivative. The minimization is stopped if the derivative is smaller than the target minimum derivative. The default values are respectively 1000 and 10 kcal/molÅ for the steepest descent and conjugate gradient method. To reduce the calculation time, in this study the maximum number of iterations is 10000. The minimization stops after reaching the convergence level.

## Appendix D

### Paper presented at conferences

M. Gandamipfa, P.E. Ngoepe and L. Ackermann," Feasibility study of DFTB+ parameterization Li, Ti and O systems"., Presented at South African Institute of Physics (SAIP) 57th Annual Conference, held at the University of Pretoria, in July 2012.

M. Gandamipfa and P. E. Ngoepe," Self-Consistent-Charge Density-Functional Tight-Binding (SCC-DFTB) Set of Parameters for Simulation of Bulk and Molecular TiO<sub>2</sub> nanotubes "., Presented at University of Limpopo Post-graduate Research Day (Faculty of Science and Agriculture), held at Bolivia Lodge, in October 2012.

M. Gandamipfa, P.E. Ngoepe and L. Ackermann," Computational study of anatase TiO<sub>2</sub> nanotube as an anode material for lithium ion batteries "., Presented at Academy of Science of South Africa (ASSAf) Third Annual South African Young Scientist's Conference, held at the CSIR International Convention Centre, in October 2012.

M. Gandamipfa, Yury Shukrinov, *et al.*, "Computer simulation of tunneling characteristics of superconducting nanostructures ", Presented at 7th SA-JNIR Student Practice Dubna-Russia 2013.

M. Gandamipfa and P.E. Ngoepe, "TiO<sub>2</sub> NANOPARTICLES ANODE MATERIAL FOR EFFICIENT STORAGE DEVICES", Presented at 2<sup>nd</sup> NATIONAL CONFERENCE ON GLOBAL CHANGE 2014, held at the Nelson Mandela Metropolitan University(South Campus), Nelson Mandela Bay, in 1-5 December 2014.

M. Gandamipfa and P.E. Ngoepe, "Feasibility studies of TiO<sub>2</sub> and LiTiO<sub>2</sub> polymorphs using Density Functional Based Tight Binding (DFTB+) ", Presented at XX International Scientific Conference of Young Scientists and Specialists (AYSS-2016), held at the JNIR, Dubna-Russia 2016, in 14-18 March 2016.

M. Gandamipfa and P.E. Ngoepe, "Computational study of anatase TiO<sub>2</sub> nanotube as an anode material for lithium ion batteries", Presented at The 9<sup>th</sup> International

Conference of the African Materials Research Society (AMR-2017), held at the Gaborone, Botswana, in 11-14 December 2017.

M. Gandamipfa and P.E. Ngoepe, "SCC-DFTB parameterization of potentials for simulation of pure TiO<sub>2</sub> and lithiated TiO<sub>2</sub>", Presented 12<sup>th</sup> CHPC National Conference, held at the Century City Convention Centre, Cape Town, in 2-6 December 2018.



# Appendix E

## Acronyms

**LIB** – Lithium ion battery

**TNT**– TiO<sub>2</sub> nanotube

**TNP**– TiO<sub>2</sub> nanoporous

**NT**– Nanotube

**HF**– Hartree-Fork

**DFT**– Density functional theory

**SCC-DFTB** – Self consistent charge density functional tight binding

**SKF**– Slater Koster file

**LCAO**– Linear combination of atomic orbitals

**GGA**– Generalised gradient approximation

**LDA**– Local density approximation

**MD** – Molecular dynamics